UNIVERSITÀ DEGLI STUDI DI PARMA

DOTTORATO DI RICERCA IN INGEGNERIA CIVILE E ARCHITETTURA

UNIVERSITÀ DI PARMA

XXXI CICLO

Flexible barriers against rapid events: interaction with moving masses and structural behavior control

---

Coordinatore:

Chiar.mo Prof. Andrea Carpinteri

Tutore:

Chiar.mo Prof. Andrea Segalini

Co-tutore:

Chiar.mo Prof. Roberto Brighenti

Dottoranda:

Laura Spaggiari

Anni 2015/2018

I have never let my schooling interfere with my education

(Mark Twain)

Declaration of originality

I hereby declare that all work presented in this thesis is my own work, and all else is appropriately referenced.

Declaration of copyright

Contents

List of Figures

List of Tables

Chapter 1: Introduction

Nowadays, hydrogeological instability is a very critical issue for our country because of its impact on population, infrastructures and economic and productive sectors. Italy, due to its particular geological, geomorphological and hydrographic conformation, is naturally predisposed to failure phenomena. After the Second World War, the intense urbanization, which took place without considering the areas where dangerous and potentially harmful hydrogeological events could occur, led to an increase of the exposed and vulnerable elements and, therefore, of risk. In addition, climate changing caused an increase of the frequency of extreme weather events and, consequently, of dangerous and destructive natural phenomena. This makes essential to use more advanced and reliable defense technologies, which are able to guarantee high performance and reliability.

Flexible and permeable structures are ideal for stopping natural phenomena characterized by rapid moving masses, thanks to their high deformation capacity and their water permeability. Differently from rigid walls, they distribute the impact energy over longer impact duration and thus reduce the peak impact force (Boetticher et al. 2011). In recent years, the use of flexible barriers has become very frequent; the reason is that, compared with rigid structures, these systems can be easily installed in irregular and narrow mountain areas, with less costs for transport and lower impacts on natural environment.

Rigid barriers were widely used in the past for mitigation of risk connected to several phenomena like rockfalls and debris flows. Therefore, thanks to a large engineering experience, their designed method and behavior are known. This does not apply to flexible systems, design of which is still characterized by a high level of uncertainty.

For this type of structures, which are often installed in sites difficult to reach, is essential to guarantee high performances in terms of structural efficiency and reliability, but also to have some information about their functioning over time. The latter purpose can be made possible only by automatic monitoring systems, which can register the structural changes of the barriers and send remotely the data without any direct intervention of technicians, saving time and money.

This study is born in conjunction with Incofil Tech Srl, a company that, for several years, has intensified its activities into slope consolidation systems and protection against unstable rock blocks and avalanches through flexible barriers. This project was made possible also thanks to the Autonomous Province of Trento that, through Law n. 6/1999, has provided a substantial financing to support these research activities.

The main objective of the present work is to improve the existing protection barriers through both the development of a new energy dissipation device, which guarantee higher structural performances, and the implementation of an innovative monitoring system, that allows to control remotely these structures after their installation (Figure 1.1). With this new monitoring technology, it will be possible

to obtain information regarding the wear status of the barrier and indications about some natural phenomena in progress. The improved monitoring database deriving from data acquired from this system will be useful for planning territory safety interventions; this aspect is very important especially for public bodies, because it represents a tangible support to choose where is better to invest money for slope stabilization and when to carry out maintenance works. A widespread use of these solutions will give the possibility to have an updated slope scale mapping of the natural events occurring. In this way, the territory will be characterized by different space-time risk coefficients, allowing statistical elaborations and forecast model implementation.
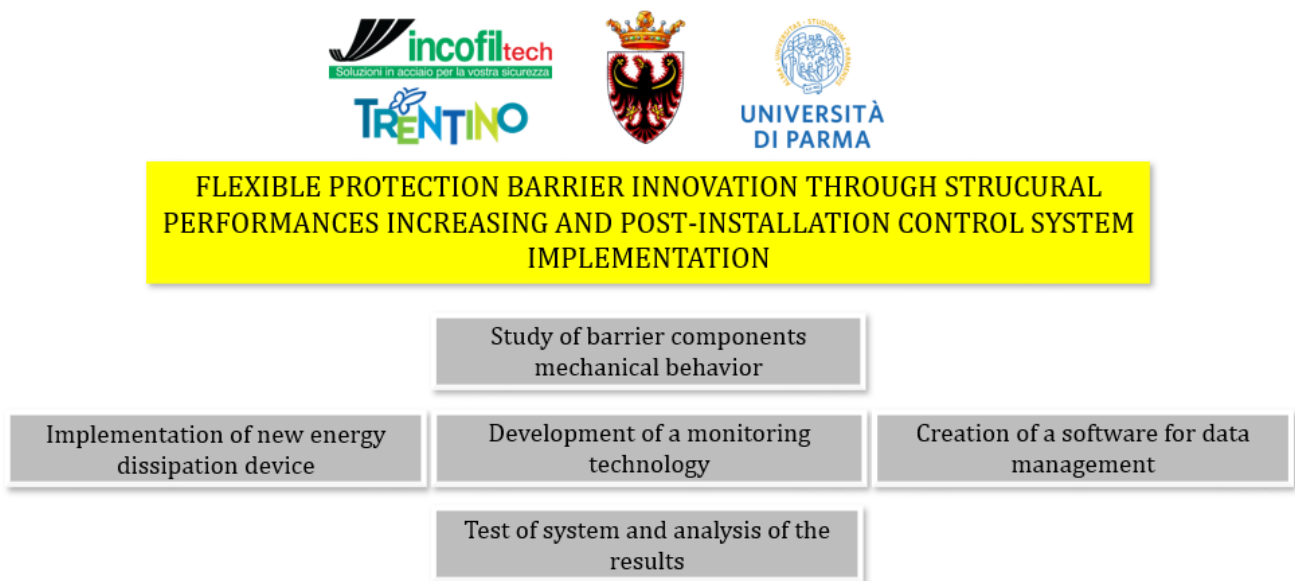
Figure 1.1: Objective of the project supported by the Autonomous Province of Trento, which made possible the most activities of this research

Flexible barriers are usually identified based on the boulder energy they can withstand. This approach is appropriated for rockfall phenomena but it is not applicable to debris flows, which are rapid mass movements composed by a mixture of solid particles of various sizes and water, generally originated from collapses (landslide, erosions etc.) and associated with extreme meteorological events. Because of their multi-phase nature, in which solid, fluid and air always interact and coexist, debris flows are a very complex phenomenon, difficult both to investigate and to simulate. Due to its velocity and unpredictability, it can cause loss of human lives and damages to environment and structures.

In order to safeguard the infrastructures and prevent victims is it important to understand the behavior of the protection system under the influence of these flows. For this purpose, Brighenti et al. (2013) proposed a simplified analytical model with the aim of estimating the tensions acting on the supporting cables, knowing the geometry and the mechanical features of the flexible barrier and the characteristics of the impacted debris flow. The most difficult aspect is the application of the simplified model regarded the calibration and validation of the model parameters, due to the limited amount of data available in the literature.

This study presents some results obtained from laboratory tests regarded the impact of a simulated debris flow against a scaled physical model of the barrier. A granular flow composed of aggregates of known particle size was released in a channel with variable inclination and known length and height. Using this experimental setup, several tests were carried out by varying the inclination of the channel and the geometry of the barrier; the flow velocity was monitored using a PIV camera (Particle Image Velocimetry), the height of the flow was monitored using ultrasonic level sensors and the forces on ropes were recorded using load cells.

In order to determine the required mechanical parameter for the barrier, a test procedure similar to the one proposed by Ferrero et al. (2015) on site was carried out in laboratory. Different static load combinations were imposed on each structural cable of the scaled barrier and the induced deformations were measured using a theodolite. This allowed studying how the load on each single cable influenced the deformation of the others. The results of this experimental study are very useful and can be taken as a good starting point for the application of the simplified analytical model for the analysis of real cases.

Chapter 2: Debris flow description and characterization

Debris flow is typically ascribed among landslides of flow type; this means that the rearrangement of grain contacts is pervasive during the motion, promoting significant internal distortion of the moving mass (Iverson 2014; Varnes 1978). To find a clear distinction between the flow-type phenomena in literature is not easy; moreover, the comparison between the definitions given by different Authors is often misleading. This Chapter gives a detailed review of scientific literature related to debris flow phenomena, in order to highlight the main characteristics and allow to understand the logic and thematic flow of this dissertation. Main geological and geomorphological evidences are discussed. Different references are considered and discussed to distinguish debris flow from other flow like landslide phenomena.

2.1 Classification and differences with other flow phenomena

Debris flows are very complex phenomena characterized by the presence of different materials and high water content. Several times the term debris flow is used erroneously to indicate different events. This is a consequence of two main reasons: the first is related to the complex and multiphase nature of the debris flow and the second is due to the scientific background of the authors. In fact, depending on their scientific field, the authors classified debris flow based on one (or more) of these features:

a) Water and solid content;
b) Grain size distribution;
c) Channel presence (channelized or shallow debris flow);
d) Triggering mechanisms;
e) Morphological basin characteristics;
f) Mechanical properties of the flow.

Stini (1910) defined debris flow for the first time as a "viscous mass, consisting of water, soil, sand, gravel, rocks and wood mixed together". Some years later, Sharpe (1938) focused the attention on the characteristic rapid velocity of these events and defined the material of which a debris is composed.

Varnes (1954, 1978), and Cruden and Varnes (1996) included debris flow in the flow type landslide, giving a definition of debris as a material containing a percentage of particles larger than 2 mm ranging from 20% to 80%; moreover, they individuated the range of the characteristic velocity from 0.5 to 20 m/s.

Hutchinson (1988) studied the morphology, the kinematics, failure and propagation mechanism, besides material and rate of movement; he described the important role of water supply and increasing pore pressure for the mobilization of the flow masses.

Hungr et al. (2001) gave one of the most famous definition of debris flow as a rapid to extremely rapid flow of saturated non-plastic debris in a steep channel (Plasticity Index <5% in sand and finer fraction), focusing on genetic and geomorphological aspects, avoiding a taxonomic hierarchical description that consider either movement mechanism, material properties or movement velocity.

Considering landslides of flow type only, the material involved can be characterized by its origin, its degree of cohesion and pore pressure conditions (Table 2.1). Materials involved in debris flow range from clay to boulder of several meters. The latter definition was successively modified by Hungr et al. (2014), which added the adjective "surging" to described the transient nature of this events, that occur in a series of different multiple surges. Strong entrainment capability of material and water also characterized these phenomena, thus increasing size up to 10^9 m^3 (Figure 2.1). The Authors also highlighted the relevance of the debris flow lateral confinement: the flow occurs on an established channel, thus enhancing rapidity and water content.

Figure 2.1: Aerial photo of mountain debris flow in Mesa County, Colorado (www.airphotona.com)

Beyond these definitions, it is important to underline the extremely rapid propagation of these phenomena: they move with a velocity of the order of 10 m/s, with maximum of 80 m/s and travel distance between 1 and 10 km. Summarizing, the main ingredients for the generation of debris flow are a great amount of water (e.g. heavy rainfall, snow and ice melting, dam break events, etc.), the presence of erodible/transportable debris and land instability. The system generated by the interaction of these elements is very complex to predict and has a very high destructive power.

In order to clarify the main features of debris flow, the comparison with other flow type landslides, to which debris flow is sometimes equated, can be very useful. In Table 2.2 and Table 2.3 the most important features through which a debris flow can be identified are listed according to Varnes (1978) and Hungr et al (2001). One of the clearest sediment flows classification was given by Pierson and Costa (1987), who considered the sediment concentration and grain-size distribution as fundamental parameters to rheologically distinguish debris flow phenomena from the others.

Table 2.1: Characteristics of the materials involved in flow type-landslides (Hungr et al. 2001)

Origin	Character	Condition[1]	Name
SORTED (marine, lacustrine, fluvial, eolian, volcanic, anthropogenic)	Non-cohesive (Plastic Limit < 5%)	Dry or saturated	– Gravel – Sand – Silt
	Cohesive (Plastic Limit < 5%)	– Plastic ($I_L < 0.5$) – Liquid ($I_L > 0.5$)	– Clay – Sensitive clay
UNSORTED (residual, colluvial, glacial, volcanic, anthropogenic)	Non-cohesive (Plastic Limit < 5%)	Dry or saturated	– Debris[2]
	Cohesive (Plastic Limit < 5%)	– Plastic ($I_L < 0.5$) – Liquid ($I_L > 0.5$)	– Earth – Mud
PEAT	Organic	Saturated	– Peat
ROCK	Fragmented	Dry or saturated	– Rock

[1] Related to the material found in the vicinity of the rupture surface at the time of failure, if it can be determined. In many cases, the material condition must be deduced from the behavior of the landslide, especially velocity

[2] Debris may contain a considerable proportion of organic material

Table 2.2: Main characteristics of the landslides of the flow type according to Varnes (1978)

Rate of movement	Bedrock	Debris (<80% sand and finer)	Debris (>80% sand and finer)
Rapid and higher (>1.5 m/day)	Rock flow (creep, slope sagging)	Debris flow Debris avalanche	Wet sand and silt flow Rapid earth flow Loess flow Dry sand flow
Less than rapid (<1.5 m/day)		Soilfluction Soil creep Block stream	Earth flow

Figure 2.2 describes the relationship between debris flow and the yield strength (Pierson and Costa, 1987) and highlights the importance of the sediment concentration and grain-size distribution in the identification of these type of phenomena. The left boundary B marks the rapid increase of yield strength. Before this limit, the phenomenon is called hyperconcentrated stream flow. The concept of hyperconcentrated streamflow is similarly expressed by Hungr et al (2001), who introduced the debris flood as a very rapid surging water flow, but whose sediment concentration is comparable with debris flow one.

Another phenomenon similar to debris flow is called mud flow, whose difference lies in the plasticity of the debris and water mixture, with a plastic index major of 5% (Hungr et al., 2001). This feature gives cohesion to the material, while debris flow is in general considered as a non-cohesive material flow.

Table 2.3: Flow-type landslides most important features, according to Hungr et al (2001)

Material	Water content[1]	Special condition	Velocity	Name
Silt, sand, gravel and debris (talus)	Dry, moist or saturated	No excess pore-pressure Limited volume	Various	*Non-liquefied sand (silt, gravel, debris) flow*
Silt, sand, debris and weak rock[2]	Saturated a rupture surface	Liquefiable material[3] Constant water content	Extremely rapid	*Sand (silt, debris, rock) flow slide*
Sensitive clay	At or above liquid limit	Liquefaction in situ[3] Constant water content[4]	Extremely rapid	*Clay flow slide*
Peat	Saturated	Excess pore-pressure	Slow to very rapid	*Peat flow*
Clay or earth	Near plastic limit	Slow movements Plug flow (sliding)	Less than rapid	*Earth flow*
Debris	Saturated	Established channel[5] Increased water content[4]	Extremely rapid	*Debris flow*
Mud	At or above liquid limit	Fined-grained debris flow	Greater than very rapid	*Mud flow*
Debris	Free water present	Flood[6]	Extremely rapid	*Debris flood*
Debris	Partly or fully saturated	No established channel[5] Relatively shallow, steep source	Extremely rapid	*Debris avalanche*
Fragmented rocks	Various, mainly dry	Intact rock at source Large volume[7]	Extremely rapid	*Rock avalanche*

[1] Water content of material near the rupture surface at the time of failure.
[2] Highly porous, weak rock (examples: weak chalk, weathered tuff, pumice).
[3] Presence of full or partial liquefaction of the source material of the flow slide may be observed or implied.
[4] Relative to in situ source material.
[5] Presence or absence of a defined channel over a large part of the path, and an established deposition landform (fan). *Debris flow* is a recurrent phenomenon within its path, while *debris avalanche* is not.
[6] Peak discharge of the same order as that of a major flood or an accidental flood. Significant tractive force of free flowing water. Presence of floating debris.
[7] Volume greater than 10.000 m^3 approximately. Mass flow, contrasting with fragmental rock fall.

Figure 2.3 shows the mechanical classification of Takahashi (1978, 2007), the Author stated that a complete dynamic development of debris flow also depends on the solid concentration C_S, which has to be $0.2 \leq C_S \leq 0.56$. If $C_S \geq 0.56$ neither dynamic nor quasi-static debris flow is possible and the material becomes rigid (Marchelli, 2018). This matches with the definition provided by Pierson (1986). Three different types of debris flow have thus been identified:

1) Stony type: when the inertial grain stresses prevails;
2) Turbulent muddy type: when the inertial fluid stresses prevails;

3) Viscous type: when the viscous stresses prevails.
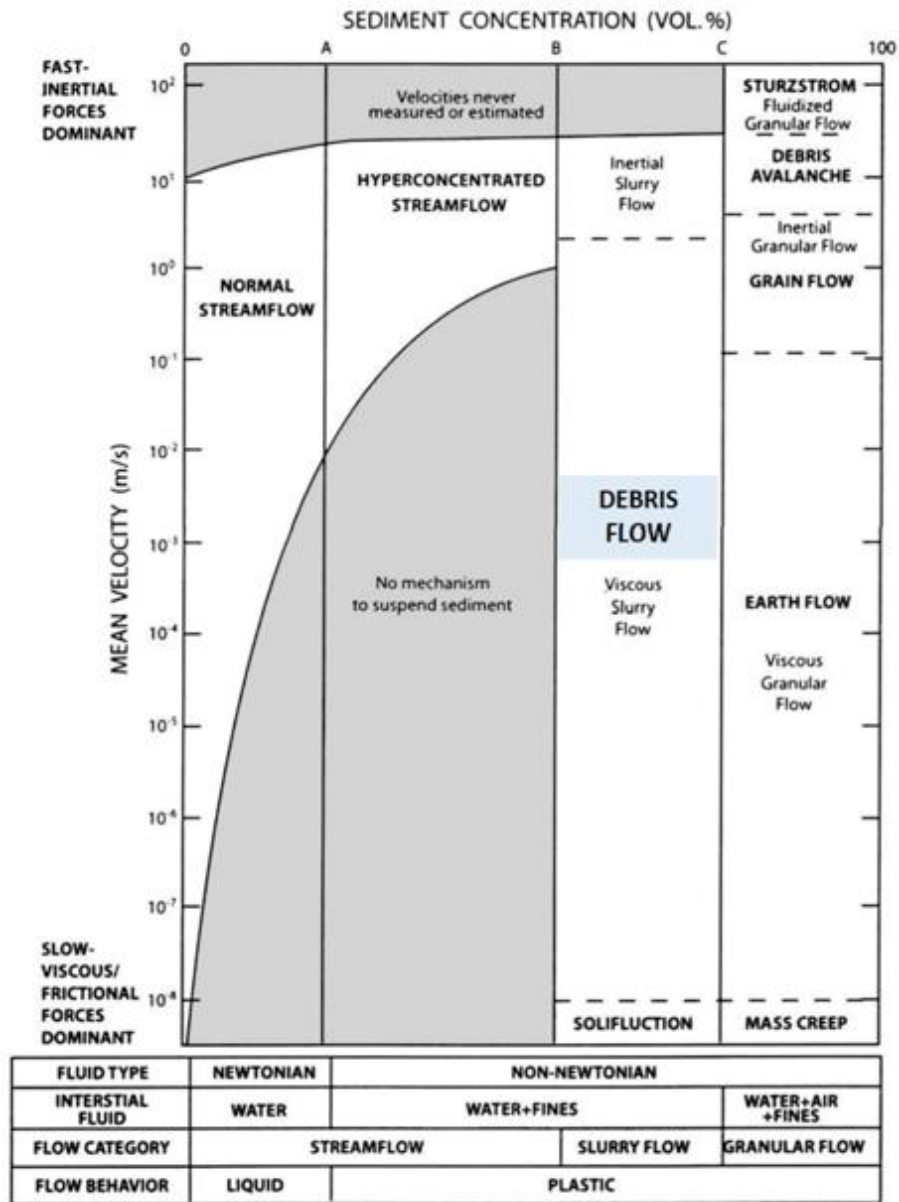
Figure 2.2: Rheological classification of sediment flows. Unified version of two schemes proposed by Pierson and Costa (1987). Exact values of the boundaries of sediments volume concentration cannot be defined, as they depend also on grain-size distribution and physical-chemical composition of the material.

Takahashi (2007) grouped the stony and the turbulent types in a unique category called inertial debris flow. Nevertheless, this classification does not consider the rheological aspects, due to the solid-fraction.

Fine particles refer to clay and sand, i.e. particles whose main size is minor than 0.04 mm. In view of this Coussot and Meunier (1996) distinguished two types of debris flow:

1) Muddy debris flow: in this case the fine fraction is large enough (more than 10%) to lubricates the grain and imposes its behavior on the whole mass;

2) Granular debris flow: the fine fraction is so low that the coarse grain contacts play the major role on the mass behavior.

Ancey (2001) and two years later Bardou et al. (2003) developed a complete classification of these events, accounting for both the mechanical and the rheological aspects. Particularly, they distinguished three types of debris (Table 2.4):

1) Muddy debris flow: this type is characterized by a viscoplastic behavior, due to the high content of fine material, containing clay. The liquid and fine particles lubricate the contacts between the coarse particles. As the matrix is more dilute, this kind of debris flow generally reaches longer runout distance and presents a deposit where the coarser grains are randomly distributed in a finer matrix. According to the fine content, either turbulent stress or viscous stresses are involved. Particularly, the more dilute the fluid is, the more the turbulent stress prevails;

2) Granular debris flow: the mechanical behavior is collisional and frictional. The prevalence of inertial grain stress to the frictional one depends on different factors, such as the internal frictional coefficient, the solid concentration, and the steepness of the slope;

3) Fluid or lahar-like debris flow: this type has a frictional-viscous behavior, due to a high fine content. This kind of flow is typical of volcanic soil areas. The clay content is small, but the matrix is rich with silt.
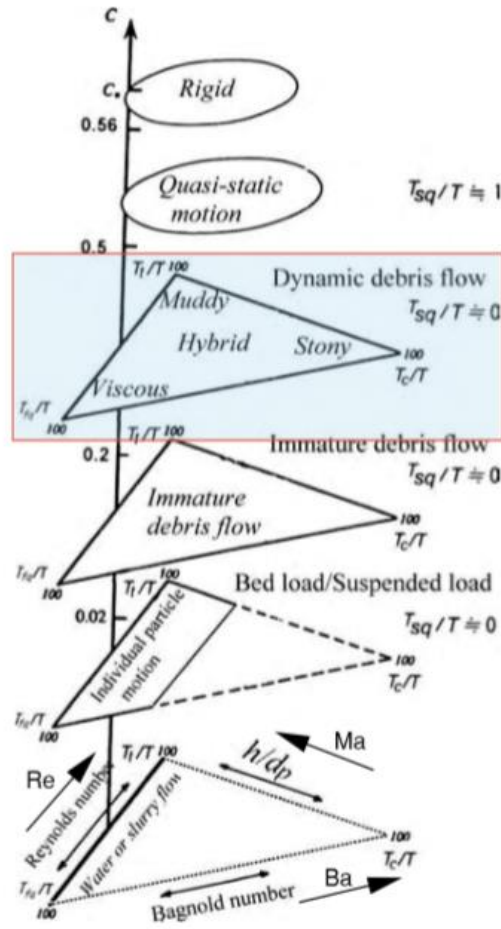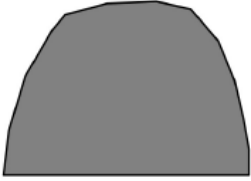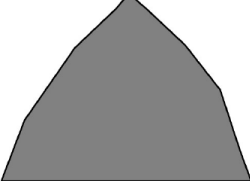
Figure 2.3: Mechanical criterion to classify the debris flow types (Takahashi, 2007). The total stresses are represented with the symbol T. The immature debris flow corresponds to the hyperconcentrated streamflow, while the quasi-static motion corresponds to the earth flow

Table 2.4: Classification of debris flow types according to Ancey (2001) and Bardou et al. (2003)

Scientific name	Viscoplastic	Collisional-frictional	Frictional-viscous
Appropriate rheophysical model	Hershel-Bulkley Bingham	Coulomb-like, collisional-frictional constitutive equation	Coulomb-like at low speed Newton-like (or power-law) at high speed
Common name	Muddy	Granular	Fluid
Deposit appearance	Smooth with clear limits in the field, very cohesive once dry Levee cross-section	Rough with no clear deposits limits in the field, non-cohesive once dry Levee cross-section	Terrace-like deposit, very cohesive once dry Whole body cross-section (not the same scale as levee cross section sketch)
Stopping slope	< 2°	< 10°	< 1°

Grain size	Grains ++ Matrix++ Clays+	Grains ++ Matrix- Clays--	Grains ++ Matrix- Silts + Clays--

The following notation is adopted:

-- Very little content

- Little content

+ High content

++ Very high content

Table 2.5: Correlation among the different nomenclature given from several Authors

Authors	Muddy debris flow	Granular debris flow	Fluid debris flow
Varnes (1954)		Debris flow	
Hutchinson (1988)	Debris flow involved weathered rock debris (except on volcanoes)	Channelized debris flow	Associated with volcanoes, lahars
Takahashi (1978)	Viscous type debris flow	Stony type debris flow	Turbulent muddy debris flow
Coussot & Meunier (1996)	Muddy debris flow	Granular debris flow	-
Hungr et al. (2001)	Mudflow	Debris flow	-
Ancey (2001)	Muddy debris flow	Granular debris flow	Lahar debris flow
Bardou et al. (2003)	Muddy debris flow	Granular debris flow	Lahar debris flow

Finally, Table 2.5 summarize different nomenclatures provide over time by different Authors, distinguishing the above-mentioned three categories. It's evident that to find a unique classification is still difficult and some debris-flow type can be associated to other landslide of flow type.

2.2 Parameters involved in debris flow events

The main geological and geomorphological parameters that should be taken into account studying debris flow phenomena are summarize in the following paragraphs.

2.2.1. Areal extension and debris flow magnitude

The first parameter is the areal extension, and consequently the volume of the debris flow deposit. From the point of view of the evaluation of a potential hazard and the design of any protection measures, the magnitude of debris flow is one of the most important parameters, because it can be correlated with peak discharge, total travel distance and flow velocity.

In Alpine regions, the magnitude of debris flow does not exceed the 10^5 m^3 (Rickenmann 1999), corresponding to a class 3 of the debris flow magnitude classification (Jakob 2005). The moderate magnitude is consequence of the relatively small basin where debris flow can occur: in fact, a study of Bianco (1999) shows that the 84% of debris flow events occur in basin with an area extension between 1 and 10 km^2 (the dataset include 150 debris flow events occurred in Italy and France).

2.2.2. Channel bed slope

Basin slope, and in particular channel bed slope, is one of the first parameter to analyze in the study of debris flow events. This parameter is easy to obtain and can immediately reveal information about possible debris instabilities and flow formation.

Table 2.6: Correlation between channel bed slope and debris flow phases

Channel bed slope	Debris flow phase
> 20°	Initiation
15° ÷ 20°	Transportation and erosion
10° ÷ 15°	Run-out
3° ÷ 10°	Partial deposition
< 3°	Deposition (debris fan)

Many researchers (Takahashi 1978, Rickenmann and Zimmermann 1993, Baoyuan et al. 1994, D'Agostino 1996, Van Dine 1996), basing on the observation of real events, have distinguished all the debris flow phases (Initiation, Transportation and erosion, Run-out, Partial deposition, Deposition) on the basis of the slope values of the channel. The results are summarized in Table 2.6.

2.2.3. Entrainment

The entrainment of material during the debris flow run-out is a fundamental parameter to take into account for hazard mapping and design of countermeasures. The presence of loose material, potentially instable, along the debris flow path can considerably increase the initial debris flow volume (McDougall and Hungr, 2005; Breien et al., 2008). The entrainment depends on:

a) Direct erosion of the most erodible fraction of the channel bed and bank during debris flow transportation phase;

b) Deposits of loose material of different nature (stream transport, glacial origin, moraine etc.) located along the channel;

c) Contemporary landslides in the same basin.

2.2.4. Triggering factors

Snow melting and rainfalls are debris flow triggering factors. The great amount of water and the reduction of soil cohesion, as a consequence of the snow melting during spring/summer season, cause a progressive reduction of the soil resistance and generate debris mobilization. It is difficult to quantify and forecast the water content that triggers landslides, but, for the design of countermeasures, this aspect has to be taken into account.

About rainfall, the most important issue is the definition of triggering threshold, which is a function of the duration and the intensity of the event and can be defined on the basis of the analysis of rain values. For example, Baravalle (1999) analyzing the rainfall values of 44 events recorded in Susa Valley (Piedmont, Italy), observed that the mean intensity related to debris flow phenomena varied between 0,97 and 12,56 mm/h and the duration between 3,5 and 95,5 h.

2.2.5. Human factors

Any man-made modifications in the basin that can change the flow path, reducing or increasing the potential unstable volume. For instance, the presence of quarry and debris landfill can increase the debris flow magnitude or, vice versa, the presence of active countermeasures can stabilize the slope, reducing the basin vulnerability.

2.3 Dynamics of the phenomenon

Debris flow typically involves a sequence of events (Iverson, 2014). Vagnon (2016) provided the following descriptions of the parameters involved during debris flow paths.

2.3.1. Triggering condition and mobilization

Necessary conditions to mobilize debris flow are identified and discussed below:

a) Heavy presence of unconsolidated materials: both in the initiating zone and along the channel a large amount of fine-grained rocks or soil debris is required, promoting a high weathering;

b) Steep slope: this aspect determines the instability of the marginal stable debris, especially when saturated. Furthermore, the steeper the channel is the higher the velocity of the following mass will be;

c) Large source of moisture and excess of pore pressure: a large but intermittent source of moisture is required for sediments saturation. This can be produced by rainfall, snowmelt,

glacial outburst floods and rapid drainage of volcanic crater lakes. In general, the most common situation occurs after long periods of continuous rainfalls, after which the soil remains partially saturated, with negative pore pressure. Then, a subsequent high intensity rainfall causes the saturation and, consequently, an abrupt positive pore-pressure situation occurs in the debris;

d) Sparse vegetation: a slope denude of vegetation intensifies the susceptibility to debris flow. This condition, according to Varnes (1978) can be enhanced by wildfires.

Iverson et al. (1997) defined the mobilization as the process by which a debris flow develops from an initially static, apparently rigid mass of water-laden soil, sediment and rock. Several Authors (Armanini, 1997; Coussot and Meunier, 1996; Iverson et al., 1997) investigated the main types of initiation processes, which can be described as:

a) Erosion of the surface of the initiating zone and mobilization of sediments: the marginally stable debris mantle becomes saturated by an intense rainfall or thawing processes and begins its motion;

b) Progressive transition of a sliding phenomenon into a debris flow: sliding-type landslides generally differ from debris flow as the latter allows internal deformations during its motion. This transition requires a sufficient conversion of gravitational potential energy into internal kinetic energy. This conversion can derive from a slope increase or from a supply of water. Nevertheless, Iverson et al. (1997) highlighted also that the required amount of water to generate this transition does not necessarily cause a complete saturation of the mass;

c) Collapse of a natural dam formed in the riverbed of a retaining system hit by an initial debris flow: a consistent volume of debris is abruptly released, promoting a debris flow event.

2.3.2. Path and shape evolution

It is widely recognized that a debris flow path can be clearly subdivided into an initiating, a transport and a deposition zone, whose characteristics are quite different (Vagnon, 2016). In these three steps of motion, the debris flow assumes different configurations.

Initiating zone

The initiating zone is characterized by its slope angle, which is one of the most influential triggering conditions. Several Authors propose significantly different values of the slope inclination required to promote debris flow initiation; this may be partly attributable to the geographic area of interest. Table 2.7 shows an overlook of the steepness values indicated by different Authors.

Table 2.7: Slope angle required to generate a debris flow in the initiating zone according to different Authors

Authors	Muddy debris flow	Observed area	Note
Takahashi (1978)	15° ÷ 23°	China and Japan	From infinite slope theory, inertial regime according to Bagnold, 1997
Costa (1984)	> 15° ÷ 20° commonly exceeded 30°	All the world	From observation of real cases
Ancey (2001)	> 11°	All the world	From laboratory experiments
Hungr et al. (2001)	20° ÷ 45° (in steeper slope the required amount of debris is not in general sufficient)	Not specified, examples from Canada and Nepal	From field observation
Iverson (2014)	> 25° generally 25° ÷ 30°	Not specified, examples from USA	From observation of real cases

Transportation zone

The transportation zone is constituted by either a bedrock channel generally covered by erodible soil or a fully erodible channel and steeper than 10°. In this stage, the velocity of the flow increases, ranging from 0.5 to 20 m/s, according to the size, the concentration and the sorting of the material, and to channel geometry. During its motion, the debris flow generally entrains loose material and water from the bed and the banks, thus growing in size. The volume increase can be even tenfold or more (Iverson, 2014). Fannin and Wise (2001), from several field observations on the Queens Charlotte Islands debris flow events, observed that, along a debris flow transportation zone, entrainment dominates for slopes greater than 10°, while deposition is not an important factor.
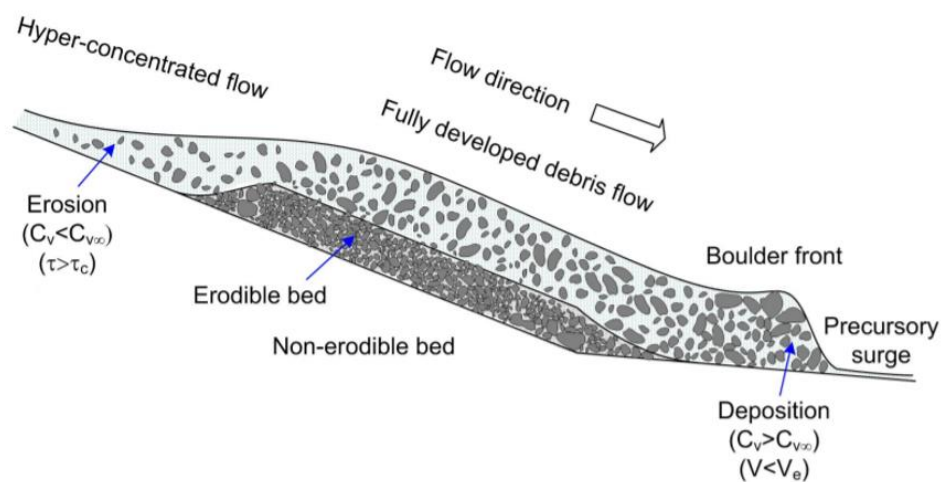
Figure 2.4: Erosion, deposition and property changes in debris flow (from H. X. Chen and L. M. Zhang, 2015)

During the motion, an inversely graded particle-size distribution can be observed, thus creating an upward coarsening. The small particles percolate downward, and the larger particles remain on the surface. Furthermore, the debris flow mass presents a vertical velocity gradient: the velocity profile shows higher velocity on top, so that the coarser grains, positioned on the surface, are pushed towards the front (Johnson et al., 2012). As a consequence, the flowing mass is characterized by a longitudinal sorting, which brings the largest clasts, or even boulders, towards the flow front, thus creating the so called head-and-tail morphology. This results in a bouldery front, relatively free of matrix, a main body of finer or liquefied debris, and a dilute tail (Figure 2.4). Thus, the front is characterized by a great permeability and high frictional resistance, while the body sustains high pore pressure, due to its lower permeability.

Deposition zone

When the whole kinetic energy of the flowing mass degrades to an irreversible form, i.e. the grain vibrational energy progressively falls to zero, the deposition process begins (Iverson et al., 1997). The energy decrease is generally due to a combination of a slope reduction and a loss of confinement (Ancey, 2001) and occurs on an established fan, called debris fan, colluvial fan or cone (Hungr et al., 2005). As regards the former, Ancey (2001) stated that, in Alpine regions, debris flows usually begin to decelerate when the slope is 10% ÷ 25%, and can propagate over gentle slopes (of less than 5%). Nevertheless, the slope deposition angle is a function of the grain concentration by volume, density, size, the total volume, and the angle of the internal friction of the flowing mass (Takahashi, 2007). Hence, in fact, Hungr et al. (2001) stated also that in general fan slopes ranges from 5° up to even 20°.

Constant deposition rate can occur also along the whole channel during runout, forming the levees on the lateral boundaries of the channel, which act as additional banks. In this case, the deposition process can occur also before the loss of confinement. In fact, while lateral levees arise, the advancing flow head becomes thicker, and the progressive slope reduction causes the deposition of the granular front. Then, the sudden stop of the granular front increases the flow depth of the body, promoting its overflow over channel banks and spreading as broad lobes (Ancey, 2001).

Chapter 3: Rockfall phenomena overview

Differently from debris flow, rockfalls are very well-known phenomena, which affect the mountainous regions all over the world (Figure 3.1). This Chapter gives a detailed description of rockfall phenomena, in particular their main characteristic and triggering factors are illustrated; different references are shown and discussed to provide a unique definition and characterization of these natural events.

Figure 3.1: Glenwood Canyon rock fall in Colorado, 2010 (www.codot.gov)

3.1. Definition and differences with other bedrock mass movements

A rockfall is a fragment of rock (a block) detached by sliding, toppling or falling that falls along a vertical or sub-vertical cliff, proceeds down slope by bouncing and flying along ballistic trajectories or by rolling on talus or debris slopes (Varnes, 1978).

These events are defined catastrophic mass movements because their weight and vertical falls distances (which define the potential energy of the rocks before their motion), which produce very high and dangerous kinetic energy. For these reasons rockfalls are the most frequent cause of landslide fatality, even when elements at risk with a low degree of exposure are involved, such as traffic along highways (Bunce, 1997).

Rockfall blocks size depends on bedding planes, joints and fractures that form mechanical discontinuities and allow the blocks to become detached from the slope. Fracture lengths and

volumes follow power law or fractal distributions, meaning that their numbers decrease exponentially as fracture length or rockfall volume increases.

The classification provided by Varnes (1978) and updated by Cruden and Varnes (1996) individuates five type of bedrock mass movements (rockfall, rock topple, rock slides rock spread and rock avalanches). Hungr et al. (2014) added slope deformation as movement type that for rock material includes mountain and rock slope deformation as subtypes of movement based on the scale of the deformation. A synthetic description of these phenomena, given by Brideau and Roberts (2014), is reported below.

Rockfall

As described before, rockfall is a bedrock mass movement on steep slopes, the dynamics of these events include free falling, rolling, bouncing and sliding motions. The initiation of a rockfall failure mechanism can occur via most of the structurally controlled failure modes and through the development of intact rock fractures.

A rockfall event can include several pieces of rock falling at the same time, but differs from a rock avalanche because it does not involve significant interactions between single blocks (Hungr and Evans, 1988).

Rockslides

Sliding in rock can occur along single planar, circular and compound surfaces or, as in the case of wedge failure, sliding along the intersection of two planes (Brideau and Roberts, 2014). Rockslides take place along discrete surfaces or relatively thin failure zones of intense shear strain (Cruden and Varnes, 1996). They can have a wide range of volume from an individual sliding block to some of the largest landslides known on Earth (Philip and Ritz, 1999; Hancox and Perrin, 2009; Pedrazzini et al., 2013; Roberts and Evans, 2013).

These landsides often have a rapid to extremely rapid velocity. Large rockslides commonly become a rock avalanche as the failed mass fragments during the transport phase, these phenomena are the most mobile mass movements.

The failure surfaces or planar slides are generally associated with stratigraphic contacts (e.g. bedding) or metamorphic fabric (e.g. schistosity), which provide mechanical zone of weakness and preferential groundwater paths or permeability contrast (Hodge and Freeze, 1977; Loew and Strauhal, 2013).

Circular and compound slides represent a continuum between mass movements controlled by the rock mass strength (circular) to an increasingly important structural control on the failure surface (compound to planar).

Rock spreads

The two types of lateral spreading based on the loading that drives the bedrock mass movement are dynamic and static. Lateral spreading most commonly occurs because of liquefaction of a seismically (dynamically) loaded saturated granular basal layer (or remolded sensitive clay) upon which the overlying material moves laterally (Seed and Wilson, 1967; Updike et al., 1988; Cubrinovski et al., 2012; Hungr et al., 2014). Kinematic freedom of spreading is facilitated by the presence of a free boundary (e.g., riverbank or shoreline) next to a soil and rock mass with a horizontally layered stratigraphy (Kramer, 2013). In surficial material lateral spreading tends to occur rapidly (cm/s), with displacement varying between centimeters and tens of meters. The volume affected can be in the range of millions of cubic meters.

Lateral spreading in bedrock is commonly associated with deep-seated slope deformation (Figure 3.2) as large stresses and some degree of material confinement are needed to produce ductile deformation of the weaker underlying material (Dramis and Sorriso-Valvo, 1994; Bozzano et al., 2013). Static lateral spreading can transport large (hundreds of meters wide, by tens of meters long and thick) intact bedrock blocks of stratified sedimentary rock over large distances.
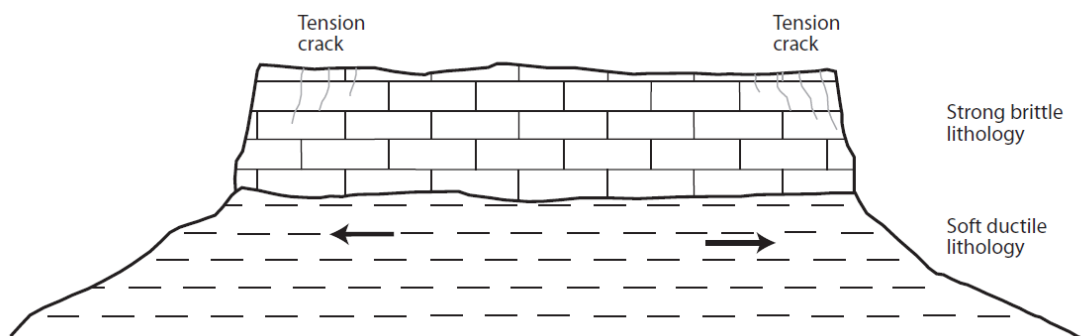
Figure 3.2: Rock spread occurs when a strong brittle lithology overlies a soft ductile one. Modified from Bozzano et al. (2013)

Rock avalanches

Rock avalanches result from rapid fragmentation of very fast-moving, initially intact rock masses during transport (Hungr et al., 2001). The fragmentation in a rock avalanche means that the term is associated with large-volume (>1Mm^3) bedrock mass movement, in order that overburden stresses are sufficient to cause dynamic fragmentation of intact rock in the moving mass.

The runout of large rock avalanche debris is longer than expected for equivalent volumes of granular material, and mobility of rock avalanche increases with volume. Scheidegger (1973) note that rock avalanche volume is inversely related to the ratio of vertical to horizontal travel distance. Hsu (1975) proposed that the term excess travel distance be used to express the

amount by which runout exceeds the expected value for an equivalent volume of granular material. Numerous mechanisms occurring during material transport of the landslide debris have been proposed to explain anomalously long runout (Davies et al., 1999; Legros, 2002; Davies and McSaveney, 2012). Recently broadband seismic signals have been used to locate large rock avalanches occurring in remote area (Ekstrom and Stark, 2013) and to investigate the dynamic processes occurring during transport (Yamada et al., 2013).

DSGSD

The term DSGSD (Deep-Seated Gravitational Slope Deformation) is commonly used to refer to the slow to very slow slope deformation processes (Figure 3.3). Geomorphic features that can indicate past or present DSGSD include grabens, trenches, uphill- and/or downhill-facing scarps, split ridges, and toe bulging (Varnes et al., 1989). Observations suggest that DSGSDs typically affect entire mountain slopes from the valley floor to ridge tops or even through the entire rock mass to the slope on the opposite side of the ridge (Agliardi et al., 2012). DSGSD typically occurs in areas with local relief greater than 500 m (Agliardi et al., 2013). The stress distribution derived from the interaction between the rock mass strength and topography plays an important role in the development of DSGSD features (Savage and Varnes, 1987; Varnes et al., 1989; Kinakin and Stead, 2005; Ambrosi and Crosta, 2011).

DSGSDs are regarded as the result of a long-term gravitation deformation of the slope (Soldati, 2013). Detailed stratigraphy and dating of tephra layers occurring in excavation of DSGSD trenches by McCalpin and Irvine (1995) suggest that the temporal displacement pattern associated with these mass movements was episodic. Moro et al. (2011) recently documented the episodic displacement of these features in associated with seismic events.

Complex bedrock mass movements

Complex landslides incorporate multiple mass movement types, distributed spatially or temporally, at a single site. This change in mass movement type is driven by a change in the kinematic conditions driving the failure mechanism (e.g., removal of material at toe of landslide due to fluvial erosion), material properties (e.g., weathering), or water content (e.g., traveling over a saturated substrate). Geertsema et al. (2006) and Geertsema and Cruden (2008, 2009) document a series of landslides in northern British Columbia where rock slope failure interacted with the surficial material in the runout zone to trigger debris or earth landslides.

Geertsema et al. (2006) suggest that the undrained loading from the initial rock slope failure caused mobilization of the surficial material and its subsequent 3.25 km runout. The entrainment (Khait landslide, Evans et al., 2009; Mount Meager landslide, Guthrie et al., 2012) or undrained loading (Brideau et al., 2012, 2006; Leyte Island landslide, Evans et al., 2007) of

saturated sediment in the valley bottom has been observed at numerous sites to influence the rheology of the failed mass and enhanced runout distance. Gullying within the earthflow mass provided water channelization that mobilizes the disintegrated clay-rich rock mass during intense and prolonged precipitation events in the spring and fall (Brideau et al., 2006).
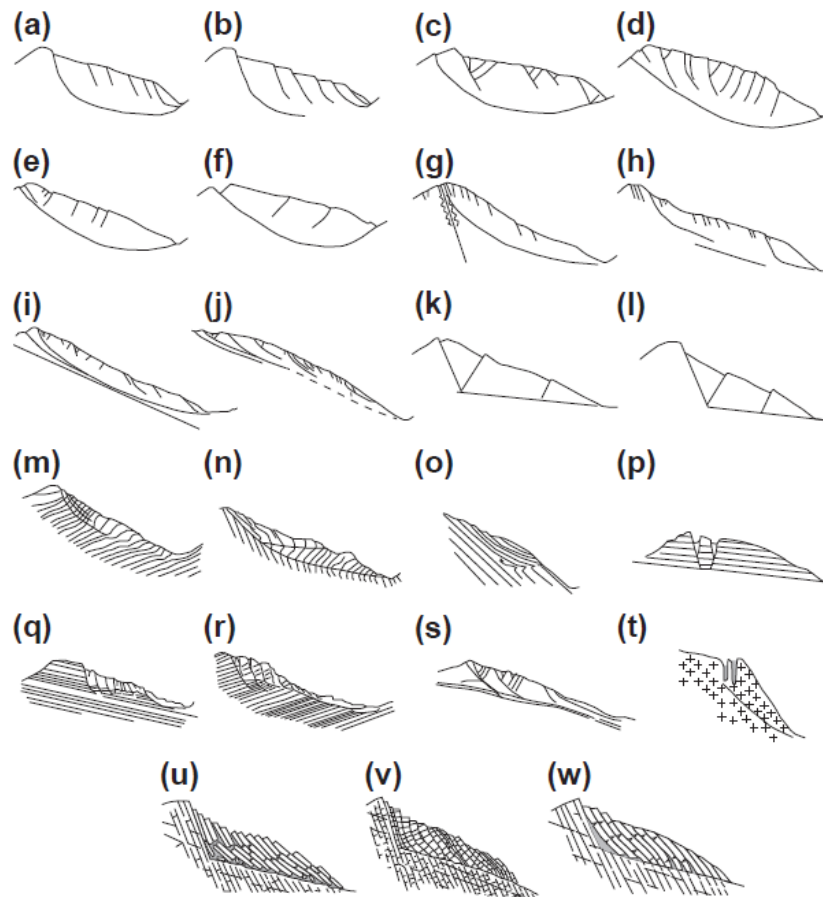
Figure 3.3: Mechanism of large-scale rock-slope failure proposed in the literature, ordered on the basis of failure geometry and structural control, from Agliardi et al. (2012). (a), (b), (c), (f) Bois et al (2008); (d) Mahr (1997); (e), (g), (h), (i) Ambrosi and Crosta (2006); (j) Agliardi et al. (2001); (k), (l) Hutchinson (1988); (m), (n) Zischinsky (1996); (o), (p), (t) Chigira (1992); (q), (r) Nemcok (1972); (s) Agliardi et al. (2009b); (u), (v), (w) Kieffer (1998)

3.2. Triggering factors

A rockfall triggering factor can be defined as an external influence that changes the forces acting on a rock (Pantandelis, 2009). The behavior of these phenomena is unforeseeable and many factors that can cause a rockfall event exist; these predisposing factors can be both natural (rainfalls, weathering, earthquakes, etc.) or artificial (vibration from blasting or machinery, earthworks that alter slope geometry, deforestation, etc.). However, the heterogeneous spatial distribution of debris landform within mountainous landscape, as well as their variance properties of material and volumes, indicates a compound interaction of multiple causal factors (Figure 3.4), jointly defining the rock-walls sensitivity to fail at various temporal and spatial processes scales (Fanos and Pradhan, 2017).

A summary of most common rockfall triggering factors and their influence on slope stability is showed in Table 3.1. The stability of rock slopes is also significantly influenced by the structural geology of the rock (Wyllie and Mah, 2004). Structural geology in this sense pertains chiefly to the natural occurring planar breaks in rock mass such as faults, joints and bedding planes, generally referred to as discontinuities, that are weaker than intact rock (Wyllie and Mah, 2004). These rocks are mechanically anisotropic in the sense that they have different shear strength in different directions, and failure is therefore more likely to occur on these planes if stress tensors are oriented favorable to these structures (Twiss and Moores, 1992). The orientations of the discontinuities will therefore affect whether failure will occur on a rock slope (Wyllie and Mah, 2004).
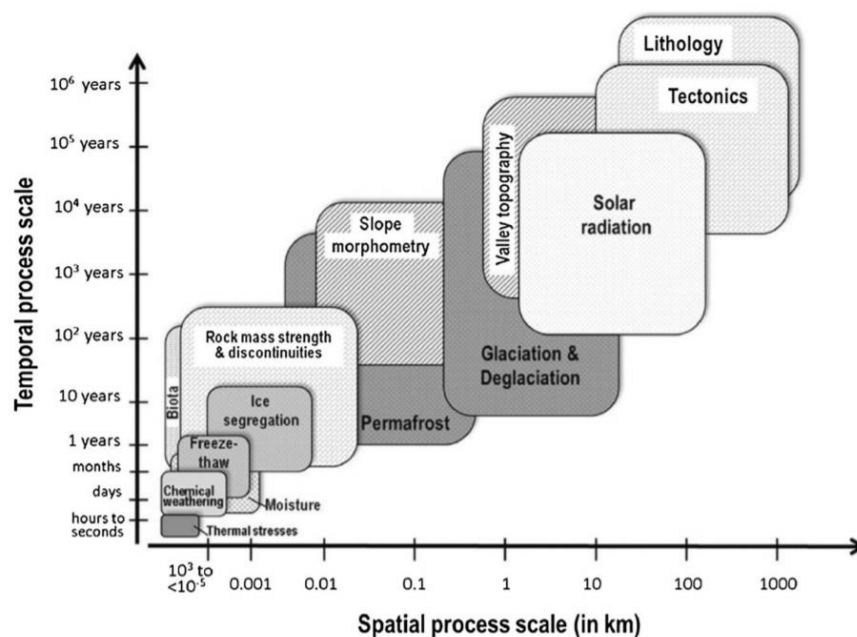
Figure 3.4: Processes-scale of probable rockfall controls with respect their spatial and temporal variability. (from Fanos and Pradhan, 2017)

The structures in rock remain fairly unaltered from day to day and other processes are required to explain the cause of the occasional rockfall. The most important mechanisms that cause rockfalls are connected to the increase of water pressure in fractures and reduction of fracture plane shear strength (Domaas and Grimstad, 2014). The shear strength of a discontinuity depends on the roughness of its surface, the degree of weathering, extent of debris present, compressive strength of rock material, normal stress on the surface and current water pressure in it (Domaas and Grimstad, 2014).

Water is almost always directly or indirectly involved with landslides and its role is particularly important (Keller, 2011). Water pressure both reduce shear strength of potential sliding surfaces by reducing effective normal shear stress on it (less friction), but also adds pressure in tension cracks, increasing forces that induce movement (Wyllie and Mah, 2004). The

increase of water pressure may occur during heavy precipitation or melting of snow (Domaas and Grimstad, 2014). If present water is further allowed to repeatedly freeze and thaw it may displace rock mass, rendering it unstable (Domaas and Grimstad, 2014). The freezing may additionally affect drainage, causing elevated water pressure (Domaas and Grimstad, 2014).

Table 3.1: Common rockfall triggering factor

Factor	Influence
Precipitation	- Potential to cause erosion of finer grained material, leaving larger blocks unstable - reduce shear strength of potential sliding surfaces by reducing effective normal shear stress on it (less friction) - adds pressure in tension cracks, increasing forces that induce movement - Causes recharge of groundwater leading to increased water pressure in fractures and reduction of fracture plane shear strength
Snowmelt	Same as precipitation
Freeze-thaw	- As water infiltrates into discontinuities and freezes, it undergoes a volume increase, leading to increased pressures - Can cause opening of cracks and joints, pushing rocks out from the slope face
Chemical weathering	Alter minerals such as feldspars to form weak clay in fractures
Wind	- Can cause erosion of small particles, leaving larger blocks unsupported - Can cause loosening of tree roots - Particles eroded more easily on south-facing slopes due to a dry conditions
Human activity	- Damage to rock face can be caused by poor blasting practices - Vibration induced by blasting can cause instabilities - Vibration can also be caused by train movement and the use of heavy construction equipment
Earthquakes	Long-duration vibrations and high accelerations

Chemical weathering facilitated by water may over time alter minerals such as feldspars to form weak clay in fractures that allows failure to occur at inclinations as low as under 20° (Domaas and Grimstad, 2014). The feldspar group is the most abundant group of rock forming minerals in the earth's crust (Keller, 2011) illustrating the process' potential importance as conditioning factor. When the thickness of the resulting debris is 25-50 % of the amplitude of

fracture plane asperities, there is little to no rock-to-rock contact and fracture shear strength properties becomes that of the infilling, which in turn greatly affects material shear strength (Wyllie and Mah, 2004). Other conditioning factors for rockfalls include human activity, such as blasting and mining, earthquakes, and the expansion of roots during their spring/summer growth season (Domaas and Grimstad, 2014).

3.3. Rockfall phases

Three zones can be identified on active rockfall slopes. The upper area, which is called source zone and is typically characterized by steep rock faces that have unfavorable combinations of slope aspect and the dip and strike of bedding planes and the most prominent joint sets. The second section is the transit zone where rockfalls propagate as individual blocks that don't interfere significantly with each other (Domaas and Grimstad, 2014); here the rockfall velocities, as well as the jump heights, are maximal. Ritchie (1963) described this motion as three main types of movement: free fall, rolling and bouncing, in order of increasing slope inclination (Figure 3.5). Finally, the deposition zone is the area where most of the rocks stop. The areas described could overlap each other, therefore the boundaries between them are not rigorous identified.

3.3.1. Source zone

At the cliff face, being a potential source area for rockfalls, often a lot of information about the potential rockfall hazard can be found. The two types of parameters that can be assessed are so-called rockfall promoters and rockfall triggers. Rockfall promoters are joint attitude, presence of joint infillings, open cracks, and rock strength. These parameters determine the preparation of loose rocks that eventually could fall down. Rockfall triggers, as described in the previous paragraph, are joint water pressures, freeze-thaw mechanisms, tree root growth and earthquakes, which initiate the actual rockfall (Dorren, 2003; Krautblatter & Dikau, 2007).

Due to the complex interaction of rockfall promoters and triggers, it is difficult to provide the failure probability of a potentially falling rock as a function of a given period (Hantz et al. 2003). Quite often rockfalls occur suddenly in places with few or no prior indications of instability. Slope instability indicators include both features related to future failure, such as open cracks or rocks in limited equilibrium, and features indicating recent and past failures, such as scars in the cliff face. Generally, past rockfall activity is a good source of information if rockfall conditions in terms of magnitude and frequency of rockfall promoters and rockfall triggers have not changed significantly.

Future rockfall activity can be detected by comparing the geological structure of the rock mass and the topography of the slope (Hoek & Bray, 1981; Goodman & Shi, 1985). In this context, the size, density, orientation and continuity of rock discontinuities are of central importance.

Methods for the quantitative description of discontinuities in rock masses are summarized by Barton (1978). Nowadays many methods exist for estimating the failure probability; they are based on relative rock failure rating systems (Mazzoccola & Hudson, 1996; Budetta, 2004; Corominas et al., 2005; Jaboyedoff et al., 2005). Frequently applied systems are the Slope Mass Rating by Romana (1988), the Rockfall Hazard Rating System (RHRS) developed by Pierson et al. (1990) and Rouiller et al. (1998). Such methods generally require ratings for geologic characteristics, the volume of the potentially falling rock, rockfall history, triggering factors (climate, water circulation), and in some cases estimates for future trends in the stability of a slope.

3.3.2. Transit zone

The transit zone is the area through which the falling rocks traverse. In many case it corresponds to the slope section where rocks are free falling along the cliffs and bouncing on the steep talus below the source zone. Once movement of a rock perched on the top of a slope has been initiated, the most important factor controlling its fall trajectory is the geometry of the slope. In particular, dip slope faces, such as those created by the sheet joints in granites, are important because they impart a horizontal component to the path taken by a rock after it bounces on the slope or rolls off the slope.

Rolling velocities can be calculated analytically using the inclination and the surface roughness of the slope (Meissl, 1998; Woltjer et al., 2008). During rolling, a rockfall fragment starts accumulating rotational energy. In the literature, different values for the proportion of the rotational energy on the overall energy can be found, given values range from 10% (Jaboyedoff et al. 2003), to 20% (Gerber 1994) and 30% (Jahn, 1988; Chau et al., 2002).

Irregularities in shape and surface transform the rolling into bouncing, especially at higher velocities (Erismann and Abele 2001). Gerber (1998) and Schwitter (1998) suggest a minimum slope angle of 35° to pass from rolling to bouncing. Dorren (2003) and Schweigl et al. (2003) however propose an inclination of 45°. After Azzoni et al. (1995), bouncing can be expected if irregularities in boulder shape where smaller compared to the ones of the slope surface. A steeper slope angle or the presence of a sudden cliff transforms bouncing or rolling into free falling. Again, different critical slope angles that allow falling can be found in literature. According to Ritchie (1963), a minimum slope of at least 76° is required (Figure 3.5). Dorren (2003) suggests 70°, whereas Erismann and Abele (2001) propose 45-55°.

Velocity increase quickly under free fall conditions (Domaas and Grimstad, 2014). When impacting a surface, a fraction of the gained kinetic energy is lost and the remaining fraction is often called the boulders restitution (Domaas and Grimstad, 2014). Restitutions of 0.14 to 0.25 are typical for first impacts (75-86 % energy loss) (Dorren, 2003) and, unless fairly

equidimensional, the boulder usually breaks (Luckman, 2013). The value of the restitution then depends somewhat on the stiffness of the substrate, varying between 0.3 and 0.7 for impacts on unconsolidated materials and 0.5 and 0.9 for impacts on bare rock according to a study by Azzoni and De Freitas (1995).
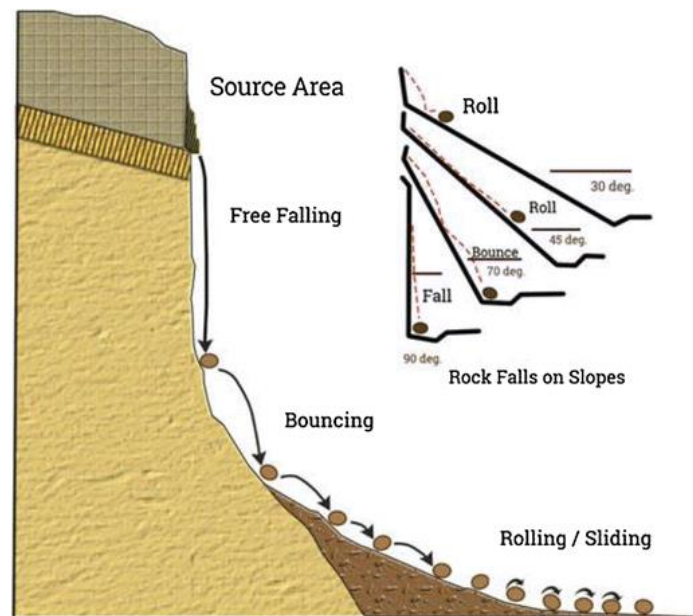
Figure 3.5: Modes of rockfall motion based on slope angle. (Ritchie, 1963) modified by (Fanos and Pradhan, 2018)

As long as the slope is sufficiently steep and restitution sufficiently high the boulder can retain all lost energy between impacts and continue downslope (Domaas and Grimstad, 2014). The value of restitution expected after impact on a certain substrate can be quantified by a coefficient of restitution which is in modelling sometimes treated as a material constant (Frattini et al., 2012).

Impacts often induce rotation of falling boulders (Domaas and Grimstad, 2014). A study by The Japan Road Association found that rockfall boulder rotational energies could approach values of 40 % of the translational energy, although in half of the experiments this fraction was under 10 % (Heidenreich, 2004). This rotational motion could still allow significant increase of run out length even in flat terrain should rock shape allow this (Domaas and Grimstad, 2014). Flat and rectangular rocks run out may not benefit from this rolling motion unless they are rolling on their sides, as planar side impact may cause up to all rotation to seize (Domaas and Grimstad, 2014). Rolling is otherwise very economical in terms of energy, as only the largest radius of the rock is at any point in contact with the surface and subject to friction (Dorren, 2003). If the rolling block starts to slide, which is common late in transit zone, boulders will usually halt due to friction unless mean slope gradient changes (Bozzolo and Pamini, 1986).

Assigning restitution coefficients to materials is an empirical approach in that its values are based solely on specific datasets, and is for that fact problematic (Agliardi and Crosta, 2003).

The actual nature of rockfall energy loss is based on slope roughness, slope geotechnical properties like grain size distribution, water content, void index and elastic module (Figure 3.6), and the boulder shapes and dynamics, but these parameters relationship to energy loss is not fully defined and the relevant parameters are difficult to ascertain in time and space (Agliardi and Crosta, 2003). So while it should be theoretically possible to compute the position and velocity of a rockfall at any time, it is severely complicated in actual conditions (Agliardi and Crosta, 2003).
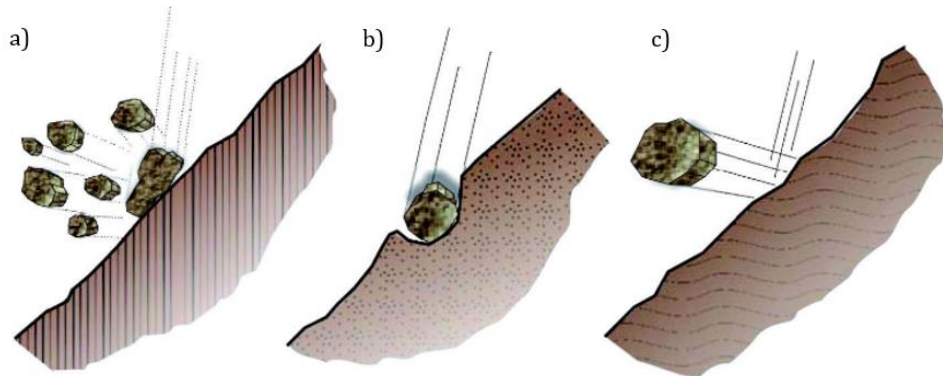
Figure 3.6: Different types of interaction between moving rock and soil in the case of a) bedrock b) deformable soil c) elastic soil

3.3.3. Deposit zone

If slope gradients drop below 30°, rockfall fragments generally come to a stop in the deposition zone (Bunce et al. 1997). This area of accumulated rockfall fragments at the foot of a cliff or slope is called scree slope or talus slope (Allaby and Allaby 1990). However, a deposit area can also act as a secondary rockfall source area (Dorren et al. 2007).

Due to their higher masses, big boulders accumulate more kinetic energy during travelling downslope, resulting in longer runout distances (Jahn 1988, Erismann and Abele 2001). More spherically shaped rocks tend to have longer runout distances than non-spherical ones. Azzoni and et al. (1991) describe single cases of discoid fragments that tilted up and behaved like wheels rolling down the slope, thus reaching the longest runout distances.

Stopping in general occurs through a rather abrupt than a gradual process (Dorren 2003). According to Krummenacher (1995), boulders stop most abruptly if the irregularities on the slope surface are of the same magnitude as the fragment sizes.

Chapter 4: Steel flexible protection barriers

4.1. Available mitigation measures

An essential aspect of risk management is the design of mitigation measures which reduce the existing risk to an accepted level of residual risk (Hubl et al., 2005). Two types of mitigation measures can be distinguished: active measures and passive measures (Zollinger, 1985).

4.1.1. Active protection measures

Active systems focus on the hazard and their objective is to prevent the phenomenon occurrence; these systems may affect the initiation phase of the landslide and act on the factors which cause the instabilities. These measures require detailed geotechnical information, and are generally more expensive than passive ones. When implemented, however, natural hazard is significantly reduced. Some examples of active protection solutions are reported below.

Anchoring

Slope stabilization can be actuated through the application of active forces to the ground (Figure 4.1). These forces increase the normal stresses and therefore resistance to friction along the failure surfaces.

Figure 4.1: Slope stabilization anchor work for landslide prevention

Anchors can be applied for this purpose, linked at the surface to each other by a beam frame that is typically made of reinforced concrete. These systems are fixed in a stable layer and are usually installed along axes which are perpendicular to the slope surface (i.e.) approximately perpendicular to the creep plane.

The capacity of these kind of support is defined as the maximum load which an individual anchor can sustain before failure. Generally, this will be the pullout or failure load of the anchoring mechanism, however, it could also be the tensile strength of the anchor, or the strength of the plate assembly on the slope surface, if either of these capacities are less than the failure load of the anchoring mechanism.

Nailing

Soil nailing is a construction remedial measure to treat unstable natural soil slopes or as a construction technique that allows the safe over-steepening of new or existing soil slopes. This technique consists of installing passive reinforcement (i.e., no post-tensioning) in existing ground by closely spaced steel bars or sections (i.e., nails) and placing a front face support (Figure 4.2).

Solid bars are usually installed into pre-drilled holes and then grouted into place using a separate grout line, whereas hollow bars may be drilled and grouted simultaneously by the use of a sacrificial drill bit and by pumping grout down the hollow bar as drilling progresses.
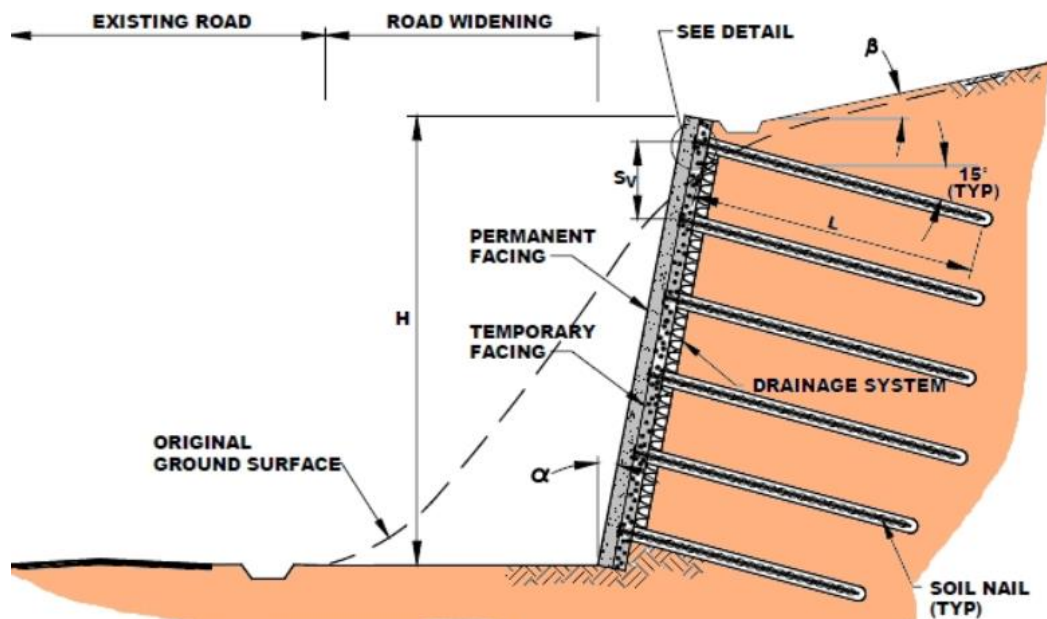
Figure 4.2: Scheme of typical soil nail installation

Piles and micropiles

Piles and micropiles are a deep foundation element constructed using high-strength, small-diameter steel casing and/or threaded bar. They are a structural element driven into the soil for transferring loads and prevent deformation. Its slenderness ratio is not limited. Pile shafts can be uniform and rectilinear, telescopic and belled out. Piles can be installed either separately or in groups. They can also form a retaining wall, a mixed curtain wall, contiguous piles, secant

piles and composite curtain walls, such as Berlin walls and similar. Piles are also used as precast beams to be placed in the structure of the building they support. A Pile will apply a constant force to a slip surface, regardless of where it is intersected by that surface. The applied load, per unit width of slope, is simply equal to the pile shear strength divided by the out of plane spacing.

$$F = \frac{P}{S}$$

Where:

P is the pile shear strength

S is the out of plane spacing

The force-distance graph that characterized the pile support behavior is typically a horizontal line, representing a constant value of applied force. The intersection point between the pile and the slip surface doesn't influence the trend showed in Figure 4.3.
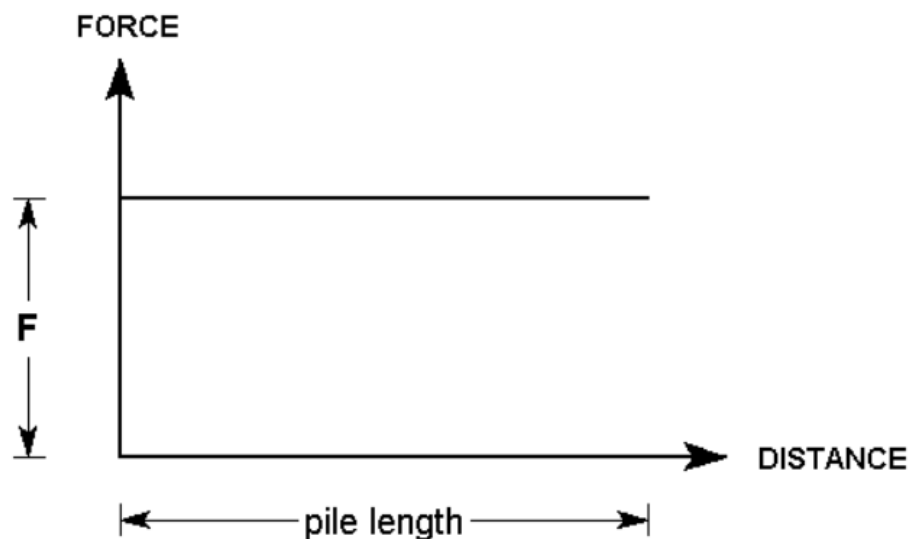
Figure 4.3: Force diagram for pile support (from www.rocscience.com)

Soil bioengineering

Soil bioengineering addresses the technologies and applications of dead and live plants for erosion control (Figure 4.4). Soil bioengineering structures start or accelerate phytosociological successions and processes, minimize erosion, and govern the groundwater supply (Hubl et al., 2005). Soil bioengineering measures are usually applied in the following situations:

a)   channels, gullies, rivers, and streams;

b)   slope stabilization and bank redevelopment;

c)   road ditch stabilization.

Most effective in soil bioengineering is the combination of surface protection constructions like seeding with stabilizing constructions. The range of longitudinal structures extends from tree spurs (rough coniferous trees), branch layering in gullies, vegetated channels, live brush mattresses, living slope grids, different fascines, vegetated revetments of different materials, log brush barrier construction, live pole construction, brunch and brush packing, and double-row palisades. At the transverse structures there are living groynes, live siltation construction, living combs, brushes and palisade constructions, brush sills, fascine sills, log cribwalls with brushlayers, as well as planted gabions and wooden crib dams.

Figure 4.4: Soil bioengineering slope stabilization and revegetation for road protection

Drainage

In saturated soils, drainage systems are one of the most effective remedial measures against slope instability due to their capacity to reduce pore-water pressure in the subsoil, increasing the shear strength of the soil (Urciuoli and Pirone, 2013). Due to their relative cheapness, subsurface drainage systems are widely used, also in combination with other stabilization works. Moreover, they provide a suitable solution to stabilization in a large number of cases, even when the landslide is very deep and structural measures are not effective (Popescu, 2002). Water drainage stabilizes unstable areas and prevents the build-up of high pore-water pressure along potential shear surfaces. The principles of drainage stabilization are based on the following (Hubl et al., 2005):

a) Prevention of superficial and subsurface runoff from the area above the slide as well as collecting wells by a horseshoe-like diversion drainage (horeshoe drainage);

b) To drain subsurface water to prevent the formation of shear surfaces (Figure 4.5).

Figure 4.5: Hillside superficial drainage

Geosynthetics

Geosynthetics are defined as a planar product manufactured from a polymeric material that is used with soil, rock, or other geotechnical-related material as an integral part of a civil engineering project, structure, or system (Adams et al., 2015). Their polymeric nature makes them suitable for use in the ground, where high levels of durability are necessary.

The primary advantages of geosynthetics are:

- Relatively low cost for many applications;
- Ease and convenience for many applications;
- Quick and effective protection against erosion problems;
- Design methodologies are available for many uses;
- Wide variety of geosynthetic products are available to meet specific needs;
- May be removed and reused if economically feasible.

On the other hand, the main limitation of these products are:

- Effectiveness may be reduced drastically if the geosynthetic is not properly selected, designed, or installed;
- Many geosynthetics are sensitive to light degradation and must be protected prior to installation;
- Geosynthetics that are not degradable should not be used where their presence or appearance is aesthetically unacceptable.

Mono-anchorage umbrella systems

The mono-anchorage umbrella system is constituted by a structure anchored to the ground by means of a tie rod of deep anchorage and/or by fastening concrete plates. This technology is designed for slope consolidation and terracing and its main components are (Figure 4.6 and 4.7):

- Cross support structure made of four metallic beams;
- Articulated joint, located in the center of the cross, that allows limited rotation of the elements;
- Front steel net panel for soil contain and secondary net;
- Central steel tube connecting to the anchoring element;
- Steel ropes that connect the facing the anchoring element;
- Single anchor which transfers to the soil the loads acting on the structure.
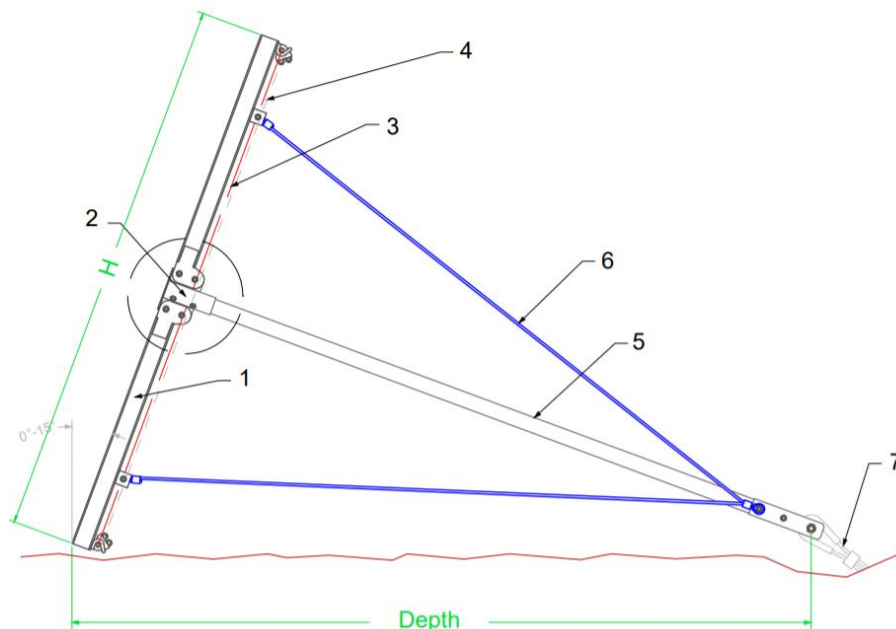
Figure 4.6: Lateral view of consolidation system and main components

These structures are used in a wide range of applications and interventions such as:

- Bridles and reins filter;
- Bank protection against corrosion;
- Landslide protection;
- Bank protection anti-erosion;
- Landslide accommodation of landslide slopes;
- Stabilization and consolidation of slopes and escarpments (Figure 4.8);
- Avalanche Danger Mitigation;
- Construction of walls, barriers and valleys;
- Jetties, marine structures and lake structures.
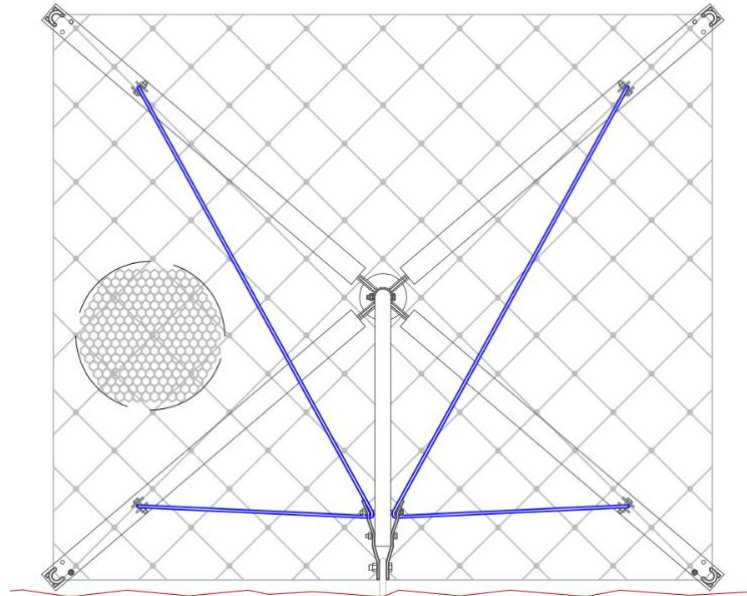
Figure 4.7: Upstream front view of consolidation system

Figure 4.8: Consolidation intervention made by mono-anchorage umbrella structures combined with soil bioengineering

In some cases, these systems are also employed for avalanche prevention (Figure 4.9). Avalanche supporting structures are designed to withstand the creeping and (at times) sliding snow layer. The structures are anchored in the ground approximately normal to the slope and extend up to the surface of the snow.

Thus a restraining effect occurs, so that the creep and glide velocities decrease steadily in the downslope direction towards the structure. Within this so-called back-pressure zone, which normally extends over a distance measured in the line of slope of at least three times the vertical snow height (depends to a large extent on the sliding motion), additional compressive stresses

in the line of slope develop. These are withstood by the supporting surface, leading to a reduction of the shear (and possibly tension) stresses in the back-pressure zone in front of the supporting structure that are responsible for the formation of snow slabs (Federal Office for the Environment and Swiss Federal Institute for Snow and Avalanche Research, 2007).

Figure 4.9: Umbrella systems for avalanche prevention

4.1.2. Passive protection measures

Passive protection systems focus on the potential damage and their aim is the protection of the infrastructures and human lives from natural events. They act during the event by intercepting and stopping it, therefore avoiding it from reaching the element at risk. Below some active mitigation solutions against slope instability are described.

Rockfall embankments

Rockfall protection embankments are an ideal solution when surface stabilization systems cannot be installed (e.g. for very wide slopes) or where interception of falling rocks is not possible due to the whole slope being inaccessible. They are commonly used as protection from natural hazards, landslides, rockfalls (Figure 4.10), avalanches, hydro-geologic problems and more. Nowadays, these structures are usually built using reinforced soil locally available on site. The location (distance from the slope), the height and the size of the embankment is evaluated in relation to the slope morphology, the characteristics of the area and the kinetic energy of the falling rocks. The advantages main of rockfall embankments are:

–   High energy absorption capacity;
–   Possibility to use local material;

– Long durability;

– Very low maintenance;

– Capacity to contain big quantities of material.

Figure 4.10: Test of rockfall embankement (www.tenax.net)

Open rigid barriers

Open rigid barriers, according to the way in which they are designed, constitute an effective measure for dosing, filtering and for energy dissipation. In particular, two main complementary approaches exist in the design of open barriers, i.e. hydraulic and/or mechanical controls of the deposits (Piton and Recking, 2016).

Figure 4.11: Slot grill barrier for dosing and filtering

Their function is to reduce the flow of debris, such as mud, stone, sand, gravel, boulders, and water from mountain side (Figure 4.11). Different types of open barrier exist; the choice of one of these typologies depends on the functions for which they are designed. In particular, hydraulic control achieves the dosing and energy dissipation functions, while mechanical control the filtering and energy dissipation (Marchelli, 2018).

Due to the variability of real events, hydraulic and mechanical control may occur also together. Moreover, despite this functional subdivision, a wide variety of rigid barrier typologies exists; a complete description of available rigid barriers is provided by Hubl et al. (2005).

Flexible barriers

Deformable restraining net barriers belong to passive measures and they have been largely used in mountainous areas to protect urbanized zones and infrastructures against debris flow and rockfall events (Figure 4.12).

These countermeasures are made of a light structure in which a series of steel cables, anchoring in the ground, keep in position a double steel mesh. This mesh stops the moving mass and transfers all the forces to the anchors in the ground.

Dissipating systems are usually installed on each cable in order to reduce the kinetic energy, taking advantage of friction effects and large cable deformation. In the next paragraphs a detail description of structural aspects of these technologies is given.

Figure 4.12: Example of debris flow barrier designed with support steel beams

4.2. Barrier net general description

Mountain areas cover about the 20% of all the European land and one-third of the European Countries have mountains on more than the 50% of the entire territory. The extreme environment makes mountain areas prone to natural phenomena such as landslides, rockfalls, mudslides, avalanches (Mentani, 2015). Nowadays steel flexible barriers are largely use for protection against rapid events like rockfall and debris flow.

Rockfall barriers are designed to dissipate the kinetic energy deriving from the impact of the falling blocks, for this reason the performance of a rockfall protection barrier is usually defined in terms of the maximum energy capacity (expressed in kilojoules) they are able to absorb. On the other hand, during a debris flow event, the energy is not instantaneously transferred to the structure as in rockfall event, but there is a continuous dissipation during net filling, so their performances are described in terms of total pressure acting on the net (expressed in kilopascals). In both cases the barrier structure is the same, with the only difference that the debris flow barrier, differently from rockfall ones, can be designed with or without support beams, depending on site characteristics.

The great versatility of these systems allows their use in difficult environmental conditions: the reduced weight, the modularity and the adaptability at the basin characteristic are at the base of their success. Furthermore, the low realization and maintenance costs made these types of countermeasure competitive compared to the most common rigid concrete or beam barriers.

A typical flexible barrier is made of several identical functional modules installed in sequence for the required length (Figure 4.13). Each module is generally 10 meters long, constituted by various components having different functions. In this paragraph the main structural components and their functions are described.

Figure 4.13: Technical drawings of typical barrier and evidence of functional module. a) Lateral view and b) Top view

4.3. Support structure

Support structure is usually constituted by steel posts (Figure 4.14 and 4.15) of different section types and base plate (Figure 4.16) to connect them to the foundations. It is designed to:

a) Support the bearing ropes and mesh connected to the posts, using connection components;

b) Transmit the forces from posts to the foundation structure during impact and maintain the structure in position.
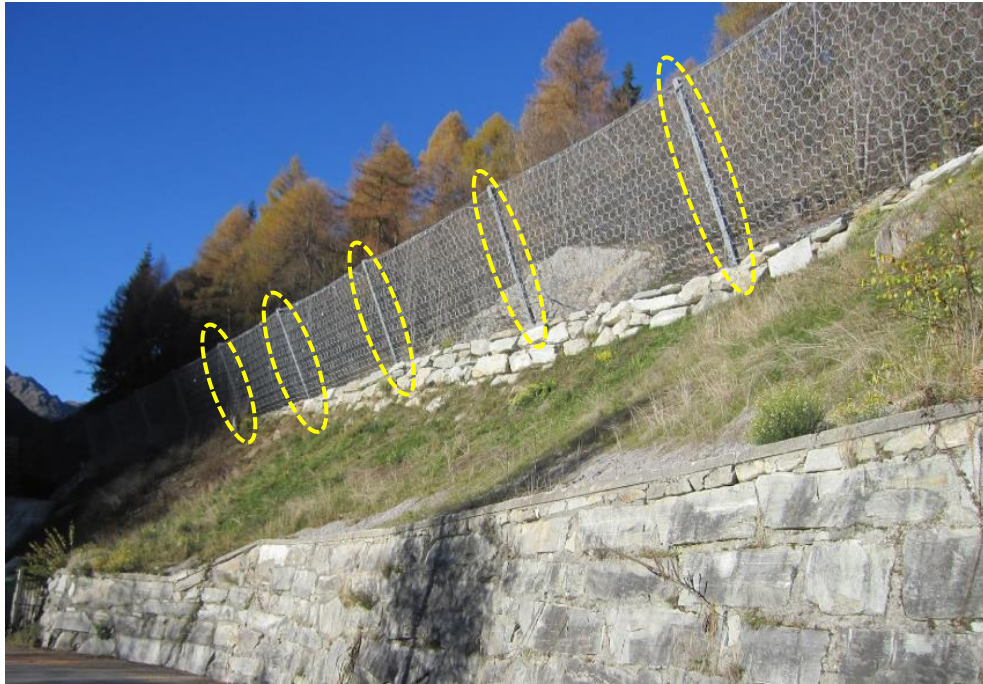
Figure 4.14: Steel posts for barrier support
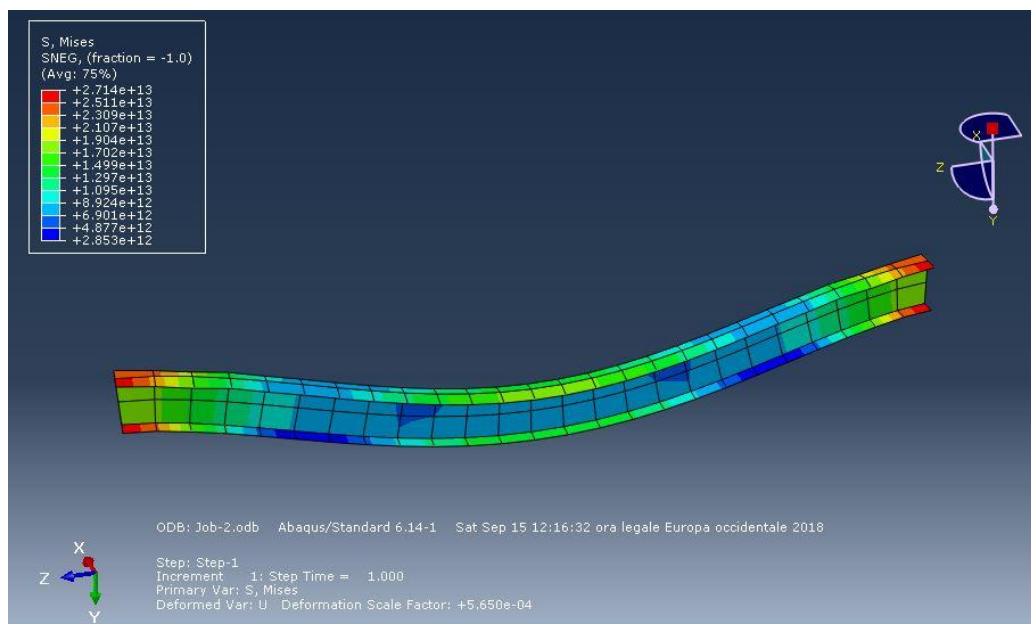
Figure 4.15: FEM modeling of loaded steel post

4.4. Interception structure

The interception structure is a metallic net of various mesh types. It has the function to intercept and stop the falling block/debris. The mesh has to bear the direct impact of the impacting body, absorbing most of the kinetic energy deriving from the event by means of elasto-plastic deformations. The interception structure bears the direct impact of the mass, deforms elastically and/or plastically and transmits the load effects to the connection components, the support structure and the foundations. It is composed of primary net and secondary net.

Figure 4.16: Barrier base plate with bearing rope guide and interception structure

4.4.1. Rockfall barrier primary net

The mesh design has an important role in order to define the overall performance of the protection system, different types of metallic nets can be used as interception structure. In the typical mesh constructions used for rockfall barriers the cables can be arranged to form a square grid net or interlaced ring mesh. These mesh types have different geometrical characteristics (weight and dimension), and mechanical properties (strength and elongation). The net is protected with a metallic coating, depending on the corrosivity of the environment for which the wire ring mesh is installed. Possible options for metallic coating are presented in Table 4.1.

To evaluate the mechanical behavior of this component under load conditions, mechanical tests are necessary. Below results obtained by testing some specimens of panel are reported; each test is conducted according normative ISO/FDIS 17745 and ISO/FDIS 17746. The testing apparatus were built and placed at the Incofil Tech's seat. All the devices are compliant with

class 1 accuracy (Figure 4.17). In order to achieve this classification each relevant measurement device was calibrated referring to ISO 7500.

Table 4.1: Description of the environment of the installation site, coating wire ring requirement

Site environment level (in accordance with ISO 9223:2012, Table 4)	Coating	Class (ISO 7989-2)	Estimated working life of the product (year)
Low aggressive: (C2) Dry conditions Temperate zone, atmospheric environment with low pollution, e.g. rural areas, small towns (over 100 m above sea level). Dry or cold zone, atmospheric environment with short time of wetness, e.g. deserts, sub-arctic areas	Zinc	A	20
	Zn95 %/Al5 % alloy	A	50
		B	25
	Advanced metallic coating	A	120
		B	50
Medium aggressive: (C3) Dry conditions Temperate zone, atmospheric environment with medium pollution or some effect of chlorides, e.g. urban areas, coastal areas with low deposition of chlorides, e.g. subtropical and tropical zone, atmosphere with low pollution	Zinc	A	10
	Zn95 %/Al5 % alloy	A	25
		B	10
	Advanced metallic coating	A	50
		B	25
High aggressive: (C4) Wet conditions Temperate zone, atmospheric environment with high pollution or substantial effect of chlorides, e.g. polluted urban areas, industrial areas, coastal areas, without spray of salt water, exposure to strong effect of de-icing salts, e.g. subtropical and tropical zone, atmosphere with medium pollution, industrial areas, coastal areas, shelter positions at coastline	Zn95 %/Al5 % alloy	A	10
	Advanced metallic coating	A	25
		B	10

Working life (product) — the period of time during which the performance of a product will be maintained at a level that enables a properly designed and executed works to fulfil the essential requirements (i.e. the essential characteristics of a product meet or exceed minimum acceptable values, without incurring major costs for repair or replacement). The working life of a product depends upon its inherent durability and normal installation and maintenance.

Results obtained from test of different type of mesh panels are reported below. In particular, three type of panel were tested:

a) Wire rope net panels, with HCP knots, which consist clips made of two half-shell pressure-closed (Figure 4.30);

b) Wire rope net panels, with SW wire knots, which are made by two bindings obtained by looping a pair of steel wires (Figure 4.41);

c) Wire ring mesh panels, where each ring is made by several loop bindings, each one obtained by looping a single steel wire. Each ring is connected with 4 contiguous rings in order to create a net as shown in Figure 4.18. For their high deformation capacity, steel wire ring net panels are the most used as primary net in flexible barrier.

Figure 4.17: Testing apparatus
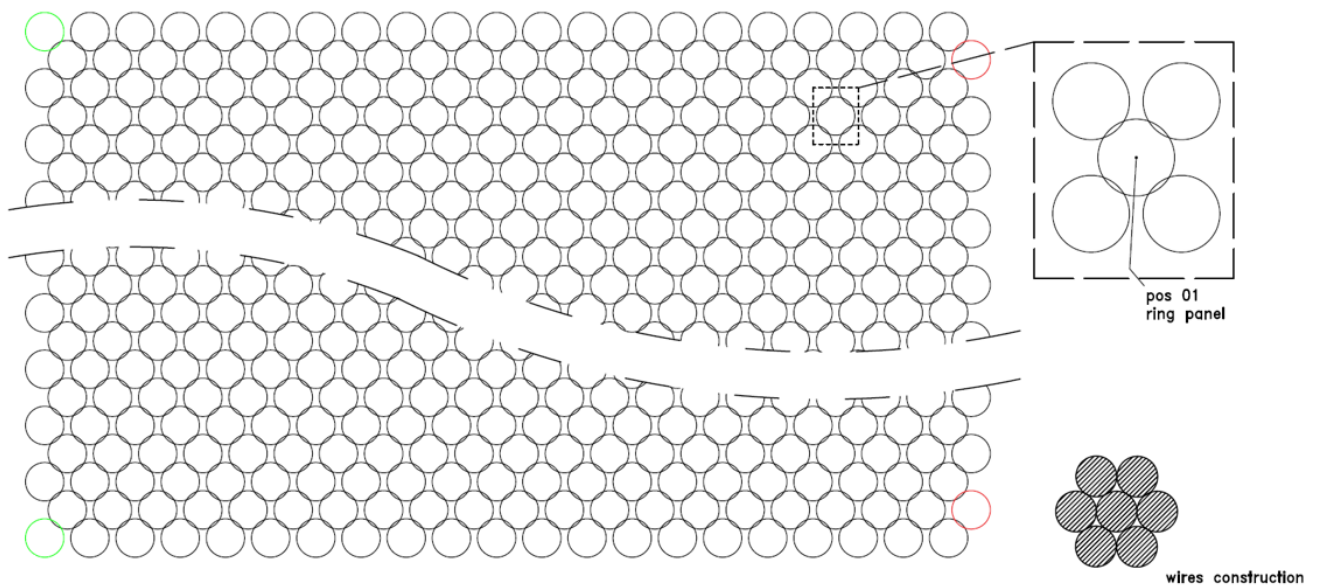
Figure 4.18: Technical drawing of ring mesh panel
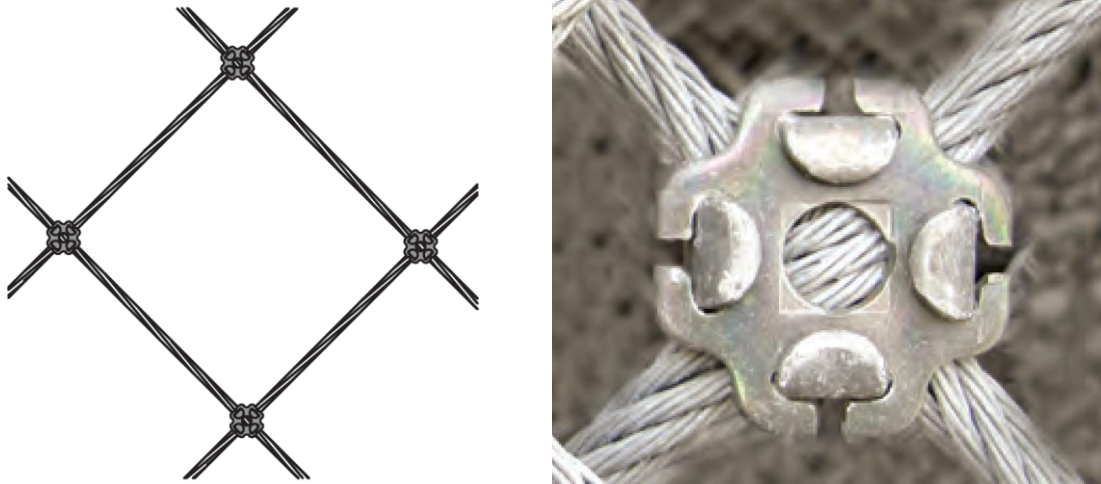
Figure 4.19: Knot type HCP (part of panels mod. INCOPAN HCP, property of Incofil Tech Srl)
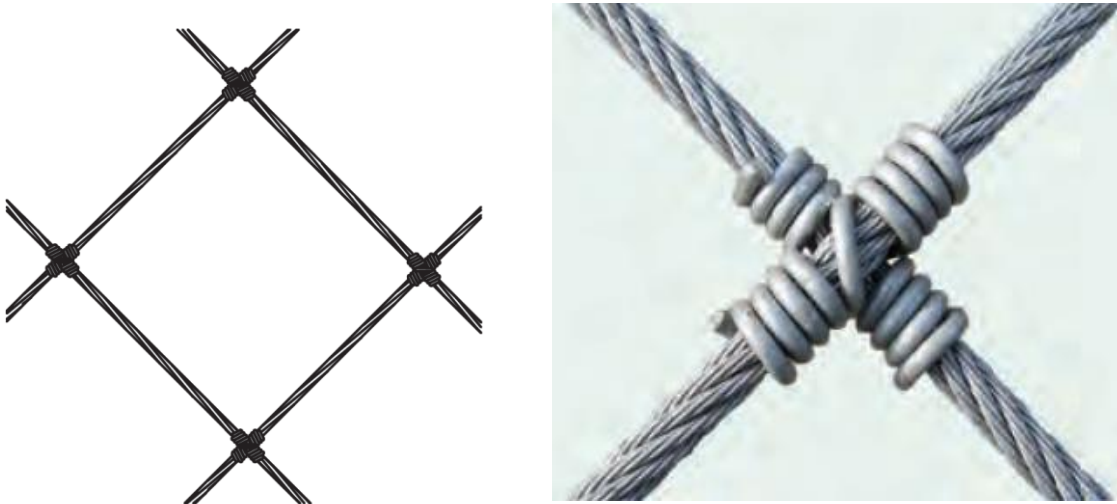
Figure 4.20: Knot type SW (part of panels mod. INCOPAN SW, property of Incofil Tech Srl)

<u>Load bearing capacity test</u>

The first test performed was the load bearing capacity test, consists in loading a sample of net perpendicularly to its plane by means of a hemispherical- shaped load sharing device (press). The press shall be located in the central point of the panel. The hemisphere of the press is formed by a durable material, such as concrete or steel. The surface of the press must be smooth, without any corners. Any attachment devices fitted on the surface of the press must not interfere in any way with the test piece during the test. The geometrical characteristics of the press are the following (Figure 4.21):

a) radius of curvature 1,200 mm;
b) maximum diameter of the sample projected on a plane 1,000 mm;
c) radius of curvature at the side 50 mm.

The test piece is loaded at the intersection of its diagonals (center of test piece), moving the press with a speed not greater than 10 mm/s. The test may be interrupted to allow the stroke of the thrust device to be restarted. The sample tested has a rectangular shape, with a 3,0 m side (average value – tolerance ± 20 %).

To allow installation of the system, the test applicant must supply the sample to the laboratory with the dimensions planned for the test or larger, and the laboratory will then carry out the sampling. It must be representative of the product in terms of materials and construction method.

The tests must be performed in the laboratory at ambient temperature, and always in compliance with standards which regulate the testing procedures for the various materials.

The puncturing test is carried out after fixing the test piece to a rigid frame and it is aimed at measuring the force-movement curve of the central point of the press measured perpendicularly to the plane of the test piece.

The test must allow failure of the specimen to be reached. The panel is considered to have failed when it is no longer able to support any increase to the applied force. The puncturing strength of a test piece is therefore defined as the maximum force imparted by the test piece during the test.
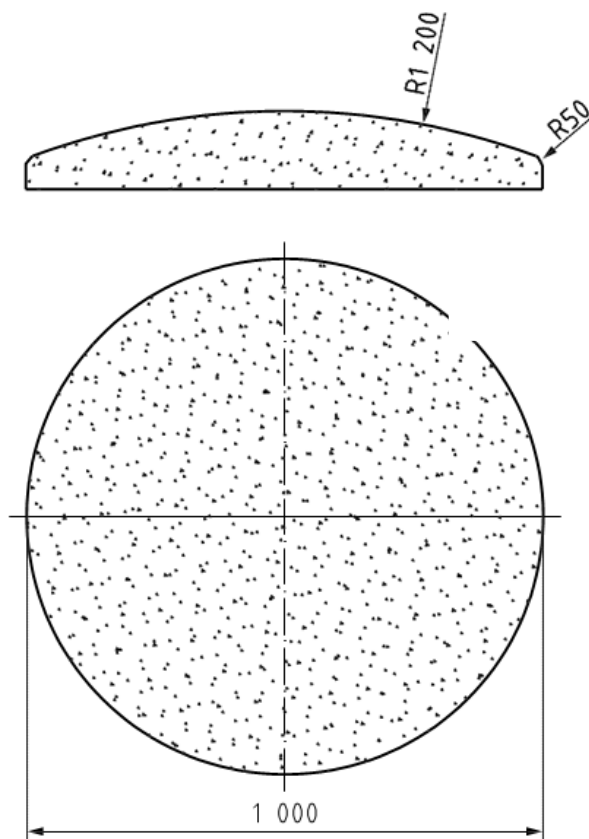
Figure 4.21: Geometrical characteristic of the press (dimension in mm)
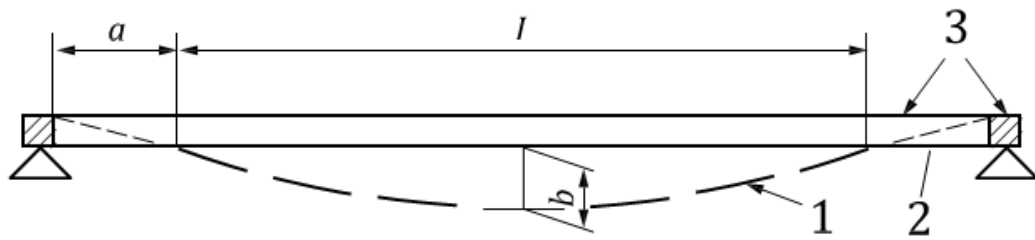
Key:
a = constraining area < 0,15×L b < 0,2 × L [m]
L = 3,0 ± 0,2 × 3,0 [m]
1 = net test piece
2 = tensioning devices
3 = rigid frame

Figure 4.22: Test configuration scheme and tolerances

Before starting the test, the test piece must be tensioned until it reaches a condition of "planarity", which is considered to have been reached when the maximum sag at the center is less than 20 % of the smallest side length of the test piece (Figure 4.22).

The wire rope is closed by two aluminum pressed ferrules of cylindrical shape made from aluminum Al 5150 A, with resistance not less than 90% of the rope-breaking load. During the test, the panel is fixed to the rigid frame by border rope, shackles and hooks. The contrast frame is made from a rigid rectangular structure, the size of which fully holds the mesh test piece and the constraint device (Figure 4.23).
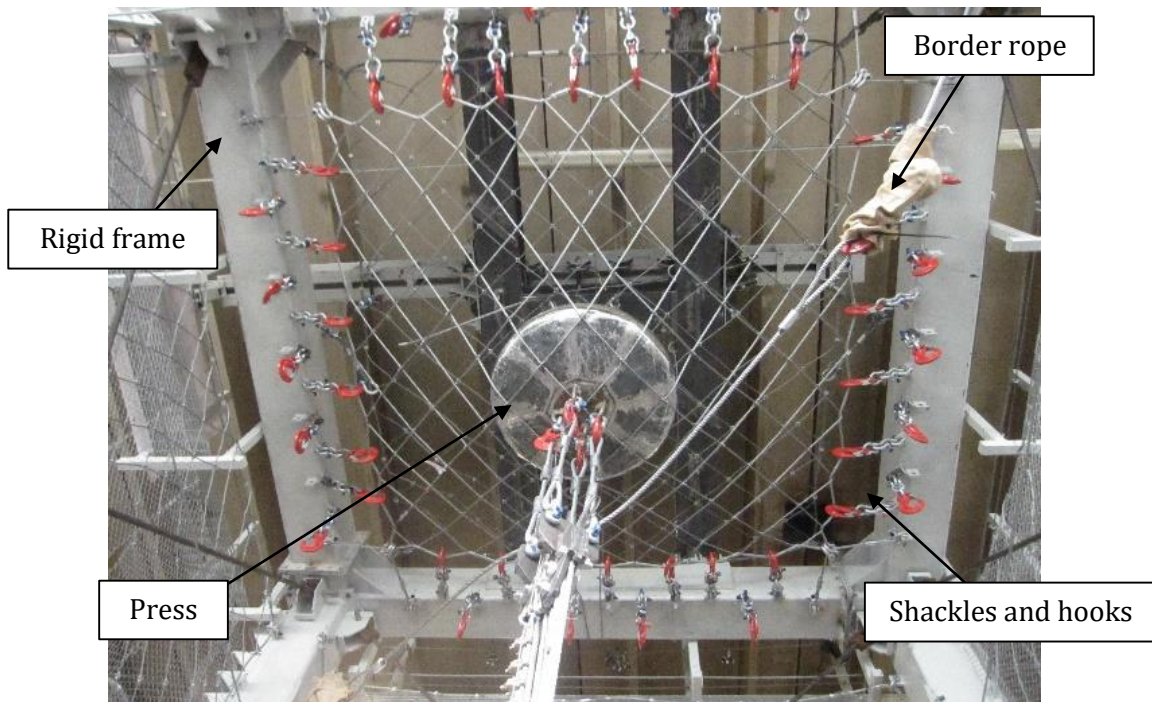
Figure 4.23: Net load bearing capacity test, example of real test configuration

HCP panel

Table 4.2: Features of tested wire rope net panel mod. HCP

Test object	N. 3 specimen of wire rope net panel − nominal dimension: 3,2x3,2 m − mesh nominal size: 300x300 mm − wire rope lot: 5204 − wire rope nominal diameter: 10 mm − wire rope nominal strength: 1960 N/mm² − knot: HCP
Type of test	Net load bearing capacity test
Standard	EAD 2300005-00-0106 (ISO/DIS 17746)
Test equipment	− Load cell Class 1 (UNI EN ISO 7500-1) with capacity of 1500 kN - calibration checks performed by Laboratories Trentino Srl on 30/06/2016 − Wire extensimeter Class 1 (UNI EN ISO 5500-1) with capacity of 4000 mm – calibration checks performed by Laboratorio Trentino Srl on 27/06/2016
Date of test	27/09/2016
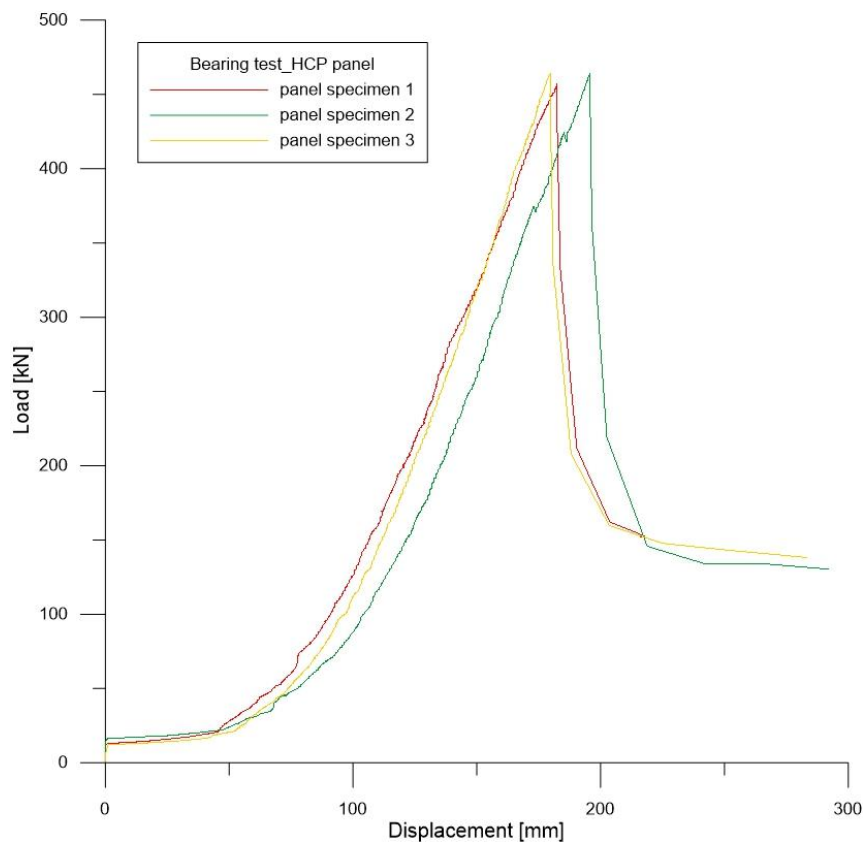
Figure 4.24: Summary of results obtained for HCP panel specimens

Table 4.3: Maximum displacements and breaking loads of tested HCP panels

Specimen	Maximum displacement [mm]	Load of tear brake [KN]	Average load [KN]	Standard deviation
1	18,2	457,0		
2	19,6	464,0	461,6	4,0
3	18,0	463,8		

Figure 4.25: Tested HCP panel; a) Specimen before test and b) Specimen brake due to loading process

SW panel

Table 4.4: Wire rope net panel SW test features

Test object	N. 3 specimen of wire rope net panel − nominal dimension: 3,2x3,2 m − mesh nominal size: 300x300 mm − wire rope lot: 5204 − wire rope nominal diameter: 10 mm − wire rope nominal strength: 1960 N/mm² − knot: SW
Type of test	Net load bearing capacity test
Standard	EAD 2300005-00-0106 (ISO/DIS 17746)
Test equipment	− Load cell Class 1 (UNI EN ISO 7500-1) with capacity of 1500 kN - calibration checks performed by Laboratories Trentino Srl on 30/06/2016 − Wire extensimeter Class 1 (UNI EN ISO 5500-1) with capacity of 4000 mm – calibration checks performed by Laboratorio Trentino Srl on 27/06/2016
Date of test	29/09/2016
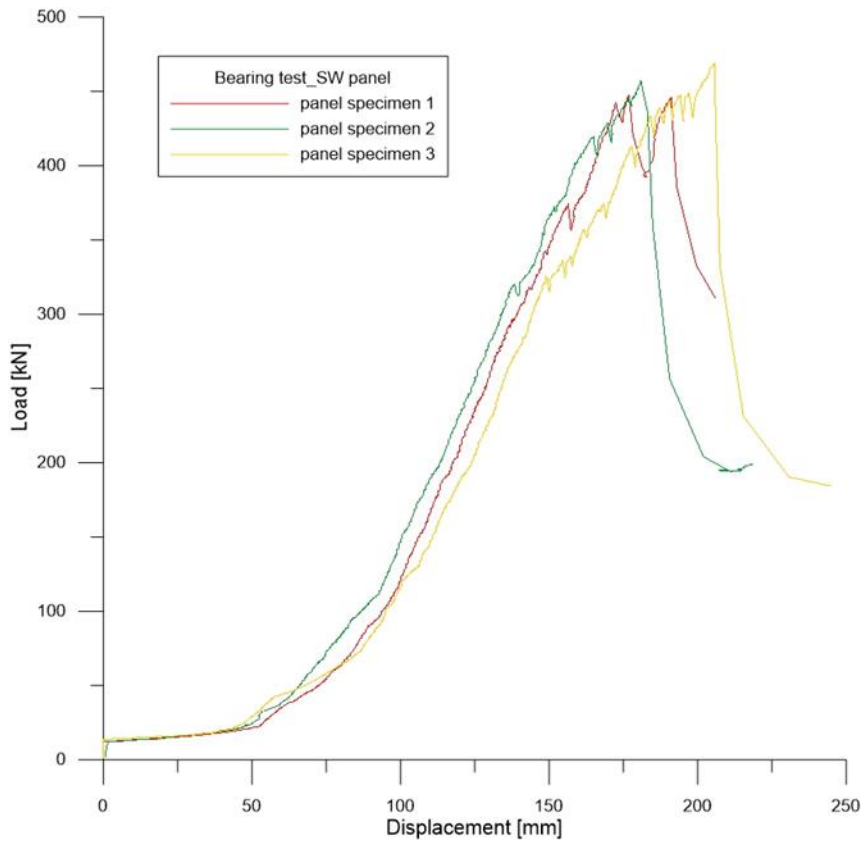
Figure 4.26: Summary of results obtained for SW panel specimens

Table 4.5: Results of test on wire rope net panel mod. SW

Specimen	Maximum displacement [mm]	Load of tear brake [KN]	Average load [KN]	Standard deviation
1	17,8	447,7		
2	18,1	457,8	458,1	10,5
3	20,58	468,79		
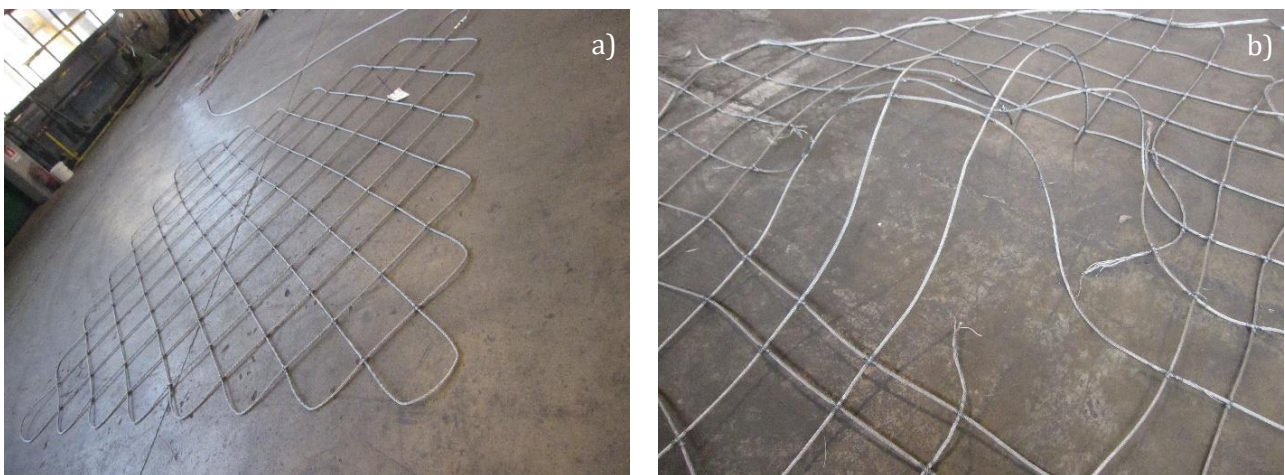
Figure 4.27: Tested SW panel; a) Specimen before test and b) Specimen brake due to loading process

Ring panel

Table 4.6: Features of tested ring panels

Test object	. 3 specimen of wire ring mesh panel − nominal dimension: 3,2x3,2 m − ring diameter: 350 mm − lot: 5224 − wire diameter: 3.5 mm − wire rope nominal strength: 1570 N/mm² − number of contact point: 4
Type of test	Net load bearing capacity test
Standard	EAD 2300005-00-0106 (ISO/DIS 17746)
Test equipment	− Load cell Class 1 (UNI EN ISO 7500-1) with capacity of 1500 kN - calibration checks performed by Laboratories Trentino Srl on 30/06/2016 − Wire extensimeter Class 1 (UNI EN ISO 5500-1) with capacity of 4000 mm – calibration checks performed by Laboratorio Trentino Srl on 27/06/2016
Date of test	22/06/2016
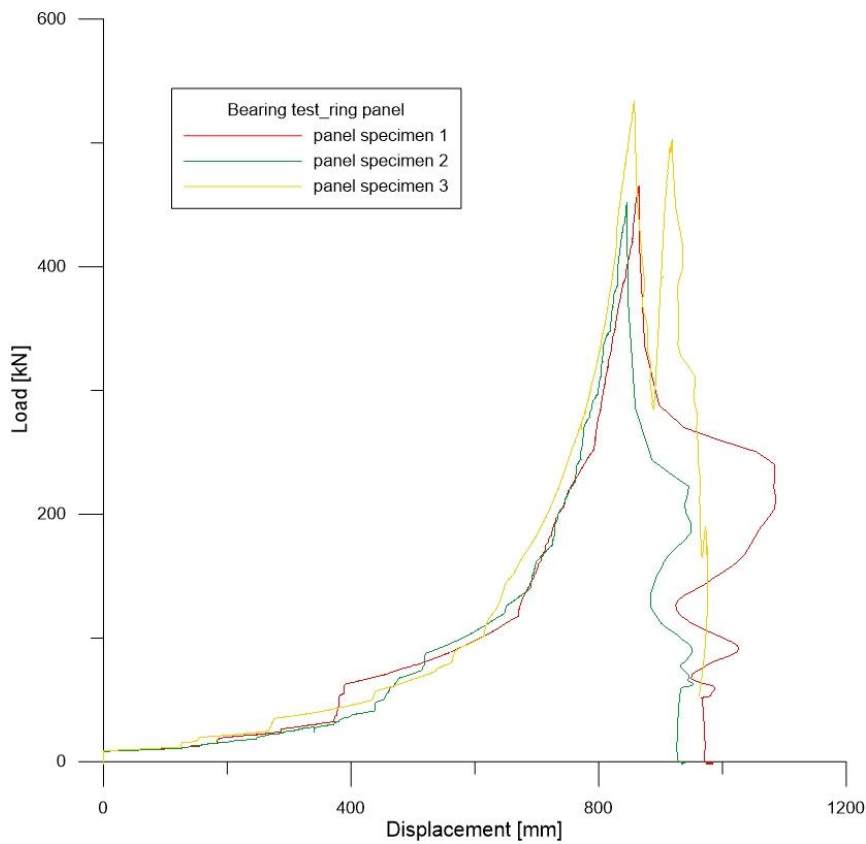
Figure 4.28: Summary of results obtained for ring panel specimens

Table 4.7: Results of test on ring panels

Specimen	Maximum displacement [cm]	Load of tear brake [KN]	Average load [KN]	Standard deviation
1	73.51	400.14		
2	84.53	451.57	483.49	43.99
3	85.82	533.66		
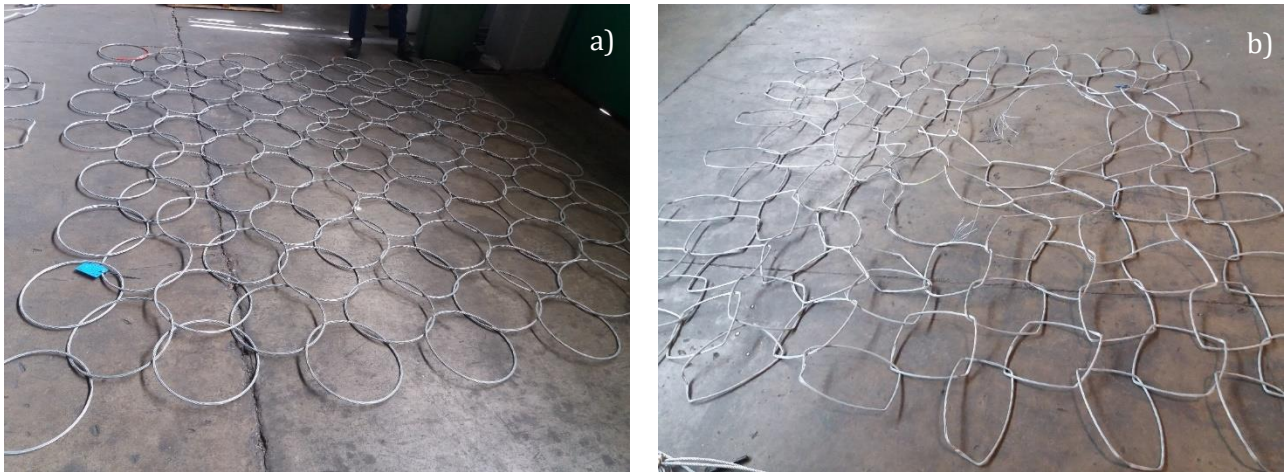
Figure 4.29: Tested ring panel; a) Specimen before test and b) Specimen brake due to loading process

Net tensile test

The second test that was performed is the net tensile test, which consist in determines the actual longitudinal tensile strength and transversal tensile strength and the relative elongation of ring net panel. For this purpose, a frame made of four steel beams, one of which is free to slide in the direction of the load (longitudinal direction,), shall be used.

The specimen shall have a width not less than 1000 mm and a minimum area of 1,0 m2. The specimen shall be fixed to the frame by means of lateral coupling devices, such as crickets or turnbuckles. The side coupling device shall be free to slide along the longitudinal beams. The test frame must be equipped with load cells in order to acquire the load applied and the overall side reaction (longitudinal and transversal reactions).

The wire rope of the panel specimens is closed by two aluminum pressed ferrules of cylindrical shape made from aluminum Al 5150 A, with resistance not less than 90% of the rope-breaking load. During the test, the panel is fixed to the rigid frame, made by steel beams, by steel sheaves (Figure 4.31). The test frame is equipped with load cells in order to acquire the load applied and the overall side reaction (longitudinal and transversal reactions).
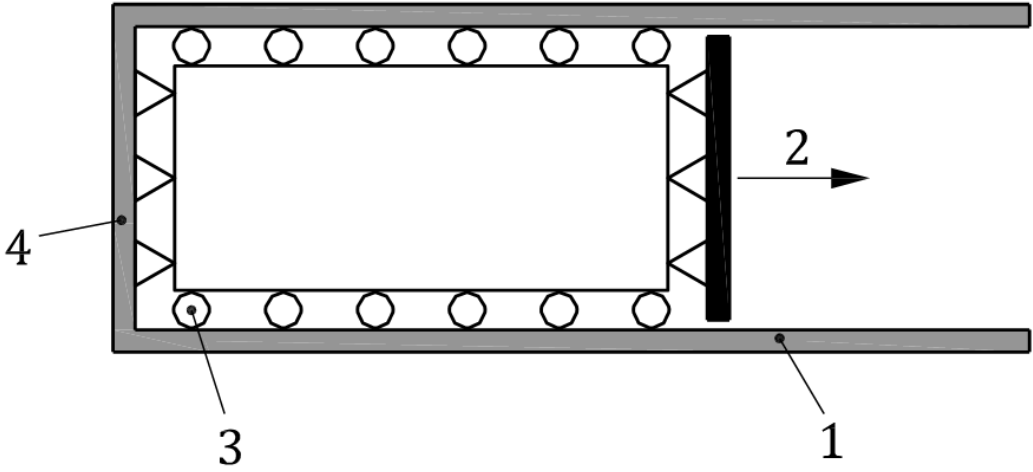
Key:
1 = fixed frame
2 = movable beam
3 = lateral constraint
4 = side connection device

Figure 4.30: Net tensile strength test configuration

Beams

Sheaves

Lateral load cells for side reaction measurement
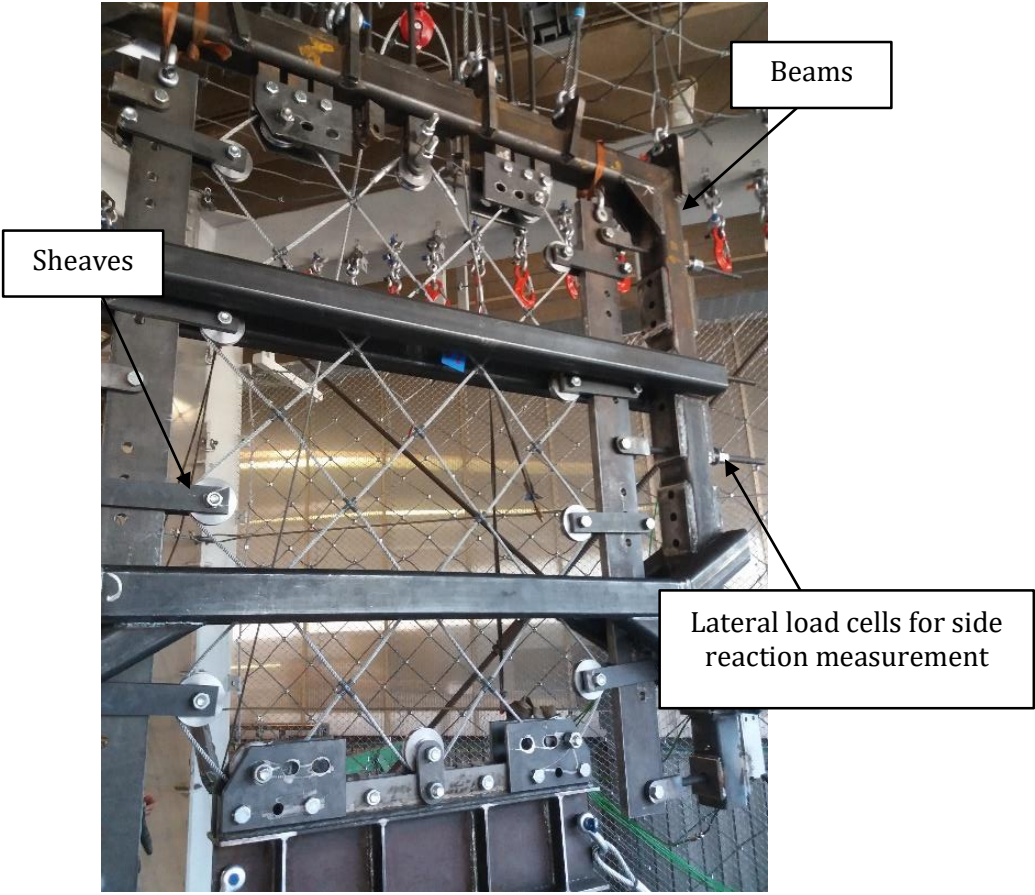
Figure 4.31: Net tensile strength test configuration

HCP panel

Table 4.8: Tensile test on HCP net features

Test object	N. 3 specimen of wire rope net panel − nominal dimension: 1,0x1,5 m − mesh nominal size: 300x300 mm − wire rope lot: 5204 − wire rope nominal diameter: 10 mm − wire rope nominal strength: 1960 N/mm² − knot: HCP
Type of test	Longitudinal tensile test
Standard	EAD 2300005-00-0106 (ISO/DIS 17746)
Test equipment	− Load cell Class 1 (UNI EN ISO 7500-1) with capacity of 1500 kN - calibration checks performed by Laboratories Trentino Srl on 30/06/2016 − Wire extensimeter Class 1 (UNI EN ISO 5500-1) with capacity of 4000 mm – calibration checks performed by Laboratorio Trentino Srl on 27/06/2016 − N. 5 load cell with capacity of 200 kN - checks performed by Laboratorio Trentino Srl on 14/06/2017
Date of test	22/09/2016

Figure 4.32: Example of transversal forces involved during the test of HCP panels
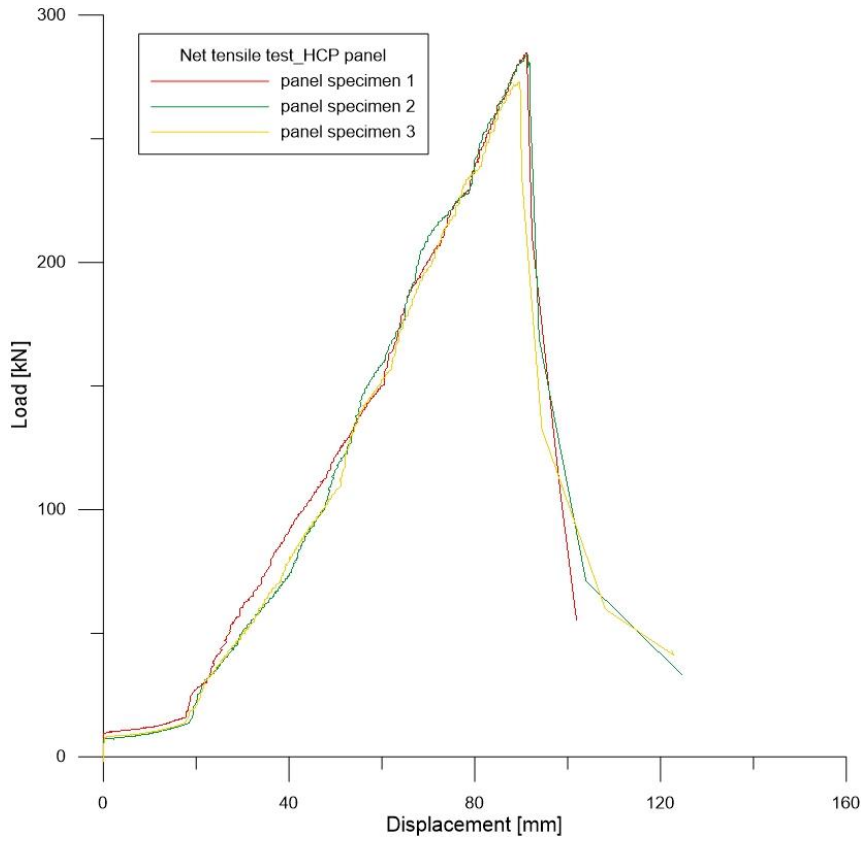
Figure 4.33: Summary of results obtained during HCP panel tensile tests

Table 4.9: Maximum displacements and breaking loads obtained from tensile test on HCP panels

Specimen	Maximum displacement [mm]	Breaking load [KN]	Average load [KN]	Standard deviation
1	9,12	284,73		
2	9,14	283,74	280,59	6,34
3	8,98	273,29		
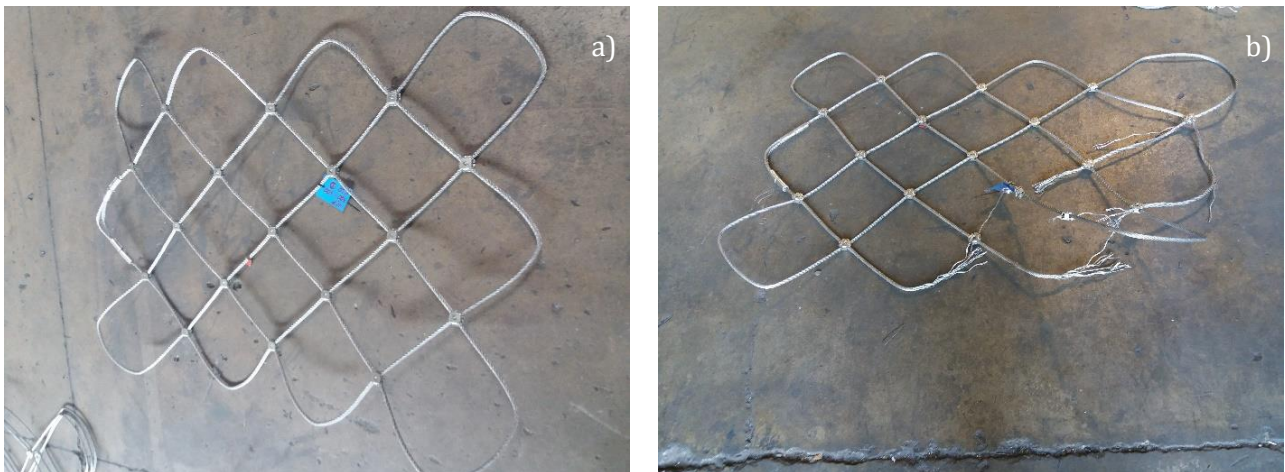
Figure 4.34: Tested HCP panel; a) Specimen before test and b) Specimen brake due to loading process

SW panel

Table 4.10: SW panel tensile test features

Test object	N. 3 specimen of wire rope net panel − nominal dimension: 1,0x1,5 m − mesh nominal size: 300x300 mm − wire rope lot: 5204 − wire rope nominal diameter: 10 mm − wire rope nominal strength: 1960 N/mm² − knot: SW
Type of test	Longitudinal tensile test
Standard	EAD 2300005-00-0106 (ISO/DIS 17746)
Test equipment	− Load cell Class 1 (UNI EN ISO 7500-1) with capacity of 1500 kN - calibration checks performed by Laboratories Trentino Srl on 30/06/2016 − Wire extensimeter Class 1 (UNI EN ISO 5500-1) with capacity of 4000 mm – calibration checks performed by Laboratorio Trentino Srl on 27/06/2016 − N. 5 load cell with capacity of 200 kN - checks performed by Laboratorio Trentino Srl on 14/06/2017
Date of test	21/06/2016

Figure 4.35: Example of transversal forces involved during SW panel tensile test
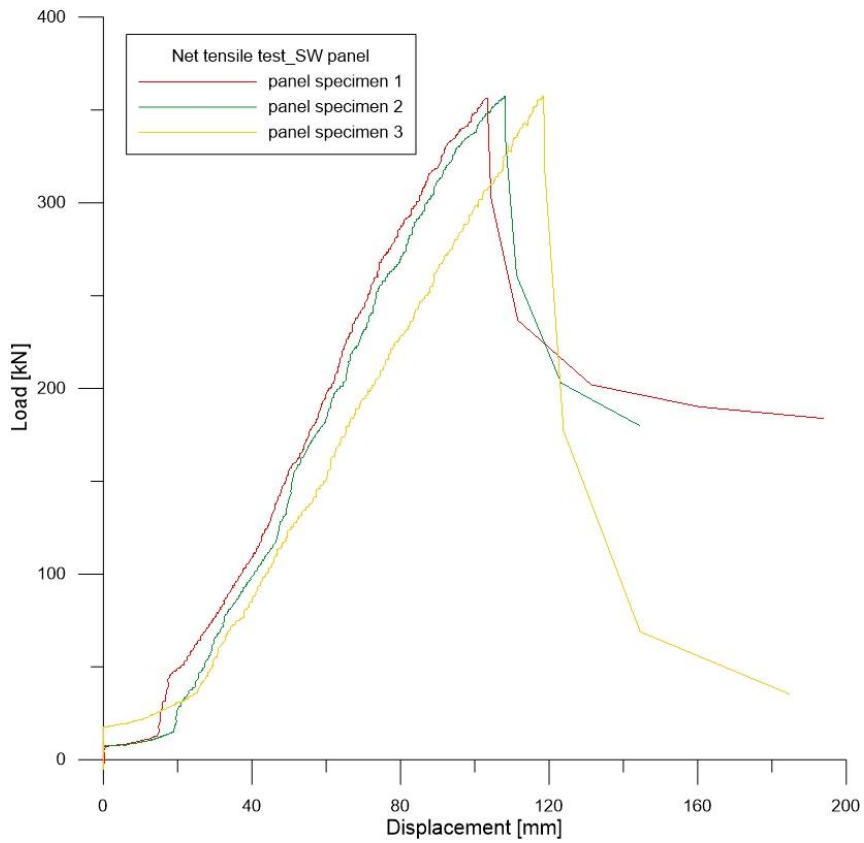
Figure 4.36: Summary of results obtained during SW panel tensile tests

Table 4.11: Maximum displacements and breaking load obtained for SW panels during tensile tests

Specimen	Maximum displacement [cm]	Breaking load [KN]	Average load [KN]	Standard deviation
1	10,33	356,56		
2	10,27	357,63	357,25	0,60
3	11,80	357,57		
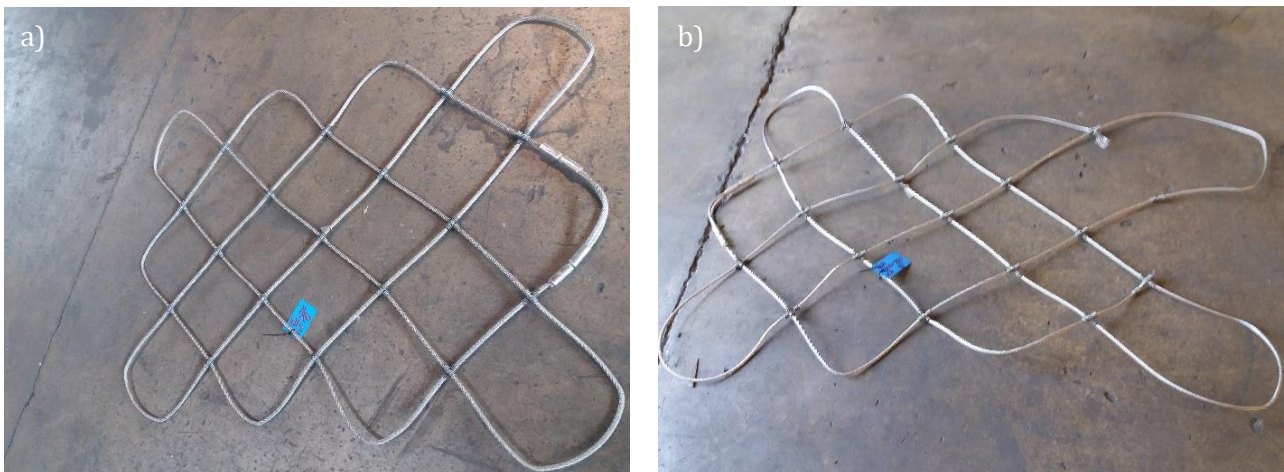
Figure 4.37: Tested SW panel; a) Specimen before test and b) Specimen brake due to loading process

Ring panel

Table 4.12: Ring panel tensile test features

Test object	N. 3 specimen of ring mesh panel − nominal dimension: 1,0x1,5 m − ring diameter: 350 mm − lot: 5224 − wire diameter: 3.5 mm − wire rope nominal strength: 1570 N/mm^2 − number of contact point: 4
Type of test	Longitudinal tensile test
Standard	EAD 2300005-00-0106 (ISO/DIS 17745)
Test equipment	− Load cell Class 1 (UNI EN ISO 7500-1) with capacity of 1500 kN - calibration checks performed by Laboratories Trentino Srl on 30/06/2016 − Wire extensimeter Class 1 (UNI EN ISO 5500-1) with capacity of 4000 mm – calibration checks performed by Laboratorio Trentino Srl on 27/06/2016 − N. 5 load cell with capacity of 200 kN - checks performed by Laboratorio Trentino Srl on 14/06/2016
Date of test	21/06/2016

Figure 4.38: Example of transversal forces involved during ring panel tensile test
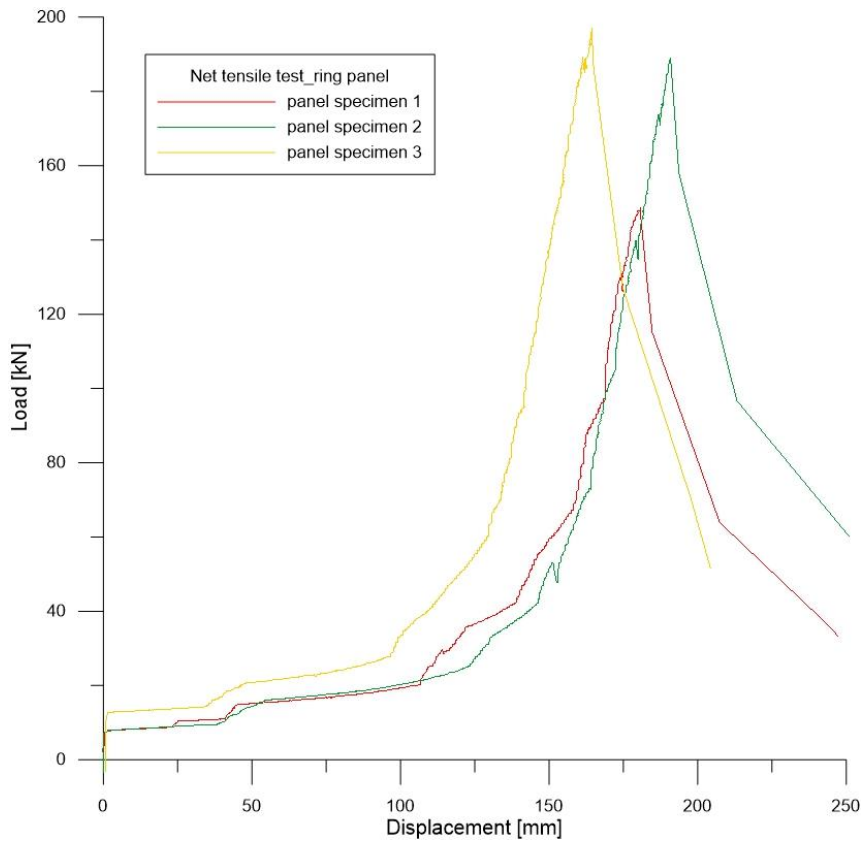
Figure 4.39: Load-displacement graph for ring panel tensile tests

Table 4.13: Ring panel tensile test results

Specimen	Maximum displacement [cm]	Load of tear brake [KN]	Average load [KN]	Standard deviation
1	18.06	148.60		
2	19.08	189.06	178.26	26.0
3	16.35	197.12		

Figure 4.40: Tested ring panel; a) Specimen before test and b) Specimen brake due to loading process

4.4.2. Secondary net

In some, cases, an additional layer can be applied on the primary net; typically, it is a metallic single or double twisted net. The secondary mesh allows loads distribution and retention of smaller material (Figure 4.41).

Figure 4.41: Combination of wire ring mesh panel and secondary net

Example of secondary net are chain-wire, chain-link and double-twisted nets, which are light systems commonly used for low-energy barriers. When the barrier is designed for higher energy levels these types of nets are no more reliable but they can be used as secondary meshes with the only function to intercept small fraction of blocks, but the principal mesh is made by strongly steel cables with larger diameters (Mentani, 2015).

Table 4.14: Feature of double torsion net specimen

Test object	N. 1 specimen of metallic net mesh 60x106 mm with 7x7 construction rope and with diameter 1,5 mm
Type of test	Longitudinal tensile test
Standard	EAD 2300005-00-0106 (ISO/DIS 17745)
Test equipment	− Load cell Class 1 (UNI EN ISO 7500-1) with capacity of 1500 kN - calibration checks performed by Laboratories Trentino Srl on 30/06/2016 − Wire extensimeter Class 1 (UNI EN ISO 5500-1) with capacity of 4000 mm – calibration checks performed by Laboratorio Trentino Srl on 27/06/2016 − N. 5 load cell with capacity of 200 kN - checks performed by Laboratorio Trentino Srl on 14/06/2016
Date of test	21/05/2017

To evaluate mechanical behavior of the secondary net a load bearing capacity test was performed. Net specimen breaking load was broken consequently of an application of 383.3 kg, after 8 minutes and 50 seconds from the test starting (Figure 4.42). The average test velocity was 0.35 kg/s. Test features and results are reported in Table 4.14 and Table 4.15.

Figure 4.42: Net specimen after test
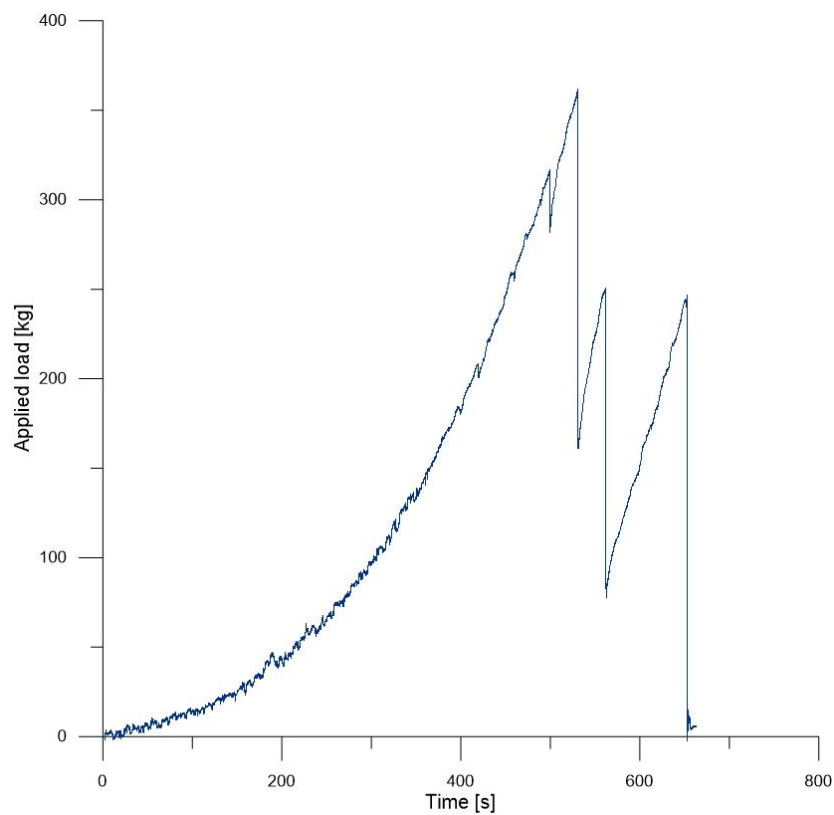
Figure 4.43: Load-time graph obtained from secondary net bearing test

Table 4.15: Results of bearing test on secondary net

Breaking load	383,3 kg
Average loading velocity	0,35 kg/s
Test duration	530,7 s
Net deformation	39,5 cm

Figure 4.44: Mass dropping

Adding falling test (Figure 4.44) was performing to attest the resistance of the net: 75 kg mass was dropped for a high of 1 meter. After the test net didn't show any damage and maintained its structural integrity. No break was occurred (Figure 4.45).
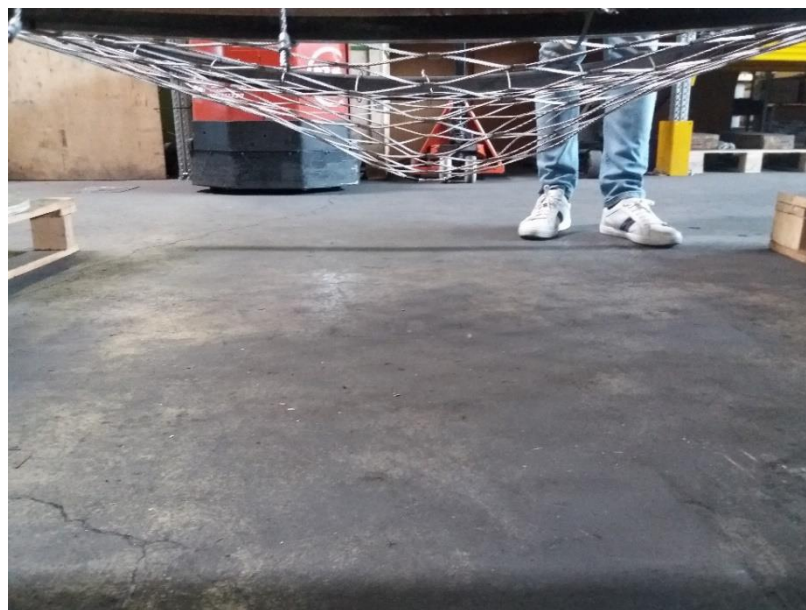
Figure 4.45: Net deformation

4.5. Connecting components

They are cables, shackles, clamps and other elements involved at the intersection nodes for the internal connection between the various constitutive elements. They have the function to connect the mesh to the supporting structure and transmit the stresses, resulting from the impact, to the foundations (Mentani, 2015).

Figure 4.46: Wire rope 12 mm section – number of wires and detail
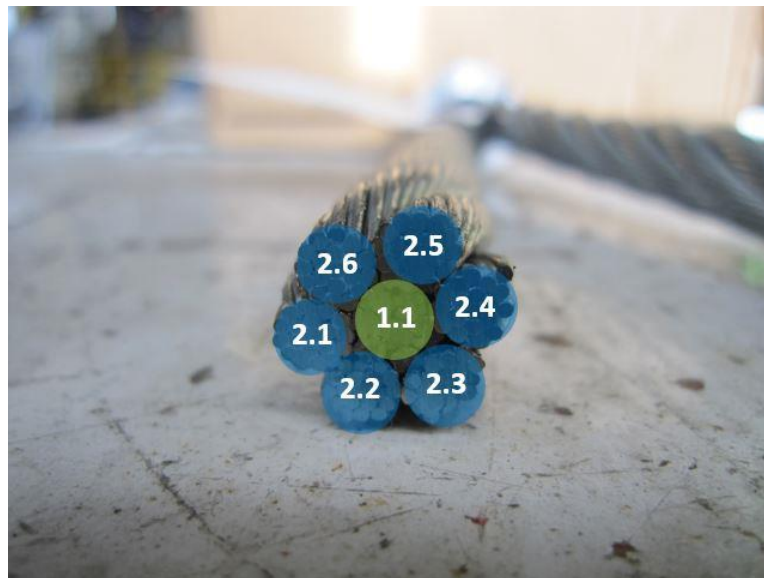
Figure 4.47: Wire groups

In this paragraph some examples of tested ropes were reported. According to UNI EN 12385-1, the minimum desired breaking load has to be proofed by traction test (Figure 4.48). The rope ends are fixed with metallic ferrules (UNI EN 13411-3) and the specimens are mounted in a calibrated test traction rig.

Load was measured by calibrated load cell. In order to obtain more information of the wire rope construction, some rope specimens were cut and rope construction was analyzed (Figure 4.46 and Figure 4.47).
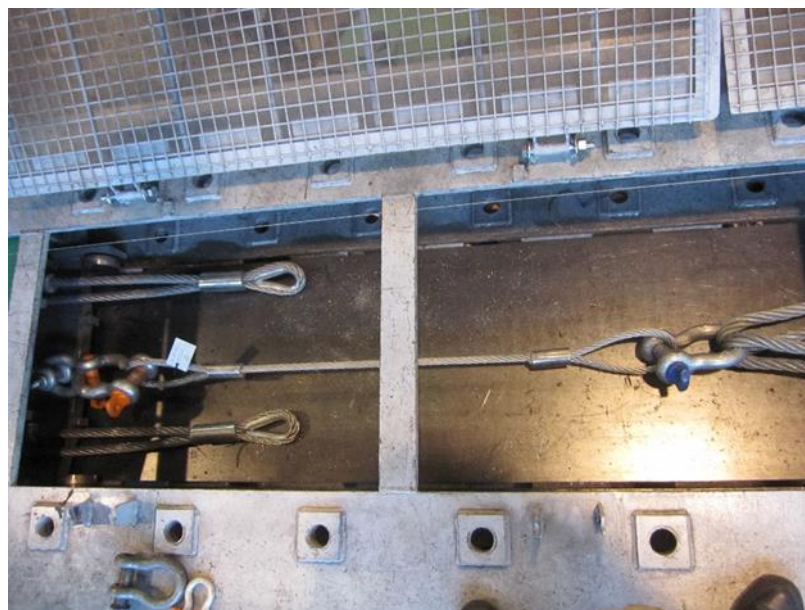
Figure 4.48: Traction test on ropes configuration

Table 4.16: Test and rope' features

Test object	N. 3 specimens of wire rope diameter 12 mm (UNI EN 12385-4). Ends are fixed with aluminium ferrules.
Construction	6x19 + WSC
Tensile strength	1960 N/mm²
Reel number	7030
Type of test	Breaking load (UNI EN 12385-1)
Test equipment	Load cell Class 1 (UNI EN ISO 7500-1) with capacity of 1500 kN - calibration checks performed by Laboratorio Trentino Srl on 05/09/2017
Date of test	22/01/2018

Table 4.17: Breaking load of the tested ropes

Specimen number	Breaking load [kN]
1	115.52
2	125.97
3	117.27
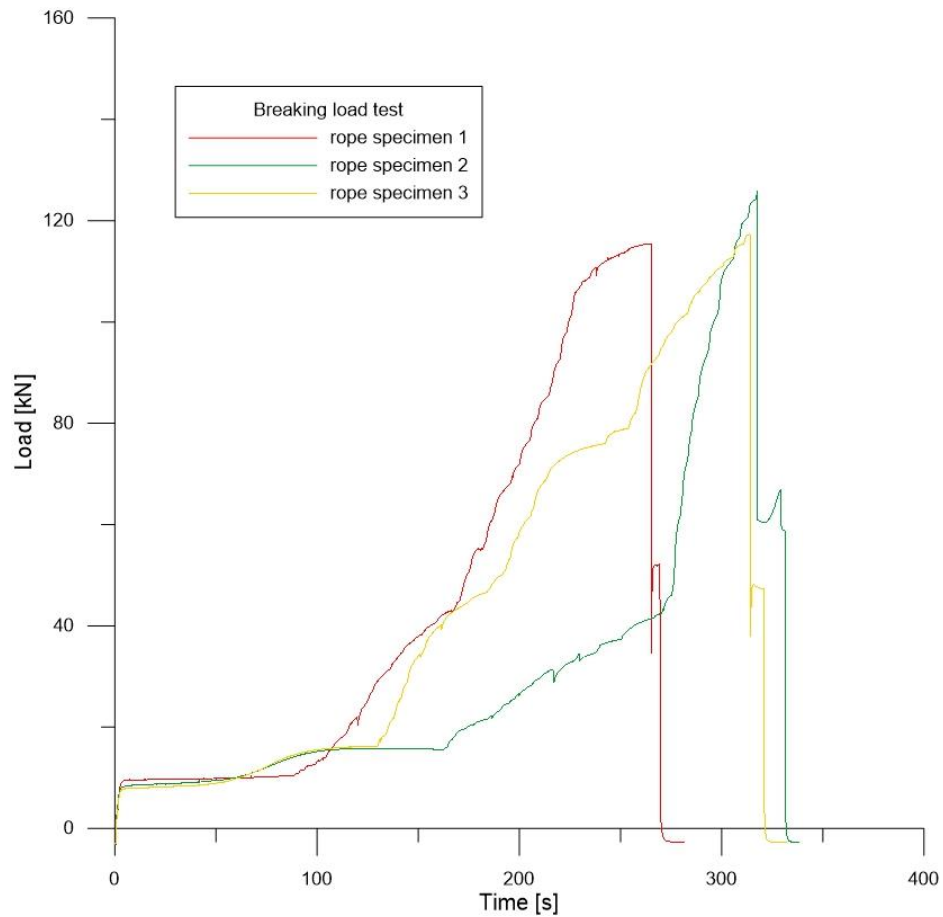
Figure 4.49: Summary of results obtained for rope specimen
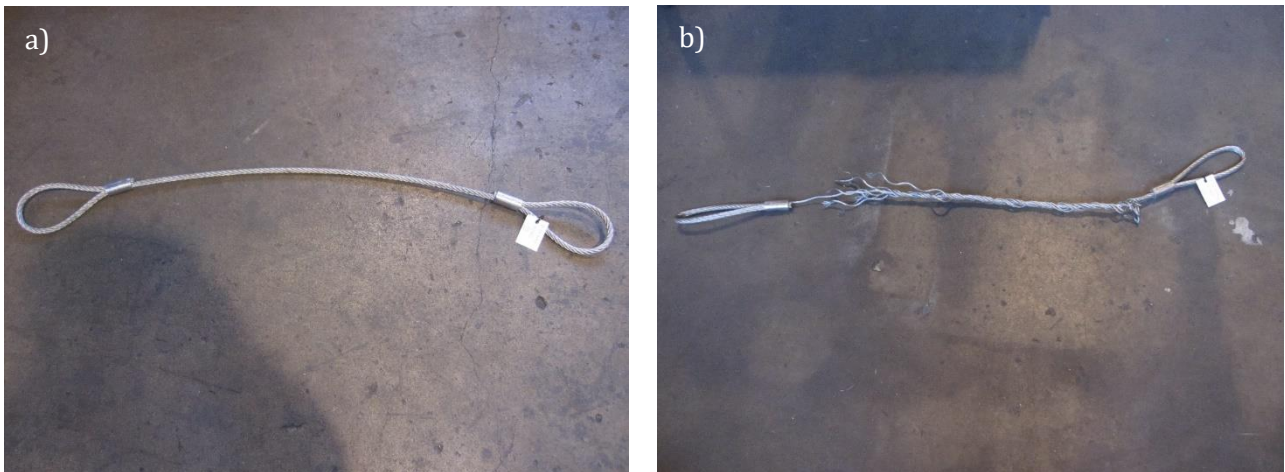
Figure 4.50: Tested rope; a) Specimen before the test and b) Rope failure after due to the reaching of the breaking load

4.6. Energy dissipation devices

The energy dissipating devices (or brake elements), which absorb the energy generated by impact and reduce the mechanical stresses in the rest of the elements of the structure, are an essential part of flexible protection barriers (Castanon-Jano et al., 2018). They can be defined as

the mechanisms incorporated into the structures that allow to absorb internal energy, helping to reduce stresses due to an impact phenomenon. These devices transform the kinetic and potential energy of the moving materials into deformation energy, fracture or heat generated by friction.

Brake elements currently on the market are grouped in 4 classes according to the way they dissipate energy (Castanon-Jano et al., 2018):

1) Brake elements by pure friction were the first brakes to be invented due to their simplicity; in most cases friction dissipation is guarantee by the sliding between wire ropes and steel elements. A disadvantage of this kind of brakes is the use of the support and connection cables in the braking mechanism, which could bring on local failures and, consequently, leads to a not reliable results;

2) Brake elements by partial failure which are the least common, probably because they can be dangerous due to the possibility of rupture in unexpected zones of the brake (Fulde et al. 2013).

3) Brake elements by plastic deformation, where the energy dissipation is due to a non-recoverable deformation of some of their components;

4) Brake elements by mixed friction/plastic deformation, which combine both for impact energy dissipation.

Implementation of new plastic deformation brake element

During the designed phase of the new brake element, four essential aspects have to be taken into account (according with Castanon-Jano et al., 2018):

a) Integrity: the brakes must be designed to avoid failure when they exhaust their available displacement, this would cause the failure of the anchorage points in the barrier, leading to instability as well as inefficacy in the rock retention;

b) Adaptability: versatile brake elements are required, in which parameters such as materials, friction level or friction coefficients among components, dimensions, etc. can vary, generating options regarding their absorption capacity. The mechanical properties of the material also affect the energy absorption, providing adaptability to the brakes which work by deformation. Trad (2011) tested brakes in two different materials: steel and aluminum, and concluded that the choice would depend on the energy required by the flexible barrier. Thus, the aluminum brake, with a lower resistance to buckling could be used in a low energy barrier while steel could be used in high energy barriers. The variation of any dimension in a component of a brake makes the force vary and hence, so too the absorbed energy;

c) Durability: in most cases brake elements will suffer the harshness of climate, it is important to consider resistance to humidity, corrosion and temperature. With respect to humidity, there are no studies determining the variability of the behavior of brakes under rainy conditions; for friction brake elements it can be assumed that, when the surfaces of the brake are wet, the friction coefficient decreases and energy dissipation capacity is lower;

d) Service limit state: it depends on the number of impacts; an event on a barrier may make the brakes work only partially, or even not to work at all, so they would be able to resist other events without making any changes in the barrier. Currently, brakes are designed to have a short useful life in relation to the other barrier components, since they are designed as the weakest element of the structure, and are connected in such a way that they are easily replaced.

The new brake element which was implemented (Figure 4.51b) is innovative, both for the geometry, unique and original, and the functioning.

This device dissipates energy through its plastic deformation; in this way no friction or local failure phenomena, which would make the brake mechanical behavior irregular and unpredictable, occur.
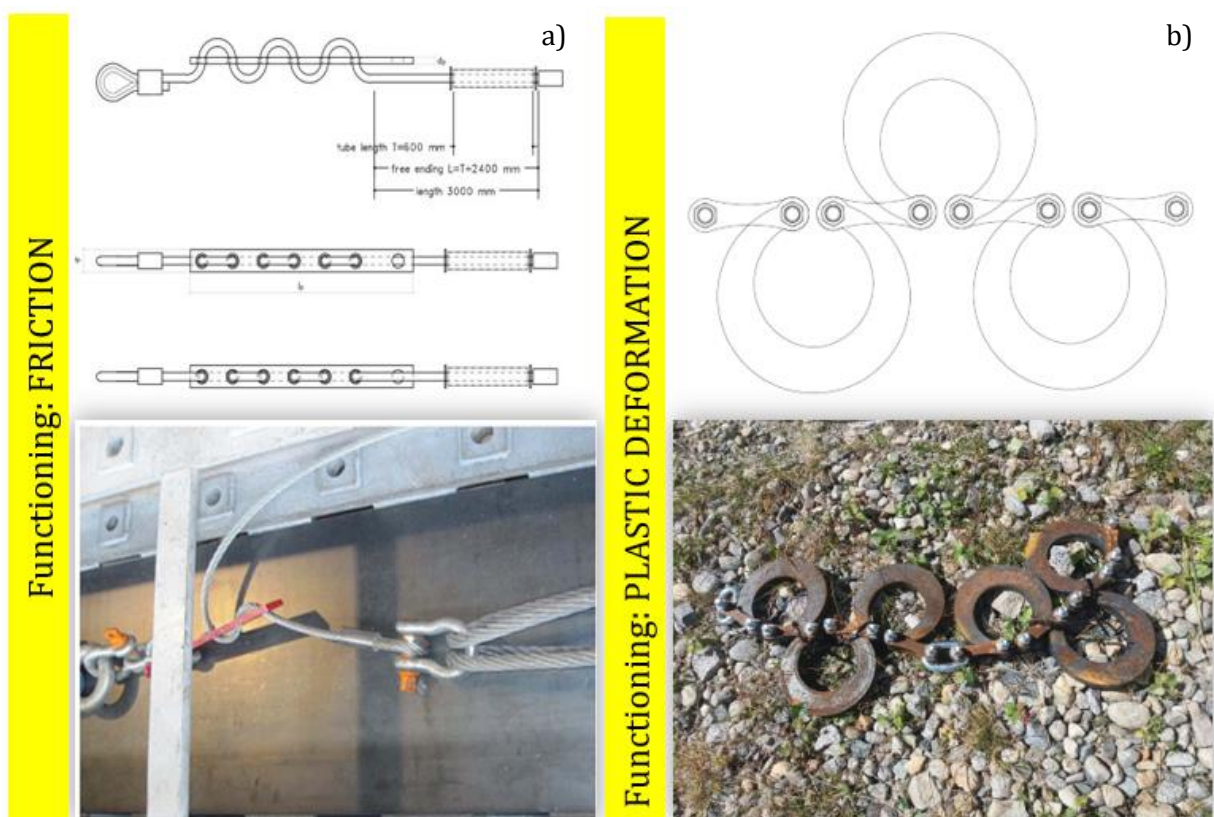
Figure 4.51: Drawings and photos showing differences between the new energy dissipation devices friction functioning (a) and the new brake which absorbs energy simply by its deformation (b)

The new brake is able to dissipate very high energy very quickly (i.e. has lower response time); this aspect reduces the overall structure deformations during an impact phenomenon and makes protection system more safe, improving its performances. The geometry of the new brake is original and different from all the solutions currently on the market, and was optimized in order to obtain the best performances in terms of absorbed energy and maximum possible elongation.

The extreme simplicity of the form, it is a ring device with opening in the top part (Figure 4.51b), will give to the brake important advantages, including the reduced cost and the immediacy of maintenance activities.

Summarizing, the main advantages that the new brake elements have comparing with the old device are the following:

- Easier and smoother maintenance;
- Minor response times;
- Significantly lower deformations with the same applied load;
- Lower cost;
- High reliability;
- Predictable behavior.

Mechanical experiments

To evaluate and quantify the mechanical response of the new energy dissipation device static and dynamic test were performed (Figure 4.54).

Static traction test was conducted in laboratory (Figure 4.54b) and the dynamic one was actuated in an old clay quarry; in the latter case load was applied through the falling of a rock connected to the brake device (Figure 4.54a). Thanks to result obtained from these experiments, numerical model of the new brake was implemented (Figure 4.54c).

Comparing the results obtained from the two different devices is possible to observe that, especially in the dynamic test, the new device is characterized by a linear stress-strain response, because its deformation is approximately constant during the increase of the applied load (Figure 4.52b and Figure 4.53b), until the reaching of maximum deformation, without discontinuous local trends, which characterized the behavior of the old brake element. On the contrary, the trend of load registered for the old brake device is not constant and is characterized by many local peaks (Figure 4.55a and Figure 4.56a) that are not predictable.

The linear and predictable behavior which characterized the new brake element considerably simplify the protection barrier design, as well as giving it considerable structural advantages.
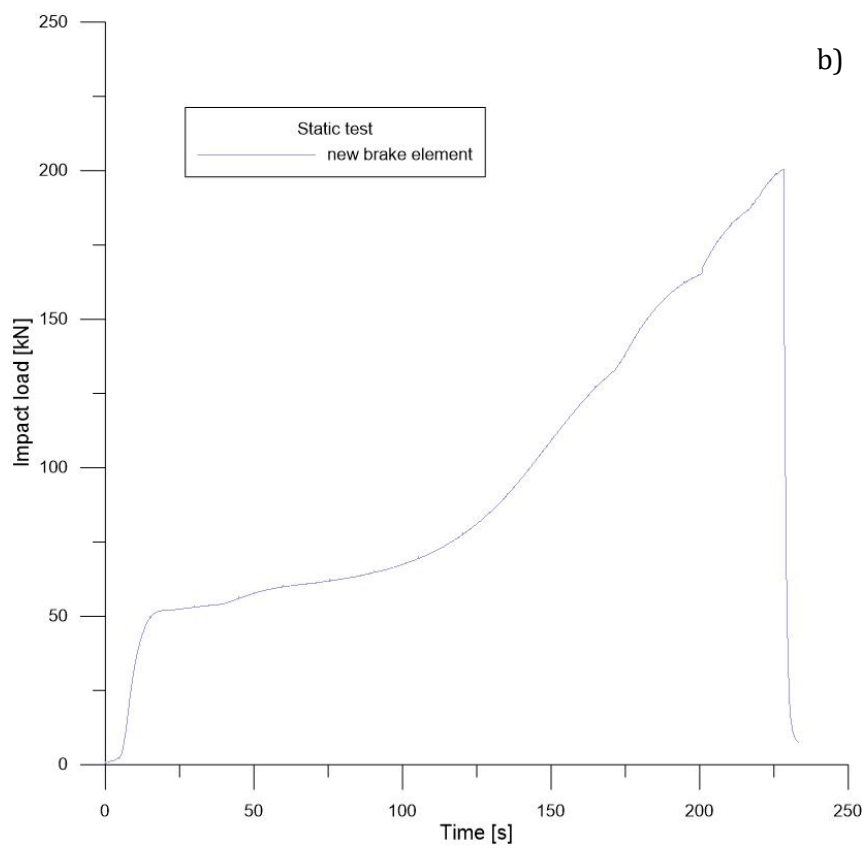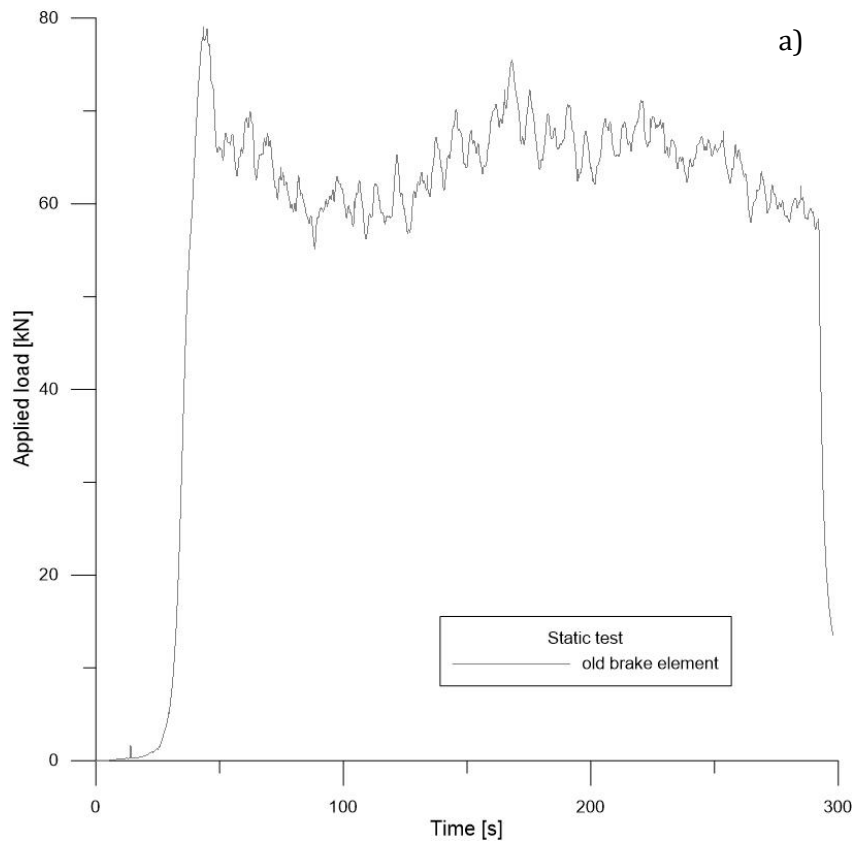
Figure 4.52: Load-time graph obtained from brake element traction static test; a) Old dissipation device and b) New dissipation device
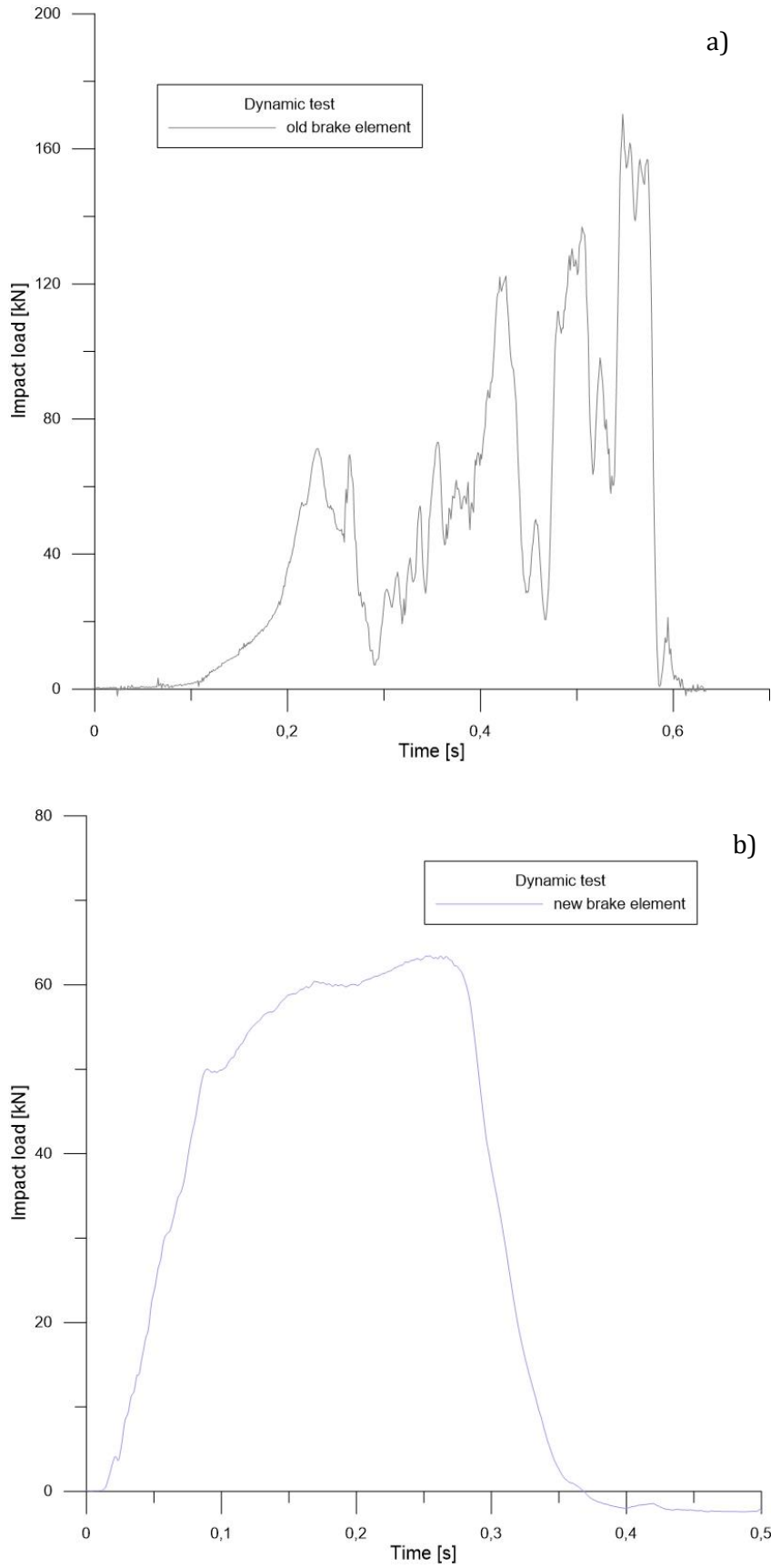
Figure 4.53: Load-time graph obtained from brake element traction dynamic test; a) Old dissipation device and b) New dissipation device
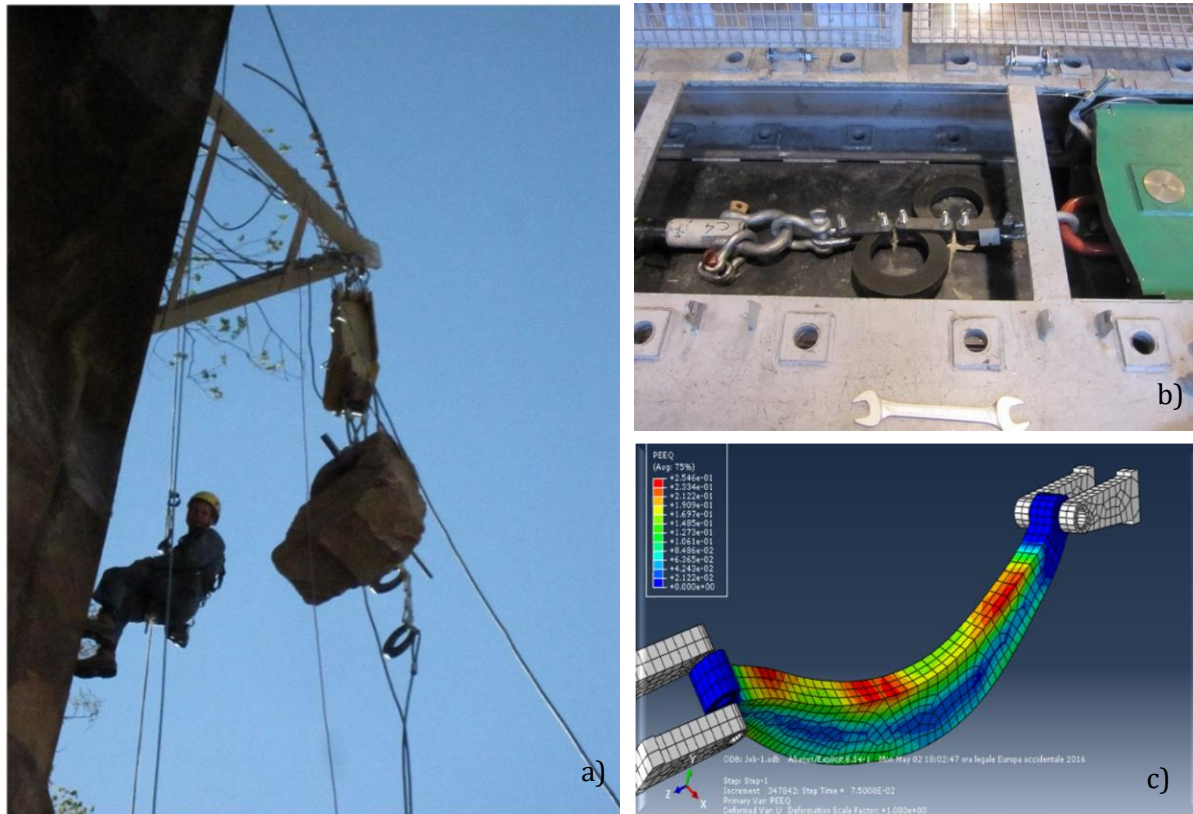
Figure 4.54: Test and elaboration conducted on new dissipation device; a) During dynamic test load was applied through a falling block; b) Static traction test performed in laboratory and c) FEM modelling

4.7. Anchors

Anchors are designed in order to transfer the load acting on flexible barriers to the ground (Figure 4.55). These elements are composed of the following components:

1) Double wire rope (available in different diameters), which makes the system light and flexible but very resistance to traction forces;

2) Circular head reinforcement made of mechanical steel, which prevents any local failures caused by the interaction between the anchor and the connecting elements (shackles, pins, etc.) and increases the system efficiency;

3) Stainless steel protective tube and oval tube, the first has the function to protect ropes and the second makes the system compact.

In order to evaluate the breaking load of the anchors and validate the numerical implemented model, several mechanical traction tests were performed in laboratory. The applied load, which increase until the reaching of the breaking value, was graph with time; Table 4.18 and Figure 4.56 displays the results obtained from three identical anchorages with rope diameter equal to 22 mm.
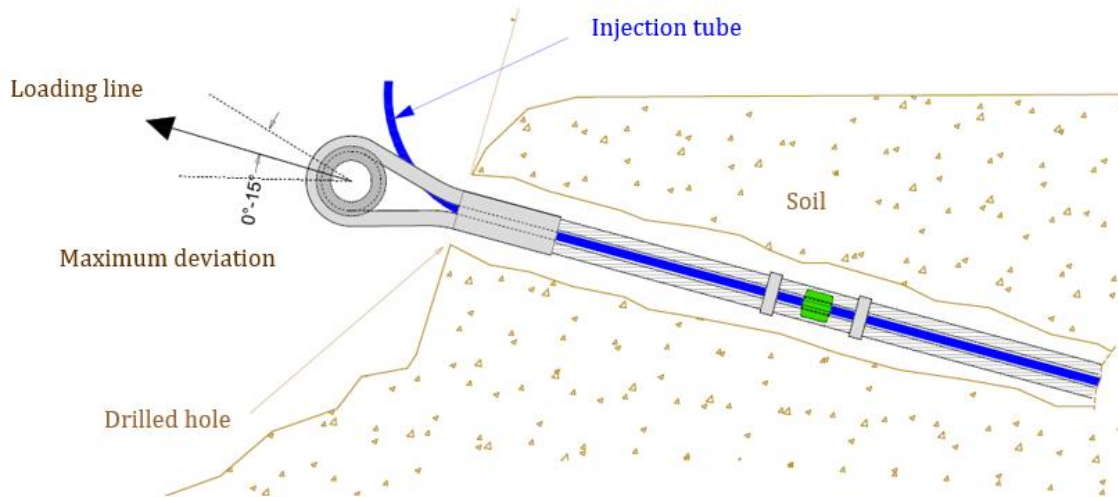
Figure 4.55: Typical installation scheme of flexible anchors

Table 4.18: Breaking load of the tested anchors

Specimen number	Breaking load [kN]
1	749.77
2	751.81
3	804.72
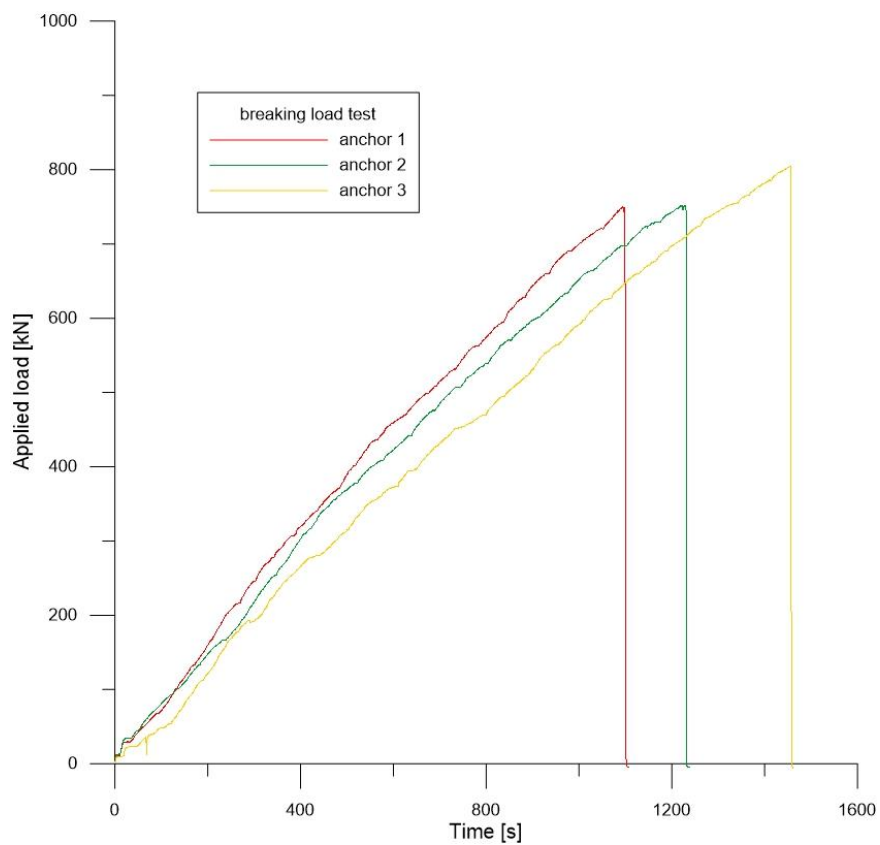
Figure 4.56: Load-time graphs obtained for three flexible anchors with 22 mm diameter rope

All the test performed are characterized by anchor brake in the middle section of the free rope part (Figure 4.54); this means that the head reinforcement protects the system against any local failure in the circular area, saving the structural integrity of the system. Therefore, the braking load of the anchor can be defined as the resistance of the used double wire rope.

Figure 4.57: Flexible anchorage system; a) Application on site; b) Numerical model of the anchor head and c) Tested anchor with broken rope

Chapter 5: Field test on rockfall barrier

5.1. Test objective

Thanks to structural components characterization and new brake device implementation, a new rockfall barrier was designed. In order to evaluate the mechanical behavior of the barrier, which dissipates energy through the new implemented brake elements (as explained in Paragraph 4.6), a field test of a rockfall barrier of energy class 4 (1500 kJ) was conducted on 10.11.2017 (Maximum Energy Level - MEL) and on 29.11.2017 (Service Energy Level - SEL) at the testing facility of cava Colombari in Biella, Italy. The set up and the corresponding monitoring and evaluation system is compliant with the requirements given in the European guideline "ETAG 027" - edition February 2008, amended April 2013, used as European Assessment Document (EAD) - using the vertical throwing method. The test area is located 20 km north of Biella, in Piemonte region in Italy, at 1340 m over the sea level (Figure 5.1). The coordinates are 45°39′ North and 7°59′10″ East.

Figure 5.1: Test site location

The test objectives were to proof the resistance of NFL_4/A rock fall protection kit (4,00 m planned working height, 10 m distance between supports, 3 modules) against the impact of a thrown object hitting the protective net, and to validate the implemented numerical model (Figure 5.2). Different tests were made on the kit: the first one (maximum energy level – MEL) was carried out using a single block with a mass of 4680 kg, impact speed ≥ 25.00 m/s and a kinetic energy of at least 1500 kJ. The other (service energy level – SEL) was carried out using two blocks crashing subsequently with the 40% of MEL energy (more than the 33% of MEL energy requested); the thrown object had a mass of 1920 kg and a speed ≥ 25.00 m/s without intermediate repair. In this Chapter only the results obtained from the first SEL test are reported.
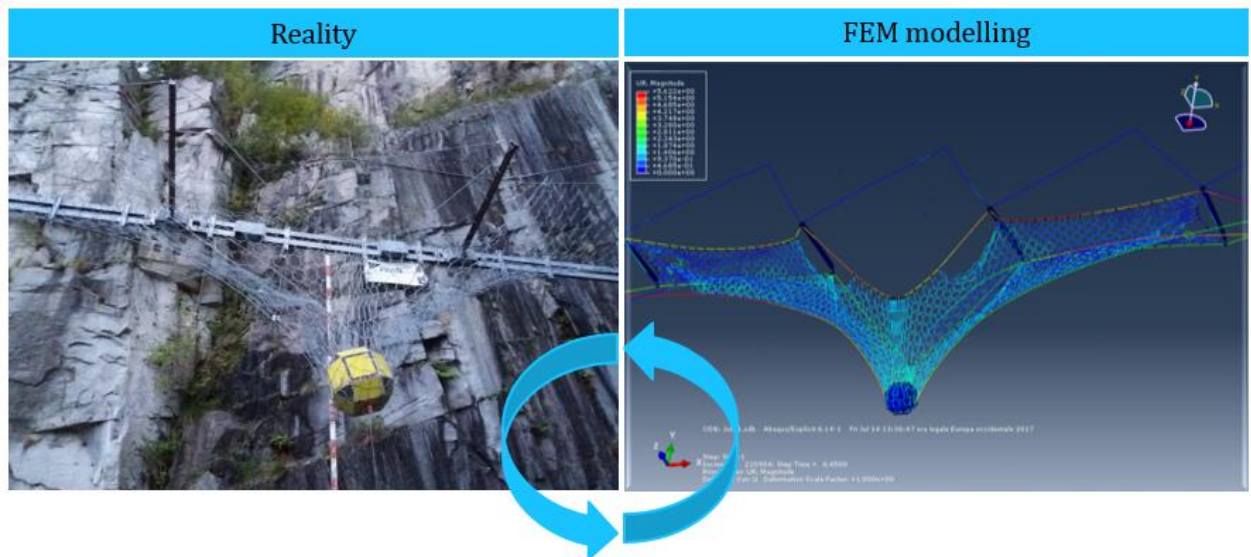
Figure 5.2: Validation of the numerical model through the results obtained from rockfall protection kit test

For the testing process a standard set up, using four posts and three spacing covered by net, was chosen according to EOTA guideline ETAG 027. The distance between the posts was approximately 10 m. The nominal height of the barrier was 4.00 m. In the test area the rock face is almost vertical. The protective net construction was mounted on a stable frame of steel supports, which were anchored into the rock. The lifting device for the thrown object consisted of a remotely controlled derrick crane with trigger mechanism. The rockfall protection kit was fastened at an angle of approximately 15° upwards in relation to the horizon. Load cells, which were polled by an electronic amplification and data logging system in intervals of 1200 values per second, were attached to the retaining cables at various positions.
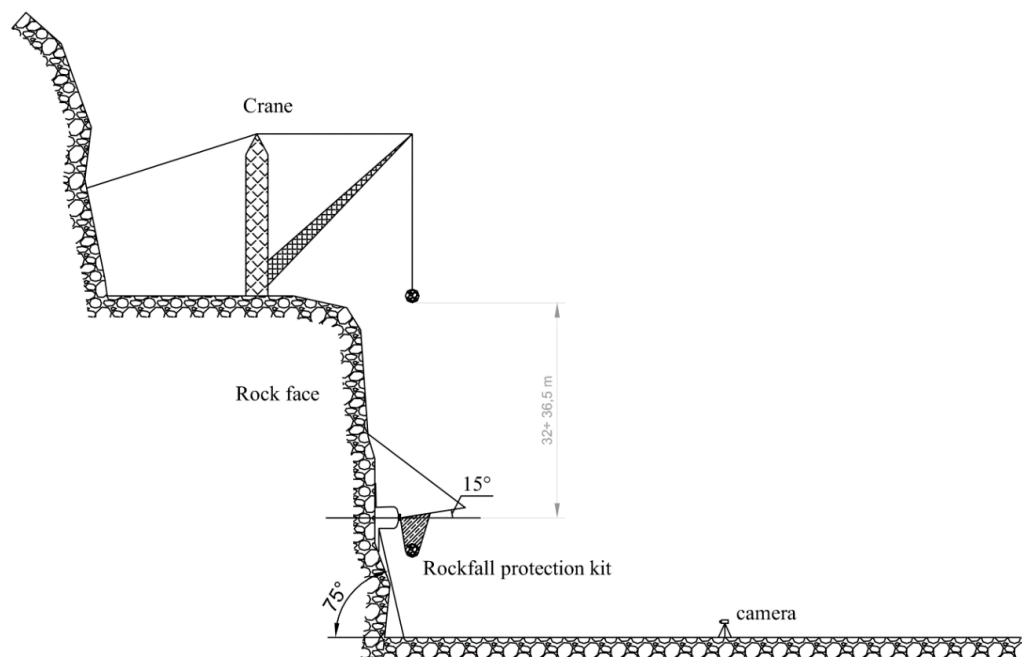
Figure 5.3: Test site sketch (lateral cross section)

The dropping sequence was captured by a high-speed video camera. It was in a frontal line of sight at the zero level, approx. 10 m below the test setup and approx. 50 m in front of the rock face (Figure 5.4). After the installation of the test setup, the characteristics of the rockfall protection kit were measured using a total topographical station and a gauging tape. The measurements were taken in compliance with European Guideline ETAG 027. The thrown object was lifted by the crane and centered above the barrier using a plumb line for each test. The impact point was set according the indications of European Guideline "ETAG 027". The block was released from a particular height to reach the necessary potential energy. The value of the impact energy is equal to the potential energy of the block, given by:

$$E = m \cdot g \cdot h \tag{5.1}$$

The necessary release heights were derived from this equation; the calculated value was 32.7 m for the SEL test. In order to provide better performance, the release height was set slightly above this minimum. To lift up the block at the correct height and to check the correct trajectory of the block, a vertical plumb line attached to the block was used. After the test, measurements of the whole kit were take again. The residual height after the impact was determined in agreement with European guideline "ETAG 027".
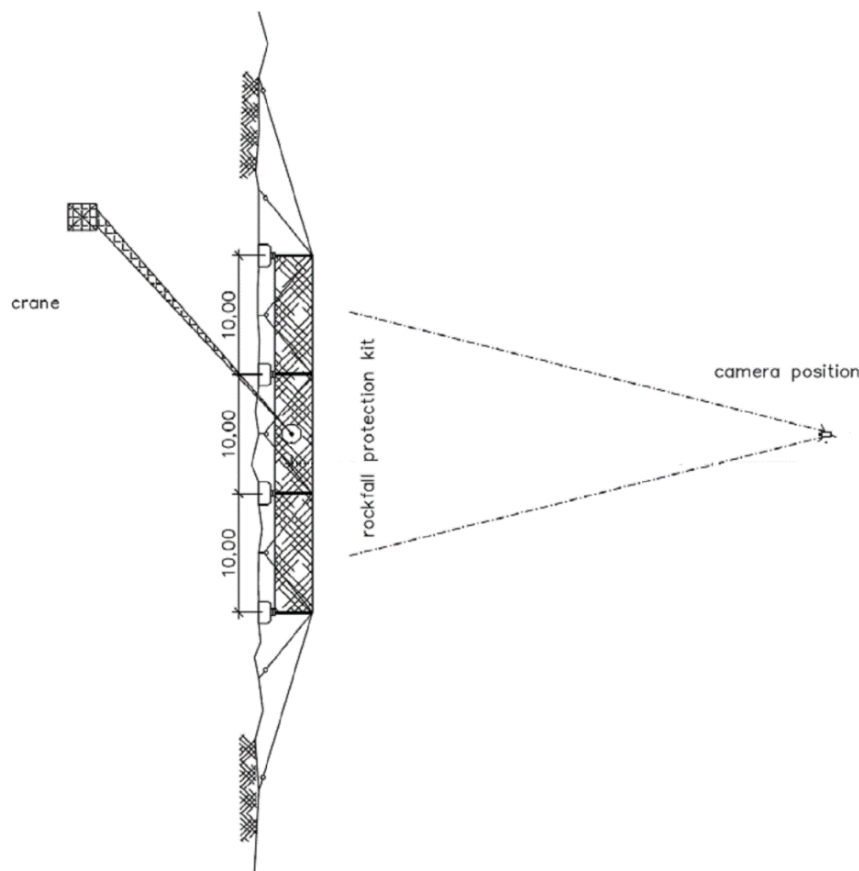
Figure 5.4: System sketches (top view)

5.2.   Documentation of the tested kit

5.2.1. Geometry of the system

The rock fall protection kit NFL_4/A consisted of three-functional module composed by four posts and three fields of net fences (Figure 5.5).

Figure 5.5: Installed kit on slope, overall view

The falling rock protection kit was made of:

a)   *Interception structure* (the net) which has the function of bearing the direct impact of the mass, deforming elastically and/or plastically, and transmitting the stresses to the connection components, the support structure and the foundations. The ring's net diameter was 350 mm; the strand diameter of the ring material was 10.5 mm;

b)   *Support structure* (the posts) which has the function of maintaining the interception structure, which is by nature not rigid, unbent. The distance between the posts axes was 10 m;

c)   *Connection components* (connecting ropes), which have the function of transmitting the stresses to the foundation. In order to allow the deformation, devices can be installed onto the structure, which allows a controlled lengthening of the connection components. The diameter of the ropes was different by the function. The diameter is between 12 and 22 mm.

5.2.2. Nominal height of barrier definition

From ETAG guideline, the nominal height hn is the minimum distance between the upper support rope and the connection line between the bases of the posts before the impact and is measured orthogonally to the reference slope. In order to calculate the nominal height of the net, a tape and an inclinometer (with a precision of ± 0.1°) were used.

Key:
α = angle of block trajectory towards horizon (90°)
β = angle of reference slope
μ = angle of connecting vector between upper bearing rope and the connection line of the baseplates
κ = angle of post inclination
h_n = nominal height
C = length of the connecting vector between upper bearing rope and the connection line of the baseplates
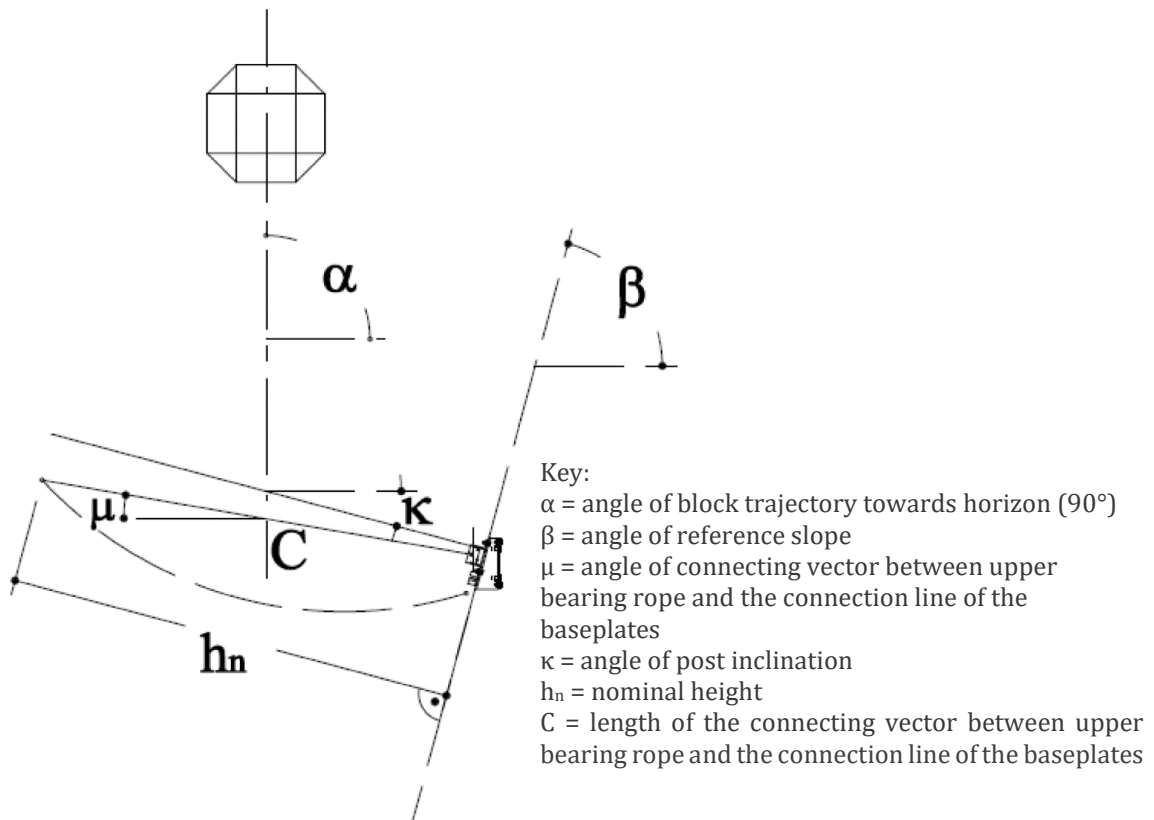
Figure 5.6: Definition of the barrier nominal height and parameters involved

The results were the distance C and the referring angle μ at which the tape was inclined during the measurement. Using this angle, and assuming the reference slope β = 75°, the deviation angle delta can be obtained by the following formula:

$$\delta = 90° - \beta - \mu \tag{5.1}$$

Assuming a triangle with C as the hypotenuse is possible to calculate the projection of C on the reference slope normal by using the relation:

$$h_n = C \cdot cos(90 - \beta - \mu) \tag{5.2}$$
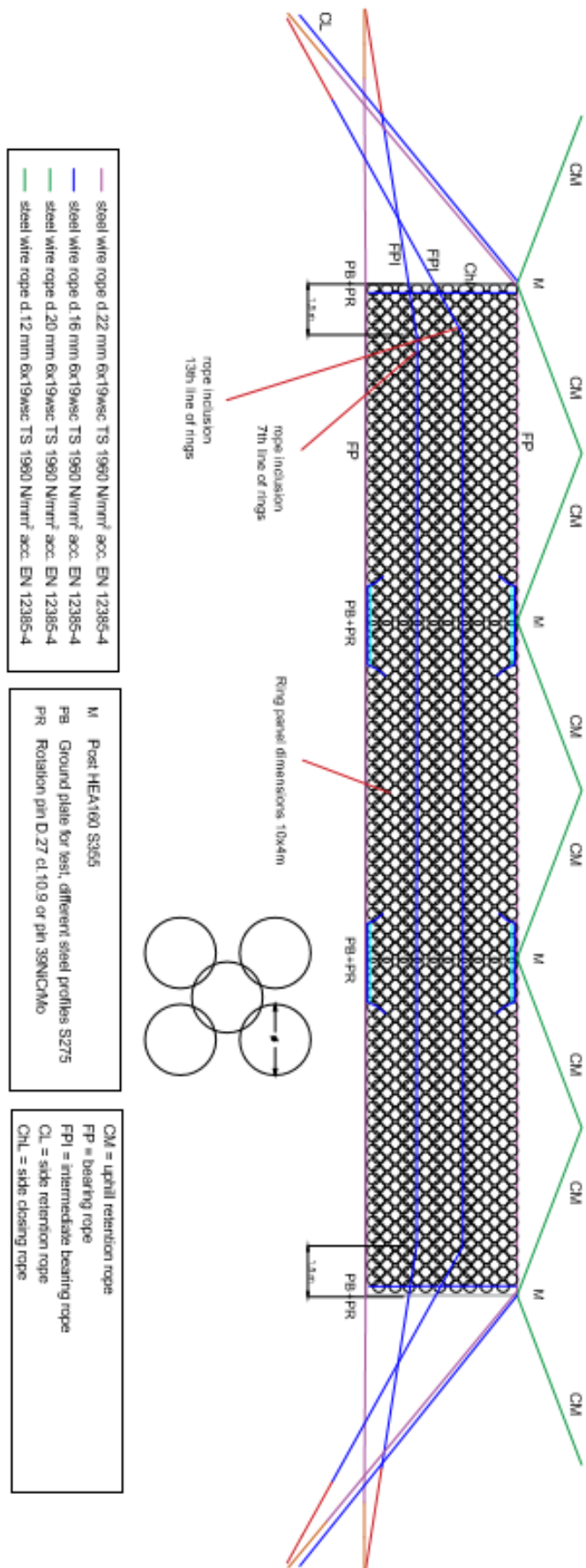
Figure 5.7: Scheme of the kit, front view

5.2.3. Detailed geometrical survey before test

Measurement and a schematic representation of the kit structure before the first SEL test are shown below. Positions of the post were calculated using a total topographical station.

Table 5.1: Coordinates of the theodolite and camera

	Total station	Camera
X	99.983	99.983
Y	100.025	100.025
Z	0.029	1.684
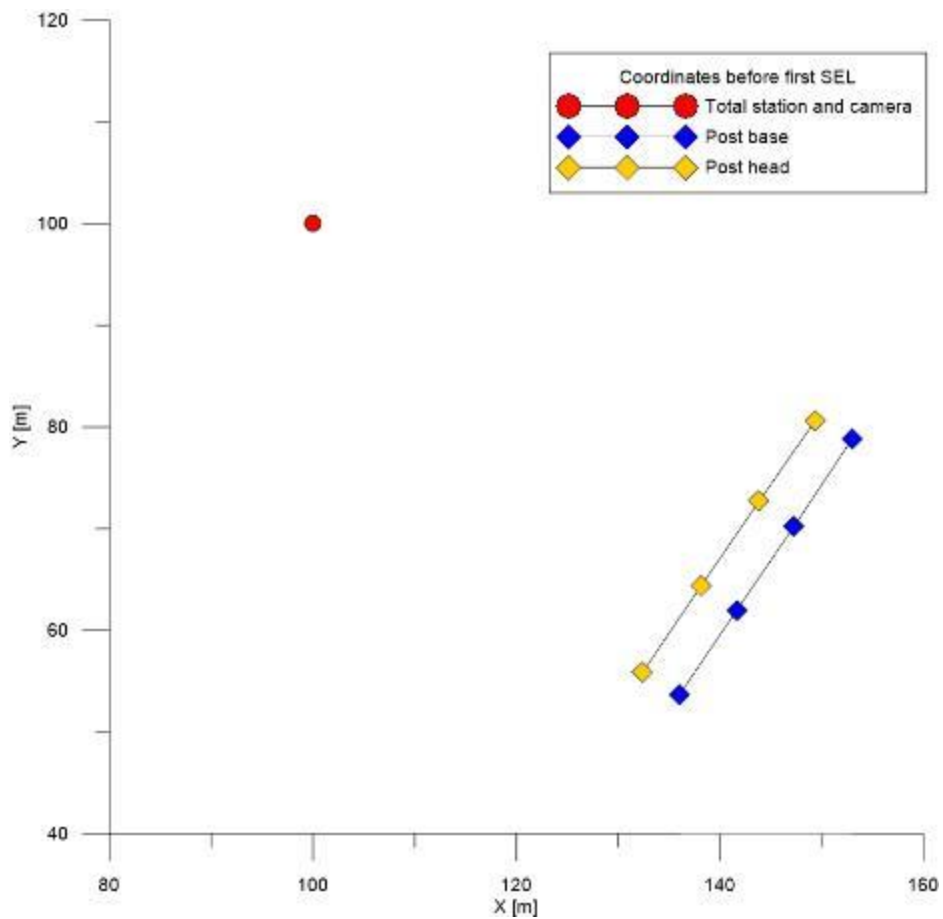
Figure 5.8: Position in the X-Y plane of the post and total station before the first SEL

Table 5.2: Coordinates and inclination of the posts before the first SEL test

		POST 1	POST 2	POST 3	POST 4
POST BASE	X	153.005	147.287	141.644	136.035
	Y	78.849	70.223	61.966	53.692
	Z	10.691	10.684	10.640	10.846
POST HEAD	X	149.369	143.858	138.111	132.439
	Y	80.635	72.708	64.327	55.932
	Z	11.934	11.943	11.839	12.121
INCLINATION		17.21°	17.44°	16.59°	17.67°

5.2.4. Gaps and opening near posts before the test

As indicated in ETAG 027 guideline, if the effective surface of the falling rock protection kit is reduced due to a displacement of the net in two directions in the lateral modules, the forming gaps (the gap is the distance between the post and the net) shall be measured. The gaps in the posts head region shall be measured as well. According to this specification, the gaps were measured before and after the tests. In Figure 5.9 a schematic representation of the gaps position before the test is given. The gaps measured before all tests are shown in the following tables.

Table 5.3: Horizontal gaps near post 1 and 4 measured before the tests

	Post 1	Post 4
	[cm]	[cm]
1st SEL	11	8

Table 5.4: Opening near post 2, post 3 and in the center measured before the tests

	Post 2	Centre	Post 3
	[m]	[m]	[m]
1st SEL	3.90	3.90	3.90

The openings projected on the plane perpendicular to the reference slope are reported in Table 5.5.

Table 5.5: Opening before the tests projected on the post plane inclined by 15°

	Post 2	Centre	Post 3
	[m]	[m]	[m]
1st SEL	3.89	3.89	3.89
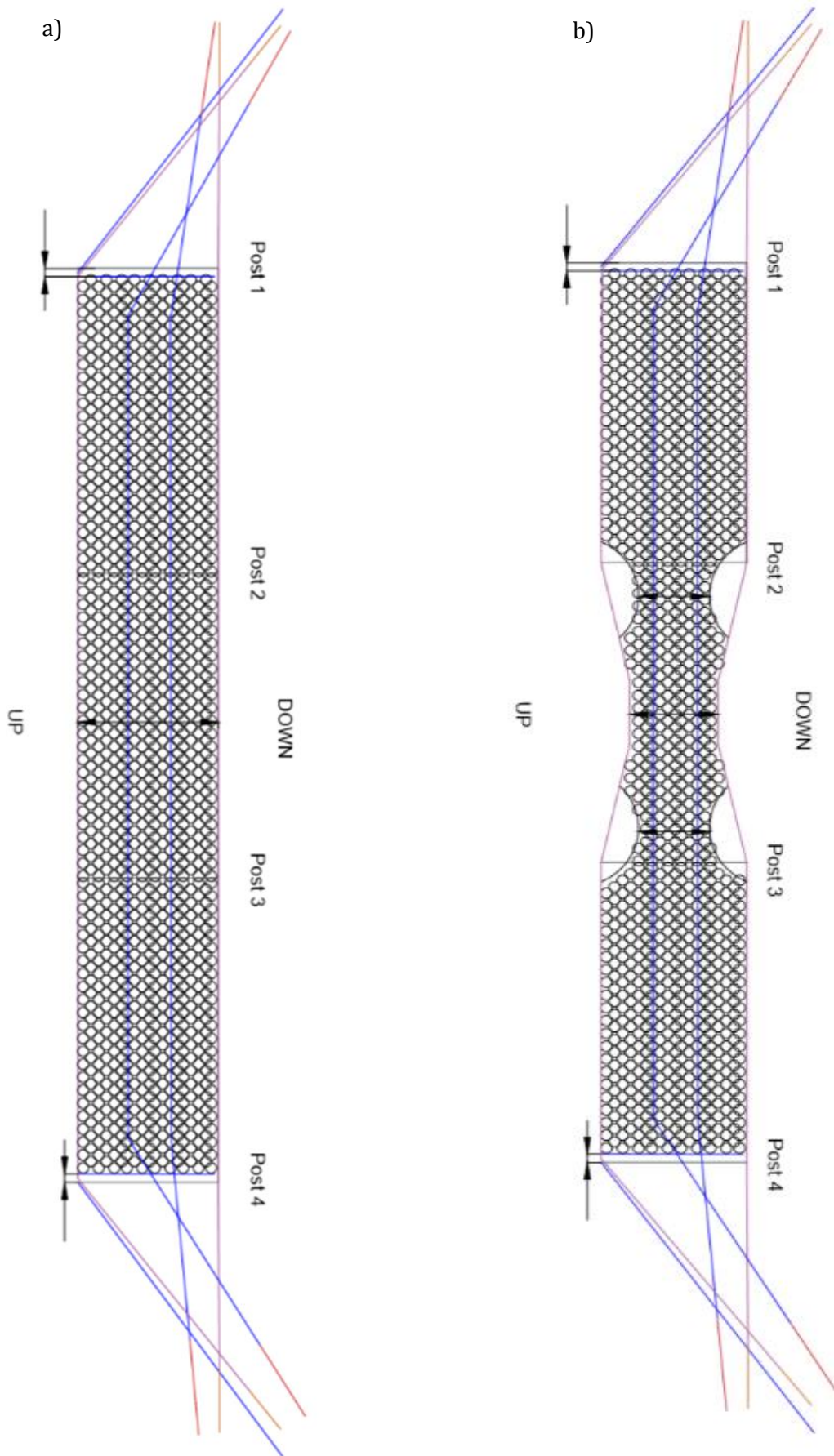
Figure 5.9: Location of gaps (view from below, looking upwards); a) Before the test and b) After the test

5.3. Test execution

5.3.1. Measurement devices and calibration

Dynamometer

During the test, a concrete block was used as objects to be thrown. The weight measurements, necessary for energy calculation, were done with a dynamometer. The device has a display precision of 1 kg in the range 40-6000 kg. Each block had one eye on the top to be lifted. In the weighing procedure, the block was lifted by crane (Figure 5.9). The dynamometer was placed between the block eye and the crane hook. For each block, three measurements were taken. The results are shown in .

Table *5.6*.

Figure 5.10: Block weighting procedure

High speed video camera

The dropping sequence was captured by a high-speed video camera (Figure 5.11). The camera was in a frontal line of sight at the zero level, approximately 10 m below the test setup and approximately 50 m in front of the rock face. The speed of the block was defined tracing the

movement of the thrown object in the photograms before the impact. Only one high-speed video camera was used. The record rate used is 500 fps with a frame resolution of 800x600 pixels.

Figure 5.11: High-speed camera; a) Location in the test area and b) Recording process

5.3.2. Block characteristics

A concrete block was used as objects to be thrown. Edges and corners had been beveled at a 45° angle along ¼ of the length of the edge. On the top of the block, there was one eye to connect the block at the derrick crane. On the bottom side, an eye was used to connect the plumb line, which allowed controlling the release height. When the block was lifted at the desired height, a release mechanism was activated to unhook the block from the derrick.

103

Figure 5.12: SEL block and release mechanism

Mass

The thrown object form was conformed to the EOTA guideline "ETAG 027". The dynamometer was used to weight the block. Measurements of the weight have been repeated 3 times. The density of the blocks, calculated using the results of weighing process and block size measurements, was between the tolerance frame of 2500-3000 kg/m^3 indicated on European Guideline ETAG 027. Characteristics of the thrown objects are given in .

Table *5.6*.

Table 5.6: Block weight measures

Energy Level	No.	Measured mass [Kg]	Average mass [kg]
SEL	1	1929	
	2	1926	1925.7
	3	1922	

Dimension

The block was made of plain concrete and its shape is a polyhedron according to European Guideline ETAG 027. The dimensions of the blocks were measured (Figure 5.13). The maximum size of the block L_{ext} was 3 times smaller than the nominal height of the kit. The measured dimension of the block are reported in Table 5.7.

Table 5.7: Block features

	Energy level	Dimension [mm]		Nominal mass [kg]	Measured mass [kg]	Density [kg/m³]	$h_N/3$ [mm]
		L_{ext}	$L_{ext}/2$				
	SEL	1000	510	1920	1926	2711	1300

Figure 5.13: Measurement detail

5.4. Test results

The Service Energy Level (SEL) test is carried out with two subsequent throws of a block into the central module of the protection kit. Both throws should attain the same kinetic energy. The objective of this test is to verify that the kit is able to contain successive impacts maintaining its residual height within an acceptable value.

5.4.1. Trajectory

The Position of the SEL launch must be in the center of the middle functional module (Figure 5.14).
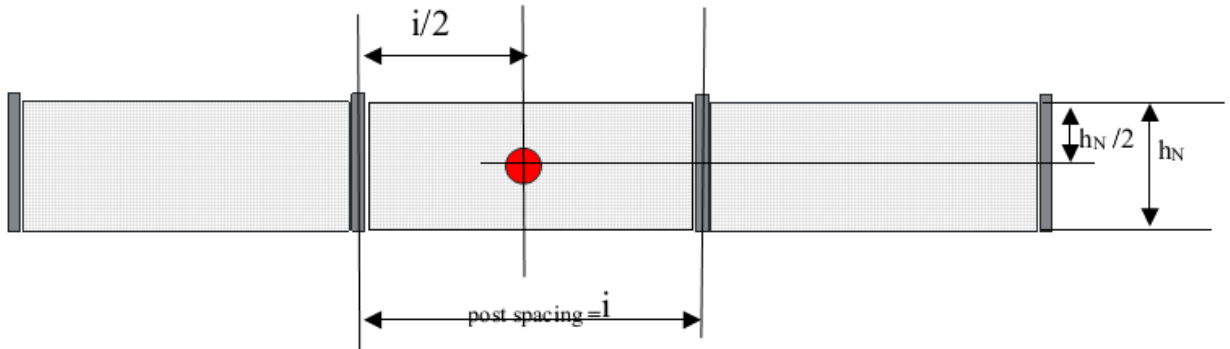
Figure 5.14: Location of impact at first SEL launch

As described in European Guideline, the trajectory of the center of mass of the block has to pass through the tolerance circle as depicted in Figure 5.15. To find the correct impact point (and the correct height of release) a plump vertical line connected to the block bottom is used. Therefore, when the block is lifted by crane, its position is set using the position of the plumb on the net.
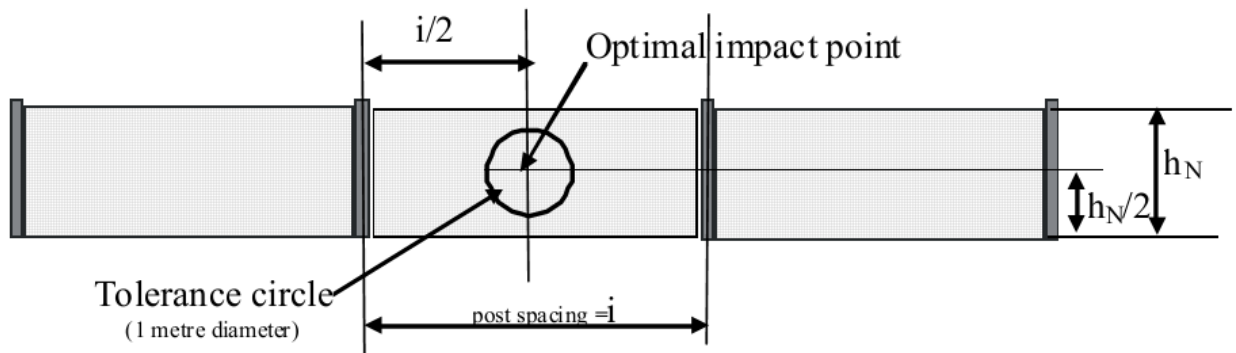
Figure 5.15: Tolerance for impact point

Figure 5.16: Impact point position for all tests (first and second SEL and MEL)

5.4.2. Effective trajectory

The position of the block lower edge before the impact is indicated in green from Figure 5.17 to Figure 5.22. In yellow is represented the position of the block lower edge after the contact with the net. The position of the block center of gravity during the fall is indicated in red.
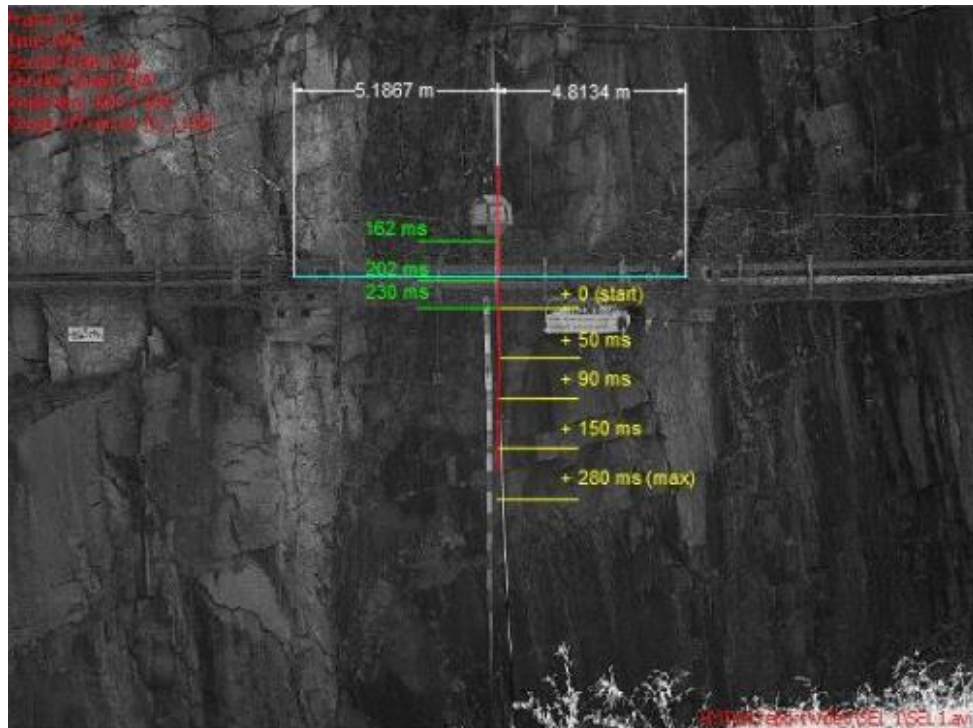
Figure 5.17: Block trajectory during SEL 1, frame 81 - start of observation
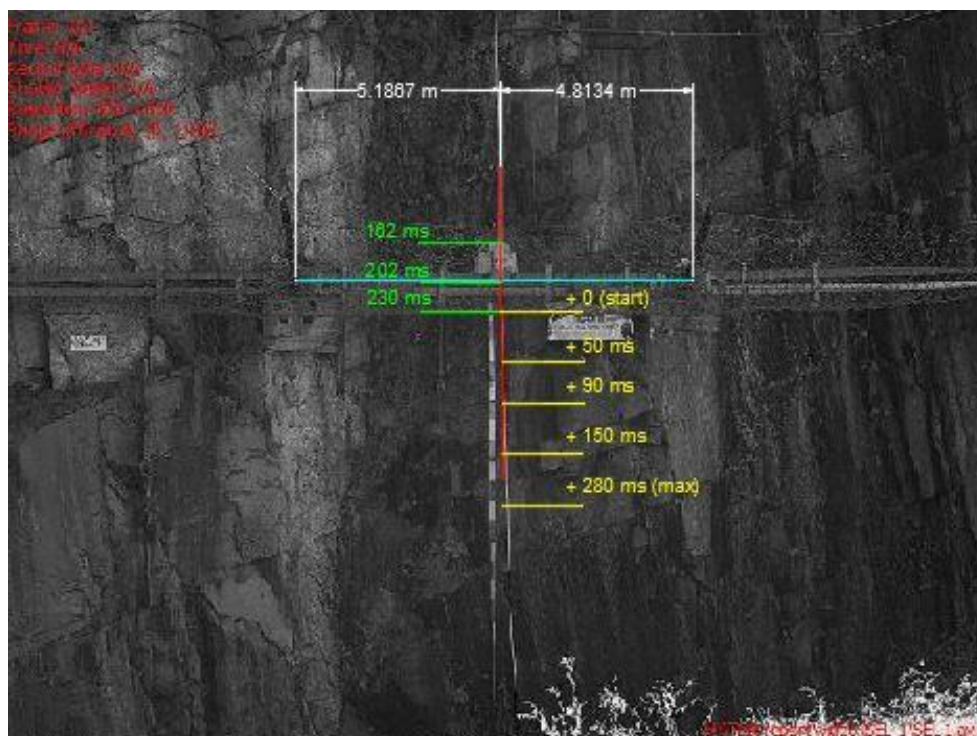
Figure 5.18: Block trajectory during SEL 1, frame 101

108
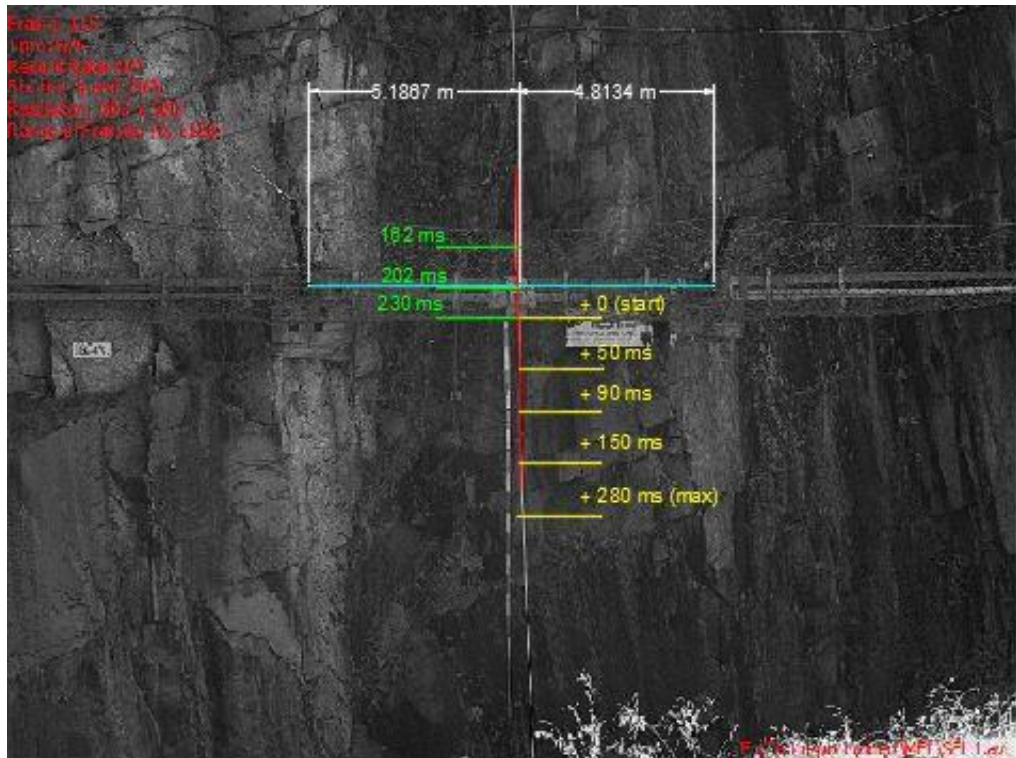
Figure 5.19: Block trajectory during SEL 1, frame 115 - contact with the net
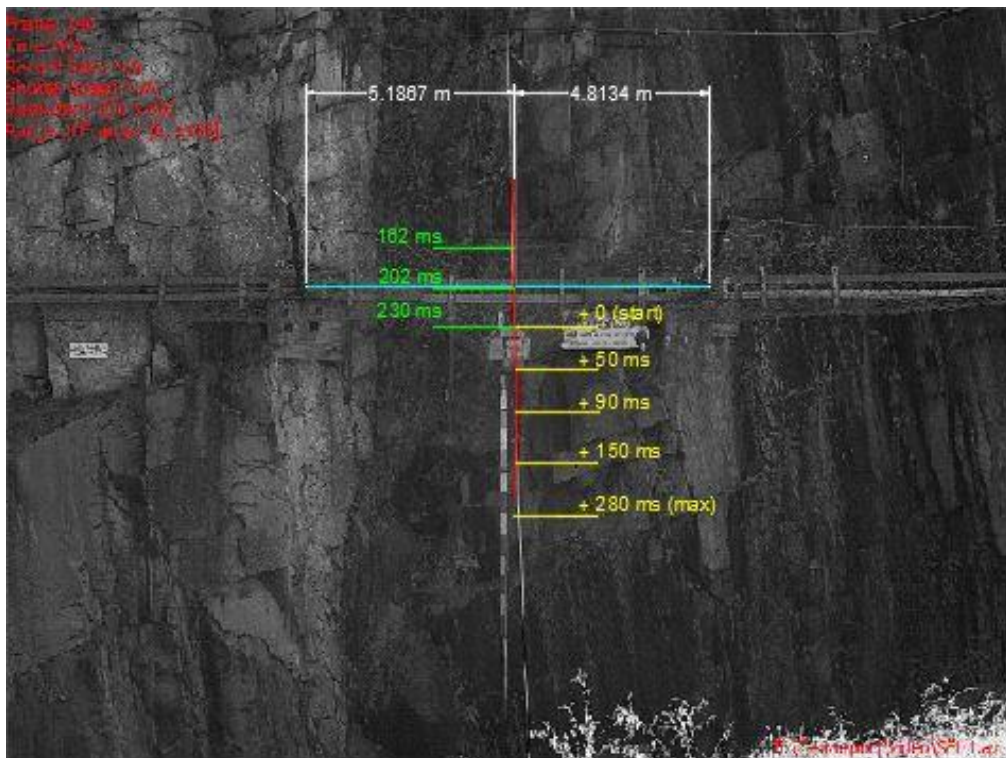
Figure 5.20: Block trajectory during SEL 1, frame 140
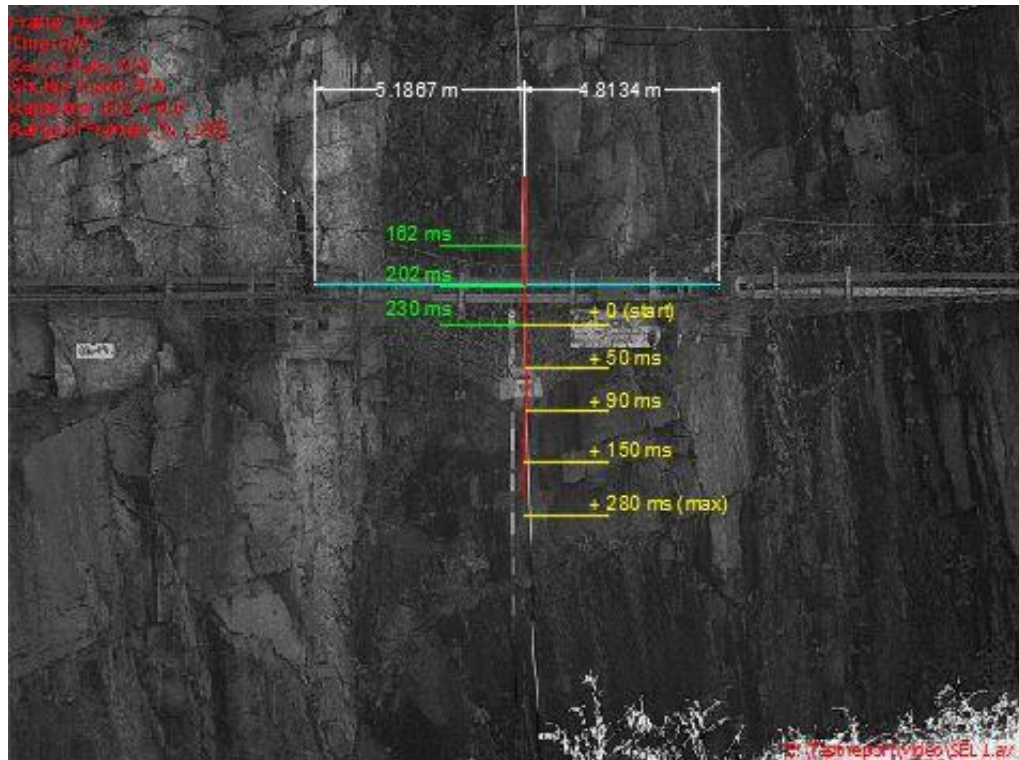
Figure 5.21: Block trajectory during SEL 1, frame 160
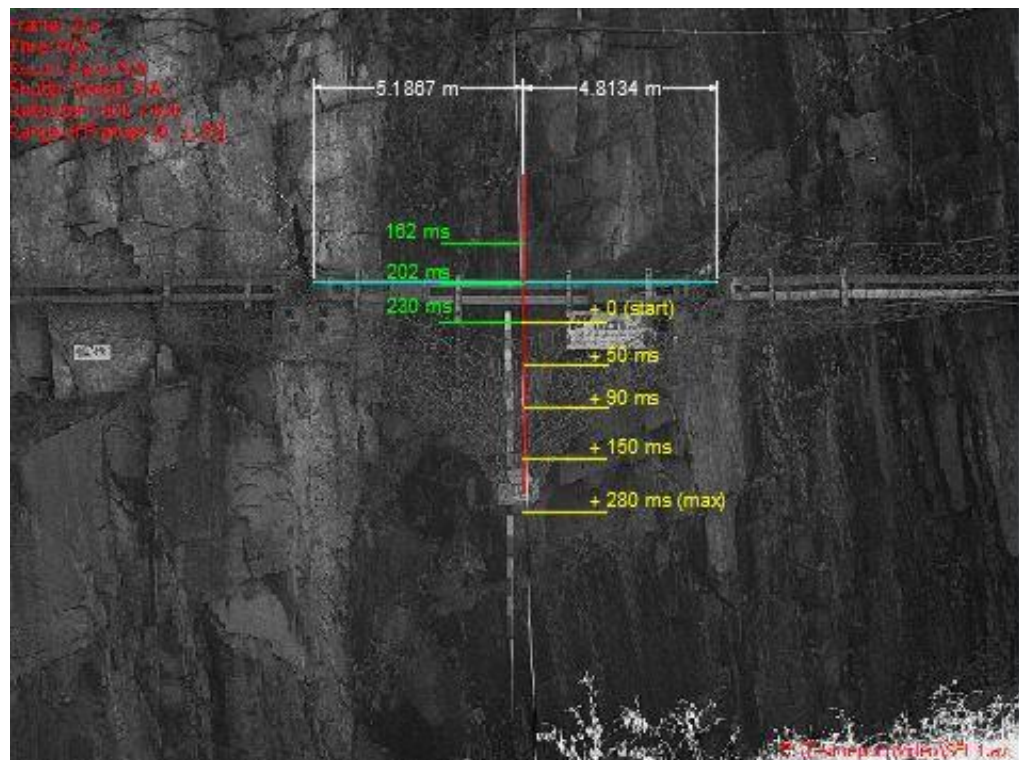
Figure 5.22: Block trajectory during SEL 1, frame 255 - maximum elongation

Proof of no ground contact

Figure 5.23: Proof of no ground contact reaching maximum elongation

5.4.3. Maximum elongation

The vertical maximum elongation (L) is derived from video evaluation. Therefore, the maximum elongation referenced to the slope (L_{75}) is calculated by trigonometric formulas. The angle between L and L_{75} is named Δ. For the geometry of the system (Figure 5.24) its value is 15°. Consequently, the projection of vertical maximum elongation onto the reference slope, named L_{75}, can be calculated by:

$$L_{75} = L \cos \Delta \qquad\qquad (5.3)$$
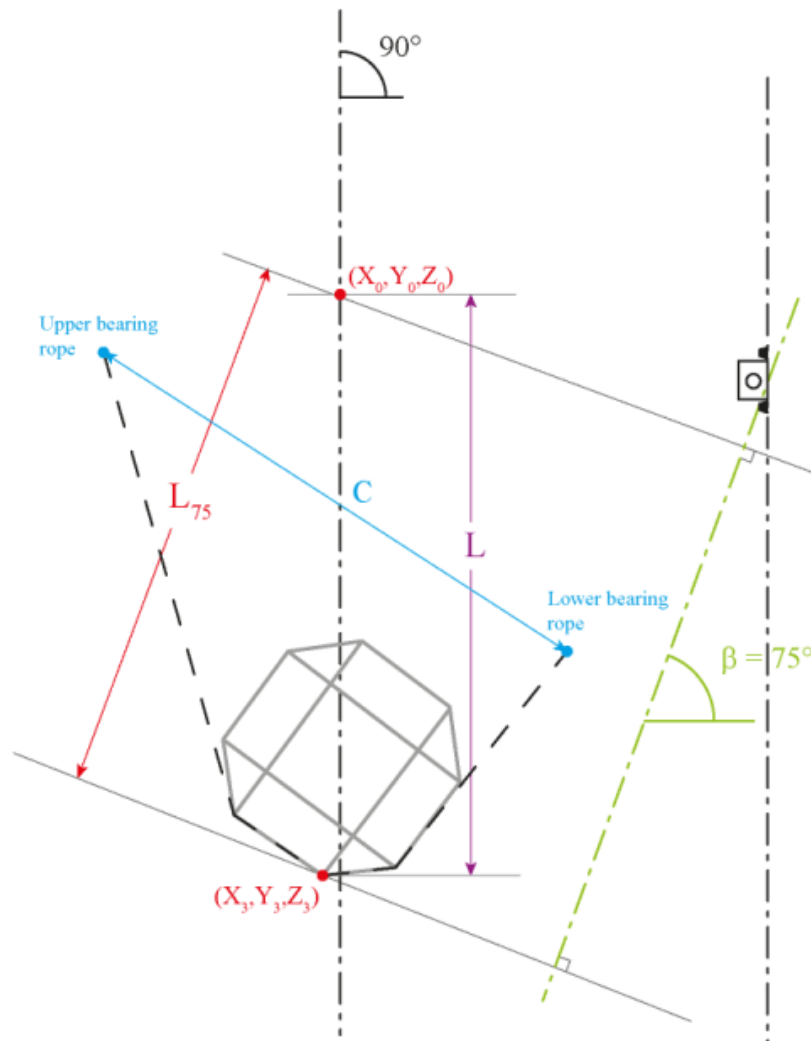
Figure 5.24: Geometry configuration of the barrier post impact

In the following pictures, the vertical maximum elongation is quoted. The annotations in white represent the vertical elongation of the net measured departing from the first point of impact.
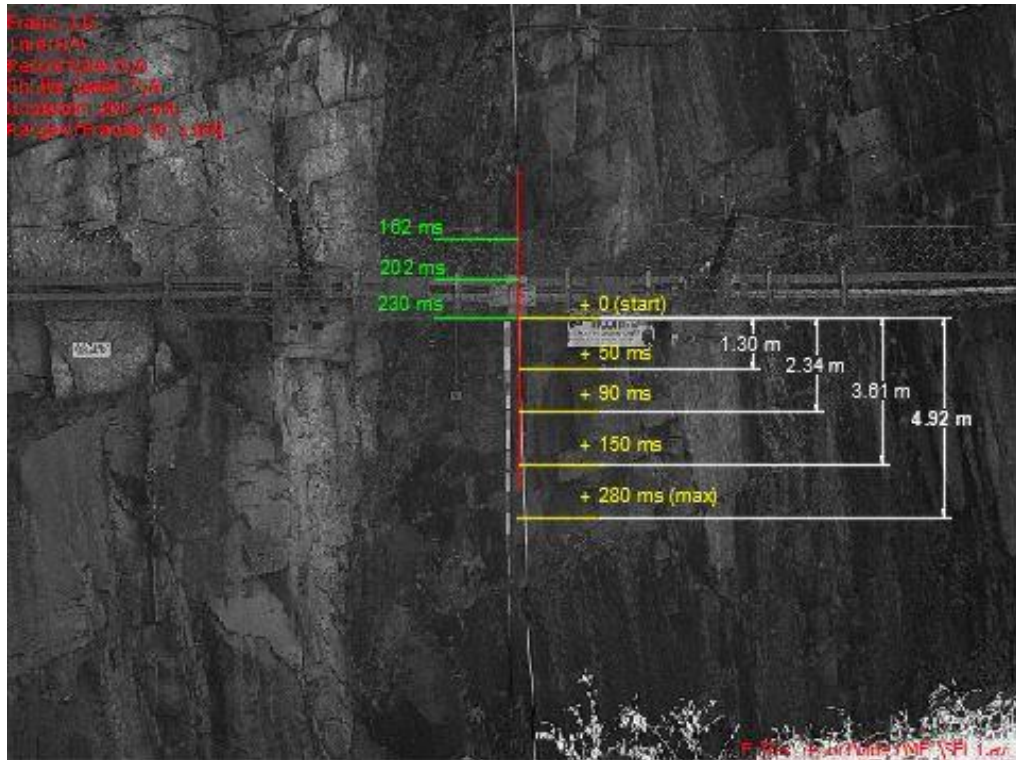
Figure 5.25: Position of the block and net deformation - frame 115 (contact with the net)
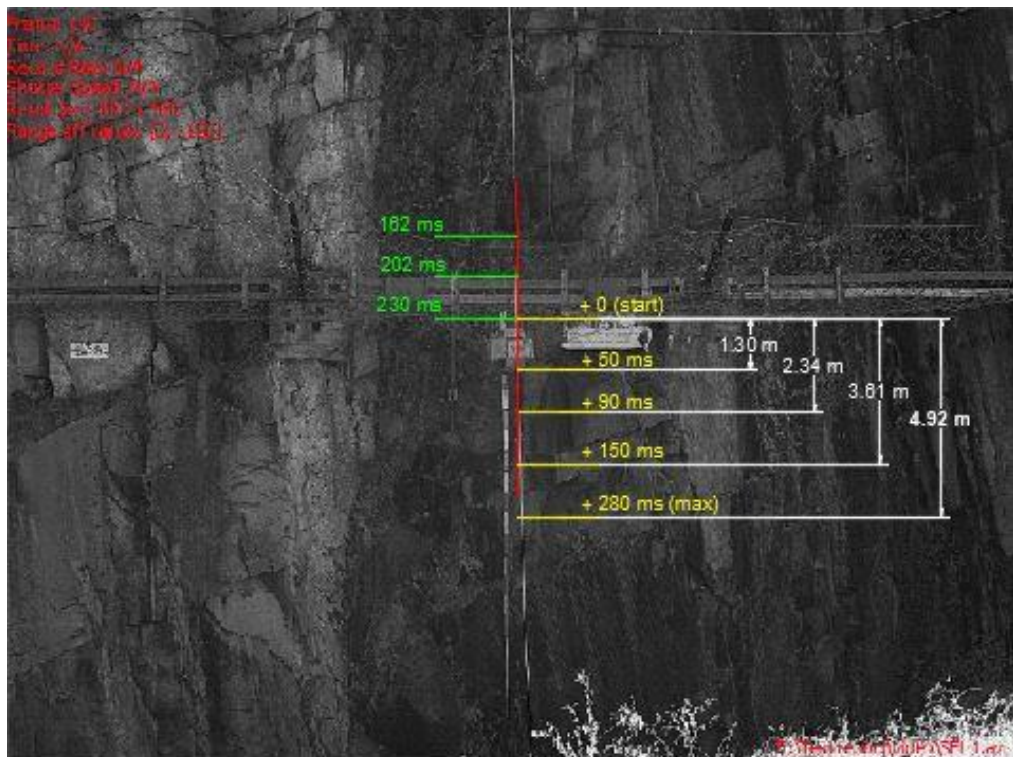
Figure 5.26: Position of the block and net deformation - frame 140

113
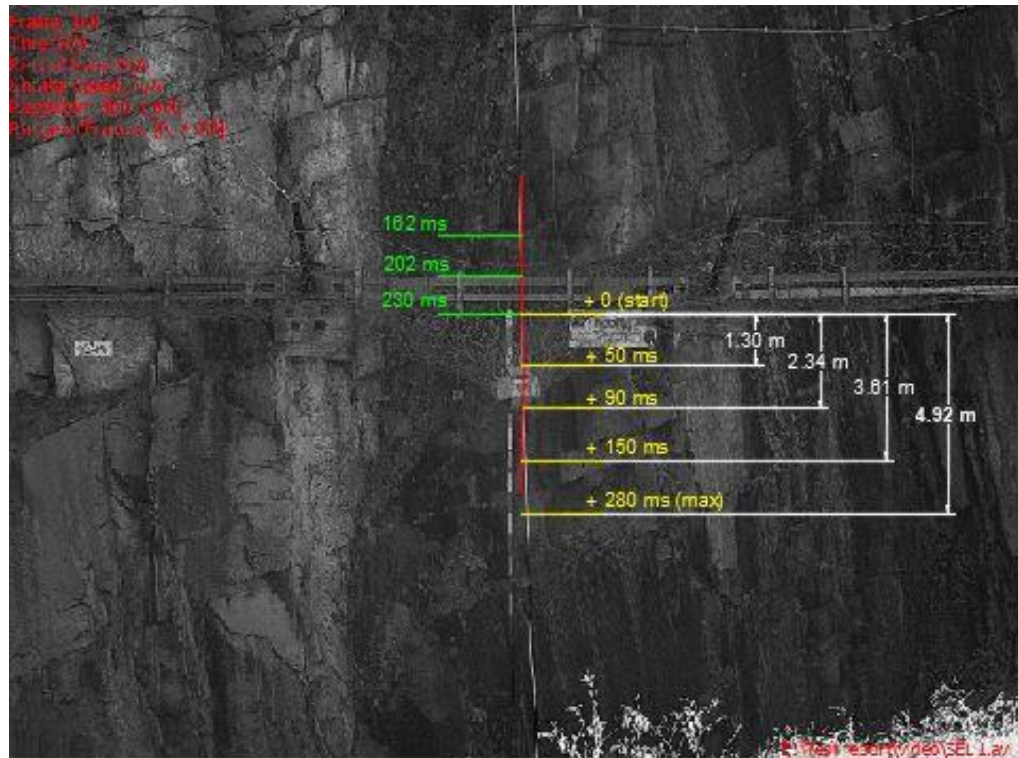
Figure 5.27: Position of the block and net deformation - frame 160
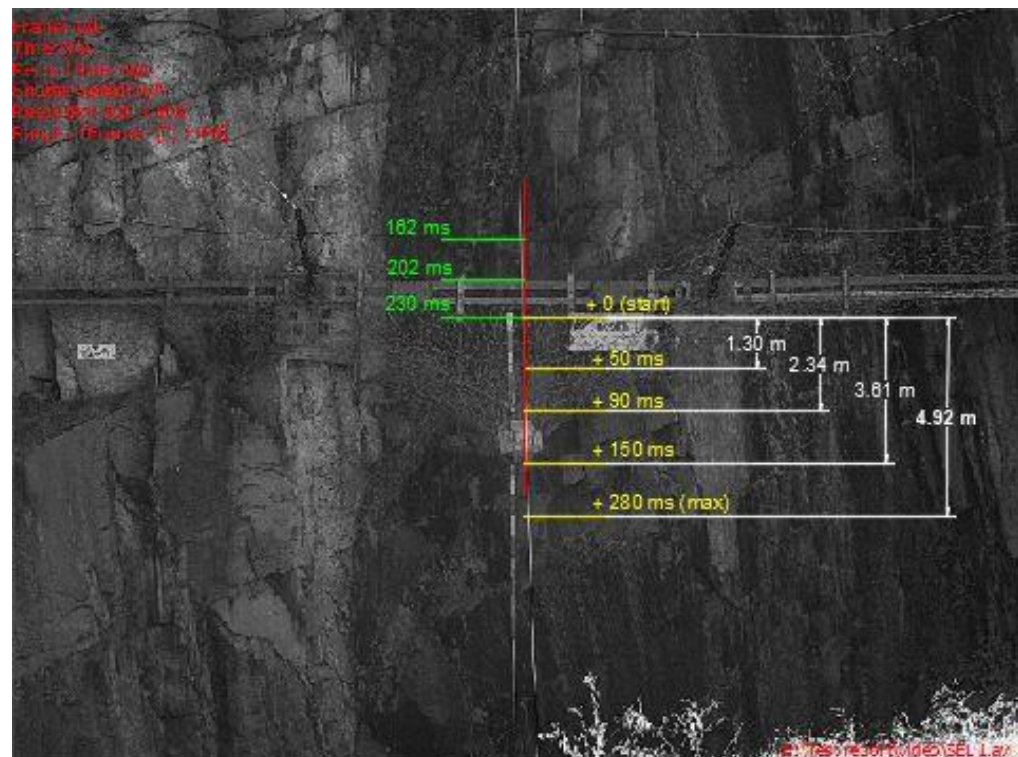
Figure 5.28: Position of the block and net deformation - frame 190
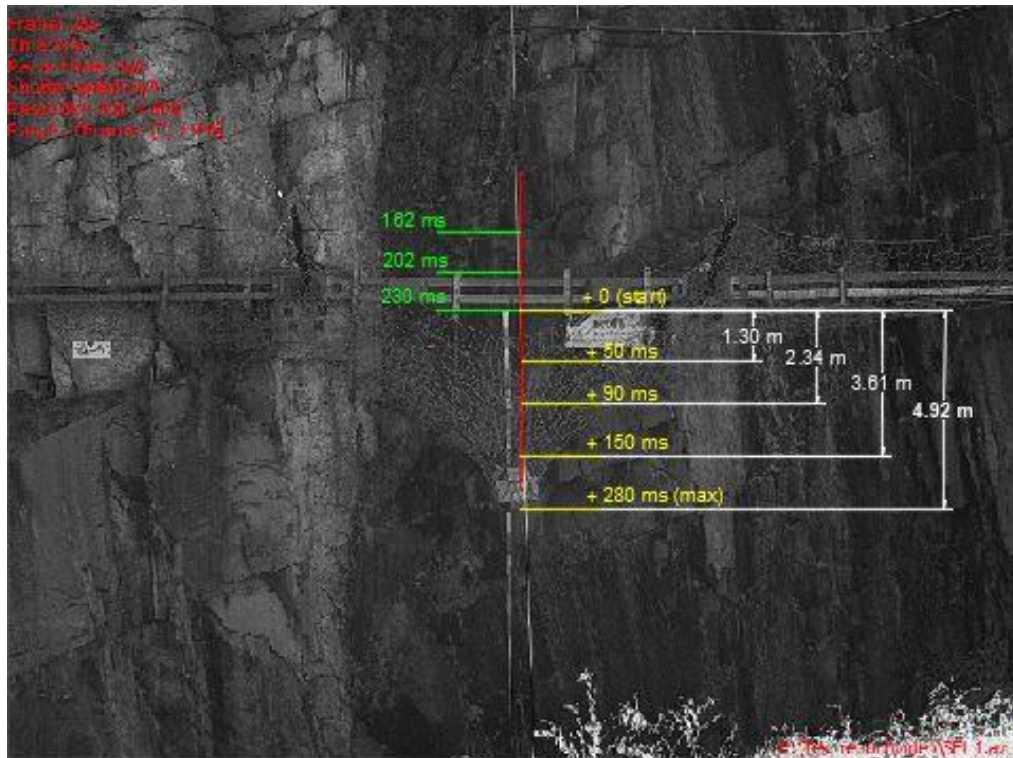
Figure 5.29: Position of the block and net deformation - frame 255 (maximum elongation)

5.4.4. Speed of the block

Two velocities have been reported: nominal and actual speed. Nominal speed is calculated using the release height, actual speed values is obtained using the video frame sequence. Nominal speed is calculated using the following formula:

$$v^2 = v_0^2 + 2a(x - x_0) \tag{5.4}$$

Table 5.8: Characteristic of the first SEL block falling

PHASE	TIME [ms]	FRAME	REFERENCE DISTANCE [m]	DISTANCE INTERVAL [m]	TIME INTERVAL [ms]	ACTUAL SPEED [m/s]
START	162	81	- 1.72	-	-	-
FREE FALL	202	101	- 0.73	0.99	40	24.75
CONTACT	230	115	0.00	0.73	28	26.07
MAX ELONGATION	510	255	4.92	4.92	280	0.00
DECELERATION [m/s²]	- 93.11					
MAX ELONGATION ALONG 15° [m]	4.75					

The value of the nominal speed with a release height of 32.7 m is 25.32 m/s.

The value of the actual speed using the video frame sequence is 26.07 m/s.

The mean velocity of the block within the last meter before the contact with the net was higher than 25 m/s as requested by ETAG027.

The block was stopped in 280 ms with a deceleration of - 93.11 m/s^2.

5.4.5. Energy of the block

The Service Energy Level (SEL) of a falling rock protection kit is defined as the kinetic energy of a regular block that impacts net. It is to be verified according to Annex A of ETAG. The value of the impact energy is equal to the kinetic energy of the block. Two different values of velocity have been individuated. For this reason, there are two different values of energy given by the following formulas:

$$E_{act} = \frac{1}{2} m_{act} v_{act}^2 \tag{5.5}$$

$$E_{nom} = \frac{1}{2} m_{nom} v_{nom}^2 \tag{5.6}$$

The block energy acting on barrier is reported in Table 5.15.

Table 5.9: Nominal and actual values of mass, speed and energy

Test Nr.	Release Height	Thrown Object's Mass		Impact Speed		Kinetic Impact Energy		Class Energy
-	-	nominal	actual	nominal	actual	nominal	actual	-
[-]	[m]	[kg]	[kg]	[m/s]	[m/s]	[kJ]	[kJ]	[kJ]
SEL 1	32.7	1920	1926	25.32	26.07	615.9	654	4

5.4.6. Detailed geometrical survey post-test and residual height

In Table 5.10 geometrical measurements of nominal and residual height are given based upon a $\beta = 75°$ reference slope. Values are based upon measurement by total topographical station, tape and manual angle measurements.

Table 5.10: Nominal and residual height projected on the reference slope 75°

Test	Nominal height	Residual height	Percentage residual/nominal height
	h_n [m]	h_r [m]	h_r/h_n [%]
I° SEL	3.90	2.85	73.0

To determine the numerical values of nominal and residual height, a tape and angle measurement were used (with a precision of ±0.1°). The results are the distance C and a referring angle μ at which the tape (with a precision of ± 1 cm) was rotated during measurement. Using this angle, and assuming the reference slope $\beta = 75°$, the deviation angle delta can be obtained as before:

$$\delta = 90° - \beta - \mu \tag{5.1}$$

Assuming a triangle with C as the hypotenuse is possible to calculate the projection of C on the reference slope normal by using the previous relation (Eq. 5.2):

$$h_r = C \cdot \cos(90 - \beta - \mu) \tag{5.2}$$

To obtain the residual height h_r after impact, the tape was placed on the upper bearing rope and lower bearing rope and then the results are subtracted. Indeed, the residual height represents the minimum distance between the lower and the upper rope after the test, without removing the block. The measured distance has to be corrected using trigonometric functions in order to obtain the value perpendicular to reference slope. Below are shown measurement and a schematic representation of the kit structure after the test.

Table 5.11: Coordinates of camera and total station

	Total station	Camera
X	99.983	99.983
Y	100.025	100.025
Z	0.029	1.684

Table 5.12: Coordinates and post inclination

		POST 1		POST 2		POST 3		POST 4	
		Pre test	Post test	Pre test	Post test	Pre test	Post test	Pre test	Post test
POST BASE	X	153.005	153.001	147.287	147.282	141.664	141.636	136.035	136.026
	Y	78.429	78.421	70.223	70.214	61.966	61.959	53.692	53.685
	Z	10.691	10.691	10.684	10.682	10.640	10.639	10.846	10.846
POST HEAD	X	149.369	149.357	143.858	143.843	138.111	138.071	132.439	132.437
	Y	80.635	80.615	72.708	72.705	64.327	64.285	55.932	55.938
	Z	11.934	11.925	11.943	11.890	11.839	11.973	12.121	12.103
INCLINATION		17.21°	17.09°	17.44°	16.71°	16.59°	15.95°	17.67°	17.42°

117

Table 5.13: Geometrical relevant values before first SEL test

Before 1st SEL test

Distance upper cable – base of system

Absolute value	C	3.90 m
Angle towards horizon	μ	13.0°
Reference plane	$h_n = C \cdot \cos(90 - \beta - \mu)$	3.90 m

Table 5.14: Geometrical relevant values after first SEL test

After 1st SEL test

Distance upper cable – lower cable

Absolute value	C	2.85 m
Angle towards horizon	μ	17.0°
Reference plane	$h_n = C \cdot \cos(90 - \beta - \mu)$	2.85 m
Relation of nominal and residual height	h_r / h_n	73%

The residual height of the kit after the first SEL test (without removing the block) was greater than 70% of the nominal height.
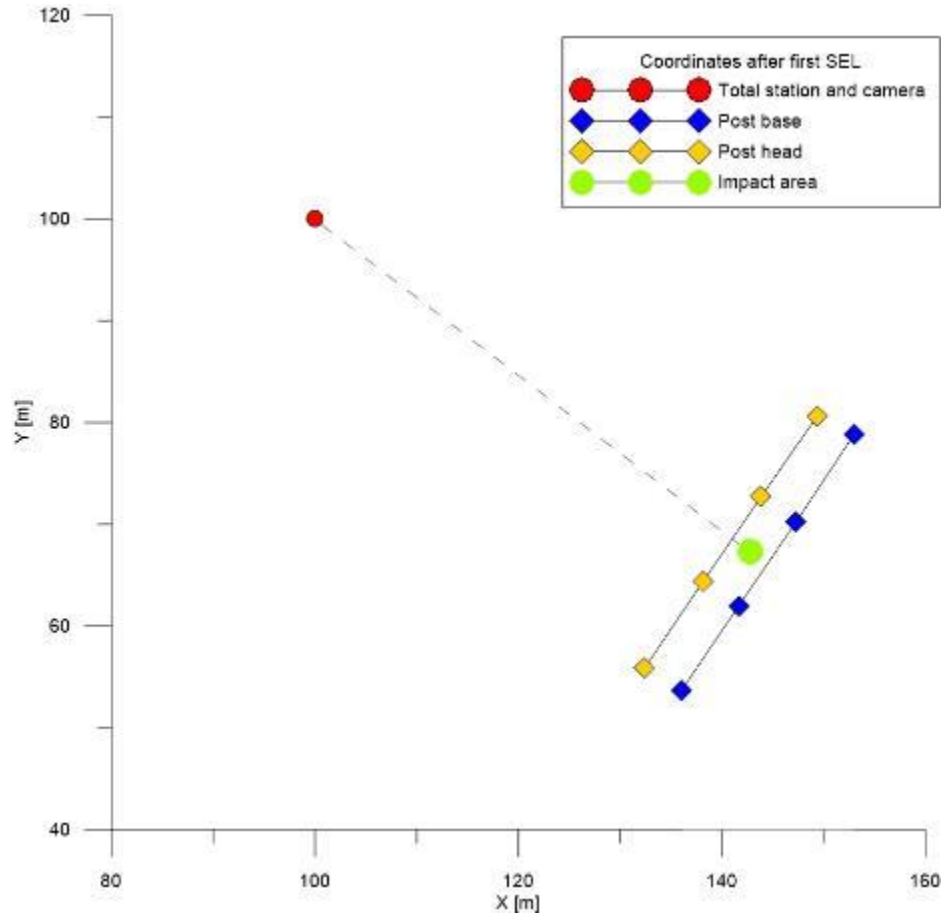
Figure 5.30: Position of the post after the first SEL

5.4.7. Gaps and opening near posts after the test

After the impact of the thrown objects, the effective surface of the protection kit is reduced due to a displacement of the net in two directions in the lateral modules; the gaps (the distance between the post and the net) were measured in static conditions without removing the block from the net, according to European Guideline ETAG 027.

The values of these gaps are given in Table 5.15 and Table 5.16. No gap sizes influence the correct determination of residual and nominal height. A general view of gaps location before and after the test is given in Figure 5.32.

Table 5.15: Measured horizontal gaps before and after the tests

	Horizontal gaps [m]			
	Post 1		Post 4	
	[cm]		[cm]	
	pre	post	pre	post
1st SEL	11	22	8	20

Table 5.16: Measured opening near posts before and after the tests

	Openings [m]					
	Post 2		Centre		Post 3	
	[m]		[m]		[m]	
	pre	post	pre	post	pre	post
1st SEL	3.90	3.13	3.90	2.85	3.90	3.00

The dimension of net and the values of openings near posts are projected on the plane perpendicular to the reference slope inclined by 75°, in order to obtain their projection on the post plane, which is inclined by 90° - 75° = 15° (Table 5.17).

Table 5.17: Opening near posts projected on the reference plane inclined by 15°

	Openings [m]					
	Post 2		Centre		Post 3	
	[m]		[m]		[m]	
	pre	post	pre	post	pre	post
1st SEL	3.89	3.11	3.89	2.84	3.89	2.98

Figure 5.31: Barrier openings near post; a) Opening near post n. 2 before the test; b) Gaps near post n. 4 before the test and c) Gaps near post n. 4 after the test
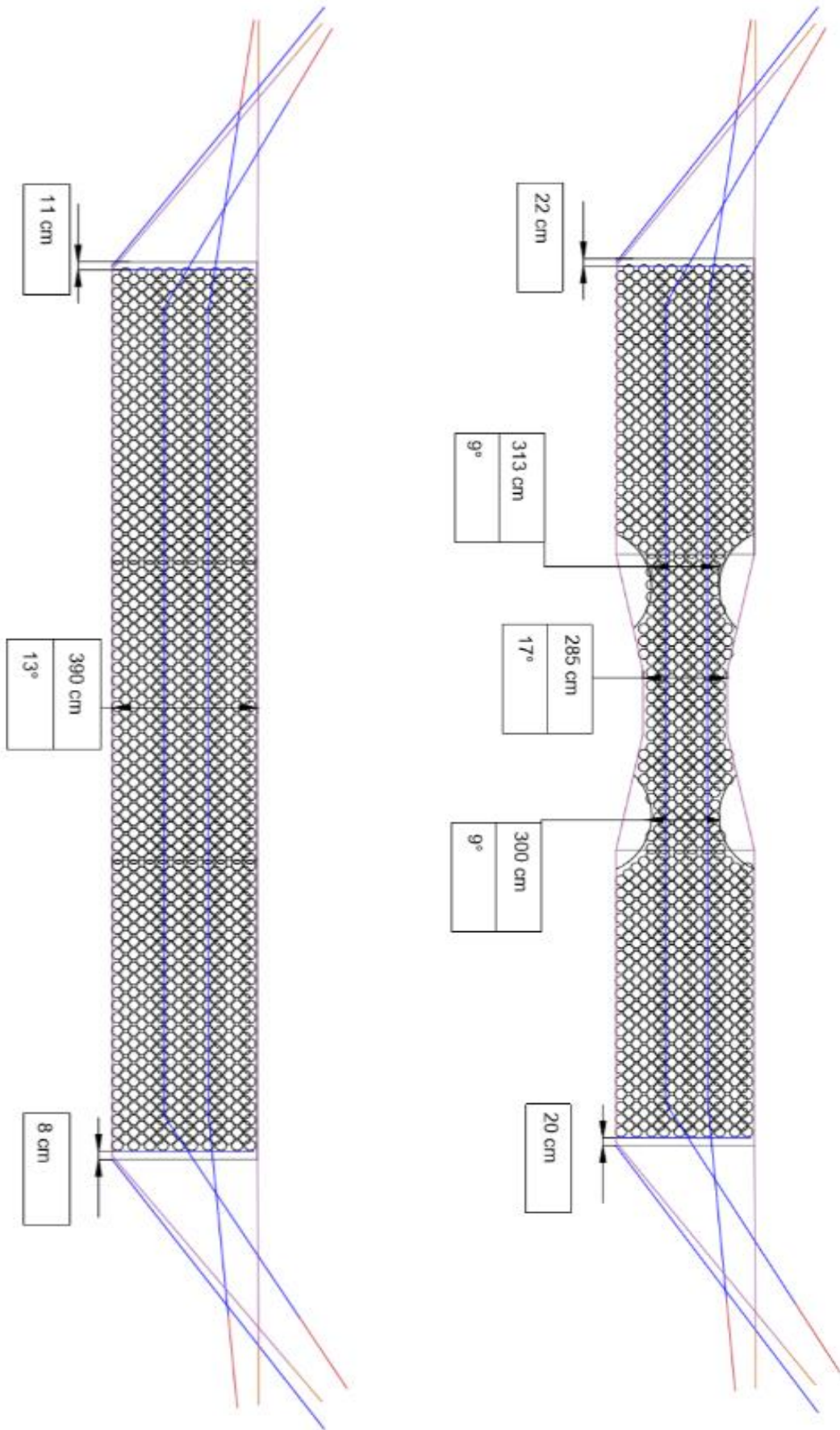
Figure 5.32: Horizontal gaps and barrier nominal height a) Pre first SEL test and b) Post tes

5.4.8. Energy-dissipation devices

Energy dissipation devices are elements that are used to dissipate impact energy and to allow a controlled displacement of the kit when it is subjected to mechanical stress. In the tested kit, energy-dissipating devices were arranged along the lateral ropes. The position of these elements is shown in Figure 5.35.

The barrier NFL 1500 kJ_4/A is equipped with new dissipation devices, implemented during this thesis work (paragraph 4.6). In particular the system includes two different types of energy dissipation device: the first one (Figure 5.33a) is used for upper and lower bearing rope and the second (Figure 5.33b) is used for the intermediate ones.
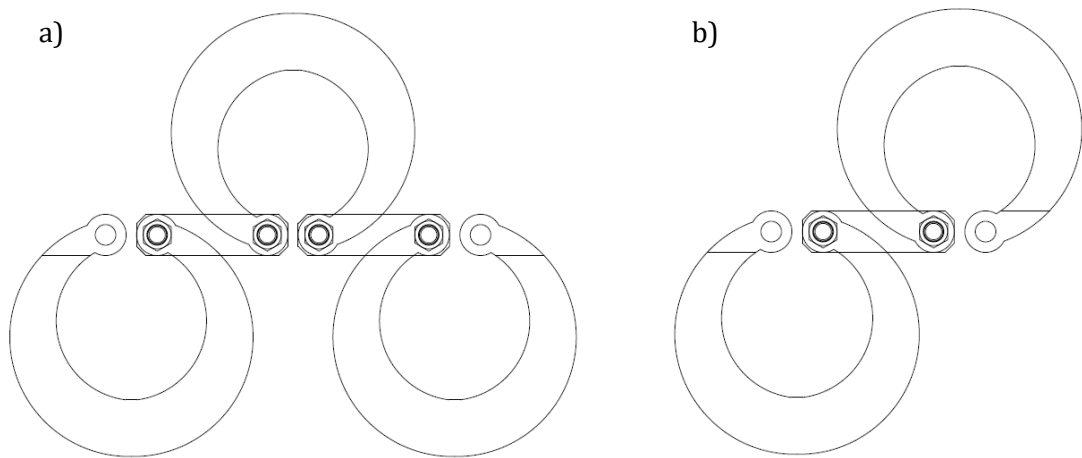
Figure 5.33: Sketch of brake elements; a) Type 1 used for upper and lower bearing rope and b) Type 2 used for intermediate bearing ropes

Figure 5.34: Brake elements on the right side before the SEL test
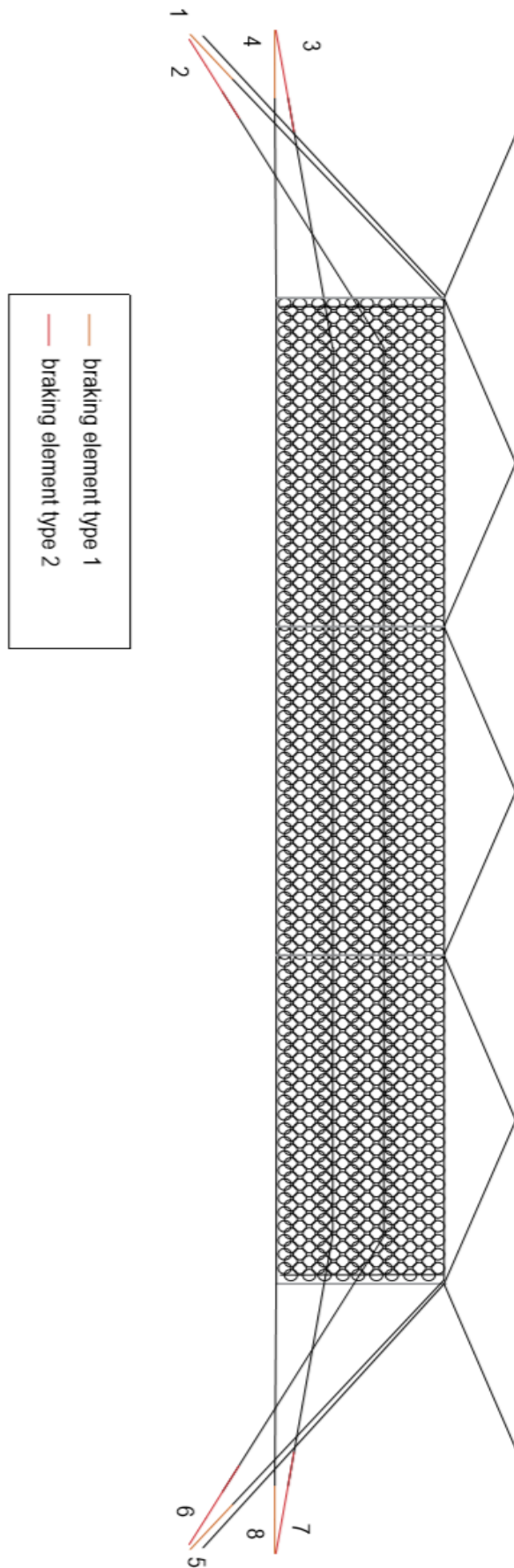
Figure 5.35: Brake elements position in the tested kit

Table 5.18: Brake elements features

Type	Number of metallic rings	Position
1	3	upper and lower bearing ropes
2	2	intermediate bearing ropes

In Table 5.19 the brake elements position in the barrier system and the runs recorded after test are reported.

Table 5.19: Runs of the brake elements

Brake	Run [cm]	Brake position	Side
1	48	Upper bearing ropes	Left
2	57	Upper intermediate bearing rope	Left
3	78	Lower intermediate bearing rope	Left
4	57	Lower bearing rope	Left
5	130	Upper bearing rope	Right
6	62	Upper intermediate bearing rope	Right
7	80	Lower intermediate bearing rope	Right
8	71	Lower bearing rope	Right

Figure 5.36: Runs of the brake elements on the right side

The values of the brake elongation reported in Table 5.19 showed the different behavior of the two barrier side: the right side (Figure 5.36) is more involved in deformation processes than the left one. Since barrier structure is perfectly symmetric, the difference between the sums of the brake runs of the two barrier side (2.40 m on the left side and 3.43 m on the right) is probably due to the test field asymmetry, which leads to a two different anchors system configurations depending on the side. The maximum brake elongation on the right side (1.30 m) was reordered in the upper bearing rope brake, which showed the minor deformation on the right side (only 48 cm). However, the upper bearing rope is the most involved in barrier deformation processes generated by the block impact, with a total displacement of 1.78 m; lower bearing rope showed a maximum elongation of 1.28 m. Differently from bearing ropes the intermediate ones worked symmetrically, showing very similar brake deformations on both sides.

5.4.9. Forces on ropes

Forces acting in the structure were recorded to demonstrate the good functioning of the rockfall protection kit. Cable forces were determined using electric load cells with a recording frequency of 1200 value/second. In order to allow the correct matching between measurements and cables the arrangement of load cells is shown in Table 5.20 and in Figure 5.38.

Table 5.20: Position of the cells

Load ID	Position in the kit
LC1	Side retention rope
LC2	Uphill retention rope (on the post n. 3 left)
LC8	Uphill retention rope (on the post n. 3 right)
LC_LT	Upper bearing ropes
LC_5	Upper intermediate bearing rope
LC4	Lower intermediate bearing rope
LC7	Lower bearing rope

The maximum load value recorded during the test are reported in Table 5.21 with their occurrence time from start. A load-time graph, which displays the force trend during time for each load cells, is showed in Figure 5.37. Recorded data highlight that the dissipation of the block energy actuated by the barrier occurred very fast: the rope loading took place in 0.4 s, during that time interval the system dissipated all the energy involved in the impact process. The maximum peak load value was recorded between 21.81 and 21.85 s for all the monitored ropes.

The uphill retention rope located on the right of post n. 3 is the most loaded (96.18 kN), probably because it wasn't connected with brake elements, which guarantee the absorption of a

part of the energy acting on it, and it is heavily loaded because the block impact location occurred in the central module (on the left of post n. 3). For the same reason, the uphill retention rope installed on the left of post n. 3 is lightly loaded. Longitudinal ropes had very similar mechanical behavior and maximum recorded loads.

Table 5.21: Maximum forces and points in time

Cell	SEL 1	
	Maximum	Time from start
	[kN]	[s]
LC1	35.27	21.81
LC2	43.15	21.82
LC8	96.19	21.84
LC_LT	61.94	21.83
LC_5	63.44	21.85
LC4	64.61	21.84
LC7	54.66	21.81
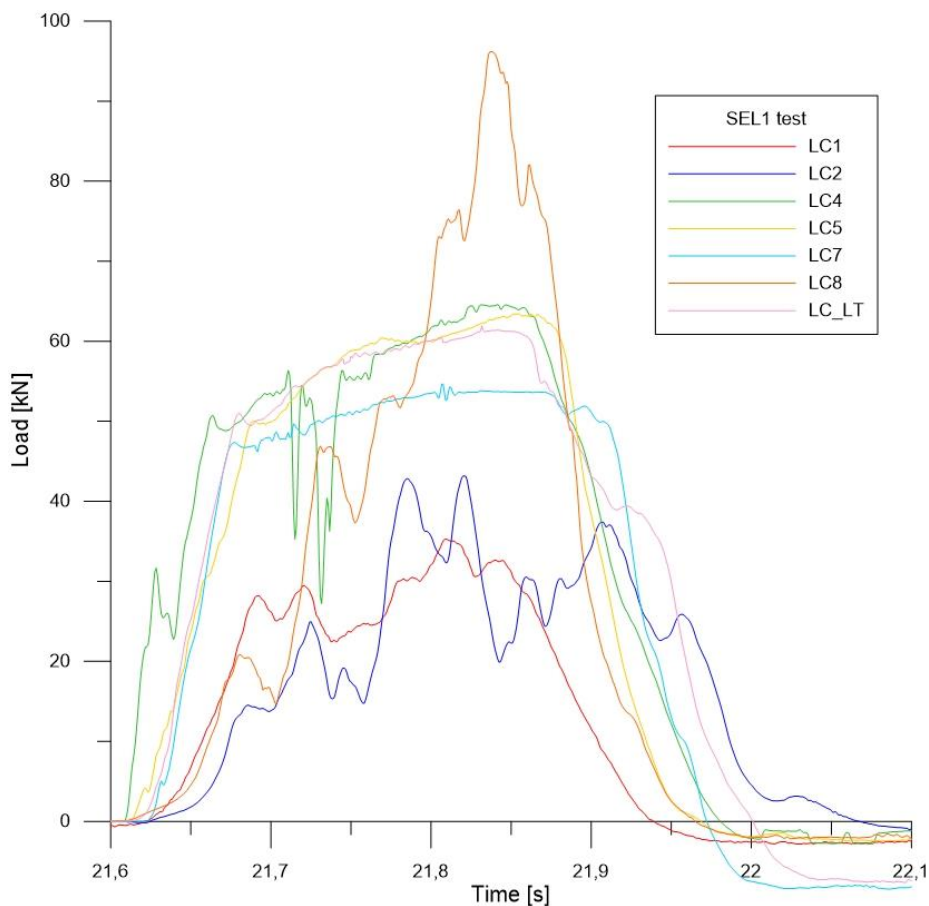
Figure 5.37: Loads recorded by load cells during the first SEL
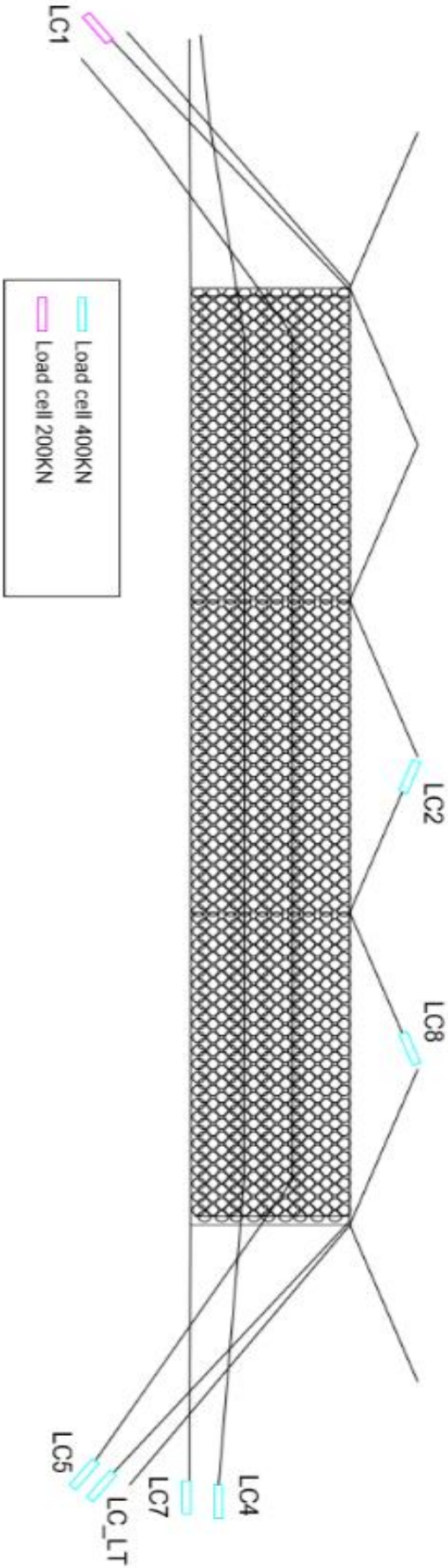
Figure 5.38: Generalized arrangement of load cells

5.5. Test conclusions

The test setup was inspected after the end of each test and documented by photos (Figure 5.31 and 5.39). The system deformed as planned and the deformation was plastic, but not critical. In spite of that deformation no damage occurred. Changes of post inclination were expected and they are documented in the previous chapters.

All blocks were stopped safely during every test. Barrier response in terms of maximum elongation, openings and residual height satisfied the requirements imposed by the reference standard ETAG 027. For these reasons is possible to affirm that the field tests allowed to verify the good functioning and the reliability of the barrier with integrated the new energy dissipation devices.

Figure 5.39: Block stopped by the barrier; a) Lateral vie; b) Bottom view and c) Overall system at the end of the test

Chapter 6: Laboratory tests on debris flow barrier

6.1. Analytical model and objectives

The aim of this work is to provide a new methodology for the active countermeasure design in order to reduce debris flow risk, with a particular focus on flexible retention barriers. The safe design of these structures requires a deepened knowledge of the uncertainties related to the involved parameters (Vagnon et al. 2015), which are extremely complex to quantify. In fact, as it will be widely explaining in this thesis, there are uncertainties in the evaluation of the unstable volume, in the evaluation of the run-out distance, in the determination of the impact load and in the load scheme of the protection structures. Furthermore, these uncertainties have an epistemic nature: this compromises the use of the major part of statistical methods. Then, unfortunately, the international regulations partially overlook debris flow phenomena: they treat the problem just marginally (and only in relation to the certification of the barrier) and specific guidelines are completely missed. Without any guidelines (at least in Europe), with a huge variety of methods to derive impact load (but none of them universally recognized) and with many methodologies to evaluate the main debris flow characteristics (volume, velocity, thickness, etc.), the design of retention structures with a certain level of reliability is a big challenge.

In this Chapter the simplified structural model developed by Brighenti et al. (2013) for the safety assessment of retention barriers against channelized debris flows is presented, and some laboratory tests on scaled barriers are interpreted through the proposed approach.

The model has been developed as a simplified and efficient tool that can be used to verify of the supporting ropes and foundations of a flexible debris flow barrier. The present analytical and numerical-based approach has a different aim then that of a Finite Element Model (FEM). The latter method for these kinds of structures has shown that a large amount of time is needed for the geometrical setup of the model and several numerical instabilities develop due to the non-linearity of the problem. The great effort required by FEM for these applications limits the possibility of investigating different geometrical configurations, load schemes, etc.; it is suitable to represent a specific configuration but does not allow investigation to be made of the influence of debris flow parameter modification (flow height and velocity, debris density, etc.). On the other hand, parametrical analyses are common practice in geotechnical design.

Consequently, Brighenti et al. (2013) decided to develop a simplified method that would allow several parametrical analyses to be performed in a short time interval. Parametrical analysis should take into account the physical and mechanical features of debris flow, which usually vary during debris development and are difficult to define in a deterministic way.

6.2. Forces acting on barrier during the impact phase

The pressure produced by the impact of a debris flow on the barrier can be estimated considering both the dynamic impact pressure and the static pressure of the deposited debris (Brighenti et al., 2013). The former can be determined considering the well-known Bernoulli theorem; the kinetic energy of the flowing material, $\rho_d/v_0{}^2 = 2$ is transformed into a pressure load when the velocity vanishes due to the impact. The dynamic pressure on the barrier can thus be estimated as (Figure 6.1a).

$$q_d(x) = \alpha \times \rho_d \times v_0^2 \tag{6.1}$$
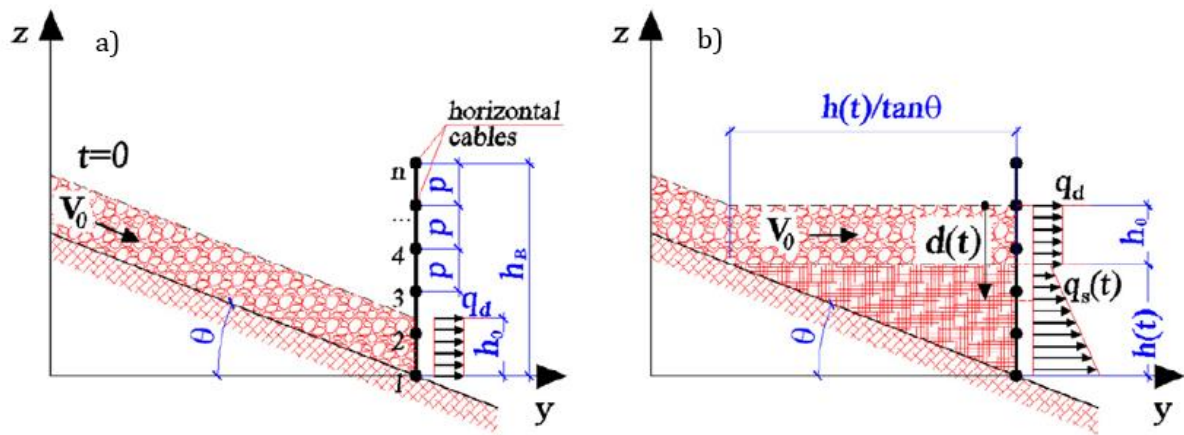
Figure 6.1: a) First impact and b) Debris accumulation behind the barrier First impact and b) (from Brighenti et al., 2013)

Generally, the debris could hit the barrier in the form of surges which fill the barrier either continuously or intermittently; the most critical impact scenario on barrier stability should always be chosen. The thickness (h_0) and velocity (v_0) of moving debris surges can be estimated from debris mobility models using appropriate rheological parameters such as those recommended by Lo (1997). On the other hand, when the debris starts to accumulate behind the barrier, a static pressure can be assumed to occur (Figure 6.1b).

The height of the accumulated material at the generic time t can be estimated, as shown in Eq. 6.2, by equating the volume of the material that arrives after such a time interval from the slope and the volume of the accumulated material behind the barrier (time t = 0 is assumed when the first particle of the debris-flow impacts the barrier) as:

$$h(t) = \sqrt{2 \times v_0 \times t \times h_0 \tan \theta} \tag{6.2}$$

In the above relation h_0 and θ are assumed to be the constant height of the debris flow surge and the inclination of the slope behind the barrier, respectively. It should be noted that, in order

130

to use Eq. 6.2 it is necessary that $h > 0$. The static pressure acting at depth $d(t)$, measured with respect to the upper free surface of the material (Figure 6.1b), can be assessed through the relation reported in Eq. 6.3, as usually occurs in geotechnical science for the assessment of the static pressure produced at a given depth:

$$q_s(d) = k \times d(t) \times \rho_d \times g = k \times \underbrace{(h_0 + h(t) - z)}_{d(t)} \times \rho_d \times g \qquad (6.3)$$

Where

k is the pressure coefficient;

g is the acceleration of gravity;

z is the vertical position of the considering point (Figure 6.1b).

The barrier is considered made up of n horizontal supporting cables, assumed to be placed at a constant relative distance p.

$$p = \frac{h_B}{(n-1)} \qquad (6.4)$$

For simplicity, the pressure load $q_i(z_i)$ acting on the ith cable is assumed to be constant along each horizontal cable. The vertical co-ordinate is assumed to be equal to

$$z_i = h_B \times \frac{(i-1)}{n-1} \geq h_0 \qquad (6.5)$$

Pressure load $q_i(z_i)$ can simply be calculated as in Eq. 6.6, where the cables are numbered starting from 1 at the bottom of the barrier.

$$q_i(z_i \geq h_0, t) = \begin{cases} 0 \; for \; t < t_1 = \dfrac{(z_i - h_0)^2}{(2v_0 \times h_0 \times \tan\theta)} \\[2ex] q_d = \alpha \times \rho_d \times v_0^2 \; for \; t_1 < t < \; t_2 = \dfrac{z_i{}^2}{(2v_0 \times h_0 \times \tan\theta)} \\[2ex] q_s = k \times \left[h_0 + h(t) - h_B \times \dfrac{(i-1)}{n-1}\right] \times \rho_d \times g \; for \; t > t_2 \end{cases} \qquad (6.6)$$

The following Eq. 6.7 should be used when the ith cable is located at vertical coordinate $z_i < h_0$.

$$q_i(z_i < h_0, t) = \begin{cases} q_d = \alpha \times \rho_d \times v_0^2, for \; t < t_1 = \dfrac{z_i{}^2}{(2v_0 \times h_0 \times \tan\theta)} & (6.7a) \\[2ex] q_s = k \times \left[h_0 + h(t) - h_B \times \dfrac{(i-1)}{n-1}\right] \times \rho_d \times g \; for \; t > t_1 & (6.7b) \end{cases}$$

In others words, Eqs. 6.6 and 6.7 enable one to evaluate the pressure exerted directly on a given cable located at coordinate z_i, once its position with respect to the flowing material and to the accumulated material is known. Eq. 6.6 is valid for cables located at a greater height than the thickness of the flowing debris at different time intervals: the cable is not yet in contact with the debris material and it is therefore unloaded; in the other case Eq. 6.7b the ith cable falls inside the portion of the barrier that impacts with the flowing debris while the cable for $t > t_2$ is in contact with the material at rest behind the barriers. Similarly, Eq. 6.7 allows one to estimate the pressure on a cable located at a coordinate z_i which is lower than the thickness of the flowing material. Since the cables are placed at a constant vertical distance p of, the distributed load (assumed, for the sake of simplicity to act in a horizontal plane) acting on a single cable of unit horizontal length is given by Eq. 6.8:

$$q_i(z_i, t) = q_i(d, t) = \begin{cases} p \times \dfrac{q(z_i, t)}{2} \; for \; i = 1, n \\ p \times q_i(z_i, t) \; for \; 2 \leq i \leq n-1 \end{cases} \tag{6.8}$$

The assumption of a constant load along the cable is an acceptable simplification from the engineering safety point of view; this hypothesis allows one to treat the problem as a two dimensional one, characterized by governing equations that can easily be handled for a simplified design of the retention barrier.

Generally, channelized debris flow barrier has an almost trapezoidal shape and is anchored to the ground (at the channel sides) by means of grouted anchors or cables. The main structural cables are horizontal and their number depends on the overall height and on the expected flow parameters (Figure 6.2).
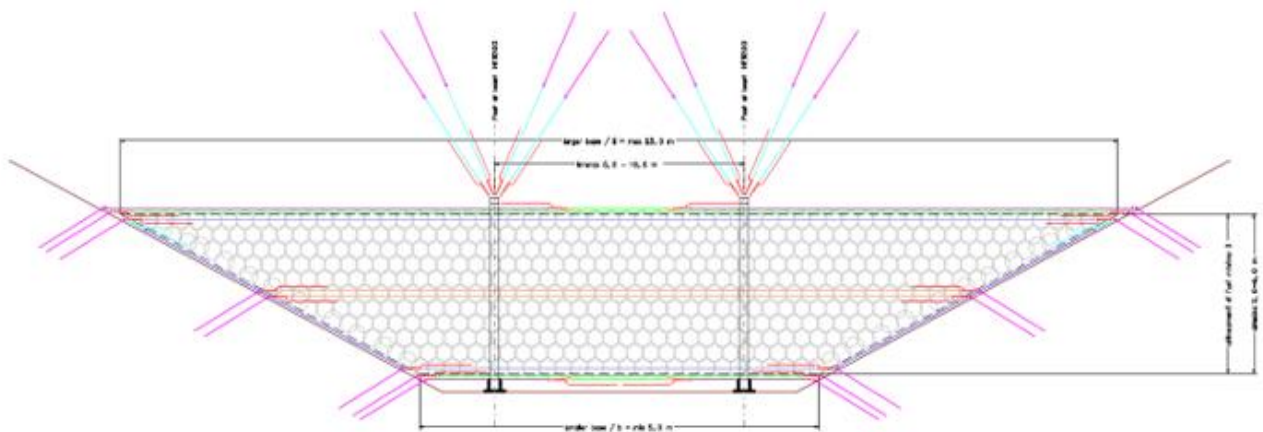
Figure 6.2: Typical structure of a debris flow barrier. The single element features and the geometrical lay-out can vary according to the make and model of the barrier and to particular installation conditions (channel size, depth, etc.).

From observation of Figure 6.3 it can be noted that the main resisting elements are the horizontal cables fixed at the ends to the foundations, while the net plays the role of retaining the flowing solid particles and of transmitting the developed forces to the longitudinal ropes. The governing equation of the equilibrium of a loaded cable can usefully be employed to describe the mechanical behavior of such a structural system.
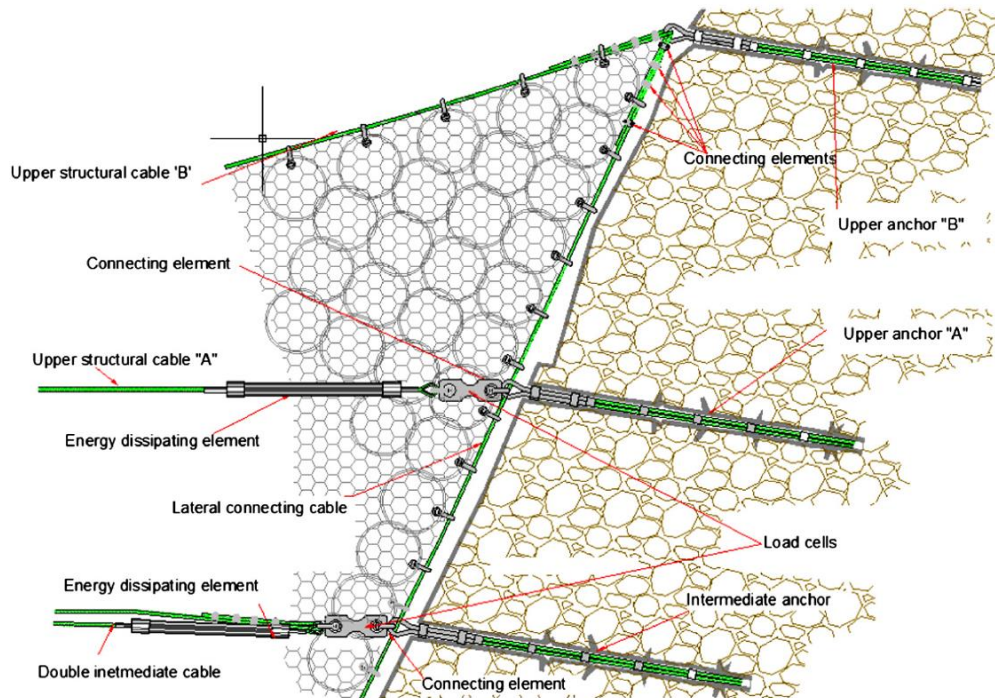
Figure 6.3: Details of the barrier foundations, dissipating elements and supporting cables. The single elements varying according to the make and model of the barriers available on the market (from Brighenti et al., 2013)

Considering a barrier constituted by several horizontal cables mounted at a constant reciprocal distance of p, the ith cable (with its ends fixed at points A and B) is characterized by a horizontal length l_i, while its total effective length (when elongated under loading) is assumed to be equal to L_i.

The distributed load acting on such a cable is assumed to lie in a horizontal plane and to be constant with respect to the x coordinate at a fixed time t. The load, however, is variable with time, since the depth $d(t)$ of the cable, with respect to the top surface of the flowing material, increases with t.

For simplicity, the model considers the main resisting ropes to be only loaded in the horizontal direction by the forces produced by the impact of debris against the barrier, while the resultant of the vertical forces transmitted by the connecting net to the single cable is considered negligible. As a consequence, only the deformation of the cables in the horizontal plane are assumed to be significant in the resistant mechanism of the structure.

Each cable is assumed to have fixed ends, i.e. the end points of the cables are prevented from displacing by a foundation system whose mechanical behavior is not the scope of this work. The equilibrium equation (Eq. 6.5) of the ith cable in differential form at time instant t is:

$$\frac{d^2 u_i(t)}{dx_2} = -\frac{q(z_i, t)}{H_i} = \frac{q_i(d, t)}{H_i} \tag{6.9}$$

After a double integration and assuming a constant distributed load at a given time instant $q_i(d)$ (for brevity, the dependence on time t is not explicitly indicated in the following relations) and the two extremities of the cable to be located at coordinates $(x, y) = (0, 0)$ and $(x, y) = (li, e)$ (referring to the horizontal plane containing the cable) corresponding to points A and B, respectively, the cable equation can explicitly be written as

$$u_i(x) = \frac{q_i(d)}{2H_i} \times (xl_i - x^2) + \frac{e}{l_i} x \tag{6.10}$$

Where $q_i(d) = q_i(z_i = h_B - d)$ is the constant horizontal load acting along the considered cable placed at a depth d below the actual top free surface of the flowing material, while H_i is the constant component along the x direction of the tensile axial force $T_i(x)$ in the cable. Such a quantity can be obtained by imposing the effective length of the cable to be equal to L_i through the equation:

$$L_i = \int_0^{l_i} \sqrt{1 + u'^2_i(x)} dx \tag{6.11}$$

Which is obtained by integrating the trivial geometric relation

$$dL_i = \sqrt{dx^2 + dy^2} = dx\sqrt{1 + u'^2_i(x)} \tag{6.12}$$

since $dy = dx \times u'_i(x)$, that quantifies the length of a generic curve, whose shape is described through displacement relation $u_i(x)$. By denoting the quantity

$$f = q_{ti} \frac{l_i^2}{8H_I} \tag{6.13}$$

in which the geometrical interpretation of f is shown (i.e. the maximum transversal displacement measured with respect to the straight line A–B) and expanding the expression of the integrand function in Eq. 6.11 in Taylor series (the dependence on the depth d is omitted in the notation for simplicity reasons), one can obtain:

$$L_i \cong l_i \left(1 + \frac{8}{3} \frac{f^2}{l_i^2} + \frac{1}{2} \frac{e^2}{l_i^2} \right) + \cdots \tag{6.14}$$

The searched term H_i, which can be shown, from equilibrium considerations, to be independent of x, can finally be obtained using Eqs. 6.10 and 6.12:

$$H_i \cong \frac{\sqrt{3}}{6} \times \frac{q_i \times l_i^2}{\sqrt{2L_i \times l_i - 2l_i^2}} \tag{6.15}$$

where the particular case characterized by $e = 0$, has been considered. The tensile force $T_i(x)$ acting along the cable can also be explicitly obtained through the following relation

$$T_i(x) = H_i \frac{ds}{dx} = H_i \sqrt{1 + u'^2_i(x)} = H_i \sqrt{1 + \left[\frac{q_i}{2H_i} (l_i - 2x) \right]^2} \tag{6.16}$$

By projecting the force H_i along the tangential direction of the cable at the point of interest or by calculating the product $H_i = ds/dx$, where s denotes the curvilinear abscissa along the cable under consideration (Figure 6.5). The components of the reaction forces in the y direction at the two edges of the cable are given by the value:

$$V_i(x = 0) = V_i(x = l_i) = H_i \frac{du_i}{dx} \bigg|_{x = l_i}^{x = 0} = \frac{q_i \times l_i}{2} \tag{6.17}$$

The elastic deformation of the cables under loading must also be considered in order to explicitly write the total effective length L_i; in such a case, the problem is characterized by another source of nonlinearity due to the dependence of the cable length L_i on the tensile force $T_i(x)$, in twin depends on Li. Under limited deformation (10–15% of the cable length) it can be assumed that the tensile force $T_i(x)$ is approximately equal to H_i (which does not depend on x) along the entire cable, i.e. $T_i(x) \cong H_i$ = const. (since $ds \cong dx$); in such a way the effective length of the cable (assumed to obey Hooke's linear elastic law) L_i can be written as:

$$L_i = l_i \left(1 + \frac{H_i}{E_i A_i} \right) \tag{6.18}$$

The limited deformation of each cable is considered in order to maintain the appropriate functionality of the structure.

The last relation used together with Eq. 6.15 allows one to calculate the effective cable length and the corresponding force H_i at the equilibrium state by solving the obtained non-linear problem. The above assumption (i.e. $T_i(x) \cong H_i$ = const.) can be justified by considering that the effective length of a cable even with a noticeable transversal deformation such as $f_i = 0.1 \times l_i$ is $L_i \cong 1.027 \times L_i$ and the axial force value along the cable lies in the range $H_i \leq T_i(x) \leq 1.08 \times H_i$, while for $f = 0.2 l_i$, $L_i \cong 1.107 l_i$ and $H_i \leq T_i(x) \leq 1.28 \times H_i$.

The relation between the distributed load qi and such a maximum displacement can thus be written on the basis of the solution of the following equations:

$$q_i(\overline{u_\iota}) = \frac{8H_i}{l_i^2} \tag{6.19}$$

with

$$H_i(\overline{u_\iota}) \cong \frac{\sqrt{3}}{6} \times \frac{q_i l_i}{\sqrt{2} \times \sqrt{\left(1 + \frac{H_i}{E_i A_i}\right) - 1}} \tag{6.20}$$

where the relation for the approximate cable effective length evaluation (Eq. 6.18) has been used together with Eq. 6.15; finally, the searched for relation $q_i(\overline{u_\iota})$ (Eq. 6.19) can explicitly be obtained:

$$q_i(\overline{u_\iota}) = \frac{64 E_i A_i}{3 l_i^4} \tag{6.21}$$

6.3. Evaluation of the interaction between cables

6.3.1. Effects of primary net connection

Since the horizontal cables of barrier are connected by the secondary net (Figure 6.4), it can be assumed that they are joined together by equivalent vertical imaginary rope that has the effect of distributing a portion of the load applied directly to each horizontal cable to the adjacent ones (Ferrero et al., 2015). This vertical single rope distributes a load part directly to each horizontal cable to the adjacent ones (Figure 6.6a). The differential equilibrium equation Eq. 6.9 for the ith horizontal cable can be rewritten as:

$$\frac{d^2 u_i}{dx^2} = -\frac{q_i(x) - q_{ic}(x) + q_{ci}(x)}{H_i} = -\frac{Q_i(x)}{H_i} \tag{6.22}$$

In which $q_{ic}(x)$, $q_{ci}(x)$ represent the portion of the direct load $q_i(x)$ acting on cable i that is transferred to the adjacent cables and the indirect loads transmitted to cable i from the other loaded cables, respectively, i.e.:

$$q_{ic}(x) = \sum_{\substack{j=1 \\ j \neq 1}}^{n} q_{ij}(x) , q_{ci}(x) = \sum_{\substack{j=1 \\ j \neq 1}}^{n} q_{ji}(x) \qquad (6.23)$$

Where

$q_{ij}(x)$ is the "indirect" load carried by cable j when the "direct" load $q_i(x)$ acts on cable i;

$q_{ji}(x)$ is the "indirect" load carried by cable I when the "direct" load $q_j(x)$ acts on cable j;

Therefore, load $q_{ic}(x)$ represents the total fraction of the "direct" load acting on cable i carried by all the other cables $j – i$, while $q_{ci}(x)$ represents the sum of the portions of the "direct" loads acting on all the other cables $j – i$ transferred to cable i. As previously mentioned, for the sake of simplicity, it can be assumed that the loads $q_i(x)$, $q_{ic}(x)$ and $q_{ci}(x)$ are constant along the x-coordinate and acting on the horizontal plane that contains each cable.

Figure 6.4: Example of a flexible barrier, horizontal cable and net under debris pressure

The problem is how to estimate the loads q_{ij} and q_{ji} in order to rewrite the equilibrium condition given by Eq. 6.22, with the proper effective total transversal load $(q_i - q_{ic} + q_{ci})$. Owing to the load-maximum deflection relationship given by Eq. 6.21, the loads q_{ij} and q_{ji} in Eq. 6.23 can be evaluated once the maximum displacement $\overline{u_{ij}}$ of cable j (produced by the distributed load q_i acting on cable i (Figure 6.6a and c), or the maximum displacement $\overline{u_{ji}}$ of cable i (produced by the load q_i acting on cable j, Figure 6.6d) are known.

It should be recalled that, in a real case, the cables in a barrier are not only subjected to horizontal loads but also to vertical ones, due to the effect of the transversal connecting net (Figure 6.5). In general, considering a distributed load acting on a single inclined plane along the whole cable, the deflection of a single wire takes place in a plane that contains the cable edges and the load direction, i.e. the present model can still be applied, but in a different plane from the horizontal one. It should also be considered that the vertical components of the forces acting along a single cable are only significant for the uppermost one, since the lower and the intermediate cables of the barrier are usually either restrained by the channel bottom or symmetrically surrounded by other cables, and, as a consequence, they are subjected to a simple almost horizontal force.

By indicating the maximum displacement that occurs in cable j when the cable i shows a maximum displacement equal to $\overline{u_\iota}$ with $\overline{u_{ij}}$, an influence function $0 \leq r(z_j, z_i) \leq 1$ (Fig. 6c and d) can be written in order to correlate the above quantities,

$$\overline{u_{ij}} = r(z_j, z_i) \times \overline{u_\iota} \qquad (6.24)$$
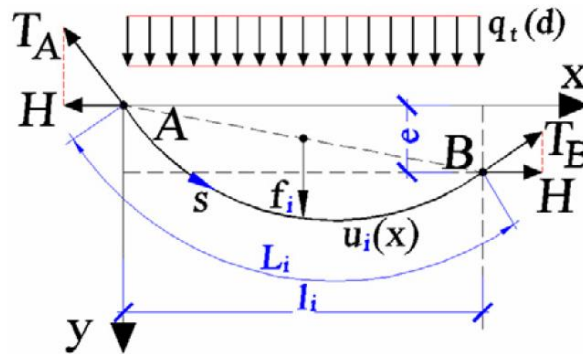
Figure 6.5: Scheme of a top view of a single cable under the forces produced by the impact of a debris-flow, with the related geometrical and static quantities (From Brighenti et al., 2013)

The value of the distributed "indirect" load, acting along a generic cable j transmitted from cable i, can be expressed as:

$$q_{ic}(x) = q_i \times \frac{r^3(z_j, z_i) \times C_j}{\sum_{k=1}^{n} r^3(z_j, z_i) \times C_k} \qquad (6.25)$$

With

$$C_j = \frac{64 E_j A_j}{3 l_j^4} \qquad (6.26)$$

138

The above relations can be obtained by writing the equilibrium condition of unit cable length $\sum_{j=1}^{n} q_{i,j} = q_i$, and the $n - 1$ displacements relationships between cable i and the remaining cables $j \neq i$:

$$\overline{u_i^3} = \left[r(z_j, z_i) \times \overline{u_j} \right]^3 \tag{6.27}$$

with $j = 1, 2, 3, \ldots, i - 1, i + 1, \ldots, n$
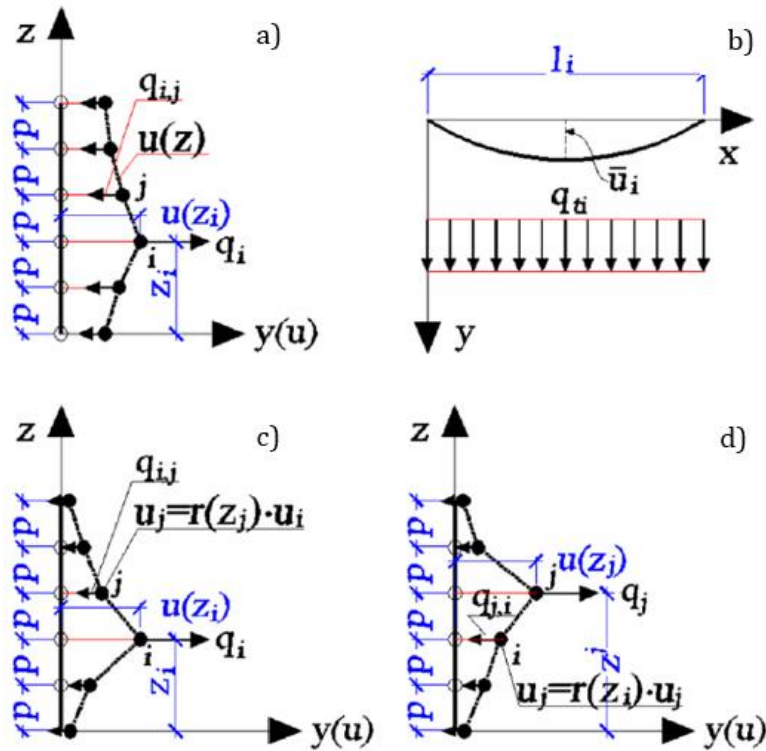
Figure 6.6: Scheme of the forces developed in cables j for a load acting on cable i (a); horizontal cable under a concentrated load (b); simplified model for the assessment of the load borne by the cables adjacent to cable i for a load qi acting on it (c and d). From Brighenti et al., 2013

Eq. 6.27 correlates the value of the maximum displacement of cable i, with respect to cable j, by mean of the function $r(z_j, z_i)$. Therefore, since there exists a direct relationship between the distributed load acting on a cable and its maximum displacement (Eq. 6.21), the load acting on a generic cable can be obtained once its maximum deflection is known.

It can be observed that function $r(z_j, z_i)$ is representative of the mechanical properties of the vertical 'equivalent' cables that connect the horizontal ones: in fact, if the net connected to the horizontal cables is very weak, when the cable i is displaced by a certain amount, the displacements in the other connected horizontal cables would result to be like those as depicted in Figure 6.6c and d, with a rapid decrease in the displacements values for an increasing vertical distance from cable i. On the other hand, in the case of a strong connecting net, the displacements

of the cables would be like those depicted in Figure 6.6a, with a lower reduction effect as the vertical distance from the displaced cable i increases. The governing Eq. 6.9 can be rewritten, using the above relations, as:

$$\frac{d^2 u_i}{dx^2} = \frac{q_i - q_{ic} + q_{ci}}{H_i} = -\frac{q_i - \sum_{j=1}^n q_{ij} + \sum_{j=1}^n q_{ji}}{H_i}$$

$$= \frac{\beta_i \times q_i \times \dfrac{r(z_j, z_i) \times C_i}{\sum_{k=1}^n r^3(z_j, z_i) \times C_k} + \sum_{\substack{j=1 \\ j \neq 1}}^n \beta_j \times q_j \times \dfrac{r(z_i, z_j) \times C_j}{\sum_{k=1}^n r^3(z_j, z_i) \times C_k}}{H_i} \tag{6.28}$$

$$= -\frac{Q_i}{H_i}$$

With

$$H_i = \frac{Q_i^2 \times l_i^2 \times E_i A_i}{24} \tag{6.29}$$

Which represent a system of nonlinear second order ordinary differential equations with $\overline{u_j^3} = u_j^3(x = l_j/2)$, $\overline{u_i^3} = u_i^3(x = l_i/2)$ and the coefficient $\beta_j = 1$ if $q_j \neq 0$ and $\beta_j = 0$ if $q_j = 0$. The latter cited coefficient needs to be introduced in order to take into account the possibility of not all the cables being loaded at the same time. In the above equations, any inertial effect is neglected since the mass of the retention barrier is very small and the horizontal acceleration of the cable and of the flowing material in contact with it can be considered to be low during the entire loading process. The above introduced function $r(z_j, z_i)$ can reasonably be assumed in the form:

$$r(z_j, z_i) = \frac{1}{\left(|z_j - z_i| + 1\right)^{m_{ji}}} \tag{6.30}$$

Where

$$m_{ij} = \frac{-\ln(c)}{\ln(|z^* - z_i| + 1)}$$

$r(z^*, z_i) = c$ is the value attained by function $r(z_j, z_i)$ at vertical coordinate $z_j = z^*$ (i.e. for a cable placed at a relative distance from cable i equal to $d_i^* = |z^* - z_i|$) while the unit value of $r(z_j, z_i)$ is attained at $z_j = z_i$ (Figure 6.7)

The assumed $r(z_j, z_i)$ value indicates that the relationship between the displacement of the different horizontal cables depends on their relative vertical distance d_{ij} and on their reciprocal position. It can be observed that $m_{ji} \neq m_{ij}$ because of the non-linear force-displacement relationship (see Eqs. 6.21 and 6.25). This is due to the difference between the relative displacement that occurs in cable i when cable j is subjected to a given displacement, and the relative displacements that arise in cable j when cable i is subjected to the same displacement. The function $r(z_j, z_i)$, if properly tuned through its coefficient m_{ij}, can represent the relationship between the displacements of two connected cables.
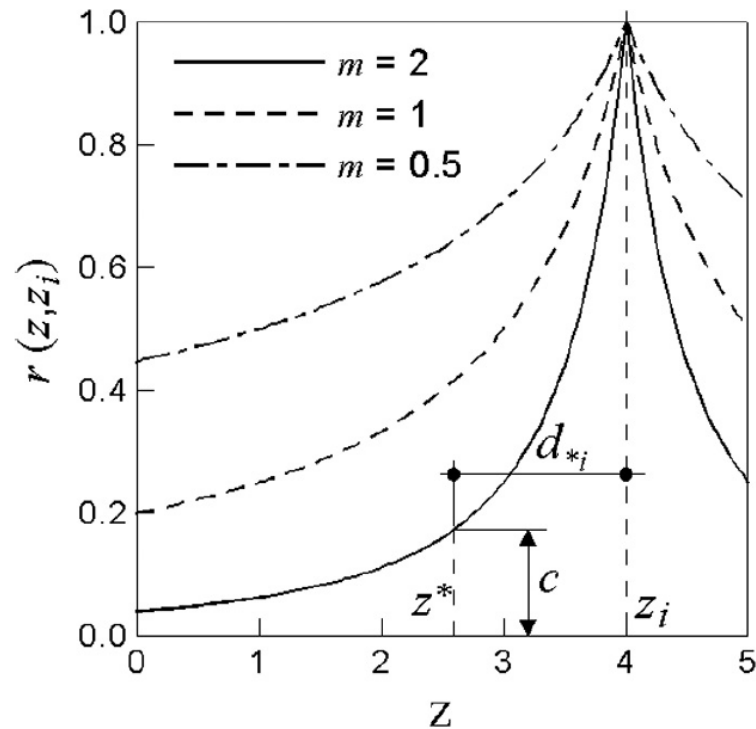
Figure 6.7: Assumed pattern of function r(zj, zi) for different values of exponent m and for zi = 4 in Eq. (30), from Brighenti et al. (2013)

Function $r(z_j, z_i)$ can be determined by considering the mechanical behavior of the transversal midsection of the barrier (Figure 6.8). The equilibrium condition in the horizontal direction for the ith cable can be written as

$$q_i = T_i \times \sin \varphi_i - T_{i-1} \times \sin \varphi_{i-1} \tag{6.31}$$

With

$$\sin \varphi_i = \frac{\overline{u_i} - \overline{u_{i-1}}}{P_i}$$

$$P_i = \sqrt{p_i^2 + (\overline{u_\iota} - \overline{u_{\iota-1}})^2} - p_i$$

$$T_i = A_{ti} \times E_{ti} \times \varepsilon_i = A_{ti} \times E_{ti} \times \frac{P_i - p_i}{p_i} = A_{ti} \times E_{ti} \times \frac{\sqrt{p_i^2 + (\overline{u_\iota} - \overline{u_{\iota-1}})^2} - p_i}{p_i}$$

Where ε_i is the strain in the vertical cable connected to the horizontal cable i. The relationship between the applied load and the maximum transversal deflection of the cable is instead given by Eq. 6.21. The above equilibrium equations can thus be rewritten as:

$$q_i = \frac{64E_i A_i}{3l_i^4} \times \overline{u_\iota}^3 = T_i \times \sin\varphi_i - T_{i-1} \times \sin\varphi_{i-1}$$

$$= A_{ti} \times E_{ti} \times \frac{\sqrt{p_i^2 + (\overline{u_\iota} - \overline{u_{\iota-1}})^2} - p_i}{p_i}$$

$$\times \frac{\overline{u_\iota} - \overline{u_{\iota-1}}}{P_i} + \tag{6.32}$$

$$-A_{ti-1} \times E_{ti-1} \times \frac{\sqrt{p_{i-1}^2 + (\overline{u_{\iota-1}} - \overline{u_{\iota-2}})^2} - p_i}{p_{i-1}} \times \frac{\overline{u_{\iota-1}} - \overline{u_{\iota-2}}}{P_{i-1}}$$

Eq. 6.32 simply gives the equilibrium of the load acting on the cable under study and those deriving from the other connected cables, expressed by means of their maximum horizontal displacements. Once the maximum transversal deflection $\overline{u_\kappa}$ of the *kth* cable is known, the maximum transversal deflections of the other cables can be obtained by solving the system of nonlinear equations.
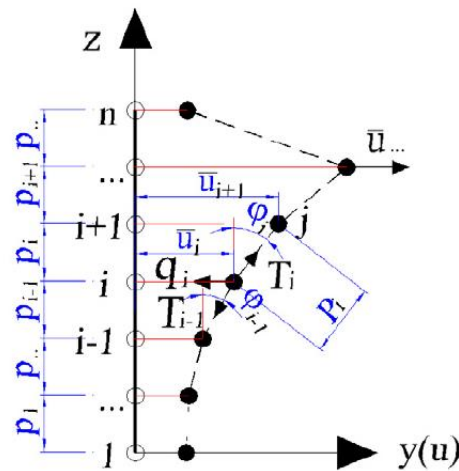
Figure 6.8: Scheme of a vertical section of the barrier; the horizontal cables are represented by filled circles from Brighenti et al. (2013)

The solution of such a system is very awkward and does not lead to an easy analytical treatment to obtain the sought values. For this reason, an iterative evolutionary algorithm of the Genetic Algorithm (GA) type has been applied.

The solution of the mathematical formulation of many physical problems is often rather difficult when classical approaches are applied. Increasing interest in that class of algorithms that are known as Genetic Algorithms (GAs), have been observed over the last few decades.

GAs operate by simulating the natural evolutionary processes of life; the Darwinian principle of survival of the fittest is applied by iteratively improving the current solution. Such algorithms include random stochastic methods of global optimization, and are used to minimize or maximize a chosen objective function considered suitable for a given problem.

When the above cited biological-based algorithm approach is used, some conditions, related to a desired objective function, can approximately be imposed; in the present case, the objective function to be minimized can be assumed to be represented by the total error e_{tot} in order to satisfying the equilibrium equations of the system (24), i.e.: $e_{tot} = min$.

$$e_{tot} = \sum_{i=1}^{n} |e_i| \tag{6.33}$$

With

$$e_i = \frac{64 E_i A_i}{3 l_i^4} \times \overline{u_i}^3 - A_{ti} \times E_{ti} \times \frac{\sqrt{p_i^2 + (\overline{u_i} - \overline{u_{i-1}})^2} - p_i}{p_i} \times \frac{\overline{u_i} - \overline{u_{i-1}}}{P_i} +$$

$$-A_{ti-1} \times E_{ti-1} \times \frac{\sqrt{p_{i-1}^2 + (\overline{u_{i-1}} - \overline{u_{i-2}})^2} - p_i}{p_{i-1}} \times \frac{\overline{u_{i-1}} - \overline{u_{i-2}}}{P_{i-1}}$$

The flow-chart of the developed Genetic Algorithm used to minimize the errors expressed by Eq. 6.33 is reported below. As can be observed, several initial random generations of the expected solution, represented by the exponents m_{ij} are required (initial population made of M individuals). The highest ranking results can be identified by performing the fitness evaluation of each individual (quantified through the violation of the equilibrium equations measured by e_{tot}), and that they can then be used for the subsequent crossover and mutation operations that are necessary to obtain the new offspring of new individuals which are again treated like the previous one. If the above process is repeated, in an iterative way, until a given error tolerance is reached, the numerical solution tends to the true solution of the problem.

```
┌─────────────┐
│    START    │
└─────────────┘
       │
       ▼
┌──────────────────────────────────────────────────────┐
│ Random generation of a population of M individuals,    │
│ with n x n design parameters for each individual        │
│ (m_{k i,j} for i, j = 1 ,.., n and K = 1, ... M         │
└──────────────────────────────────────────────────────┘
       │
       ▼
┌──────────────────────────────────────────────┐        ┌──────────────┐
│ Fitness evaluation of each generated           │───────▶│ Equilibrium  │
│ individual with respect to an Objective         │        │     Eqs      │
│ Function e_{tot}                                │        └──────────────┘
└──────────────────────────────────────────────┘
       │
       ▼
┌──────────────────────────────────────────────┐
│ Crossover using the two best individuals (with │
│ probability P_C) and elitism to obtain a new    │
│ population m*_{k I,j} (offspring)               │
└──────────────────────────────────────────────┘
       │
       ▼
┌──────────────────────────────────────────────┐
│ Mutation of a certain number of individuals     │
│ (with probability P_M)                          │
└──────────────────────────────────────────────┘
       │
       ▼
┌──────────────────────────────────────────────┐
│            Convergence check                    │
└──────────────────────────────────────────────┘
       │
  ┌────────────┐   NO           YES
  │ Maximum    │◀────────         │
  │ number of  │                  ▼
  │ interactions│           ┌──────────────┐
  └────────────┘           │     END      │
       YES  ──────────────▶└──────────────┘
```

6.3.2. Cable interaction evaluation and calibration of *r* function

Calculate the function $r(z_j, z_i)$ is possible through Eq. 6.30. So, to forecast the behavior of the vertical imaginary rope that connects the horizontal cables and distributes the applied load to each rope to the adjacent is necessary to estimate the coefficient m_{ij}. This coefficient represents the relation between the displacements of two different ropes connected through the metallic net.

In order to determine the coefficient m_{ij} a test procedure similar to the one performed by Ferrero et al. (2015) on site was carry out in laboratory. Different static load combinations were imposed on each structural cable of the scaled barrier and the induced deformations were

measured through a theodolite. This allowed to study how the load on each single cable influenced the deformation of the others (Figure 6.9). The results of this experimental study are very useful and can be taken as a good starting point for the application of the simplified analytical model for the analysis of real cases.
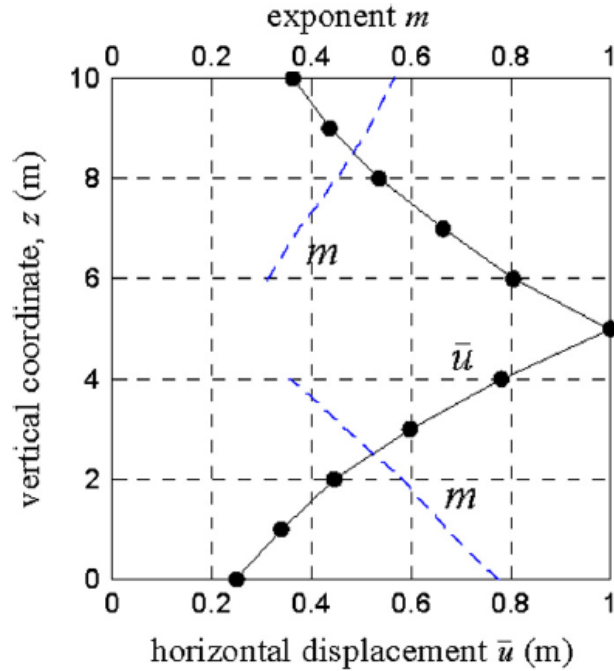
Figure 6.9: Deformed pattern of 10 identical horizontal cables, joined by vertical cables, obtained using the GA (from Brighenti et al., 2013)

Table 6.1: Technical features of tested scale barrier specimens

Barrier prototype characteristics		
Barrier	Height	36 cm
	Length	100 cm
	Nr. of ropes	4
Ropes	Reference standard	UNI EN 12385-4
	Material	Steel
	Diameter	3 mm
	Strength	1770 kN/m^2
	Construction	6x7 WSC
	Breaking load	5,72 kN
	Extremities	Loop with clamps
Net	Material	Steel
	Mesh shape	Hexagonal
	Mesh average dimension	0.5 cm

145
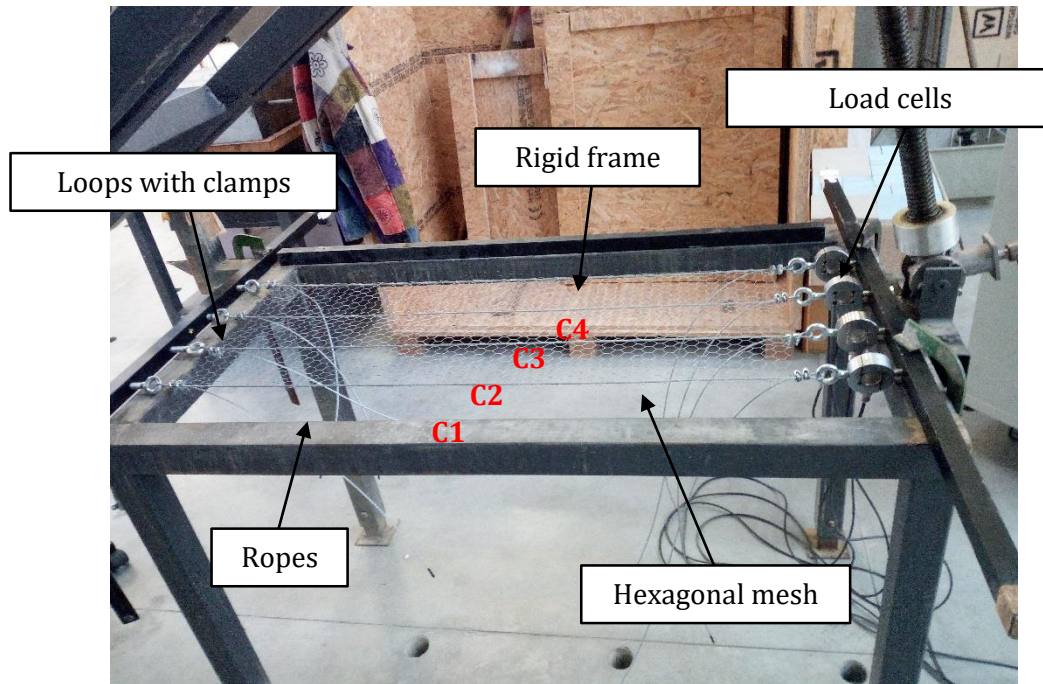
Figure 6.10: Test configuration

The laboratory tests were conducted on scale prototypes of barrier for the evaluations of the parameter A_t, which represents the transversal area of the vertical imaginary rope that connects the horizontal cables. The steel cables were loaded one at a time for evaluate the displacements caused on the others (Figure 6.11). The barrier prototypes were fixed to a rigid frame in the horizontal plane (Figure 6.10) and the steel longitudinal ropes were loaded through different masses in vertical direction. Specimens consisted of four steel ropes of 3 mm diameter (UNI EN 12385-4) on which a thin metallic net was connected. The distance between each rope is 12 cm and the total height of the barrier was 36 cm; the specimen length was 1 m. The features of the barrier prototypes are reported in Table 6.1. During the test ropes (numbered C1, C2, C3 and C4) were loaded one at a time in five steps, using different masses that applied forces to the specimen along the vertical direction; after each step vertical displacements of the loaded rope and of the unloaded ones were measured. Load combination applied to each cable are:

- *Combination 0*: no loads;
- *Combination 1*: three equidistant masses of 8 kg were applied along each single rope (for a total of 24 kg). No loads were applied on the other ropes;
- *Combination 2*: three equidistant masses of 16 kg were applied along each single rope (for a total of 48 kg). No loads were applied on the other ropes;
- *Combination 3*: three equidistant masses of 32 kg were applied along each single rope (for a total of 96 kg). No loads were applied on the other ropes;
- *Combination 4*: three equidistant masses of 50 kg were applied along each single rope (for a total of 150 kg). No loads were applied on the other ropes.

Figure 6.11: Sag of cable C1 caused by the application of masses
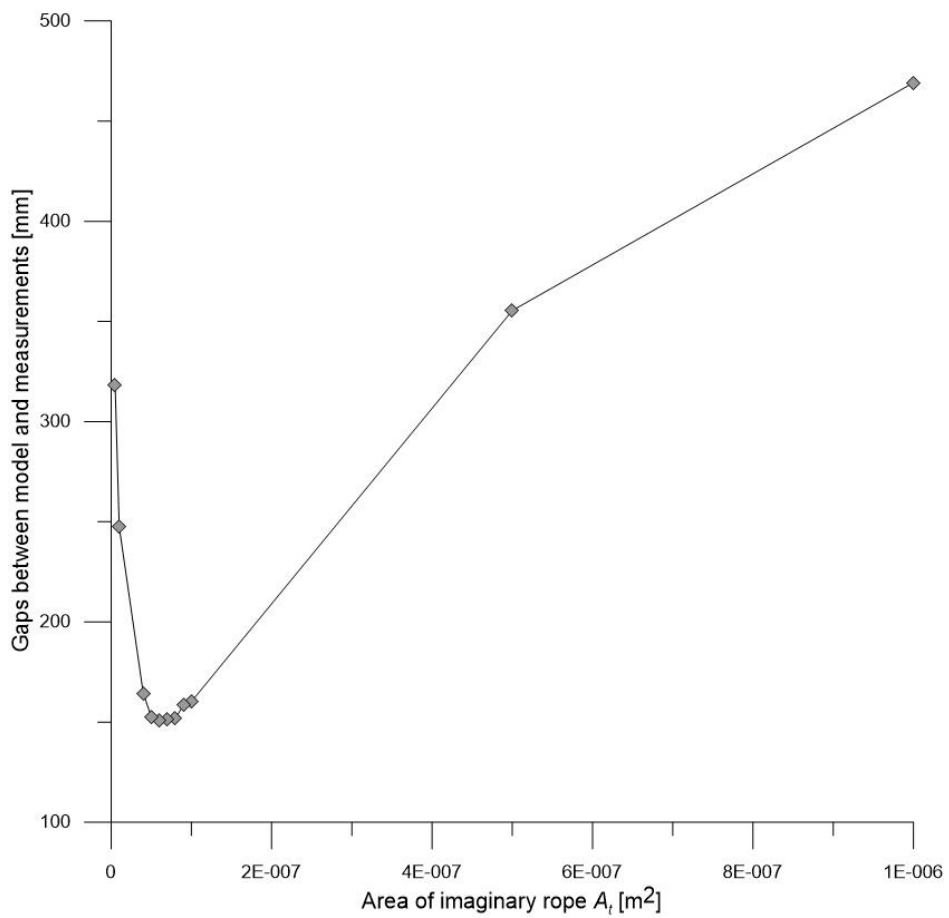
Figure 6.12: Parametric analysis of function r(zj, zi) and evaluation of the transversal area of the imaginary cable a which minimizes gaps between the numerical model and the total station measurements

To measure the longitudinal forces that the application of the different masses caused along each steel cable, four load cells with capacity between 100 and 200 kg were used (Figure 6.10). The data acquisition system was *National Instruments CompactDAQ 9174*, which allows to record continuously the forces involved in the process; this is very useful also for check the initial tension of the ropes, which should be the same before each load steps. The aim of the test was to evaluate the geometry of the scaled barrier under different loading conditions.
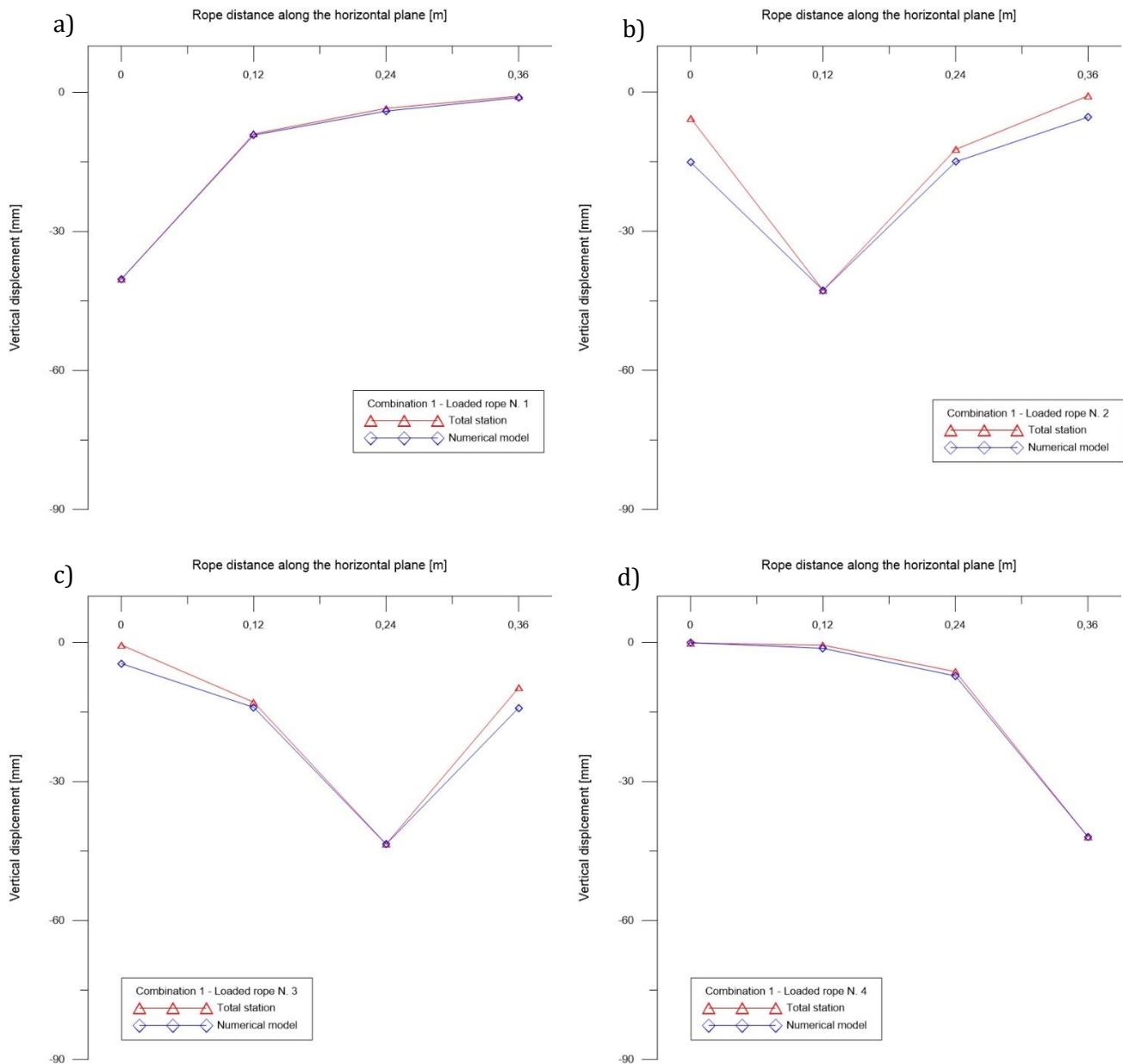
Figure 6.13: Comparison between experimental data measured with total station and the numerical model after calibration of the parameters involved in the interaction function, r(zj, zi) between cables (a=0.6e-7, load Combination 1); a) Cable 1 loaded b) Cable 2 loaded c) Cable 3 loaded d) Cable 4 loaded

To measure the vertical displacement of the ropes a total station was used. Also digital images of the tested barrier are taken using one fixed high resolution digital camera. Before the test, fixed control points were materialized sticking targets onto the rigid frame.
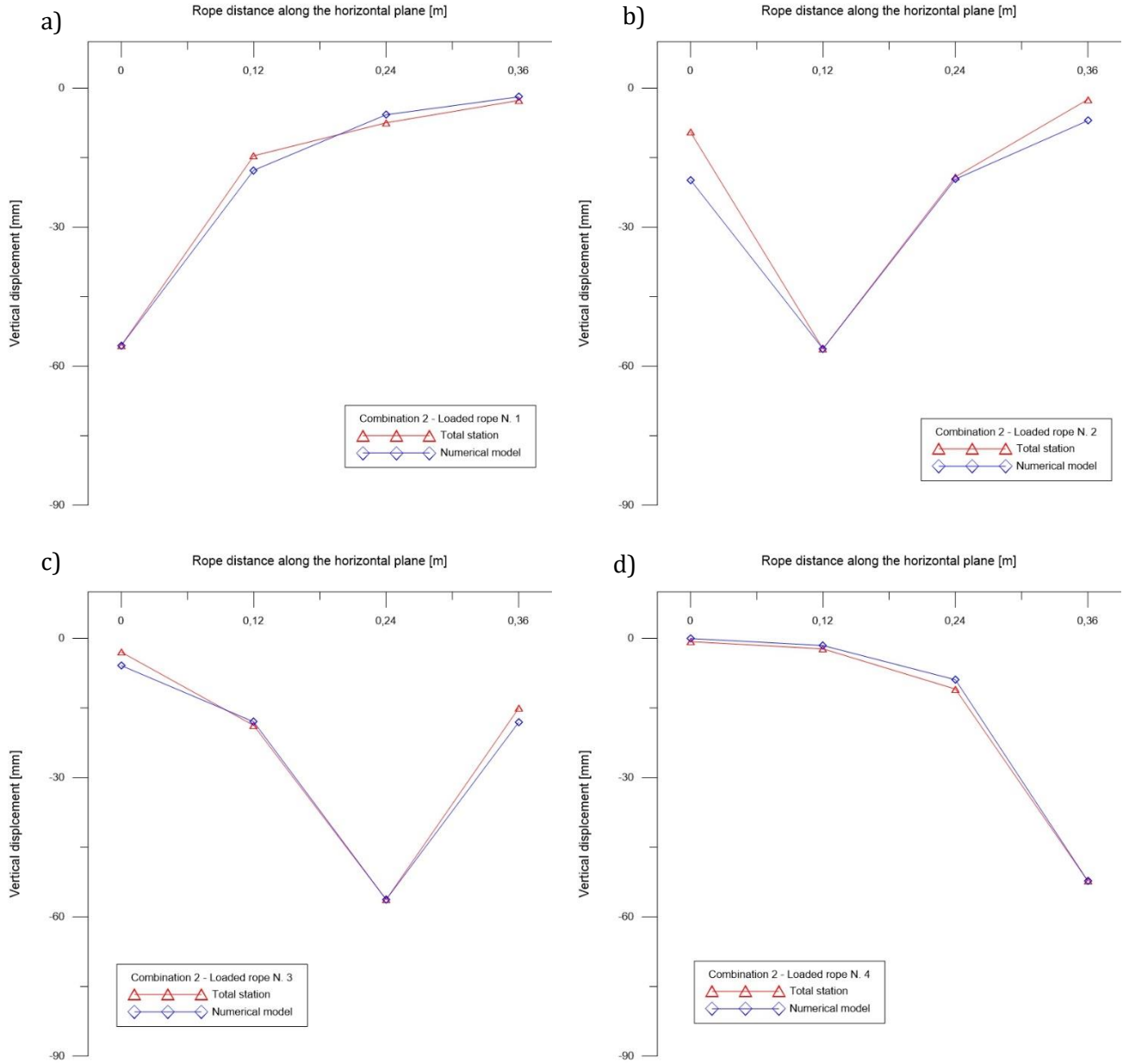
Figure 6.14: Comparison between experimental data measured with total station and the numerical model after calibration of the parameters involved in the interaction function, r(zj, zi) between cables (a=0.6e-7, load Combination 2) ; a) Cable 1 loaded; b) Cable 2 loaded; c) Cable 3 loaded; d) Cable 4 loaded

The results of the performed tests and of the parametric analysis are reported in Figure 6.12, 6.13, 6.14, 6.15 and 6.16. The simulation results, obtained through the above explained procedure using the best choice of exponents m_{ji} and the optimum value of the transversal section of the imaginary rope, are shown with blue lines; the measures made by the total station are identified by the red ones.

It can be note that displacements of the rope i caused by a load applied to rope j are different from those that occur in rope j when rope i is loaded (coefficient m_{ij} and m_{ji} are different). This is due to the non-linearity characteristic of the system of governing equations (Brighenti et al., 2013). However, the numerical model is in good agreement with the experimental data measured with the total station for an imaginary cable transversal area A_t equal to 0.6e-7.
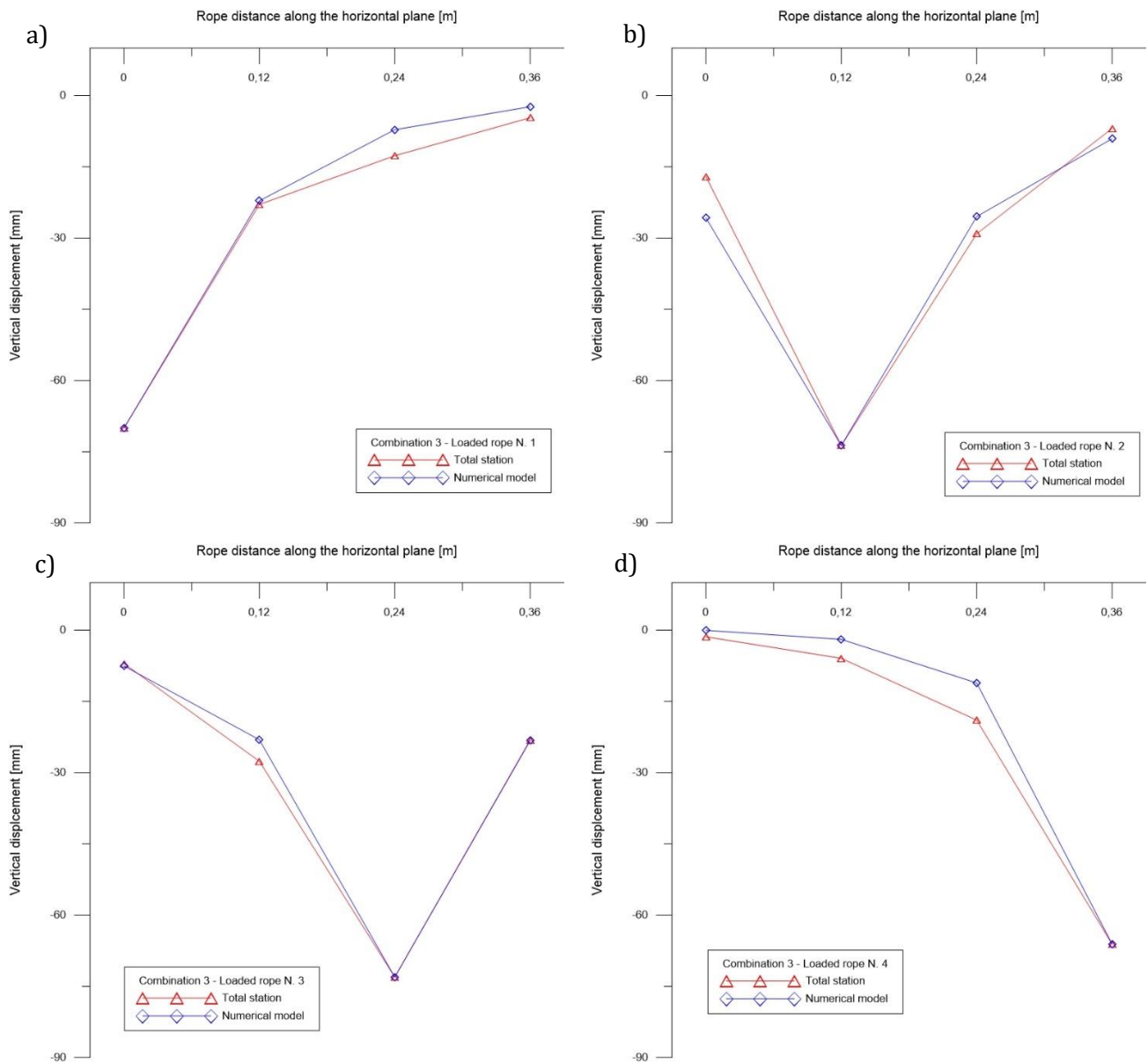
Figure 6.15: Comparison between experimental data measured with total station and the numerical model after calibration of the parameters involved in the interaction function, r(zj, zi) between cables (a=0.6e-7, load Combination 3); a) Cable 1 loaded; b) Cable 2 loaded; c) Cable 3 loaded; d) Cable 4 loaded

The Genetic Algorithm (GA) (Goldberg, 1989; Gen and Cheng, 1996) was applied to each loaded cable to find the coefficient m_{ij}, which is fundamental for the definition of the function $0 < r(z_j, z_i) < 1$ that define the interaction between ropes connected by the net. data obtained

from the tests. The coefficient m_{ij} depends on the characteristic of the net, especially on its stiffness: if the net stiffness is high the imaginary transversal rope which connects the longitudinal cables will have high stiffness too (big transversal section A_t); on the contrary, if the net has low stiffness the imaginary rope will be more flexible, with smaller transversal area A_t. The transversal area A_t of the imaginary rope that simulates the metallic net must be determined on the basis of the experiments.
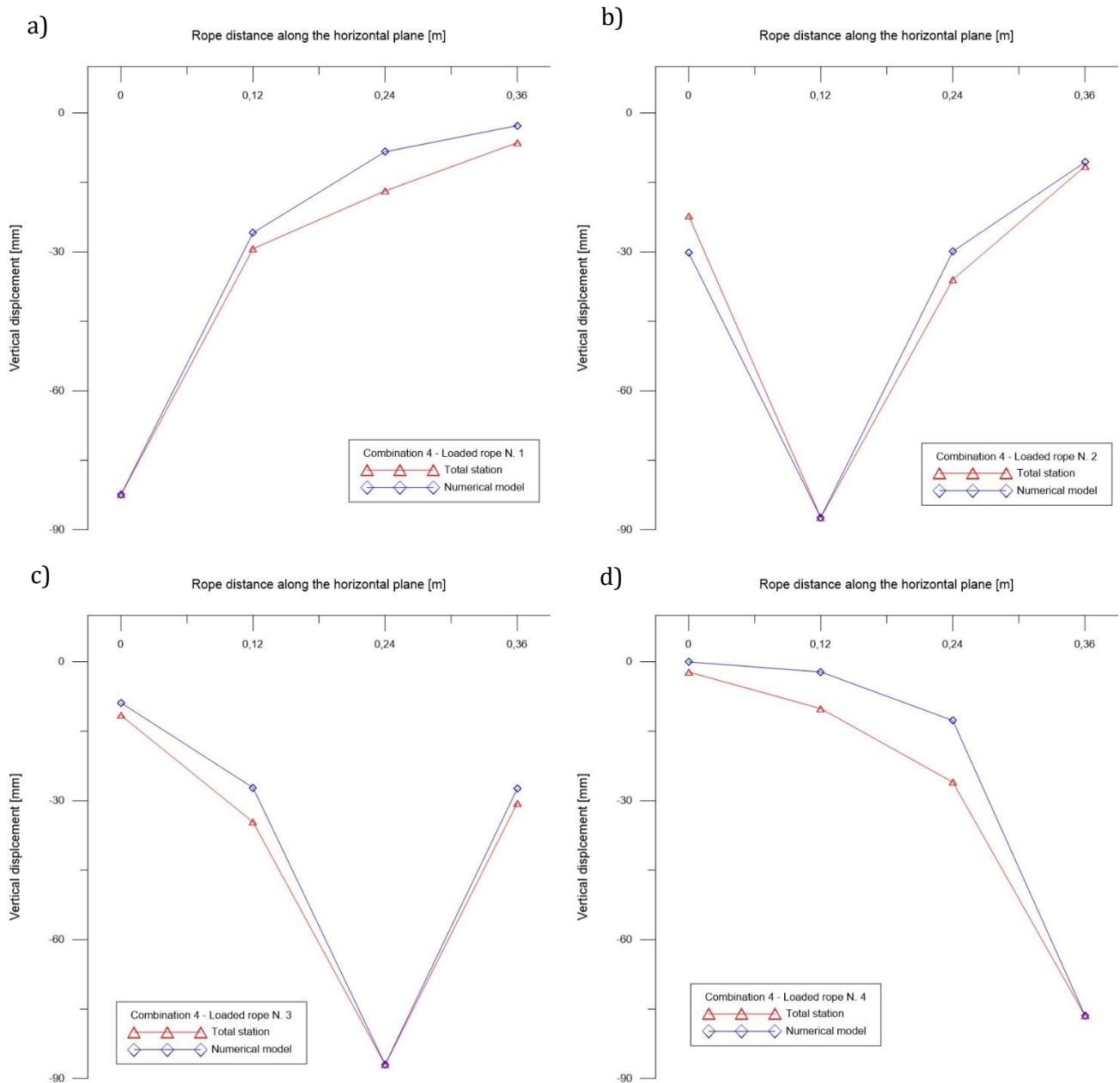
Figure 6.16: Comparison between experimental data measured with total station and the numerical model after calibration of the parameters involved in the interaction function, r(zj, zi) between cables (a=0.6e-7, load Combination 4); a) Cable 1 loaded; b) Cable 2 loaded; c) Cable 3 loaded; d) Cable 4 loaded

Comparing the rope displacement values for each combination, is possible to affirm that the agreement between the experimental and numerical data is satisfactory. It is evident that

the assumption of the interaction function (see Eq. 6.30) proposed by Brighenti et al. (2013) is suitable for the numerical simulation of the ropes interaction, once its governing parameters have been properly determined.

The results obtained from the parametric analysis are used in the numerical model proposed by Brighenti et al. (2013) to study the behavior of the barrier and its interaction with debris flow. These data were the starting point to forecast the forces that the flow generates along the horizontal ropes.

6.4. Laboratory tests

6.4.1. Test description and objectives

The total absence of premonitory signals, the high velocity and the long travel distance make debris flows one of the most dangerous and destructive gravitational movements on Earth. Many countermeasures have been designed to protect and reduce the risk related to these phenomena. About the design of these structures, there are many aspects to examine carefully in order to quantify and overcome the uncertainties concerning the evaluation of impact pressure.

For instance, the partial absence of regulations in the international standards and the issues in determination of flow characteristics are forcing the designers to adopt incorrect approaches developed for other phenomena (e.g. rock fall events). Furthermore, the lack of available monitoring data from real events forces researchers to perform small scale experimental tests; obviously, these tests are affected by scale effects that are still discussed by the scientific community. However, these tests, due to their repeatability and low costs, appear to be a good starting point to reduce the lack of knowledge on impact estimation.

In order to verify the impact mechanism, the complex chain process leading to a flowslide has been analyzed through a series of tests in an artificial flume apparatus. It is composed by two channels sections, each 1-meter-wide and 3 meters long with variable inclination angles. The first section is used to analyze the triggering mechanisms, while the second allows for the analysis of the propagation phases. Both channels are equipped with suitable sensors for monitoring the main physical variables involved in each phase.

The flexible barrier is a reproduction of existing protective structures against debris flow events. The main elements of the flexible barriers consist of:
a) Light steel net able to retain the debris and facilitate its drainage;
b) Four wire ropes, fixed on two lateral posts perpendicular to the channel bottom, sustaining the light steel net and transferring the load that builds up in the barrier to the load cells.

The aim of these tests is to collect and analyze the preliminary results obtained from the flume tests, in order to highlight how the barrier stiffness and the drainage capability strongly influence the impact peak pressure acting on the barrier itself and verify the attendance of the numerical model developed by Brighenti et al., (2013), which calculates the forces along the ropes involved in the process.

6.4.2. Test equipment

At the CAMILab laboratory of the University of Calabria, in the framework of the SILA – PONa3_00341 project *"An Integrated System of Laboratories for the Environment"*, a large artificial channel was built, able to reproduce a rainfall-triggered landslide, analyze the correlated measurements, and observe post-failure evolution.

The physical model was designed so as to lend the channel great flexibility and versatility when used. It is equipped with a sensor system to measure the main physical parameters which govern deformation and failure processes, a video recording system, lasers to measure displacements and devices to measure the velocities involved.

The presence of two independent channels also makes it possible to analyze the propagation phase and allow the positioning of impact structures so as to evaluate any mitigation strategies. The channel has a rectangular section which is homogeneous and constant along its entire length.
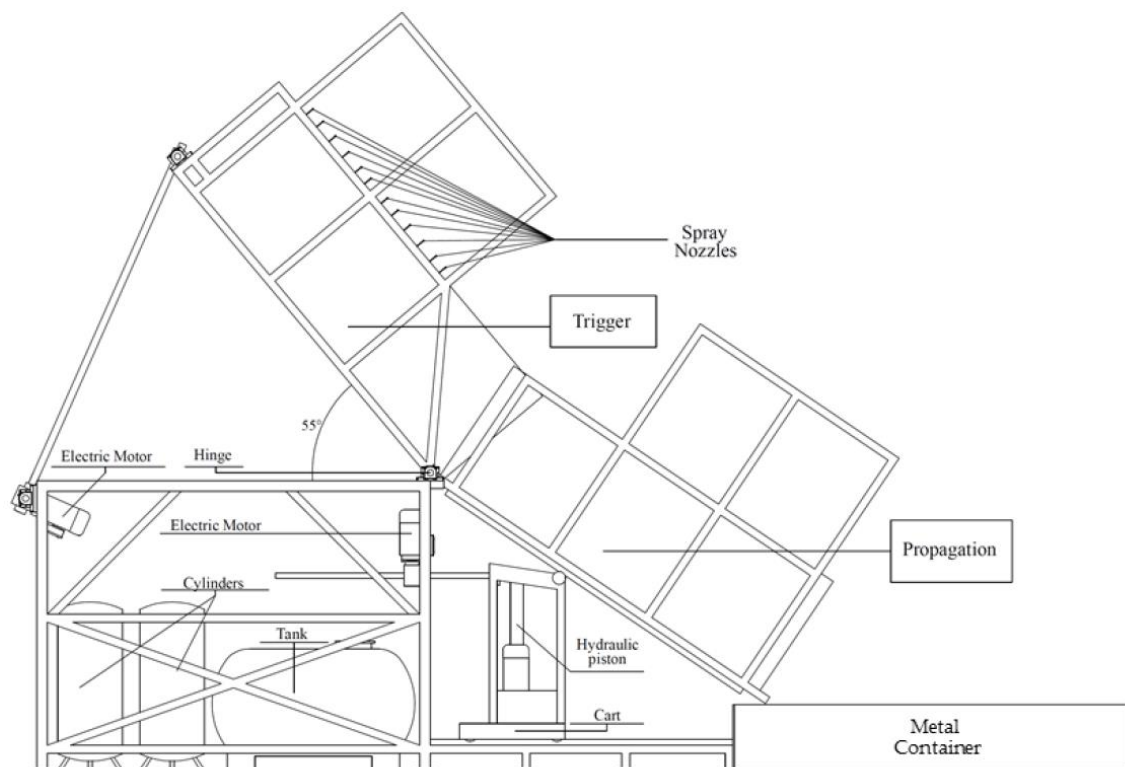
Figure 6.17: Channel lateral sketch

153

The structure, supported by metal tubes, is 1 m high, 6 m long overall, divided into 3 m for the trigger and 3 m for propagation, and 1 m in width. The section and plan of the mechanical component of the structure are reported in Figure 6.17, while Figure 6.19 shows three photographs of the channel.
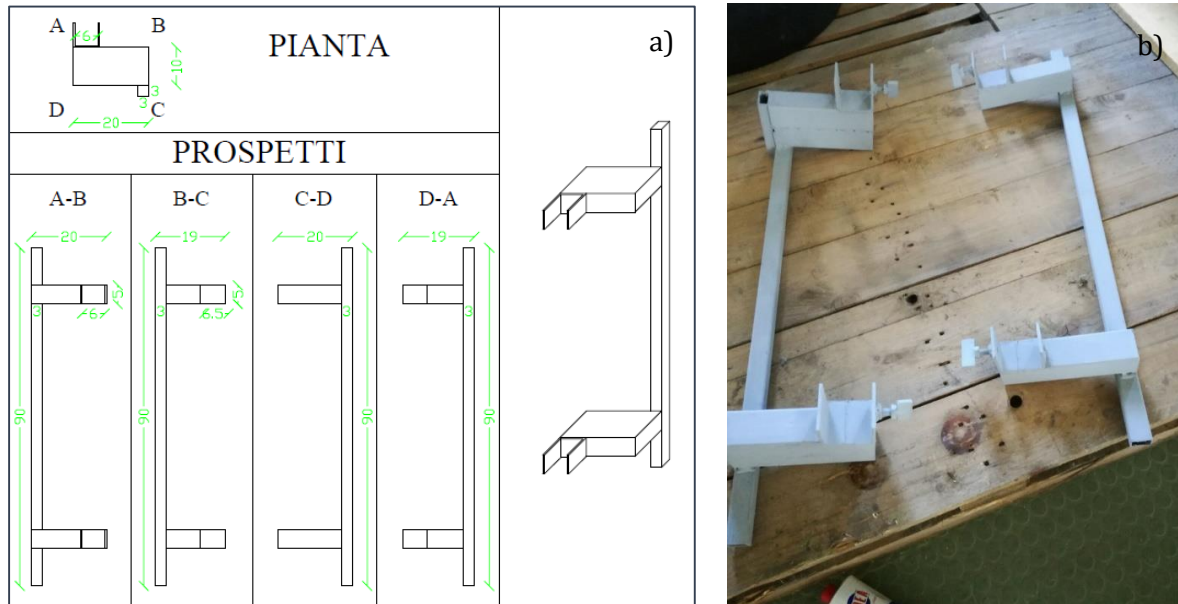
Figure 6.18: Specially designed support for the connection between the rigid channel and the flexible prototype of barrier; a) Technical drawings b) Support photo

Both the side walls and the bottom wall are made out of transparent plexiglass panels to ensure that movement can be both viewed and filmed during the landslide. On the flume bed it is possible to reproduce both an impermeable and permeable bottom-base. In the former case, an impermeable rough bed is laid, which acts as an interface with the test soil, consisting of a plastic sheet on which gravel grains are glued.

The model allows different configurations to be defined in relation to the objectives to be pursued. Besides the analysis of the triggering conditions and propagation in cohesive soils, the behavior of loose granular soils can also be examined via the insertion of further instruments. Installing supports, specially designed, on the flume (Figure 6.18), it is possible to connect flexible barriers on a small scale and simulate the behavior of a debris flow. A debris flow consisting of aggregates of particles of known sizes may be triggered in the upper flume, modifying its initial set-up. Using this experimental configuration, different tests can be carried out by changing each time the inclination of the lower flume (thus making the propagation velocity change) or the configuration of barriers.

Thus, thanks the instrumentation already present and to that of the installable support, all the necessary dimensions can be identified for perfect definition of the barrier and for understanding the phenomenon. Indeed, thanks to high-resolution video cameras with dedicated PIV software the velocity attained by the flows may be determined, while through

ultrasonic altimeters the height reached by the flow is identified. To complete the instrumentation a series of load cells may be installed, allowing measurement of the forces on the ropes, which form the barrier, during and after the impact with the debris flow.

Moreover, by defining an almost real stratigraphy it is also possible to analyze the effect of rainfall on these materials, thereby seeking to determine the quantities that most affect its behavior. Finally, thanks to the small-scale model, the behavior of the system of protection under the influence of such flows may be better understood, with a view to improving environmental protection and reducing the associated risk.

Figure 6.19: Photos of channel used for debris flow laboratory test at the University of Cosenza (CAMILab); a) Front view of the channel bottom and granular material preparation; b) Test configuration with change of the inclination of the downstream part of the channel; c) Channel lateral view with some granular material accumulated behind the barrier after the test

6.4.3. Measurement devices and PIV techniques

At the bottom of the propagation channel prototypes of flexible barriers (the same described in the previous paragraph), have been installed. This portion of the channel is equipped with:

a) four ultrasonic level measurers for the evaluation of the flow height (Figure 6.20a and c);

b) four load cells connected to longitudinal ropes (Figure 6.20b, in order to measure the forces that debris impact caused on them (the same used for the laboratory test described in the previous paragraph);

c) five high definition digital video cameras and appositely dedicated software PIV (Particle Image Velocimetry), which allows reconstruction of the overall displacement, flow fields and velocity.

Thanks to the image acquisition system with the relative dedicated PIV software, besides monitoring the displacements perpendicular to the surface of the deposit, it is also possible to know longitudinal changes. For image acquisition high-resolution (1296 x 966) five video cameras (ICX445 – Basler) are used, with one positioned in the triggering zone, two in the propagation zone and two at the side of the channel, thanks to jutting metal supports. Two lenses are used with the video cameras (C-Mount High Res - 1/2" - 4 mm - F/1.4 w/lock and Mega–Pixel Lens Fixed FL 8 mm - 2/3" - f/1.1 - f/16), as well as a 10-meter digital cable.

The dedicated PIV system permits optical evaluation of the flow domain of the deposit during the various test phases. It supplies, in a certain section, the projection of the field of instantaneous velocity. From the comparison of the two successive images the velocity of the space-time relation is evaluated, in other words the pixels between the position of the same particle in two successive photos, and the acquisition time of the two photos. The laser device emits two pulses, separated by an interval Δt, which illuminate the particles and make them visible to the camera. By means of a synchronizer, the camera takes two photos when the signal is emitted by the laser. The two images undergo correlation processes whereby the movements of particles present in each area are compared (32x32 or 64x64 pixel measurement grid). The density of particles (>25 per window) ensures that correlation processes and average are satisfied. Indeed, such processes restore spatially averaged velocities within the measurement grid.

$$\overline{U} = \frac{\Delta x}{\Delta t}; \quad V = \frac{\Delta y}{\Delta t} \tag{6.1}$$

Using PIV acquisition software, the images captured can be processed, correlating and validating the flow domain. To obtain values that are compatible with the real phenomenon, the choice of photogram acquisition frequency is decisive: the interval between two shots must capture the particles in the two consecutive images.

Besides, also in the case of bi-dimensional flow, if the interval is too long, there is a loss of information between the two images and the velocity obtained can no longer be assimilated to instantaneous velocity, but is instead an average velocity. Instead, if the interval is excessively short the displacement is too small and the disturbance due to "noise" and the imperfect correlation between pairs of windows becomes dominant with respect to the real same displacement: a field of velocity is obtained which does not correspond the real one. The value of Δt will have to oscillate about ~10 μs.

Hence the technique, through high-resolution image acquisition, allows us to recognize individual soil particles and detect the development of processes generated during the simulation. The output supplied by PIVview2C software can be obtained according to the format required and the size desired. Essentially, screen views are supplied with velocities and displacement values with the relative text files.

Figure 6.20: Photos of measurement devices used for laboratory flume test; a) Ultrasonic level device for measurement of the flow height; b) Load cell connecting barrier and rigid structure for measurement of rope tension; c) Instrumented channel and devices numeration

6.4.4. Test setup

The characteristics of the tested barrier prototype components (longitudinal steel ropes and light metallic net) were the same of the previous paragraph. Different tests were performed varying the following parameters:

a) Geometry of the barrier (n. of longitudinal ropes);
b) Channel inclination.

In Table 6.2 different test configurations are shown. The various experiments were performed without the influence of the rainfall event, and the trigger occurred by tilting the upper flume. Moreover, by defining an almost real stratigraphy it is also possible to analyze the effect of rainfall on these materials, thereby seeking to determine the quantities that most affect its behavior. The material used for simulating the flow was a granular dry material consisted of

non-spherical particles with diameter between 1.5 and 3 cm (Figure 6.21). The characteristics of the moving mass are reported in Table 6.3.

Figure 6.21: Granular material simulating debris flow; a) Front view; b) Lateral view

Table 6.2: Flume test features and varying parameters

Test ID	N. of ropes [-]	Channel inclination [°]
1	4	30.00
2	4	33.25
3	4	36.50
4	3	36.50
5	2	36.50

Table 6.3: Characteristic of the granular material used during laboratory experiments

Material type	Gravel
Diameter range	1.5÷3.0 cm
Volume	0.25 m^3
Density	1500 kg/m^3
Initial shape	Trapezoidal

6.4.5. Test Results

In this section the results obtained from laboratory test are reported. The final aim of the experiments was the validation and the calibration of the numerical model development by Brighenti et. Al (2013), which represents an important tool for debris flow barrier design.

Flow height

Flow height data were recorded by four ultrasonic gauges: two installed 10 cm behind the barrier (US3 and US4) and two one-meter-distant (US1 and US2), in order to evaluate some differences between flow behavior along the middle section of the channel and near the boundaries represented by plexiglass walls (Figure 6.20c).
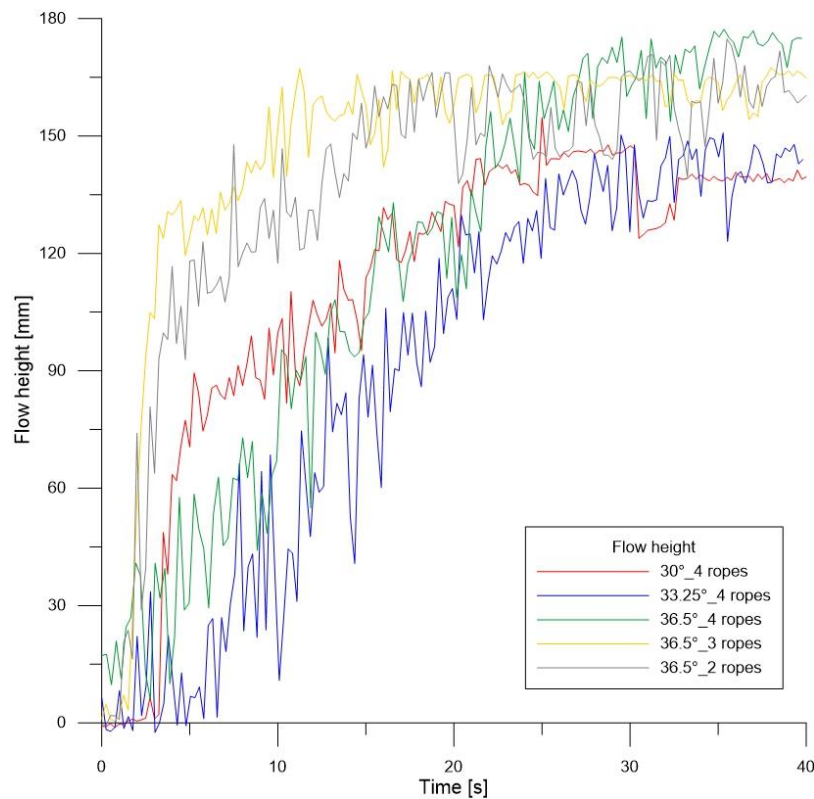
Figure 6.22: Flow height recorded during the experiments by one of the ultrasonic gauge installed behind the barrier

Figure 6.23: Material accumulated behind the barrier at the end of the experiments; a) Case 1 with channel inclination 30° and 4 longitudinal ropes; b) Case 2 with channel inclination 33.25° and 4 longitudinal ropes; c) Case 3 with channel inclination 36.5° and 4 longitudinal ropes
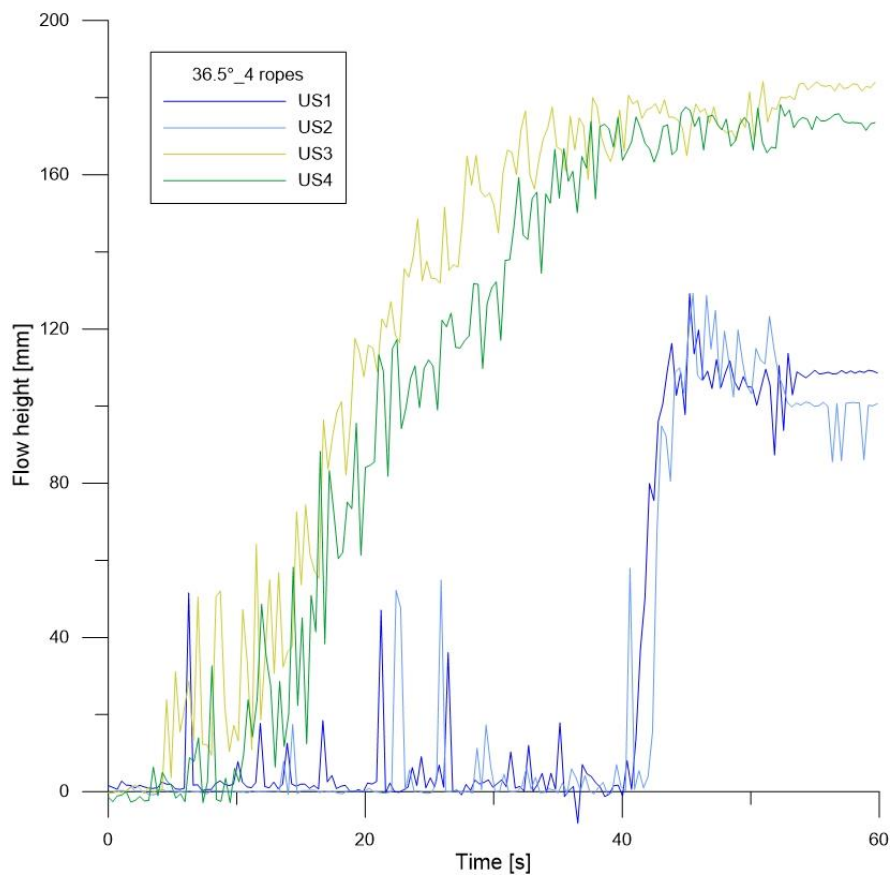
Figure 6.24: Flow thickness values recorded by the ultrasonic gauge during test n. 3 characterized by channel inclined of 36.5° and barrier prototype with 4 longitudinal ropes

160
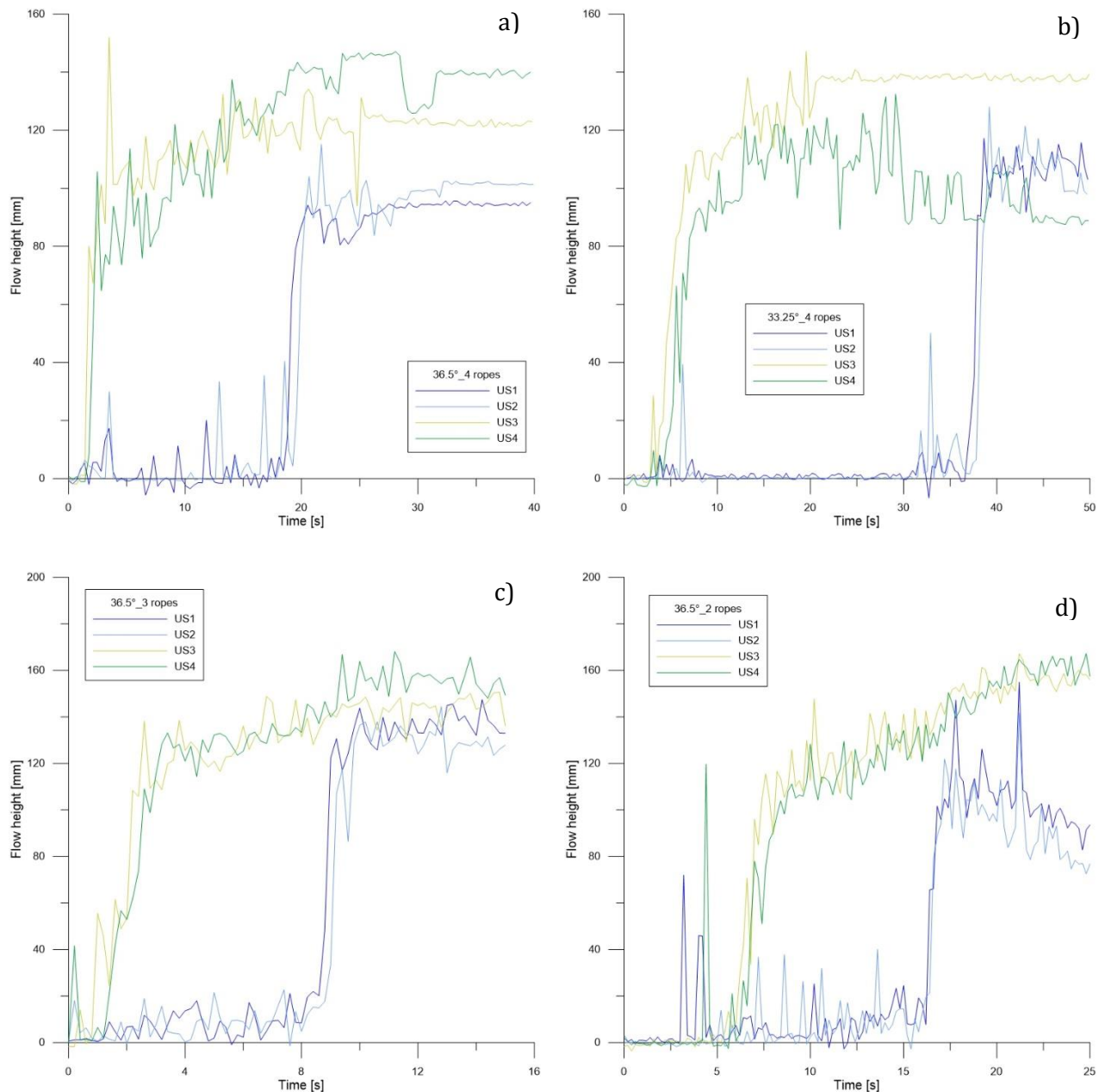
Figure 6.25: Flow thickness values recorded by the ultrasonic gauge; a) Test 1; b) Test 2; c) Test 4 and d) Test 5

In Figure 6.22 graph represented the variation of flow height during the impact, recorded by one of the two sensors located 10 cm upstream the prototype, is reported. The graph shows the trend of the flow height, which increases with time and, more or less 20 second after the first impact, become constant (no more material depositing behind the barrier). Is possible to observe that the final height of the granular material upstream the prototype (Figure 6.23) is lower in the cases n. 1 and 2, characterized by minor channel inclination, respectively equal to 30° and 33.25°; on the contrary, during test n. 3, 4, and 5, where the inclination was of 36.5°, the recorded flow thicknesses were higher (Figure 6.22). Particularly, in case 1 and 2 the thickness of the material deposited along the vertical section 10 cm distant from the barrier is about 13.5

161

cm, for the experiments 3, 4 and 5 it is equal to 17.5 cm. It is also evident that in case 4 and 5 the final flow height is slightly lower than in case 3, in spite of the same channel inclination. This is probably due to the different stiffness of the barrier, which led to a bigger deformation in case 2 and 3, characterized by a minor number of longitudinal ropes; in these cases, the system is able to contain a higher quantity of material thanks to its major deformability, reducing the flow thickness behind the barrier.

Figure 6.24 shows the values recorded by the ultrasonic gauges during test n. 3, characterized by a channel inclination of 36.5° and 4 longitudinal ropes connected along the barrier by the metallic net. The graph highlights the difference between the material thickness trend near the barrier (10 centimeters) and 1 meter far from it: the maximum values are major upstream the prototype, more or less 7 cm higher; the peak is reach more fast in the distant section and the thickness of the accumulated material behind the barrier shows an increasing curve trend. Finally, is possible to note that the data derived from ultrasonic gauges 1 and 2, located in the same transversal section, shows the same behavior in the center of the channel and next to the plexiglass wall; the same occur for gauges 4 and 3. This means that the flow behavior is not influence by the presence of the vertical wall. Similar behavior can be observed for test 1, 2, 4 and 5.

Particle displacement and flow velocity

For PIV technique time interval choice is fundamental: if it is too long the probability of the particles to come out from the laser range, and therefore not be included in the second image, is larger; moreover, there is a loss of information between two images and the speed obtained is not instantaneous but is an average speed. On the other hand, if the interval is too short, the particles displacement is too much small and the disturbances due to the noise and the non-perfect correlation become dominant over the real displacement.

PIV technique, through the acquisition of high resolution images, allows to recognize the individual soil particles and to identify their paths during phenomenon evolution. The simulation gives all the information necessary to characterize the process. The output file restituted by software *PIVview2C* can be obtained according to the required format and the desired quantities; screens are provided with speed and displacement values with the relative text files, which contain all the position P(x, y, z) of the discretization used for simulations (the z values are always null because it is a bi-dimensional simulation).

All the text files returned by the software have been elaborated with *MatLab* and the results were represented by a matrix, where the four columns are the x and y position, speed and time. In particular, two point were considered: one is near the flexible barrier and one is located in the same position of the central altimetric sensor.

Table 6.4: Number of elaborated images for each test

Test ID	N. of ropes [-]	Channel inclination [°]	N. of elaborate images [-]
1	4	30.00	300
2	4	33.25	530
3	4	36.50	/
4	3	36.50	315
5	2	36.50	310
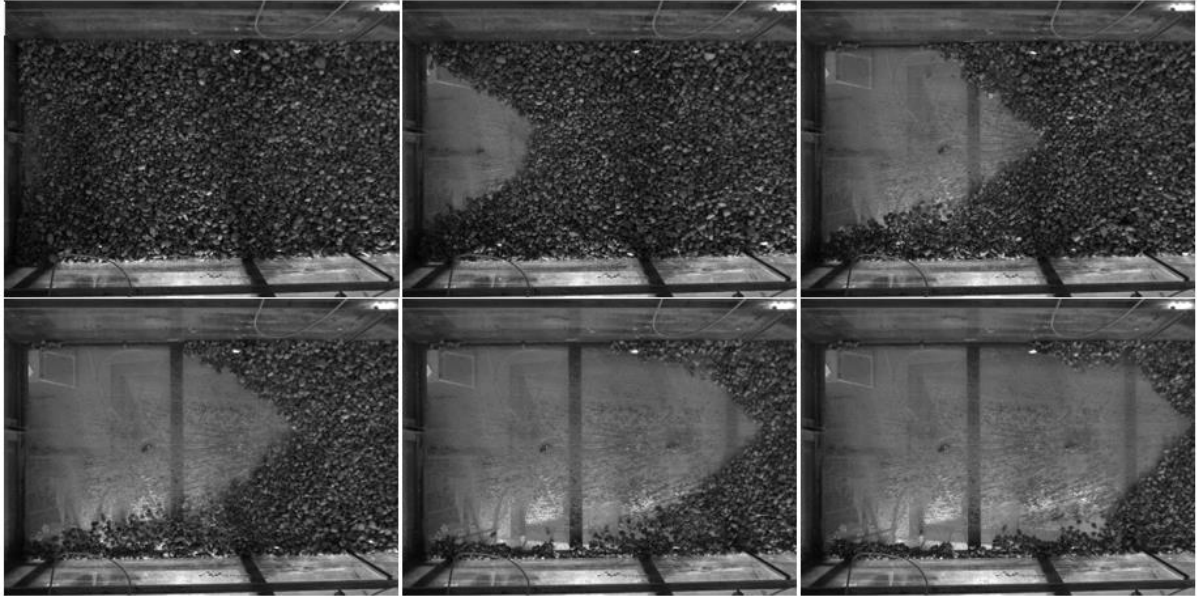
Figure 6.26: Images of trigger phase recorded during experiment n. 3

In Table 6.4 the number of images elaborated for each tests is reported. Unfortunately, simulation N. 2 has not been achieved for camera acquisition technical problems (data have not been saved progressively, therefore it is impossible to set up the simulation). It can be seen that the number of analyzed images is different between the tests, this because the phenomenon occurred with different times. The considered images only concern the phenomenon evolution phase, excluding all the time interval during which the inclination changes but the material is stable (before the trigger). Images simulated with the software are just referred to the propagation channel; results obtained were compared with measurements derived from other instruments installed along the channel. The trigger is induced thanks to gravity action, changing the inclination of the channel upstream section by means of an electric engine. When the equilibrium conditions changed and mass forces prevailed on friction, mass movement occurred. The trigger inclination was the same for each test performed and it was around 40°; for this value the material moved in different steps: before a few particles were separated from the rest of the accumulated material, then successive waves of mass moved in downstream direction.
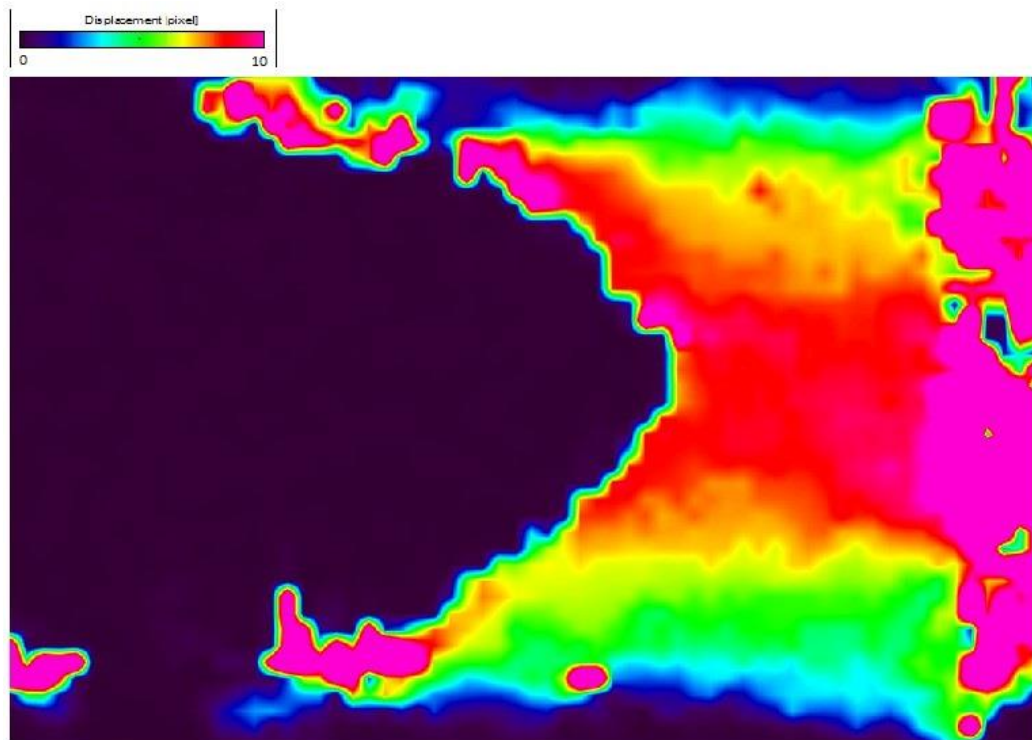
Figure 6.27: Image derived from PIV software elaboration represented mass particles moving during the trigger

In Figure 6.26 images referred to the trigger phase of the test n. 1 are shown. It is evident that all the material accumulated at the end of the channel was mobilized, creating an empty space with semi-elliptical form and maximum axis located at the center of the channel section. No material remained in upstream channel portion at the end of the experiments.

Shape deriving from mass movement are also evident in Figure 6.27, which represents particle displacements along the upstream channel section. From the image is clear that, during the initial phase of the experiments, the displacement of particles locating in the central portion of the mass are higher than side particles ones, generating a semi-elliptical empty space.

Figure 6.28 shows particles movement direction during the initial trigger phase. The majority of mass particles are characterized by displacement along the x coordinate, in the principal channel direction towards prototype installed downstream; on the contrary, some particles located on the boundary or isolated showed chaotic behavior and different movement directions.

During the second phase of the experiment particles reached the downstream portion of the channel, at the end of which is installed the flexible barrier prototype, and then accumulated behind it. In order to elaborate the images deriving from the experiment second phase (called impact phase) a measurement grid 32x32 pixels was used (Figure 6.29). Two sensor were located in the final portion of the channel to lead to a correct images elaboration (Figure 6.29), the first one was positioned around 1 meter far from barrier and the second one was immediately behind it; coordinates of sensor are reported in Table 6.5.
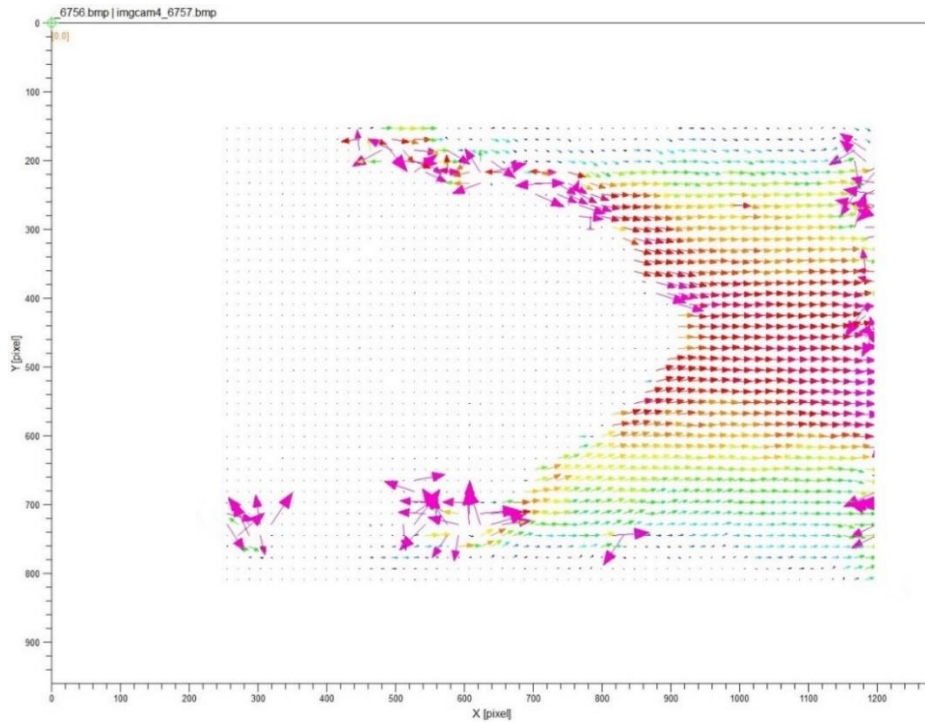
Figure 6.28: Image derived from PIV software represented mass movement direction

Table 6.5: Downstream sensors coordinates

Sensor ID	Location	x	y
S1	1 meter far from barrier	142	465
S2	Behind the barrier	977	465
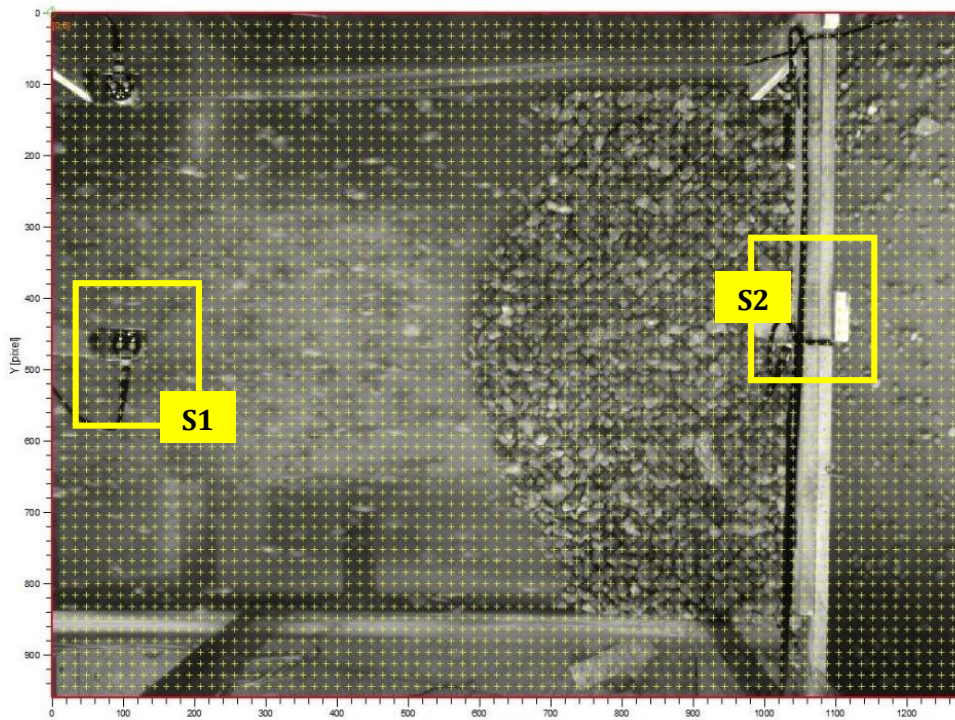
Figure 6.29: Measurement grid used for PIV images elaboration at the end of the channel

The mass behavior observed during the impact phase was the same for all the test performed, independently on the downstream channel inclination: at the first time only few particles reached the barrier, bouncing on it and stopping, then the different mass waves came and deposited behind the prototype (Figure 6.30).

Figure 6.30: Images of the impact phase recorded during experiment n. 3 and elaborated through the dedicated PIV software
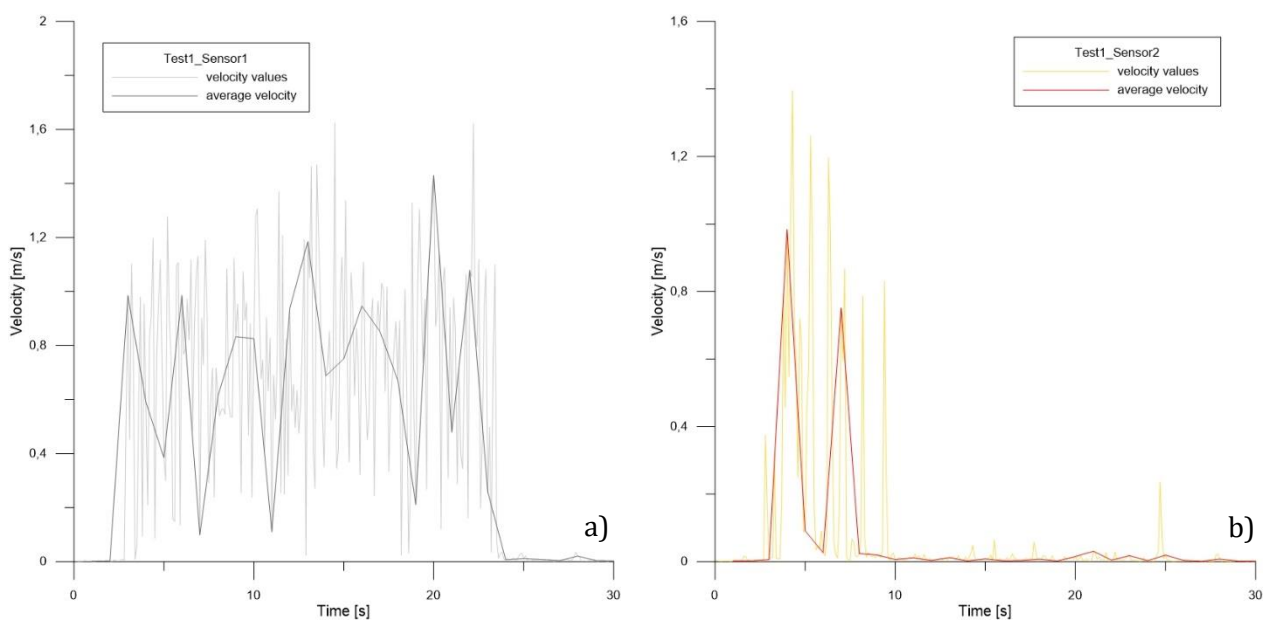
Figure 6.31: Test n. 1 velocity value obtained from PIV software analysis; a) Data deriving from sensor n. 1 one-meter-far from the barrier; b) Data deriving from sensor n. 2 immediately behind the barrier

For each time step velocity values were saved and elaborated. In Figure 6.31, 6.32, 6.33 and 6.34 the trend of the average particle velocity varying with time during the different tests are shown; data deriving from sensor n. 1 are represented in gray and in red are reported data obtained from the elaboration of the sensor n. 2 images. Velocities deriving from sensor n. 1 are higher than velocities obtained from sensor n. 2; this means that particles 1 meter far from the barrier move faster than particles at the end of the channel.
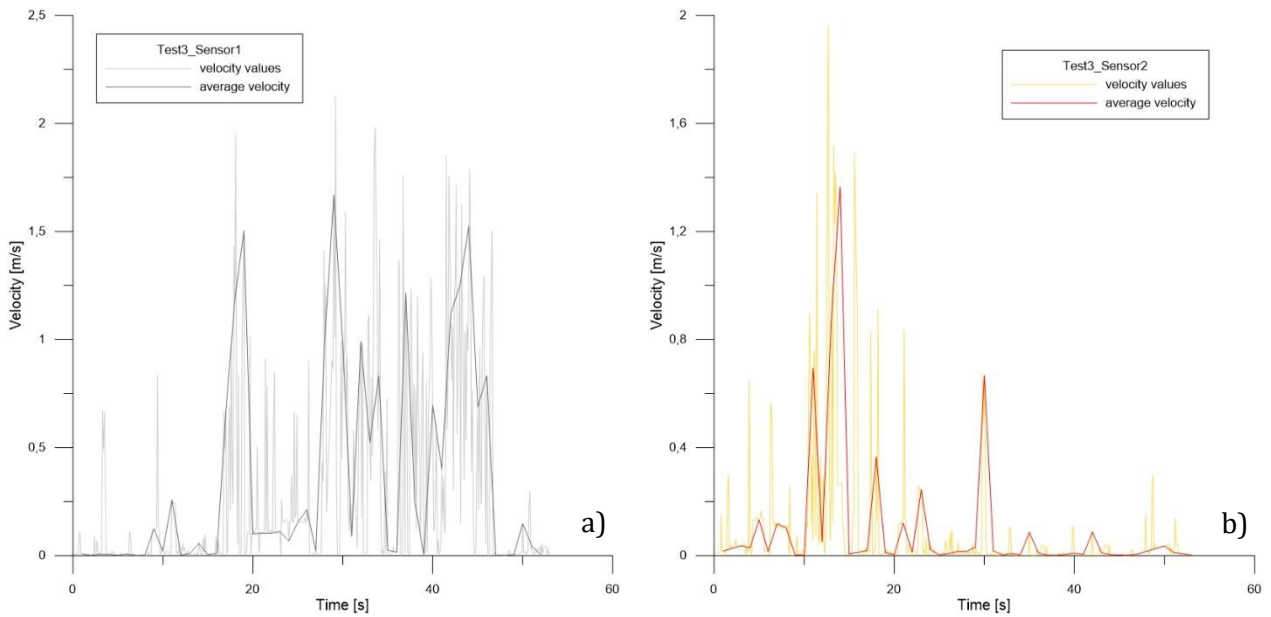
Figure 6.32: Test n. 3 velocity value obtained from PIV software analysis; a) Data deriving from sensor n. 1 one-meter-far from the barrier; b) Data deriving from sensor n. 2 immediately behind the barrier
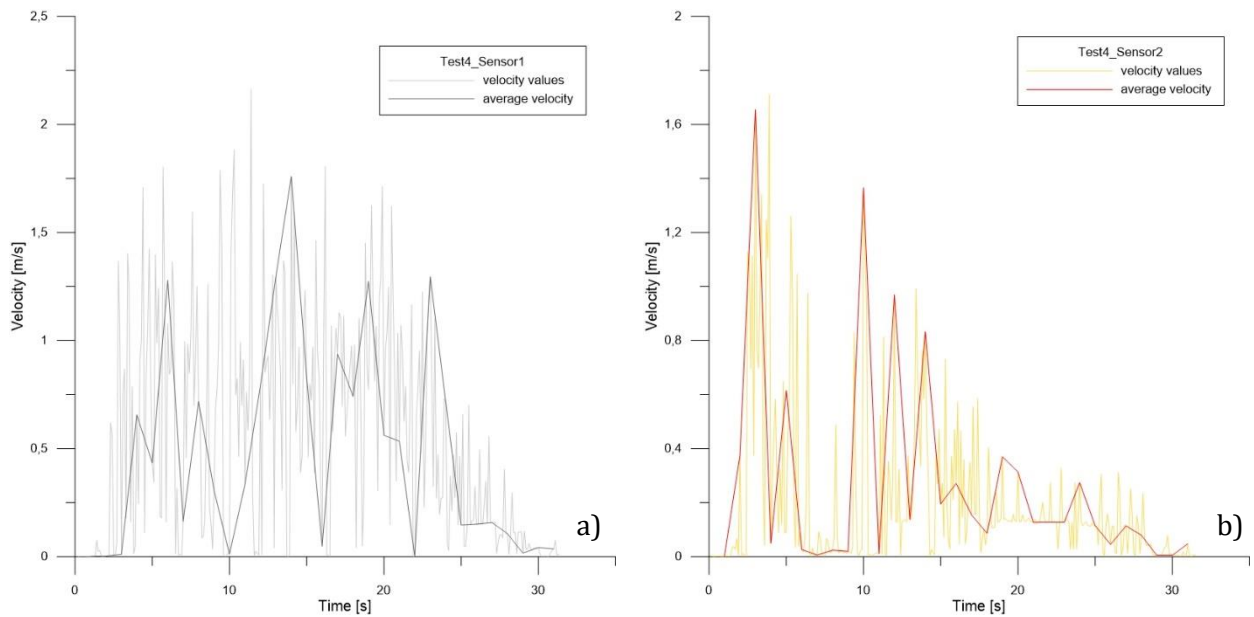
Figure 6.33: Test n. 4 velocity value obtained from PIV software analysis; a) Data deriving from sensor n. 1 one-meter-far from the barrier; b) Data deriving from sensor n. 2 immediately behind the barrier
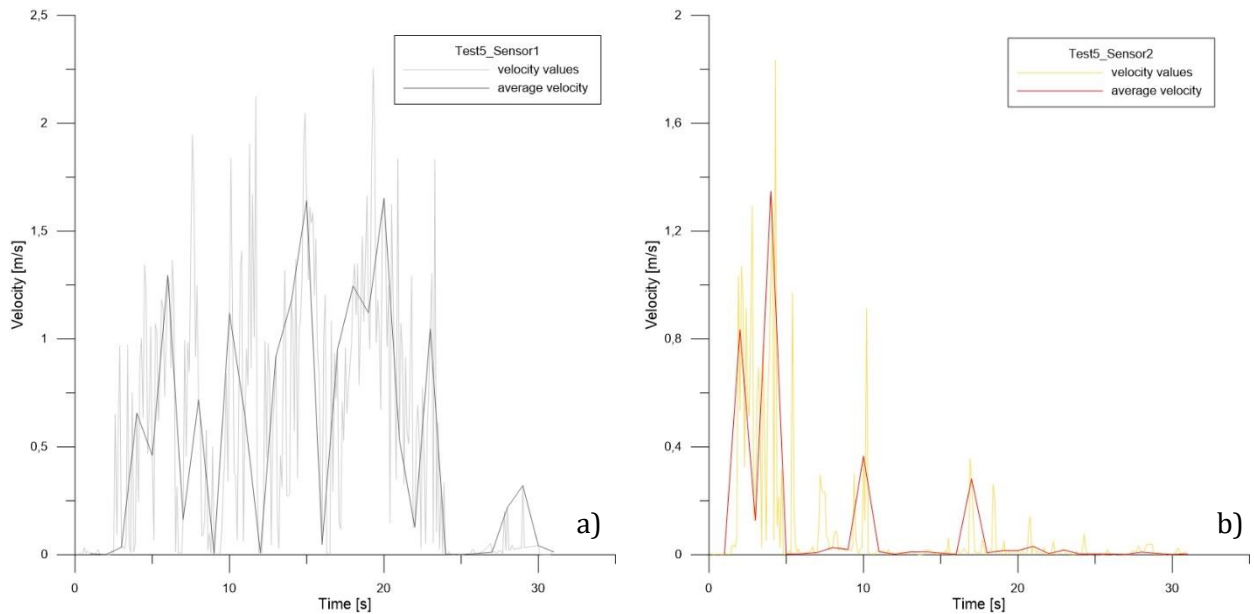
Figure 6.34: Test n. 5 velocity value obtained from PIV software analysis; a) Data deriving from sensor n. 1 one-meter-far from the barrier; b) Data deriving from sensor n. 2 immediately behind the barrier

This fact is probably due to the high trigger inclination of the upstream channel portion, which was more or less 40°; when the inclination decrease in the downstream channel section (30°, 33.25° or 36.5°), the velocity progressively decreases with it.

Comparing data from different tests is possible to observe that velocity in the downstream section is lower for test n. 1 (maximum average velocity 1 m/s), which was characterized by an inclination of 30°, than in tests n. 3, 4 and 5, with an inclination of 36.5°. Velocities behind the barrier show some local peak at the beginning of the impact phase and become null after 10÷20 seconds; the cause is that, after that time interval, the accumulated material under the sensor n. 2 reached its stable configuration. The same thing happened 1 meter far from the barrier, after 30÷40 seconds.

Loads

During experiments loads were measured with load cells (the same used for r function calibration laboratory tests and described in previous paragraphs) installed on the left side of the barrier prototype; data were recorded continuously with frequency of 1000 Hz thanks to *National Instruments Compact DAQ 9174* acquisition unit.

Each longitudinal rope was connected with one load cell by means of eye bolts and clips closing the rope loops (Figure 6.35). Load cells position and the corresponding connected ropes are shown in Table 6.6.
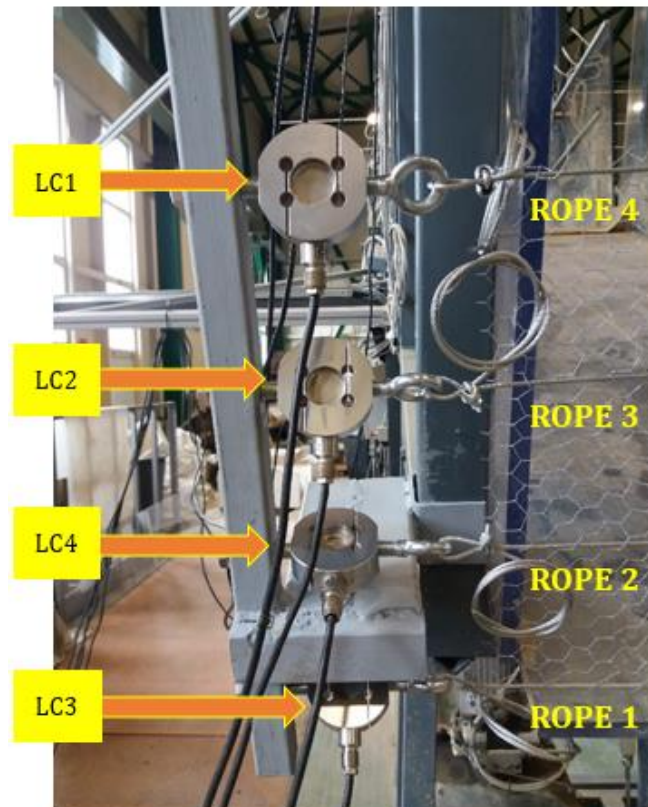
Figure 6.35: Load cells connection and identification for tests n. 1, 2 and 3, characterized by 4 longitudinal ropes

Table 6.6: Load cell position and test configuration

	Rope ID	Rope position	Load cell	Load cell capacity
TEST 1, 2, 3	1	Lower	LC3	200 kg
	2	Lower-intermediate	LC4	200 kg
	3	Upper-intermediate	LC2	100 kg
	4	Upper	LC1	100 kg
TEST 4	1	Lower	LC3	200 kg
	2	Intermediate	LC4	200 kg
	3	Upper	LC1	100 kg
TEST 5	1	Lower	LC3	200 kg
	2	Upper	LC1	100 kg

Results obtained from experiments are reported in Figure 6.36 and in Figure 6.37. In the cases of 4 longitudinal ropes (tests n. 1, 2 and 3) the higher load transferred to the steel cables by the impacted mass was registered along rope n. 2, which is the lower-intermediate one.

Particularly, the difference between the force acting on rope n. 2 and the others is very evident for channel inclination equal to 36.5° (31.98 kg, see Figure 6.36). In all these three cases the observed forces in the upper rope were approximately zero. During experiment n. 3, which was characterized by barrier with 3 longitudinal ropes, the lower cable was the most loaded; however, forces values of the upper cable are not negligible (Figure 6.37c).
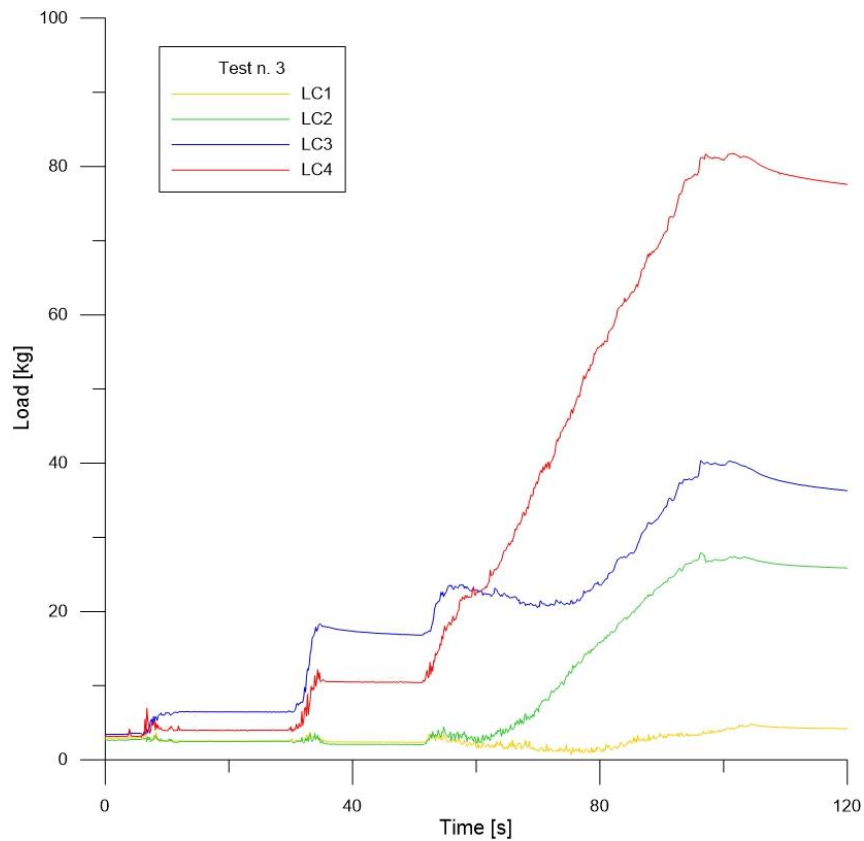
Figure 6.36: Load-time graph deriving from test n. 3 data elaboration (barrier prototype with 4 longitudinal ropes and channel inclination 36.5°)

When barrier had only two ropes connected by metallic net, loads acting on them are comparable and the gap observed during the previous experiments is not present (Figure 6.37d).

For channel inclination equal to 33.25° and 36.25° (test n. 2, 3, 4 and 5) the mass reached the barrier by steps (different material waves occurred), this generate a steps trend in load-time graphs, where the load increasing is very clear. This did not happen during the first experiment because, due to the lower channel inclination, the material continuously stopped along the downstream section and reached the barrier only when the residual mass push down the still particles, leading the entire mass to impact the prototype as one single flow (Figure 6.37a).

At the beginning of each test ropes were pre-tensioned applying an initial force between 2.28 and 3.67 kg. All peak values (local and absolute) are locating at the same position in load-time graphs, it means that impacts on different ropes occurred at the same time. Analyzing values reported in Table 6.7 is possible to observe that the higher load was 104.91 kg and it was

recorded during test n. 4 in the lower rope. The less critic situation is the first one, characterized by the minor channel inclination of 30° and 4 longitudinal ropes; in this case the maximum load value was 53.18 kg and it was registered for the lower-intermediate rope.
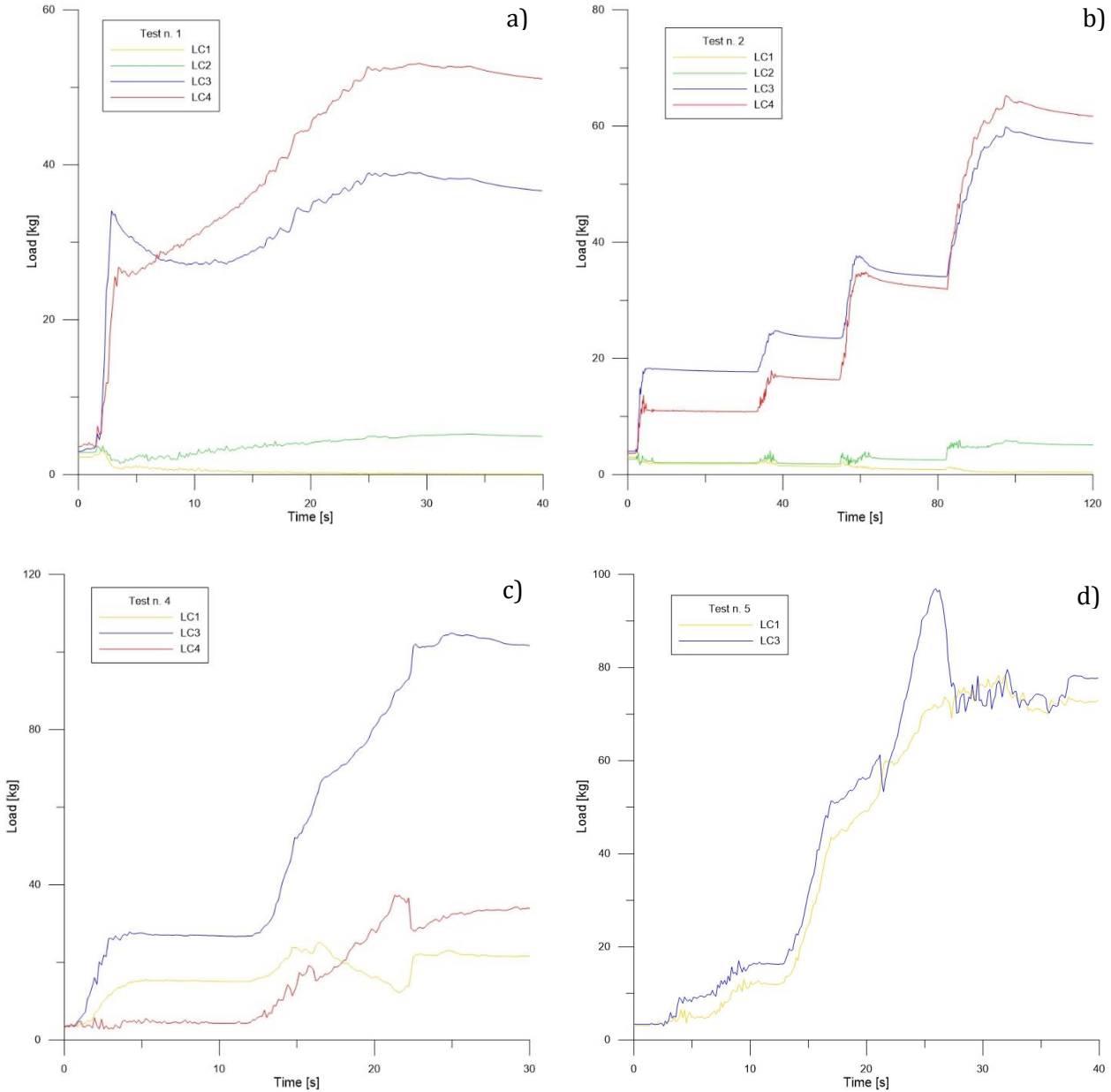
Figure 6.37: Load-time graphs deriving from the elaboration of data recorded with load cells;; a) Test 1; b) Test 2; c) Test 4 and d) Test 5

Maximum force entities increase with channel inclination; for the same inclination (36.5° in test n. 3, 4 and 5) the situation with 4 longitudinal ropes (test n. 3) is more equilibrated than the others, because load is better distributed and the maximum force value is 81.86 kg in lower-intermediate rope. For tests n. 4 and 5 maximum load were significantly higher, 104.91 kg and 96.94 kg respectively.

Table 6.7: Initial tension gave to different ropes at the beginning of each test and maximum loads recorded

	Rope ID	Rope position	Load cell	Initial tension [kg]	Maximum load [kg]
TEST 1	1	Lower	LC3	3.63	39.05
	2	Lower-intermediate	LC4	2.99	53.18
	3	Upper-intermediate	LC2	2.87	5.26
	4	Upper	LC1	2.28	3.48
TEST 2	1	Lower	LC3	3.52	57.90
	2	Lower-intermediate	LC4	3.67	65.41
	3	Upper-intermediate	LC2	2.68	6.12
	4	Upper	LC1	2.99	3.28
TEST 3	1	Lower	LC3	3.44	40.39
	2	Lower-intermediate	LC4	3.18	81.86
	3	Upper-intermediate	LC2	2.66	27.96
	4	Upper	LC1	2.93	4.95
TEST 4	1	Lower	LC3	3.26	104.91
	2	Intermediate	LC4	3.30	37.75
	3	Upper	LC1	3.10	25.45
TEST 5	1	Lower	LC3	3.34	96.94
	2	Upper	LC1	3.08	78.75

In Figure 6.38 the sum of maximum forces on single ropes during each test are shown; it is evident that maximum loads acting on barrier increase with channel inclination. For 30° (test n. 1) sum of maximum loads is equal to 97.34 kg, this value for 33.25° is 131.54 kg (test n. 2) and increase again for 36.5°, becoming 153.72 kg distributed in 4 ropes (test n. 3), 160.49 kg shared between 3 ropes (test n. 4) and 168.80 kg on two ropes (test n. 5). Finally, is possible to affirm that the situation generated from test n. 5, with only two longitudinal ropes and channel inclination equal to 36.5°, is the most critical one.

6.4.6. Numerical model validation

Laboratory tests described in the previous paragraph were carried out in order to assess the numerical model reliability. For this purpose, the values recorded by load cells during the

experiment were compared with forces calculated by the analytical model implemented by Brighenti et al. (2013), which was designed to describe loads acting on the barrier.
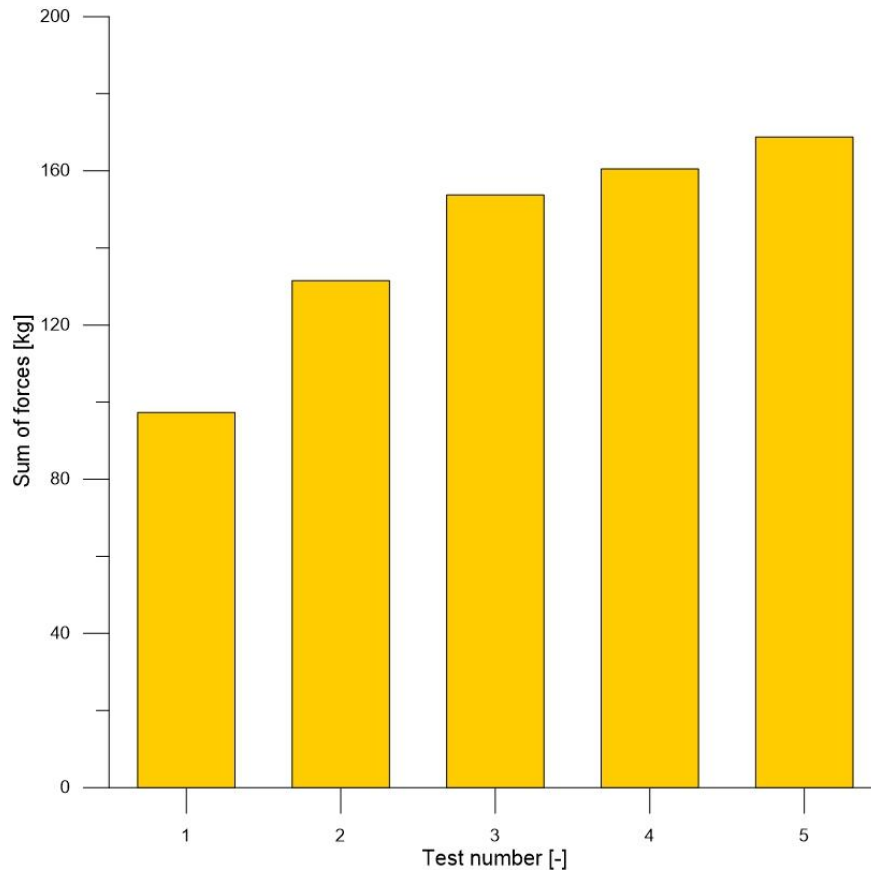
Figure 6.38: Sum of maximum forces acting on barrier ropes during each test

The input parameters, concerning both barrier construction and site characteristics, are shown in Table 6.8; the values assigned to the empirical coefficient α and to the earth pressure coefficient k were determined considering the indications available in literature.

The exponent mji of functions $r(zj, zi)$, which represents the influence that one loaded cable has on the others, was calculated according to the GA method described in Brighenti et al. (2013). Brake elements features were not considered in the present analysis, because the scaled barrier prototype did not include them (i.e. the energy dissipation due to the deformation of brake devices was zero).

A comparison between results obtained from the numerical model and data recorded during the experiment, in terms of induced tensions in longitudinal ropes during time, is shown in Figure 6.39, 6.40 and 6.41 for tests characterized by channel inclination equal to 36.5° and different number of ropes (respectively experiments n. 3, 4 and 5). The loads measured in each ropes are plotted against time, together with data deriving from the analytical model (Figure 6.39, Figure 6.40 and Figure 6.41).

Table 6.8: List of input parameters insert in the numerical model for the calculation of forces acting on the barrier

	Parameter	Value	Origin
	NUMERICAL MODEL INPUT DATA		
	Parameter	Value	Origin
BARRIER	Height	0.36 m	Prototype construction
	N. of ropes	Depending on the test	Prototype construction
	Rope diameter	3 mm	Prototype construction
	Rope distance	Depending on the test	Prototype construction
	Rope elastic module E	2.1e11	Prototype construction
	Rope length	1 m	Prototype construction
	Brake activation energy	Not considered	Prototype construction
	Brake maximum elongation	Not considered	Prototype construction
	r function	$r(a = 0.6 \times e - 7)$	From GA
FLOW AND CHANNEL	Flow impact height h_0	Depending on the test	Ultrasonic gauges
	Flow impact velocity v_0	Depending on the test	PIV technique
	Flow density	1500 kg/m^3	Literature
	α coefficient	1.0	Literature
	Earth pressure coefficient k	0.5	Literature
	Acceleration of gravity	9.81	Literature
	Channel inclination	Depending on the test	Test configuration
	Friction coefficient	0.8	Literature

Graphs show the good agreement between data obtained from the experiments and the results of the analytical model. Particularly, for test n. 3 (Figure 6.39), tension in the lower-intermediate cable n. 2 (the higher one) calculated by the program is very close to the real one measured by load cell n. 3; also the peak time is quite the same (100 s) with the only difference that in the model load starts to increase about 10 seconds before in time. Load in lower and upper-intermediate ropes are slightly overestimated; also for these ropes, the load increase occurs before in time and the peak is shortly early. The forces in the upper rope calculated by the program, as in the real setting, are negligible.

Also for test n. 4, characterized by four longitudinal ropes, results returned by the program are in good agreement with load cells values. Load acting on rope n. 2 (the lower one) calculated by the analytical model is very close to the real one, but in this case the forces increasing and the maximum peak are late in time (about 10 seconds). Load acting on rope n. 1 (the lower one) returned by the numerical model is about 13 kg higher than the real one measured with load

cell. On the contrary force acting on the upper cable is slightly late (the peak at 15 s is missing) and underestimate by 5 kg.
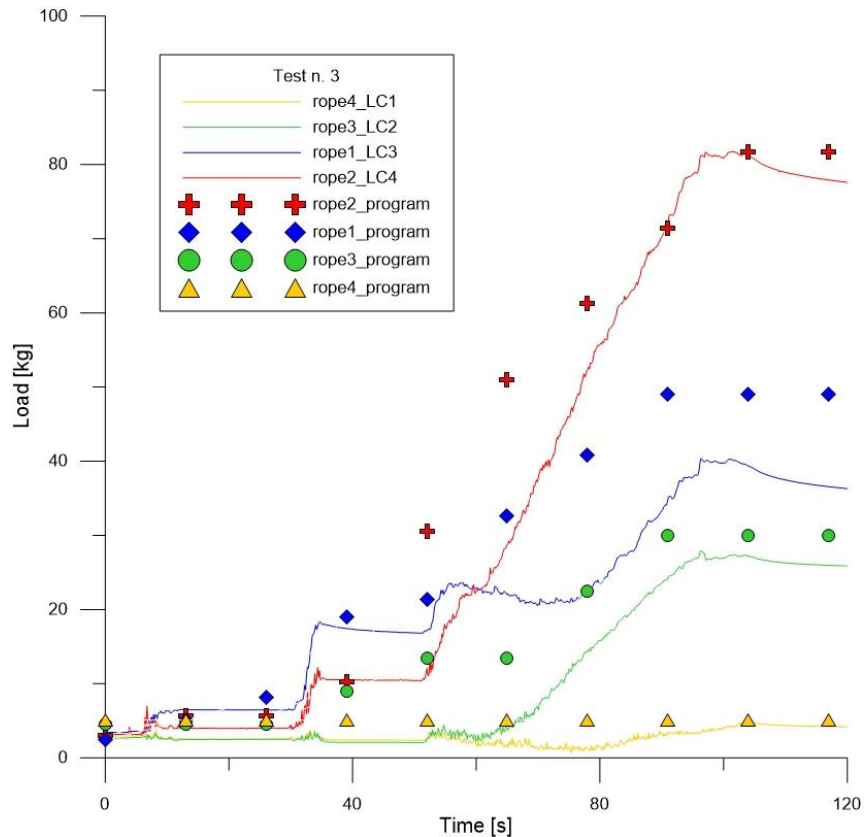
Figure 6.39: Comparison between load value deriving from numerical program and load cell measurements for test n. 3

Finally, the program analysis conducted on test n. 5 (in which the barrier had only two longitudinal cable) shows load trends very similar to the reality (Figure 6.41); force increasing and final tension on rope is almost equal. The main difference is that the peak registered for the lower cable n. 1 by load cell n. 3, occurred at 25 s, is not present.

An overall analysis of the graphs highlights that the numerical model returned load trend during time very similar to reality: maximum tension values are closed to the real ones measured during the experiments at debris end; final loads are generally slightly overestimated but in some cases peak values are missing (test n. 5 – rope 1 – 25 s). This means that the numerical model gives a very good interpretation of the scaled phenomena, but it returns always an increasing trend of load with time, missing some local peaks which characterized the real behavior of the impacted barrier. However, these peaks are lower than the maximum load values returned by the program, except for in the last case (test n. 5) where the load of rope n. 1 is approximately underestimated by 25 kg.
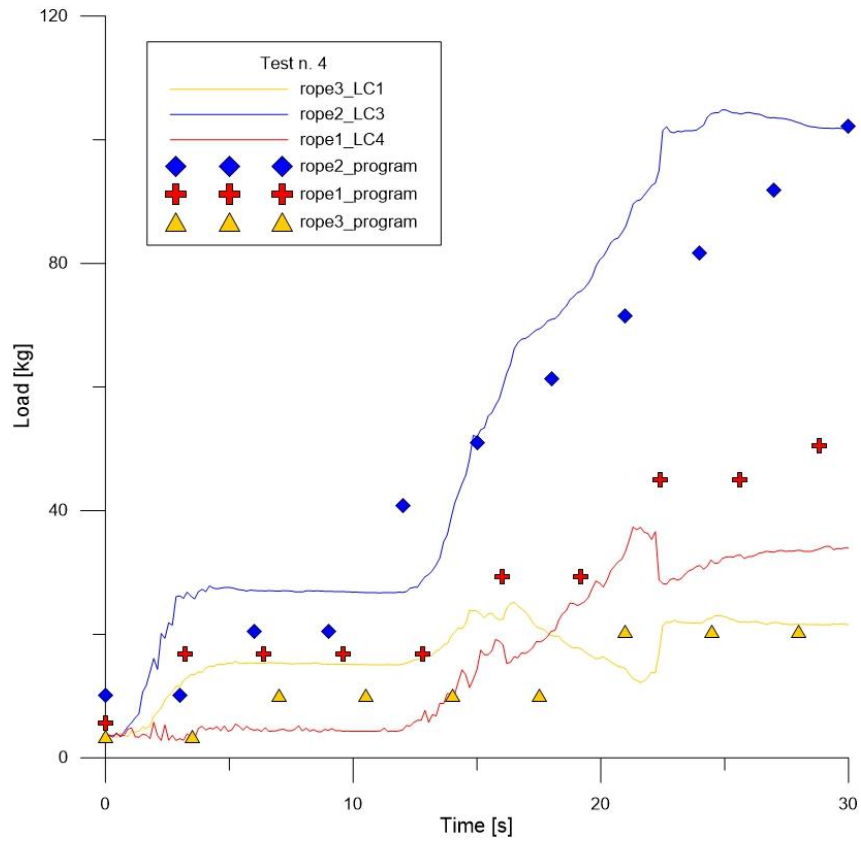
Figure 6.40: Comparison between load value deriving from numerical program and load cell measurements for test n. 4
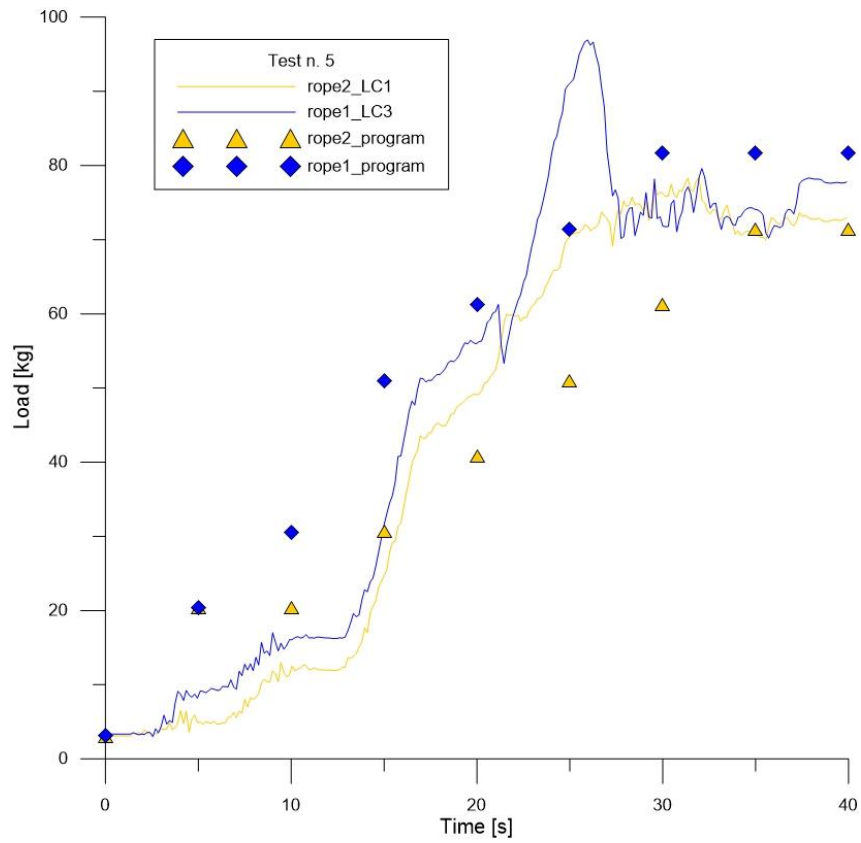
Figure 6.41: Comparison between load value deriving from numerical program and load cell measurements for test n. 5

Chapter 7: Monitoring system implementation

7.1. Motivation and objectives

Hydrogeological instability is a very tangible problem, in Italy as all over the world, because of the impact on the population, urban structures and economic-productive sector. Natural disasters are an example of socio-economic development in contrast with environment; in fact, there are many tragic evident connections between natural processes, land use and urban planning. In our country the intense urbanization, which took place after the Second World War without a real evaluation of the area potentially exposed to hydrogeological risk, led to a large increase of exposed and vulnerable elements. In addition, climate changes generate the probability of occurrence of unpredictable and extreme weather events and, consequently, of dangerous and destructive phenomena.

Frequently protection barriers are installed in mountainous region, in very impervious areas difficult to reach; at this conditions, it is very difficult for the authorities to check regularly the effective structures good-functioning or the presence of some damages due to impact events occurred. For these reasons protection systems assume an ever more important role in territory risk management and they must guarantee both of high structural performances and reliability over time.

The aim of the present work is the development of an innovative monitoring technology for flexible barriers structural behavior control. This system gives important information about the status of protection of the structures after their installation on site, checking the effective rate of work and the residual tension acting on barrier components and highlighting critical situations in progress. Moreover, a widespread installation of these system in unstable slopes will give indications about large scale phenomenon occurrence and will generate an important data base for a better territory risk mapping and management; thanks to data deriving from barriers monitoring, slopes can be mapped basing on space-time distribution of risk indicators, allowing statistical elaborations and the implementation of forecast models calibrated with updated data obtained from instrumented barriers. The improved data base will represent an important tool for public body, for choose where and when finance stabilization/maintenance interventions and for the implementation of rapid alarm system, taking into account precipitation phenomena and meteorological parameters.

Therefore, the instrumented barriers play a double role: firstly, they are passive-protection systems against natural rapid events like rockfall and debris flow, secondly they provide information about their efficiency over time and indicate the presence of some instability phenomenon in progress.

Summarizing, the main advantages that the implementation of the monitoring system gives to existing protection barriers are the following:

a) Remote control of the structures good-functioning and of their rate of work after over time, without the necessity of operator periodic control in uncomfortable installation areas, saving time and money;

b) Warning of any critical situation which compromises the barriers efficiency and make necessary extraordinary maintenance, repairing or evacuation interventions;

c) Creation of a data base which provides indication about phenomena occurrence in unstable slopes and generation of continuously updated territory maps, based on risk parameters space-time distribution.

7.2. System general features

7.2.1. Principal components

The monitoring system, from now on called Rockfall Safety Network, is design to be easily integrated in different types of flexible barriers and has two principal functions:

1) Evaluate the barrier working level;

2) Individuate the unstable slope areas.

Figure 7.1: Post head detail, where the monitoring modules are positioned

The system can detect both strong intensity events, identified as a steel post rotation and/or a brake deformation, and low intensity ones, recognizable by an increasing load acting on the upstream cables. The data deriving from monitoring processes gives important indications about rapid mass movements, even of modest entity, which involves the barriers.

The Rockfall Safety Network consists of a data acquisition unit which is connected with different modules, called BPM, located near the steel post heads (Figure 7.1). The data acquisition unit is composed by:

a) ASE801 datalogger (Figure 7.2), which is the mind of the system and organizes the operations of acquisition, data transmission and radio devices management. It queries all the devices installed on barriers with a frequency defined by customers that can be easily changed during the monitory activity;

b) Photovoltaic panel and charge regulator that guarantee the continuous and autonomous alimentation of the acquisition system. The size of the solar panel depends on site, solar radiation and instrumentation sampling time;

c) UMTS router for data transfer to the calculation center;

d) Radio Master device for the connection between BPM modules and the datalogger.

Figure 7.2: Datalogger integrated in Rockfall Safety Network System

7.2.2. BPM modules

BPM modules are designed to measure physical significant parameter which identify the working rate of the flexible barrier; they consist of the following different elements:

a) Electronic card for sensor recording and management;

b) MEMS sensor able to measure the three components of magnetic and gravitational fields, which allows to monitoring the inclination of the posts. MEMS also includes temperature sensor to correct temperature changes effects on measurements; Technical features of MEMS sensor are reported in Table 7.6.

c) Electrolytic cells, which has to obtain redundant data about post inclinations. The double measurement of the same physical quantity allows the validation of the MEMS recorded data. This sensor has a higher sensitivity than MEMS accelerometer and is able to measure

minimal inclination variations (with resolution of one thousandth of degree). Technical features of electrolytic sensor are illustrated in Table 7.7;

d) Load cell made of 39NiCrMo3 steel, installed on the upstream cable, designed to measure the traction loads acting on steel rope connected with post head. This device allows to obtain information about the tension trend during the barrier working life and it is installed between the post head and the upstream cable by means of shackles;

e) Radio Gdata device, necessary for the connection between the single monitoring BPM modules and the datalogger;

f) Lithium batteries for the single BPM modules alimentation and metallic box to protect all the electronic module components.

7.2.3. Barrier integration

The daily comparison between data deriving from installed monitoring devices allows to individuate any phenomena impacting on protection structures. Moreover, the analysis of the information derived from different instrumented barriers located in the same slope will generate a GIS territory danger maps, very useful for natural risk management.

Generally, the Rockfall Safety Network installations are characterized by the presence of one BPM module every 20 meter along the barrier length (i.e. one out two post is instrumented with the monitoring module); this configuration allows to obtain information about the rate of work of barrier along its entire extension (Figure 7.3).
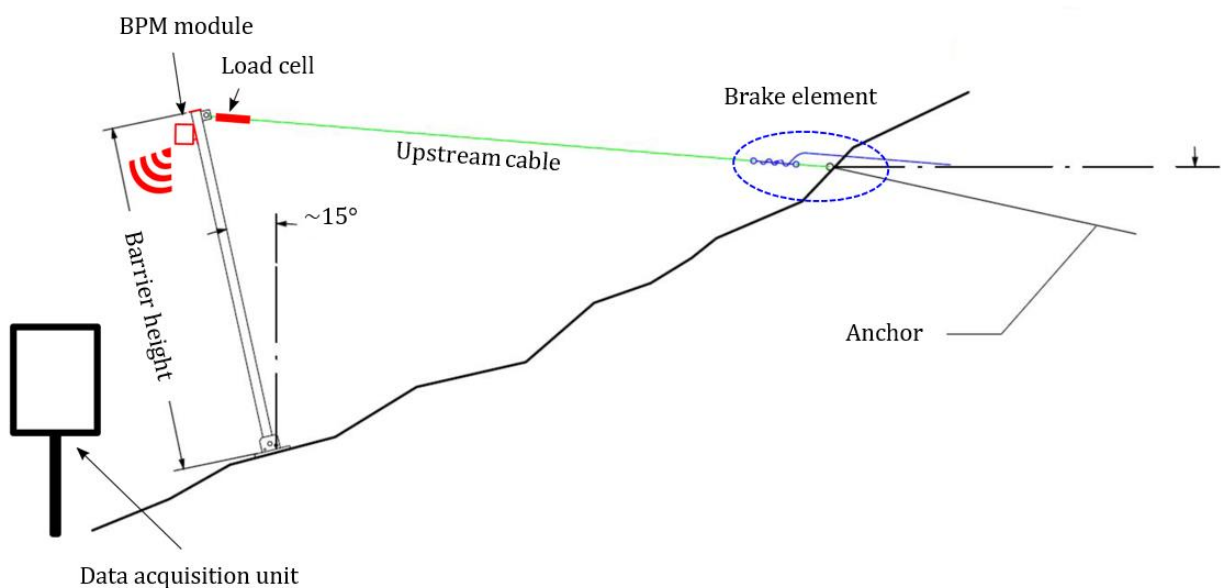
Figure 7.3: Typical installation of Rockfall Safety Network on flexible protection barriers and system main components

7.3. Hardware development

BPM modules are the Rockfall Safety Network heart and they are designed to guarantee an efficient and complete monitoring service and high performances in terms of reliability. In this paragraph, the main components of monitoring BPM modules are described; in particular, the designed processes of load cells and inclinometer sensors are illustrated and technical choices are motivated.

7.3.1. Load cell

A load cell is a transducer device which is commonly used to generate an electrical signal characterized by a magnitude directly proportional to the measured applied force.

Many types of load cell exist, the choice of which one use depend on the application and the monitoring needs, their designs can be distinguished on the base of the type of the produced output signal; a brief description of the three principal load cell categories is reported below:

– Strain gauge load cells:

strain gauge is a planar resistor, which deforms when the material of which the load cells is composed deforms too (Figure 7.4). The deformation of the gauge changes its electrical resistance, by a value directly proportional to the applied force.
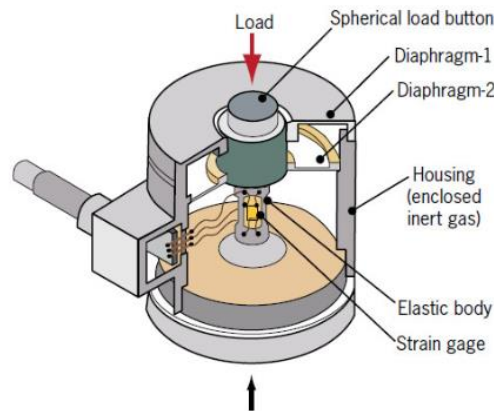
Figure 7.4: Typical strain gauge load cell configuration (from www. teskan.com)

These devices are characterized by very good resonance values, high stiff and long life cycles in application, for this reason they represent the most common type in the field of industrial applications. Strain gauge load cells are generally accurate within 0.03 to 0.25% and are often used for experimental stress analysis and electrical measurement of resistance to strain;

– Hydraulic load cells:

hydraulic cells are force -balance devices, their functioning consists in measure weight as a change in pressure of the internal filling fluid (Figure 7.5). In a rolling diaphragm type

181

hydraulic load cell, a load or force acting on a loading head is transferred to a piston that in turn compresses a filling fluid confined within an elastomeric diaphragm chamber. As force increases, the pressure of the hydraulic fluid rises. This pressure can be locally indicated or transmitted for remote indication or control.

Output is linear and relatively unaffected by the amount of the filling fluid or by its temperature. If the load cells have been properly installed and calibrated, accuracy can be within 0.25% full scale or better, acceptable for most process weighing applications.

An important advantage of this kind of sensor is that it has no electric components, for this reason it is ideal for use in dangerous and difficult areas. Typical examples of hydraulic load cell applications include tank, bin, and hopper weighing.

A disadvantage of this technology is that it is more expensive than other types of available load cells and cannot compete on market. Nevertheless, when the test site is in a remote location, this is the most applicable load cell type because the power supply is not needed;
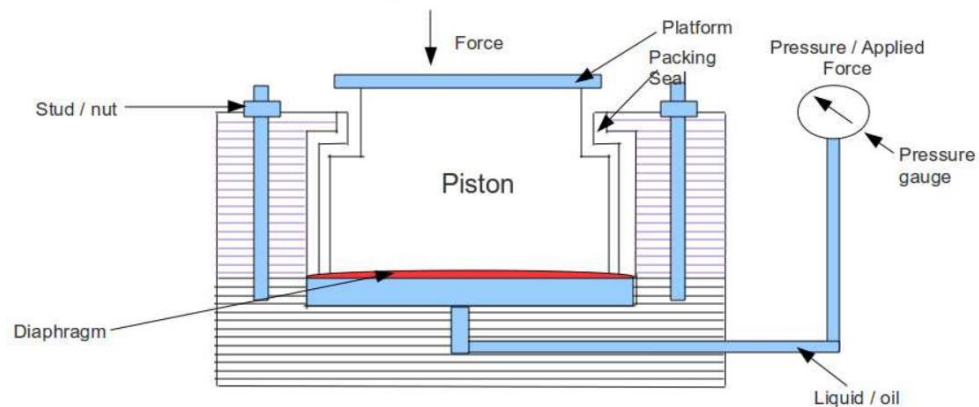
Figure 7.5: Hydraulic load cell working mechanism (from www. instrumentationandcontrollers.com)

– Pneumatic load cells:

like hydraulic load cells also the pneumatic type functioning is based on the force-balance theory. These devices consist of multiple dampener chambers in order to reach higher accuracy than the hydraulic one (usually the first dampener chamber is used as a weight calibration section). Due to their high precision, pneumatic load cells are generally used to quantify relatively small weights.

The pneumatic load cells main advantages are their being inherently explosion proof and the effective independence from temperature variations. Moreover, differently from hydraulic devices, they don't contain fluids that might compromise the process in the case of diaphragm ruptures.

Disadvantages include the relatively slow response time and the need of regular maintenance works (clean operations, dry, regulated air or nitrogen);

– Piezoelectric load cells:

the piezoelectric load cells are based on the same functioning concept of the strain gauge ones; the only difference is that the voltage output (whose magnitude is proportional to the cell deformation) is provided by a basic piezoelectric material.

Typical applications of piezoelectric load cells include the dynamic or frequent loading conditions, where strain gauge load cells can fail with high dynamic loading cycles.

For Rockfall Safety Network strain gauge load cells, which convert the load acting on them into electrical signals, were specifically designed. Strain gauge technology is very suitable for flexible barrier monitoring application, due especially to its accuracy and lower unit cost.

Resistance circuit design

Strain gauge load cells usually consist of a spring element on which strain gauges have been placed. This element is generally made of steel or aluminum, that means it is very sturdy, but also minimally elastic.

When a force is applied to a steel element it slightly deforms, but then returns to its starting position, with an elastic response as a consequence of every imposed stress. As already described, these very small deformations can be detected with strain gauges and then interpreted by electronic analysis in order to calculate the applied load.

The intended load for a load cell is always aligned in the direction of the center of the earth, in other words in the direction of gravity. Only that force component of the load should be acquired. That is not the case for force sensors, which are similar in design, and are also frequently specified as load cells: they are usually designed to acquire loads that occur in all directions. The direction of the earth's gravitational force is not relevant to how they are installed.

Four types of available strain gauge load cells can be distinguished for different applications (www.hbm.com):

a) Compression/traction force load cells: several high-capacity load cells are positioned under/on a steel structure that is loaded with a weight from above;

b) Bending beam load cells: several load cells are positioned under a steel structure and are loaded with a weight from above;

c) Single point load cells: a load cell is located under a platform that is loaded with a weight from above;

d) Tensile load cells: a weight is suspended from one or more load cells.

In Rockfall Safety Network monitoring system load cells are designed to measure the traction forces acting between the post head and the upstream cable, for this reason they belong to the traction load cells category (Figure 7.6a).
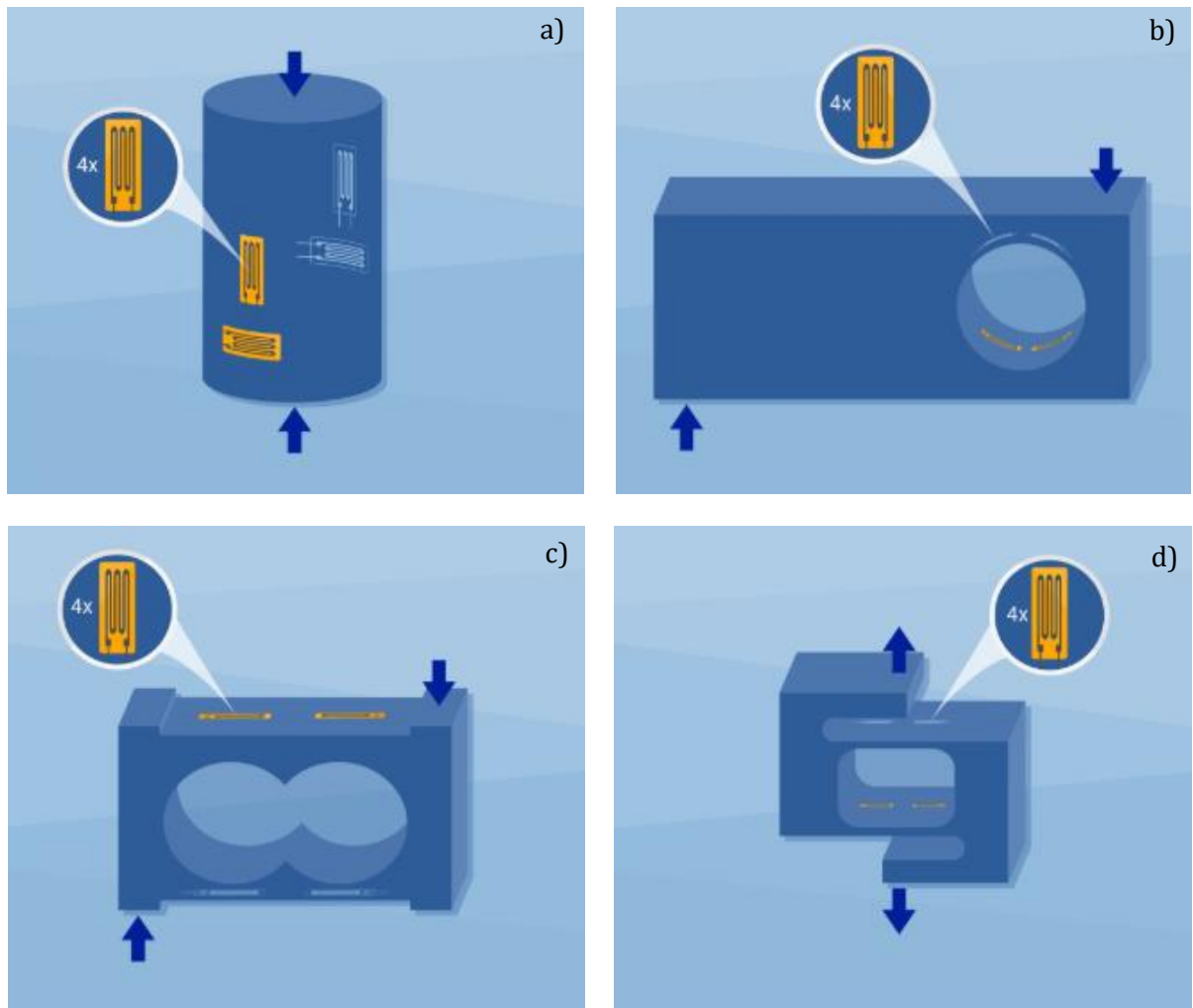
Figure 7.6: Examples of different load cell types (from www.hbm.com); a) Compression/traction force load cell; b) Bending beam load cell; c) Single point load cell and d) Tensile load cell

Strain gauges are arranged in what is called a Wheatstone bridge circuit. This particular configuration is characterized by four strain gauges connected in a ring.

The resistance measurements can be divided into three types; basing on the resistance magnitude is possible to distinguish:

- low resistance measurement;
- medium resistance measurement;
- high resistance measurement.

The Wheatstone Bridge circuit is design to measure very low resistance values, which ranges from a few milliohms to micro ohms.

The Wheatstone bridge consists of two simple series-parallel arrangements of resistances connected between a voltage supply terminal and ground producing zero voltage difference between the two parallel branches when balanced.

A Wheatstone bridge circuit has two input terminals and two output terminals consisting of four resistors configured in a diamond-like arrangement (Figure 7.7): R_x represents the unknown resistance to measure; R_1, R_2, and R_3 are referred to resistor of know resistance, in particular the resistance of R_2 is defined adjustable. The resistance R_2 is adjusted until the bridge is balanced and no current flows through the galvanometer. Then the voltage between the two midpoints B and D will be zero. Therefore, the ratio of the two resistances in the known tract $R_1 - R_2$ is equal to the ratio of the two in the unknown tract $R_x - R_3$.
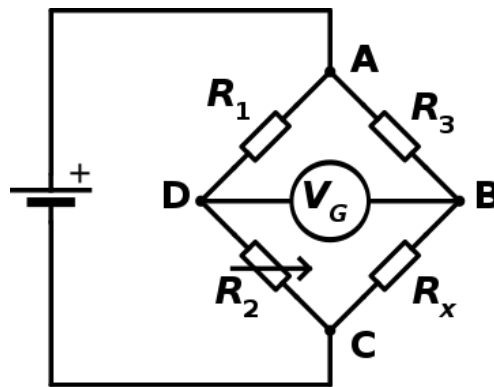
Figure 7.7: Scheme of Wheatstone bridge resistance circuit

If the bridge is not balanced, the current flow direction indicates if R_2 is too high or too low. At the balance point the following relation is verified:

$$\frac{R_2}{R_1} = \frac{R_x}{R_3} \tag{7.1}$$

The Wheatstone bridge equation required to give the value of the unknown resistance R_x, which at the balance point can be calculate as described below:

$$V_{out} = (V_D - V_B) = \left(V_{R_2} - V_{R_x}\right) = 0 \tag{7.2}$$

For construction:

$$R_D = \frac{R_2}{R_1 + R_2} \ and \ R_B = \frac{R_x}{R_3 + R_x} \tag{7.3}$$

At the balance $R_D = R_B$, therefore

$$\frac{R_2}{R_1 + R_2} = \frac{R_x}{R_3 + R_x} \tag{7.4}$$

Consequently

$$R_2 \times (R_3 + R_x) = R_x \times (R_1 + R_2) \tag{7.5}$$

And

$$R_2 R_3 + R_2 R_x = R_x R_1 \times R_x R_2 \tag{7.6}$$

Finally

$$R_x = \frac{R_2 \times R_3}{R_1} \tag{7.7}$$

Detecting zero current with a galvanometer can be done with to extremely high precision. If R_1, R_2, and R_3 are known to high precision, R_x can be calculate with the same precision. Very small changes in R_x compromise the balance situation and can be immediately detected.

Strain gauge type choice

Basing on working principle is possible to distinguish mechanical, electric or piezoelectric strain gauge. With electrically resistive strain gages, which are the ones used for Rockfall Safety Network application, the applied load is transferred to the strain gage from the measurement object and causes a change in its electrical resistance.
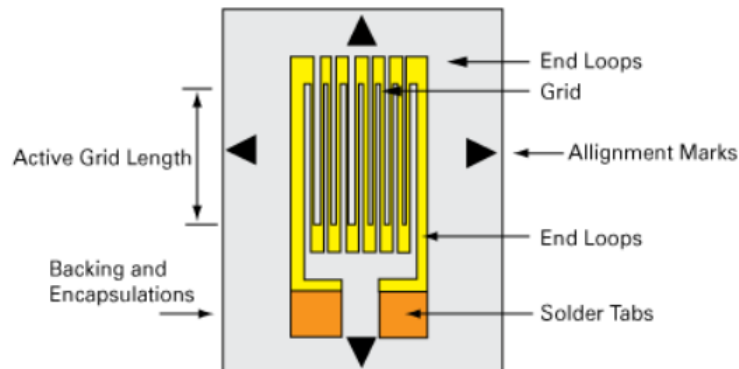
Figure 7.8: Scheme of strain gauge typical components

The metallic foil-type strain gauge consists of a grid of wire filament (a resistor) of approximately 0.001 in. (0.025 mm) thickness, bonded directly to the strained surface by a thin layer of epoxy resin (Figure 7.8). When a load is applied to the surface, the resulting change in surface length is communicated to the resistor and the corresponding strain is measured in terms of the electrical resistance of the foil wire, which varies linearly with strain (www.omega.com).

For the good functioning of the load cell is fundamental that the foil diaphragm and the adhesive bonding agent must work together in the strain transmission, the adhesive represents also as an electrical insulator between the foil grid and the surface.

The sensitivity of a strain gauge can be defined by the gauge factor, defined as the unit resistance change per unit length variation.

$$K = \frac{\Delta R/R}{\Delta l/l} \tag{7.8}$$

Gauge factor is related to Poisson's ratio μ by

$$K = 1 + 2\mu \tag{7.9}$$

The questions that should be considered during the selection of a type of strain gage from the ranges available from the manufacturers arise due to the variety of strain gage applications and due to the conditions affecting the strain gages during service. There is no strain gage that fulfils all requirements. For this reason, numerous different strain gages are available and are supplemented with special types when required (Hoffmann, 1989).

The individuation of the correct strain gauge type is fundamental for the load cell good functioning and could help to avoid expensive design mistakes and to obtain more reliable results.

In Table 7.1 the parameters which were took into account during the strain gauge choice are summarized according to the selection system proposed by Hoffmann (1989). The Author described the most important factors affecting the selection of a type of strain gage individuating five problem categories, which should be consider in the load cell design (measurement problem, mechanical conditions at the point of measurement, environmental conditions, mechanical conditions at the point of measurement and application conditions).

For Rockfall Safety Network application linear strain gauge type was chosen to build the load cells. Its technical features are reported in Table 7.2. This choice was based on the following considerations:

a) Grid length

If the object is sufficiently large, strain gages with 3 to 6 mm length of measuring grid are optimum, both with regard to quality and their ease of application. The arrangement of the connections to the side of the measuring grid and an extremely narrow grid design take account of space restrictions at the bonding point. The idea, often encountered, that a strain gage's sensitivity is dependent on its length is incorrect. A metal strain gage's sensitivity is proportional to the relative elongation, i.e. strain, and not to the absolute

elongation. In this respect the absolute length of the strain gage has no effect on its sensitivity;

Table 7.1: Strain gauge application features for the implementation of Rockfall Safety Network load cell

STRAIN GAUGE SELECTION CRITERIA

1. MEASUREMENT PROBLEM

Secondary: safety system

2. MECHANICAL CONDITIONS AT THE POINT OF MEASUREMENT

Stress state: uniaxial

Stress field topography: homogeneous

Type of loading: static

Ratio of the useful portion of the measurement to the disturbance portion: 0.5

3. ENVIRONMENTAL CONDITIONS

Measurement circuit: full bridge

Strain gauge supply: continuous

Cable: 2 meters of electric cable with 4 wires

4. MECHANICAL CONDITIONS AT THE POINT OF MEASUREMENT

Duration of measurement: long term

Temperature range: ±60°C

Disturbance effects: humidity, water, ice, external forces (shock, impact)

5. APPLICATION CONDITIONS

Component material: Steel 39NiCrMo3

Spatial conditions: heat shrink with resin

b) Grid width

Using a wider grid, if not limited by the installation site, improves heat dissipation and enhances strain gage stability. However, if the test specimen has severe strain gradients perpendicular to the primary axis of strain, consider using a narrow grid to minimize error from the effect of shear strain and Poisson strain;

c) Normal stress

Tensile and compressive stresses both come under this heading. Normal stresses arise when tensile or compressive forces act against one another. For the same cross-sectional area, the stress in the material is greater the stronger the force. For the same force the stress changes in inverse proportion to the cross-sectional area (large cross-sectional area leads to a low stress and small cross-sectional area generates high stress). The opposing force is often not recognizable, because it is applied by the fastenings or supporting parts. Normal stresses can also occur in moving objects, e.g. in the hawser between a tug and a

ship. Here the tug's tensile force is counteracted by the force from the water current. The mechanical stress is expressed by the quotient of the force F and the cross-sectional area A of the stressed material:

$$\sigma = \frac{F}{A} \tag{7.8}$$

d) Resistance

Nominal gage resistance is the resistance of a strain gage in an unstrained position. You can obtain the nominal gage resistance of a particular gage from the sensor vendor or sensor documentation. The most common nominal resistance values of commercial strain gages are 120 Ω, 350 Ω, and 1,000 Ω. Consider a higher nominal resistance to reduce the amount of heat generated by the excitation voltage. Higher nominal resistance also helps reduce signal variations caused by lead-wire changes in resistance due to temperature fluctuations;

e) Temperature compensation

Ideally, strain gage resistance should change in response to strain only. However, a strain gage's resistivity and sensitivity also change with temperature, which leads to measurement errors. Strain gage manufacturers attempt to minimize sensitivity to temperature by processing the gage material to compensate for the thermal expansion of the specimen material for which the gage is intended. These temperature-compensated bridge configurations are more immune to temperature effects. Also consider using a configuration type that helps compensate for the effects of temperature fluctuations.

Table 7.2: Chosen strain gauge technical features

Type	Linear
Nominal resistance	350 Ω
Active gauge length (a)	4.5 mm
Active gauge width)b)	3.2 mm
Matrix length (c)	9.8 mm
Matrix width (d)	2.2 mm
Maximum bridge voltage	12
Termination	Solder pads
Temperature compensation	Steel
Temperature range	-75÷200°C
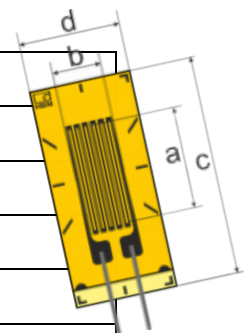
For the same type of strain gage, a change in the bridge configuration can improve the sensitivity to strain. In Table 7.3 a summary of the possible configurations is reported.

Table 7.3: Strain gauges configuration possibilities

Measurement Type	Quarter Bridge		Half-Bridge		Full-Bridge		
	Type I	Type II	Type I	Type II	Type I	Type II	Type III
Axial Strain	Yes	Yes	Yes	No	No	No	Yes
Bending Strain	Yes	Yes	Yes	Yes	Yes	Yes	No
Compensation							
Transverse Sensitivity	No	No	Yes	No	No	Yes	Yes
Sensitivity	No	Yes	Yes	Yes	Yes	Yes	Yes
Sensitivity at 1000 με [mV/V]	~0.5	~0.5	~0.65	~1.0	~2.0	~1.3	~1.3
Installation							
Number of Bonded Gages	1	1*	2	2	4	4	4
Mounting Location	Single Side	Single Side	Single Side	Opposite Sides	Opposite Sides	Opposite Sides	Opposite Sides
Number of Wires	2 or 3	3	3	3	4	4	4
Bridge resistors	3	2	2	2	0	0	0

(*) A second strain gage is placed in close thermal contact with structure but is not bonded.

For load cell construction, four strain gages are used to reproduce the full-bridge circuit and obtain maximum sensitivity and temperature compensation (Figure 7.9). Two of the gauges are usually in tension, and two in compression, and are wired with compensation adjustments.

The strain gauges were positioned on the load cells below at the point where the greatest deformation occurs when force is applied.
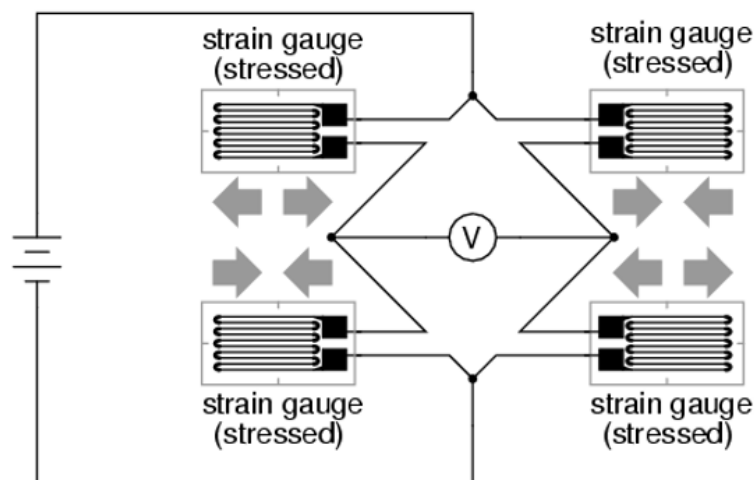
Figure 7.9: Full-bridge strain gauge circuit configuration used for load cell construction

Load cell construction

In order to measure forces acting on the barrier post head a load cell was specifically designed (Figure 7.10). Strain gauges were glued on it in order to create the full bridge circuit (Figure 7.11). The material used for load cell construction is steel 39NiCrMo3, which is the most widespread quenched and tempered one. This type of steel was chosen for its good hardenability, high toughness and excellent warm. It is particularly indicated load cell design because it reaches a high resistance even in relative big sections and is discreetly malleable with machine tools. It is mainly employed for gears, shafts, axles and for all those mechanical parts dynamically stressed.

Table 7.5 chemical composition and mechanical characteristics for section with 40 ≤ d ≤ 100 mm of steel 39NiCrMo3 are reported.
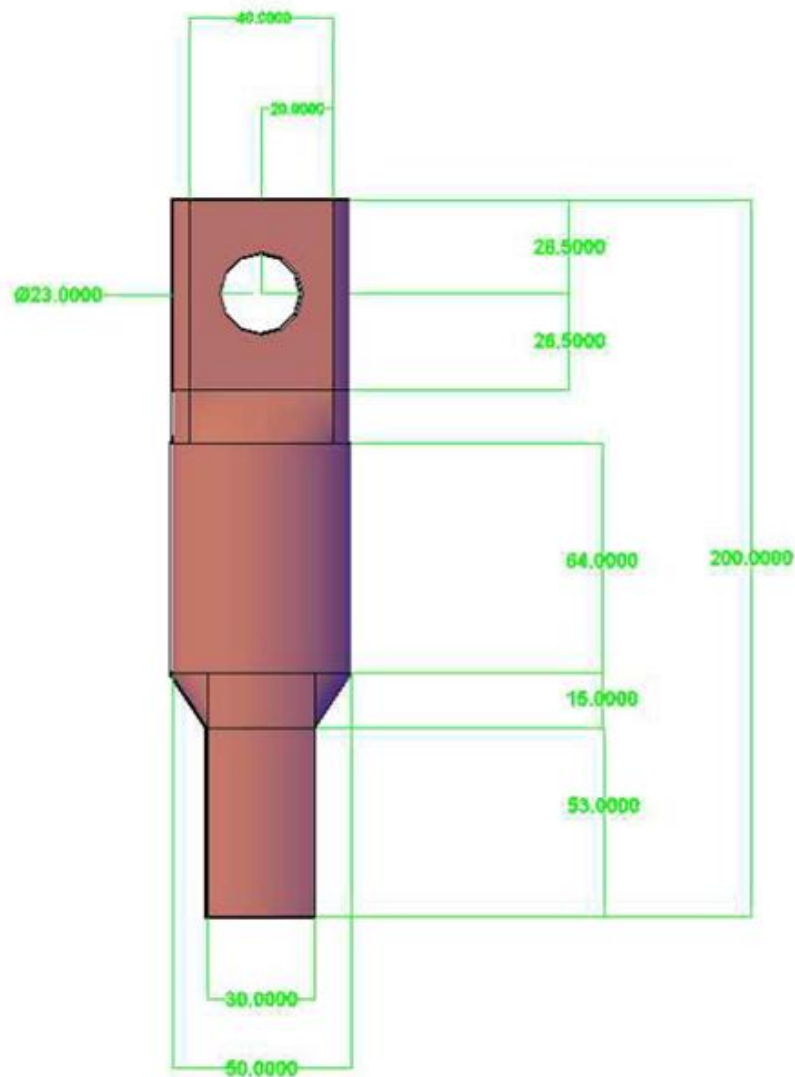
Figure 7.10: Sketch of load cell designed to measure the load acting on barrier upstream cable (quotes in mm)

Table 7.4: Chemical composition of 39NiCrMo3

C [%]	Si [%]	Mn [%]	P [%]	S [%]	Cr [%]	Mo [%]	Ni [%]
0.35 ÷ 0.43	≤ 0.40	0.5 ÷ 0.8	≤ 0.025	≤ 0.035	0.6 ÷ 1	0.15 ÷ 0.25	0.7 ÷ 1

Table 7.5: Mechanical characteristics of 39NiCrMo3 for the reduced section (EN 10083-1:2006) with a diameter 40 ≤ d ≤ 100 mm

Yield strength R_e min [N/mm^2]	Tensile strength R_m [N/mm^2]	Elongation A min [%]	Necking Z min [%]	Impact Toughness KV[b] min [J]
735	930÷1130	11	40	35

In spite of the high resistance of the chosen steel, the load cell geometry was designed to allow deformation perceptible by the strain gauges, for this reason the transversal circular section is only 50 mm, which is a good compromise between resistance and deformability.

In some cases, the cell capacity is lower than the breaking load of the barrier upstream cables along which it is installed; in order to not compromise the structural integrity of the system a by-pass solution, made by shackles and rope whit the same breaking load of the upstream cable, were implemented (Figure 7.13).
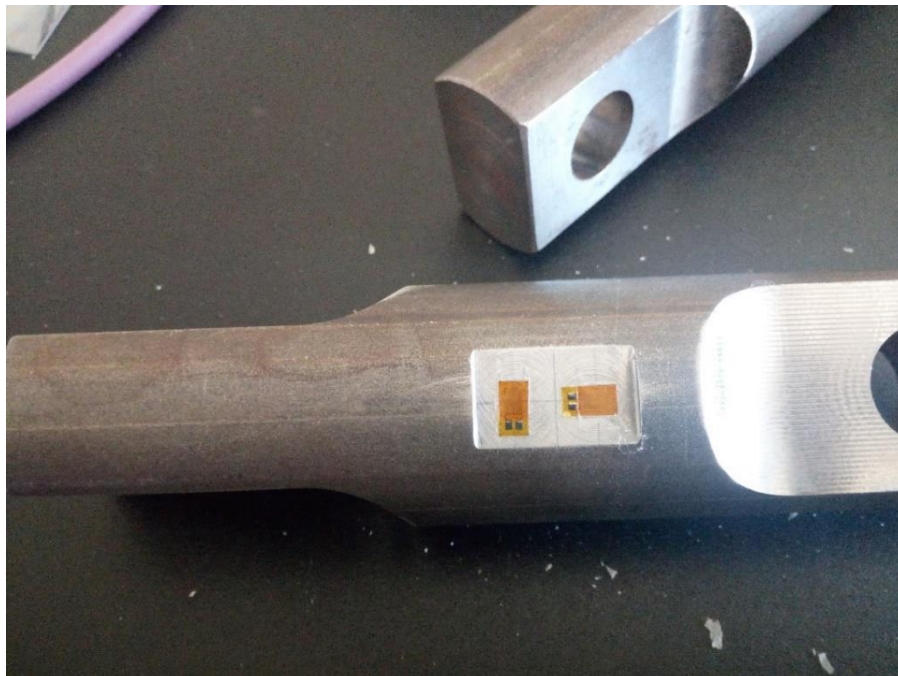
Figure 7.11: Strain gauge glued on steel to reproduce the Wheatstone full bridge
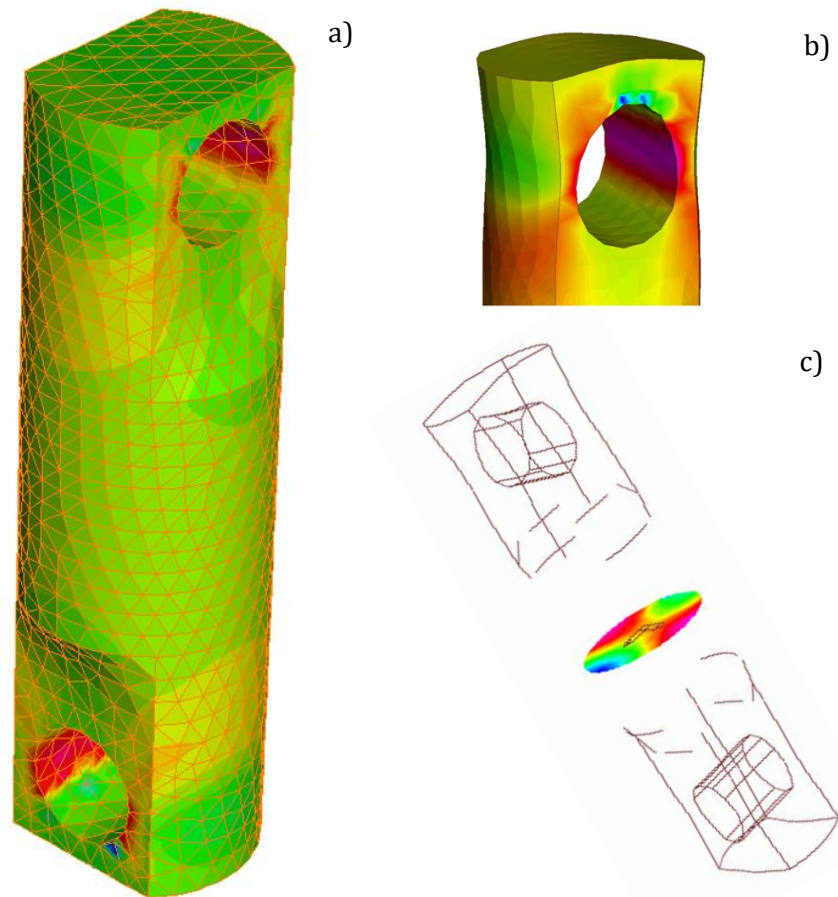
Figure 7.12: FEM modelling of the load cell; a) Entire model and domain discretization; b) Hole and c) Central section

In order to protect the resistance circuit against the atmospheric agents the strain gauges and the electric connections were covered with a special shrink and resin. To verify the good functioning of the final load cell configuration, FEM analysis were conducted (Figure 7.12) and laboratory tests were performed (Figure 7.14).
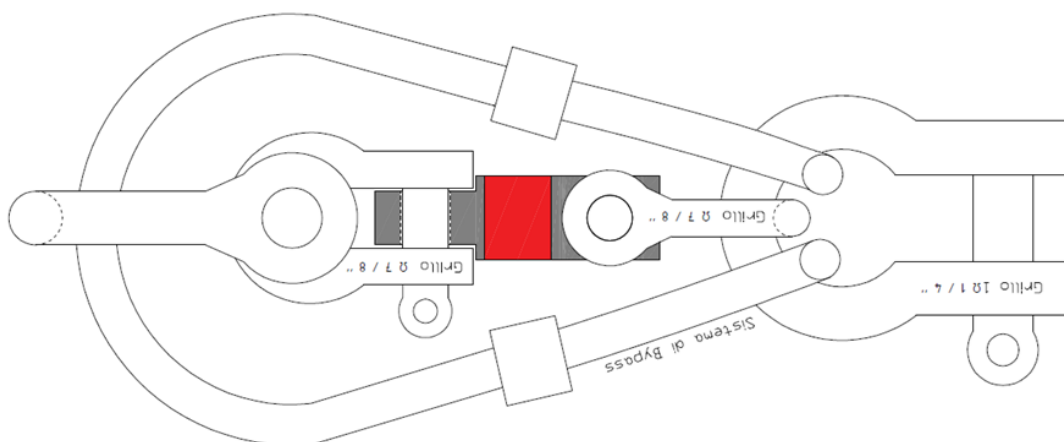
Figure 7.13: By-pass solution designed to keep the same breaking load of the barrier upstream cable

Figure 7.14: Laboratory test on load cell; a) Traction test configuration and b) load cell with circuit protection cover
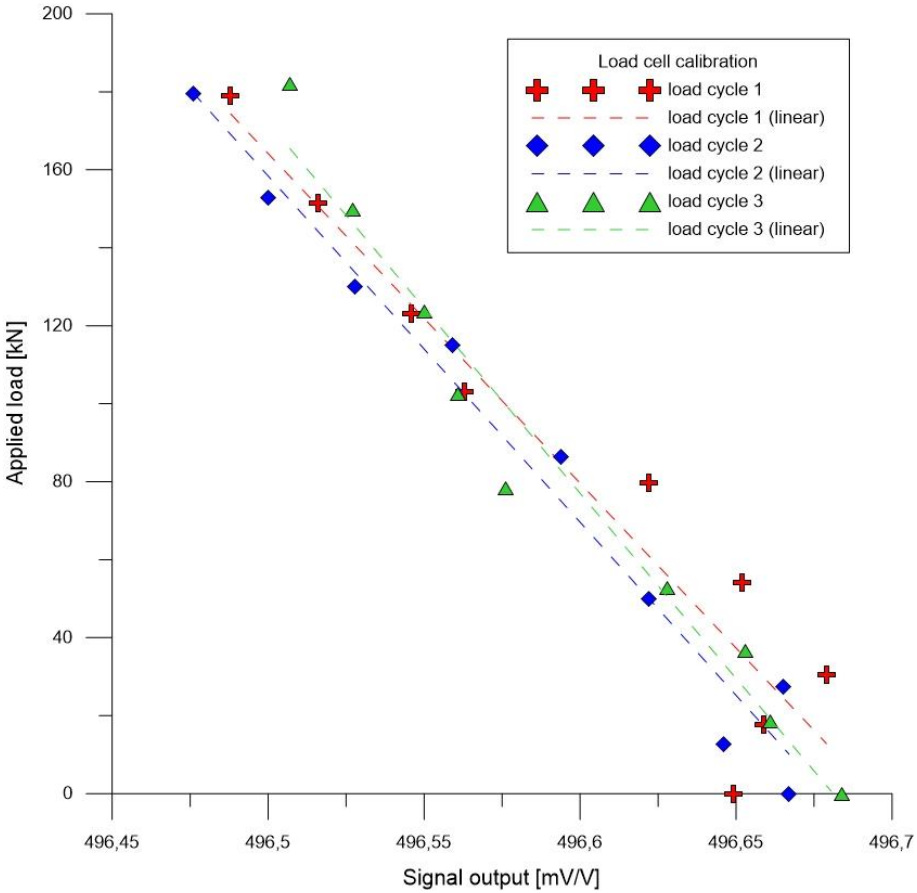
Figure 7.15: Load cell calibration cycles

During laboratory tests a traction force was applied and the output electric signal was registered for some defined load steps. In Figure 7.15 the results of calibration process are shown. Three load cycle were actuated, each one characterized by nine load steps. With the increase of the applied traction loads the signal output decreases with a trend which can be approximated with a line (dashed line in graph). For three different load cycle very similar line trends were obtained, this means that the device is reliable and the derived measurements are correct.

7.3.2. Inclinometer sensor

For the measurement of post inclination two different multi-parameter sensors are applied:

1) 3D MEMS (accelerometer, magnetometer and temperature sensor) able to identify post inclination change. This kind of sensor is much more adaptable and it is used when great displacements are expected (in the order of centimeters);

2) 2D electrolytic cell, which permits to monitor small displacement with a 10 times higher accuracy.

Technical features of 3D MEMS and 2D electrolytic sensors are reported respectively in Table 7.6 and in Table 7.7. Thanks to this configuration the system can measure both very little and big displacements, the use of this tool guarantees best quality of the displacement recorded. Moreover, the presence of two different types of sensor in the same system gives redundancy to results, which is fundamental to reduce the uncertainties and have robust interpretation of the phenomenon.

Table 7.6: MEMS sensor technical features

Sensors included	Accelerometer 3D, Magnetometer 3D, Thermometer;
Accelerometer range	± 2 g
Accelerometer sensitivity	0.244 mg/LSB
Accelerometer stability	± 0.008 %/°C
Accelerometer accuracy	± 1 %
Magnetometer range	± 1200 μT
Magnetometer sensitivity	0.1 μT /LSB
Magnetometer stability	± 0.1 %/°C
Magnetometer hysteresis	± 1 % FS
Thermometer sensitivity	0.96 °C/LSB
Thermometer repeatability	1 °C

...

Table 7.7: Electrolytic cell technical features

Sensors included	2D electrolytic cell
Electrolytic cell range (linear)	± 25°
Resolution of electrolytic cell	< 0.2 arc minutes (.003°)
Repeatability of electrolytic cell	± 0.1 %
Accelerometer accuracy	± 0.1 %
Temperature coefficient Null Scale	20 arc seconds/°C 0.1 %/°C

In order to verify the good functioning of the BPM module (composed of load cell, 3D MEMS sensor and 2D electrolytic cell) some laboratory test were performed (Figure 7.16). The results obtained are shown in Figure 7.17.
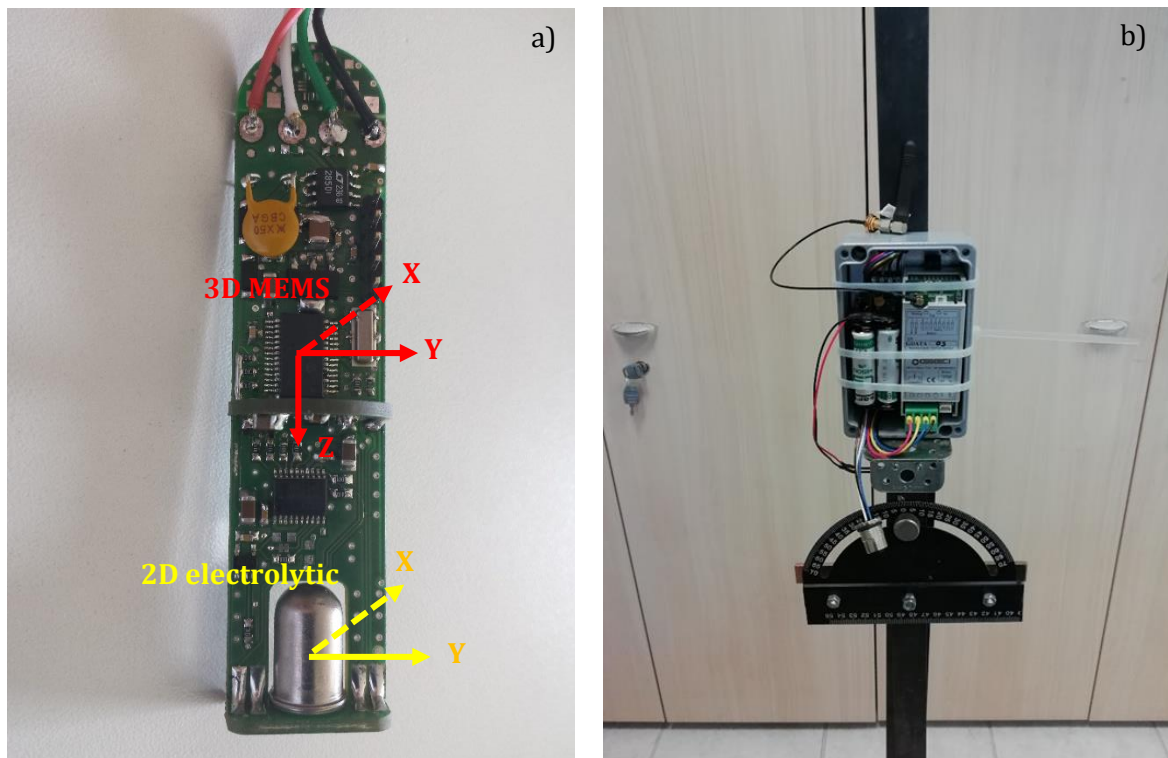
Figure 7.16: 3D MEMS and 2D electrolytic sensors used for measurement of the post inclination change; a) Pcb board on which MEMS and electrolytic sensor are fixed and b) Arrangement of sensor in the metallic protection box during calibration procedure

During the calibration procedure, BPM box orientation (containing both MEMS sensor and electrolytic cell) was changed.

Analyzing the results obtained from these experiments the linear relationship between the inclination and the electric signal is evident. In particular an increase of the BPM box angle

with the horizontal plane (Figure 7.16) generates a reduction of the electric signal magnitude if the X axis is considered; on the other hand, for the Y axes, a direct proportion between the BPM box orientation and the electric output signal exists.

However, the linear trends deriving from the calibration data are perfectly linear, attesting the good functioning of the inclinometer sensors.
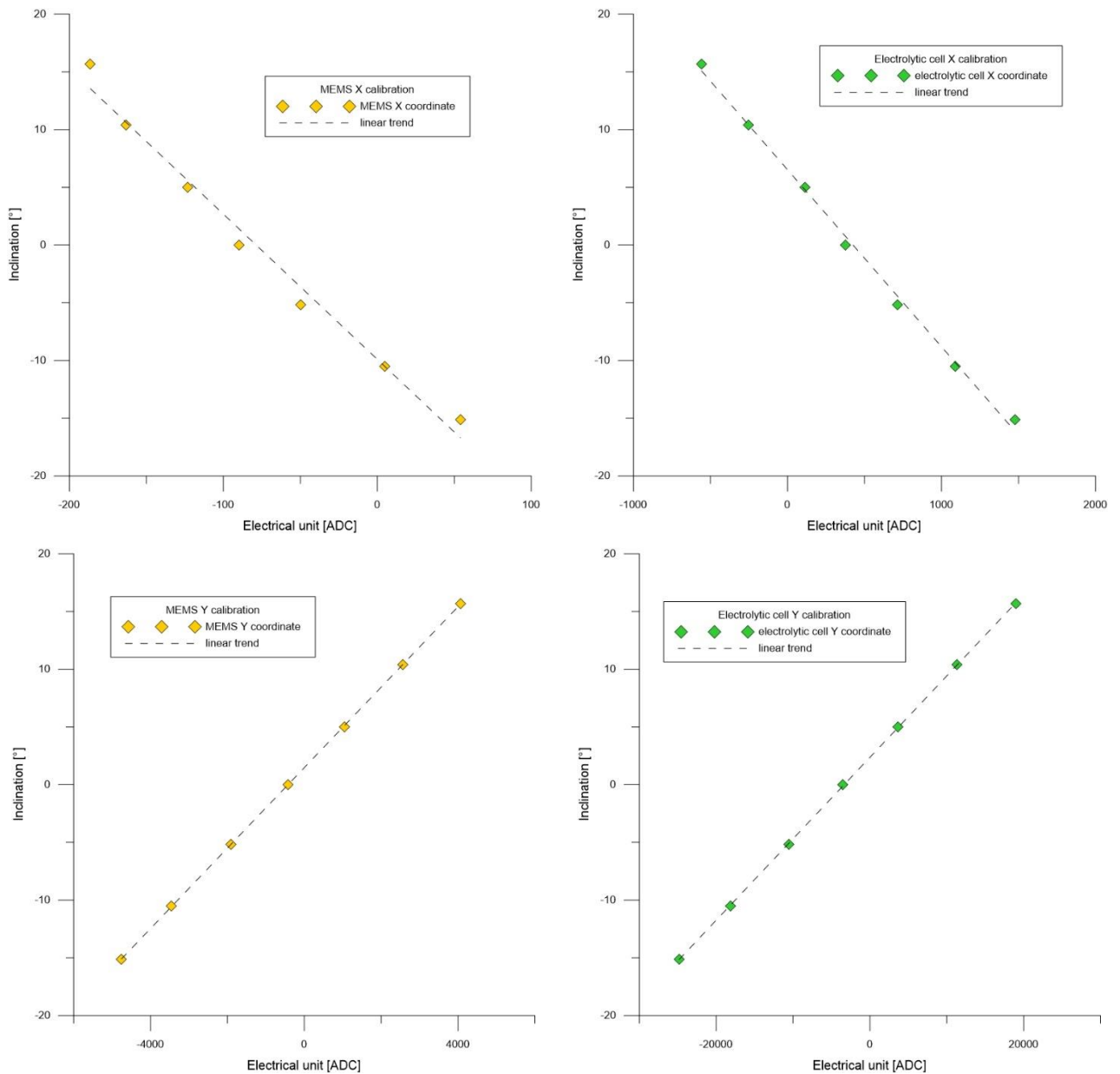
Figure 7.17: Inclinometric sensors calibration results; a) MEMS sensor – X coordinate; b) Electrolytic cell – X coordinate; c) MEMS sensor – Y coordinate and c) Electrolytic cell – Y coordinate

197

7.4. Software technology

The data provided by the monitoring system allow the creation of a database of measurements, which will constitute an extremely useful tool for slope phenomena interpretation. The relative barrier post head displacement recorded during each stage can immediately be compared with those anticipated during the design phase and an alarm can be automatically issued at the appearance of big differences.

Software technology was implemented in order to manage data deriving from monitoring processes (Figure 7.18). The main objectives of the system are to store, process and display all the information which can be useful for phenomena interpretation.

As was explained in the previous paragraphs, the mind of the system is the proprietary ASE801 data logger that manages the readings, the local storage and remote communication of data using GPRS/UMTS/HDSPA technology. The system can be optimized either for low power consumption or for early warning purposes by loading the appropriate proprietary operating system. The ASE801 data logger can manage other standard type of sensors, based on 4 20 mA and mV/V signals, making an ideal instrument for any monitoring needs. It locally stores data and makes them available through a web or ftp server with controlled access.
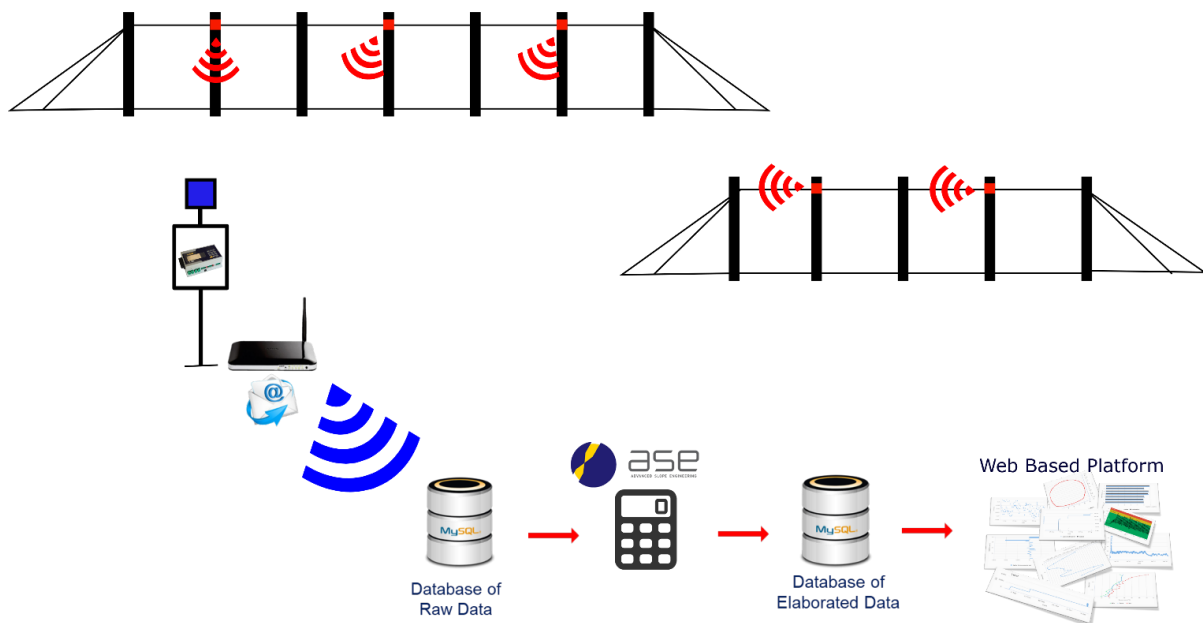
Figure 7.18: Schematization data acquisition, transmission and elaboration processes

Due to the frequent spatial distribution of barrier monitoring, the demand for a network of distributed data loggers has become a necessity. Moreover, their distribution in remote areas, frequently not reached by electrical power line, forces the development of data loggers with extremely low power consumption while maintaining the real time connection between each other and with the web. These needs have been summarized in the development of data logger

198

networking based on 6LoWPAN and 802.15.4e standards, achieving an unsurpassed level of networking resilience, reliability and scalability, as well as, up to 8x lower power consumption in harsh, dynamically changing RF environments.

The control unit reads each BPM module with a temporization defined by customers. This temporization can be changed during the monitoring. For each single reading of every module, the control unit collects 64 data and saves the average value. This operation is a first check of the data collected, reducing the influence of outliers. The aim of this particular process is to guarantees much reliable results.

Data recorded by datalogger are sent to a specific MySql database, which allows to storage and save them, avoiding any accidental loss of information. After saving, data are automatically processed through a dedicated program based on statistical self-learning algorithms, able to process the raw information and verify it in real-time, evaluating its validity. Results deriving from calculation process are saved in a specific section of the same database. The decision to divide the database into several sections was made in order to have both raw and elaborated data available.

The automatic software is able to highlight accidental or systematic errors during the elaboration, through statistical analysis. The algorithm automatically identifies outlier values and exclude them from the elaboration in order to give back a more reliable result. The software analyses the temporal evolution of a sample of data and, with an integrated analysis of different parameters, recognizes the validity of a certain datum. Doing this, there is a little time shift regarding reliability of the result and some changes could occur in the case of a real time monitoring. The time shift depends on the temporization of acquisitions. Data representation is possible thanks to a dynamic web-based platform, which gives an immediate indication of the phenomena occurring in the reference slope. The platform has a controlled access and can be consulted from different devices (PC, smartphone, etc.) and allow to:

a) Graph monitoring data with specific sampling periods defined by users;
b) Georeference the instrumented structures;
c) Export graphs in different formats (.csv, .xls, .jpg, .svg, .png, .pdf);
d) Correlate monitoring data deriving from different sensors.

Chapter 8: Conclusions and further developments

The present research work focuses on flexible and permeable barriers against rapid natural phenomena. These passive protection systems, thanks to their high deformation capacity, water permeability and easy installation, are widely used all over the world in order to stop the moving masses and dissipate the impact energy.

Rockfall and debris flow are very different events, due to their morphology, evolution and impact action. Nevertheless, both events are generally mitigated through flexible steel barriers. In Chapter 2: and Chapter 3: the most important features of debris flow and rockfall phenomena are illustrated and the definition given by different Authors are compared, in order to understand how they would interact with the protection system.

In Chapter 4: steel barrier structure is thoroughly described. In particular, Rockfall systems are designed with respect to the maximum energy capacity (expressed in kilojoules) they are able to absorb; on the other hand, a debris flow barrier is defined in terms of the total pressure acting on the net (in kilopascals). In both cases the structure is the same; the only difference is that the debris flow barrier, differently from rockfall ones, can be designed with or without support beams, depending on site characteristics.

Several breaking tests were performed on structural barrier components. The applied forces reproduced the same load conditions acting on single steel elements on site. The analysis of the results allows to characterize the barrier mechanical response during an impact phenomenon, providing useful information for a correct system design.

Particular attention was dedicated to the dissipation devices, whose aim is the moving masses kinetic energy absorption. During the study of this component it emerged that the old brake element featuring a pure friction function, during which friction is generated thanks to the sliding between a wire rope and a steel punched plate, shows several problems. The main issues are the unpredictable behavior, caused by the presence of local failures, and the activation energy, which is different case by case depending on many factors characterizing the rope-plate interaction. For these reasons a new dissipation device was designed, in order to obtain a more reliable mechanical response.

The new brake element is innovative, both for the geometry, unique and original, and the functioning principle. This device dissipates energy through its plastic deformation, thus avoiding the occurrence of friction or local failure phenomena, which would make the brake behavior irregular and unpredictable. It is able to dissipate high energy in a small time interval; this aspect reduces the overall structure deformations during an impact phenomenon and makes protection systems more safe, improving their performances.

The geometry of the new brake is original and different from all the solutions currently on the market, and was optimized in order to obtain the best performances in terms of absorbed energy and maximum possible elongation. The main advantages that this element demonstrated during production stages and static and dynamic test, compared with the old friction one, are: easier and smoother maintenance, minor response times, lower deformations with the same applied load, high reliability, lower cost and predictable behavior.

Thanks to structural components characterization and new brake device implementation, a new rockfall barrier, featuring an energy dissipation capacity of 1500 kJ, was designed. In Chapter 5: the results obtained from a real field tests on this new system are shown; the main objective was to verify the good functioning of the barrier which dissipates energy through the new brakes.

A first test was conducted on 10.11.2017 (Maximum Energy Level - MEL) and a second one on 29.11.2017 (Service Energy Level - SEL) in an old quarry in Biella, Italy. The set up and the corresponding monitoring and evaluation system were actuated according to the European guideline "ETAG 027" - edition February 2008, amended April 2013, used as European Assessment Document (EAD) - using the vertical throwing method.

The test setup was inspected after the end of each test and documented by photos. The system deformed as planned and the deformation was plastic, but not critical. In spite of that deformation, no damage occurred. Changes of post inclination were expected and consequently documented. Blocks were stopped safely during every test. Barrier response in terms of maximum elongation, openings and residual height satisfied the requirements imposed by the reference standard.

The energy approach is not applicable to debris flow barriers; due to its multi-phase nature, in which solid, fluid and air always interact and coexist, debris flow represents a very complex phenomenon and its interaction with barrier is very difficult to simulate. For a good design of the protection structures it is important to understand their behavior under the influence of debris events. For this purpose, Brighenti et al. (2013) proposed a simplified analytical model in order to evaluate the tensions acting on the supporting cables, knowing the geometry and the mechanical features of the flexible barrier and the characteristics of the impacting flow. The most difficult aspect is that the application of the simplified model regarded the calibration and validation of the input parameters.

In Chapter 6: the equations governing the model theory are presented and the results obtained from laboratory test on scaled barrier prototypes are reported; in particular, two different sets of experiments were performed:

1) Different static load combinations were imposed on each single rope and the induced deformations were measured using a theodolite, in order to evaluate the $r(z_j, z_i)$ function, which described the relationship between the barrier horizontal cables i and j. The displacement values estimated by a calculation program based on the Genetic Algorithm (GA) were compared

with the real rope deformation measured in laboratory; the difference between these values was minimized varying the area A_t of the transversal cable which simulates the secondary net and distributes a load fraction directly to each horizontal cable to the adjacent ones. When the optimum value of A_t was found, the comparison of the rope displacement values shows a good agreement between the experimental and numerical data. Thus, the obtained A_t value was used as input parameter during the second series of experiments;

2) A granular flow composed of aggregates of known particle size was released in a channel, at the end of which a scaled barrier prototype (the same type used during the first series of experiments) was installed. Several tests were carried out by varying the inclination of the channel and the geometry of the barrier. In order to estimate the input parameters required by the numerical model, the flow velocity was monitored using a PIV camera, while the height of the flow was monitored through ultrasonic level sensors and the forces on ropes were recorded thanks to load cells. The tension acting on ropes measured by load cells were compared with values returned by the Brighenti et al. (2013) analytical model, showing load trend during time very similar to reality: maximum tension values are close to the real ones measured at debris end, while final loads are generally slightly overestimated, but in some cases peak values are missing. This means that the numerical model gives a very good interpretation of the scaled phenomenon, but it misses some local peaks which characterized the real behavior of the impacted barrier. However, these peaks are generally lower than the maximum load values returned by the model, which may become an important tool in the preliminary design of flexible debris flow barriers.

Several times, flexible barriers are installed in sites very difficult to reach. For this reason, it is essential to acquire some information about their functioning over time; this can be made possible only by automatic monitoring systems, which can register the structural changes of the barriers and send remotely the acquired data without any direct intervention of technicians, saving time and money. Finally in Chapter 7: the development process concerning an innovative monitoring technology for barriers structural behavior control, called Rockfall Safety Network, is described.

The system can detect both high intensity events, identified as a steel post rotation and/or a brake deformation, and low intensity ones, recognizable by an increasing load acting on the upstream cables. It consists of a data acquisition unit connected with different BPM modules located near the steel post heads; the main components of a single BPM module are:

- MEMS sensor able to measure the three components of magnetic and gravitational fields;
- Electrolytic high-sensitivity cells, which has to obtain redundant data about post inclinations.
- Load cell designed to measure the traction loads acting on steel rope connected with post head;
- Radio Gdata device, necessary for the connection between the single monitoring BPM modules and the datalogger.

This system gives important information about the status of protection structures after their installation on site, checking the effective rate of work and the residual tension acting on barrier components and highlighting critical situations in progress. Moreover, a widespread installation of these system in unstable slopes will give indications about large scale phenomena occurrence and will generate an important database for a better territory risk mapping and management.

Therefore, the instrumented barriers play a double role: firstly, they are passive-protection systems against natural rapid events like rockfalls and debris flows, secondly they provide information about their efficiency over time and indicate the presence of eventual instability phenomena in progress.

The first possible development of this work concerns the validation of the analytical model described in Chapter 6: through the test of real-scaled debris flow barriers, following the same innovative procedure actuated in laboratory during the presented research activities for both the calculation of the function $r(z_j, z_i)$ and the flume test. These experiments will allow to verify the good functioning of the analytical model also for real-scaled debris systems, for different geometry and channel inclination values.

The last further development of this research concerns a planned installation of rockfall barriers featuring the new Rockfall Safety Network system. The intervention will be actuated in November 2018 in the locality of Vobarno (Brescia, Italy), in order to safeguard the infrastructures located downstream of an instable rock surface (Figure 8.1).

Figure 8.1: Instable area in Vobarno (Italy) where the instrumented barriers will be installed

Table 8.1: Rockfall Safety Network configuration for Vobarno installation

Barrier ID	Energy [kJ]	Length [m]	BPM modules distance [m]	N. of BPM modules
01	5000	60	20	3
02	5000	40	20	2

The barriers will be provided by Incofil Tech Srl and are characterized by an energy dissipation capacity of 5000 kJ and a total extension of 100 meters (two barriers 40 and 60 meters long). Flexible barriers will be equipped with a total of five BPM modules, which will be installed every 20 meters along the barriers length (i.e. one out of two posts will be monitored). The configuration of the monitoring system is illustrated in Table 8.1. This installation represents the first on site application of Rockfall Safety Network and will be very useful for the validation of the good functioning of the system over time.

Acknowledgements

References

Adams M, Nicks J and Lynch C (2015). Lateral deformation of GRS bridge abutments. Geosynthetics;

Agliardi F and Crosta GB (2003). A methodology for physically based rockfall hazard assessment. Natural Hazards and Earth System Science, 3:407-422;

Agliardi F, Crosta GB and Frattini P (2012). Slow rock-slope deformation. In Clague J and Stead D (eds.). Landslides: Types, Mechanisms and Modeling, Cambridge University Press, pp 207-221;

Agliardi F, Crosta GB and Zanchi A (2001). Structural constraints on deep-seated slope deformation kinematics. Engineering Geology, 59:83-102;

Agliardi F, Crosta GB, Frattini P, Malusà MG (2013). Giant non-catastrophic landslides and the long-term exhumation of the European Alps. Earth and Planetary Science Letters, 365:263-274;

Allaby A and Allaby M (1990). The concise Oxford dictionary of earth sciences: 410. Oxford Univ. Press;

Ambrosi C and Crosta GB (2006). Large sackung along major tectonic features in the Central Italian Alps. Engineering Geology, 83:183-200;

Ambrosi and Crosta G (2011). Valley shape influence on deformation mechanisms of rock slopes. Geological Society, London, Special Publications, 351:215-233;

Ancey C (2001). Debris flows and related phenomena. Balmforth, NJ and Provenzale A (eds), Geomorphological Fluid Mechanics, pp 528–547. Springer Berlin Heidelberg, Berlin, Heidelberg;

Armanini A (1997). On the dynamic impact of debris flows, Recent developments on debris flows. Lecture Notes in Earth Science, 64:208-224;

Azzoni A and De Freitas HM (1995). Experimentally gained parameters, decisive for rock fall analysis. Rock Mechanics and Rock Engineering, 28(2):111-124;

Azzoni A, Rossi PR, Drigo E, Giani GP and Zanetti A (1991). In situ observation of rockfall analysis parameters. Proceedings in 6th International Symposium on Landslides, 1:307-314;

Baoyuan X, Lixian W, Zhong Z and Guosheng W (1994). Torrent classification and mapping of hazard zones in mountain area of Beijing. Proceedings of the International Symposium on Forest Hydrology, Tokyo, Japan, October. 513-520;

Bardou E, Ancey C, Bonnard C and Vuillet L (2003). Classification of debris flow deposits for hazard assessment in alpine areas. In Proceedings of the 3rd International Conference on debris flow hazards mitigation, pp 799–808;

Baravalle S (1999). Caratterizzazione degli eventi pluviometrici connessi a colate detritiche in ambito alpino: applicazione alla provincia di Torino. Master degree Thesis;

Barton N (1978). Suggested methods for the quantitative description of discontinuities in rock masses, International Journal of Rock Mechanics and Mining Sciences, 15:319–368;

Bianco G (1999). Sulla valutazione dei volumi di materiale solido associati a eventi di debris-flow (quale elemento conoscitivo per la scelta delle misure relative al controllo e alla difesa idraulica dei territori e della rete idrografica di fondovalle). Atti dell'Accademia delle Scienze di Torino, 133: 1-28;

Boetticher A, Hubl J, Wendeler C, Volkwein A (2011). Modeling the impact of shallow landslides on flexible protection barriers. Marschallinger R, Zobl F (eds) Mathematical geosciences at the crossroads of theory and practice, Salzburg, Austria, pp 659–670;

Bozzano F, Esposito C, Franchi S, Mazzanti P, Perissin D, Rocca A and Romano E (2013). Analysis of a subsidence process by integrating geological and hydrogeological modeling with satellite InSAR data. Esa Living Planet Symposium Proceedings. Edinburgh (UK);

Bozzolo D and Pamini R (1986). Simulation of rock falls down a valley side. Acta Mechanica, 63:1-4;

Breien H, De Blasio F, Elverhoi A and Hoeg K (2008). Erosion and morphology of a debris flow caused by a glacial lake outburst flood, Western Norway. Landslides 5: 271-280. DOI: 10.1007/s10346-008-0118-3;

Brideau MA and Roberts NJ (2014). Mass movement in bedrock. Davies T (ed.), Landslide Hazards, Risks, and Disasters, pp 43–90. Elsevier, Amsterdam;

Brideau MA and Stead D (2012). Evaluating kinematic controls on planar translational slope failure mechanisms. Geotechnical and Geological Engineering, 30:991-1011;

Brideau, MA, Stead D and Couture R (2006). Structural and engineering geology of the east gate landslide, Purcell mountains, British Columbia, Canada. Engineering Geology, 84:183-206;

Brighenti R, Segalini A, Ferrero AM (2013). Debris flow hazard mitigation: a simplified analytical model for the design of flexible barriers. Computer and Geotechnics, 54:1-15;

Budetta P (2004). Assessment of rockfall risk along roads. Landslide and flood hazards assessment, 4(1):71-81;

Bunce C (1997). What factors are associated with the outcome of individual-focused worksite stress management interventions? Journal of Occupational and Organizational Psychology, 70:1–17;

Bunce C, Cruden D, and Morgenstern, N (1997). Assessment of the hazard from rockfall on a highway, Canadian Geotechnical Journal, 34:344–356;

Castanon-Jano L, Blanco-Fernandez E, Castro-Fresno D and Ballester-Muñoz F (2017). Energy dissipating devices in falling rock protection barriers. Rock Mechanics and Rock Engineering, 50:603–619;

Chau K, Wong R, Wu J (2002). Coefficient of restitution and rotational motions of rockfall impacts. International Journal of Rock Mechanics and Mining Sciences 39(1):69-77;

Corominas J, Copons R, Moya J, Vilaplana JM, Altimir J, Amigò J (2005). Quantitative assessment of the residual risk in a rockfall protected area. Landslides, 2:343–357;

Coussot P and Meunier M (1996). Recognition, classification and mechanical description of debris flows. Earth-Science Reviews, 40:209–227;

Cruden D and Varnes D (1996). Landslide types and processes. Turner AK (ed), Landslides investigation and mitigation. Transportation research board, US National Research Council, Washington DC, Special Report 247, pp 36–75;

Cubrinovski M, Henderson D and Bradley BA (2012). Liquefaction impacts in residential areas in the 2010–2011 Christchurch earthquakes. In: International Symposium on Engineering Lessons Learned from the Giant Earthquake, Tokyo, Japan, 3–4 Mar 2012, pp. 811–824;

Davies TR and McSaveney MJ (2012). Mobility of long-runout rock avalanches. Landslides Types, Mechanisms and Modeling, pp 50–58;

Davies TR, McSaveney MJ and Hodgson KA (1999). A fragmentation-spreading model for long-runout rock avalanches. Canadian Geotechnical Journal, 36:1096-1110;

D'Agostino V (1996). Analisi quantitativa e qualitativa del trasporto solido torrentizio nei bacini montani del Trentino orientale. A.I.I.A. - A.I.I. Scritti dedicati a Giovanni Tournon. Novara. 111-123;

Domaas U and Grimstad E (2014). Fjell- og steinskred. Høeg, K, and Lied K (eds), Skred: skredfare og sikringstiltak: praktiske erfaringer og teoretiske prinsipper. Oslo: Universitetsforlaget;

Dorren L (2003). A review of rockfall mechanics and modelling approaches. Progress in Physical Geography: Earth and Environment, 27(1);

Dorren L, Berger F, Jonnson M, Krautblatter M, Moelk M, Stoffel M and Wehrli A (2007). State of the art in rockfall – forest interactions, Schweizerische Zeitschrift fur Forstwesen, 158:128–141;

Dramis F and Sorriso-Valvo M (1994). Deep-seated gravitational slope deformations, related landslides and tectonics, 38:3-4;

Ekstrom G and Stark C (2013). Simple Scaling of Catastrophic Landslide Dynamics. Science, 339:1416-1419;

Erismann T and Abele G (2001). Dynamics of Rockslides and Rockfalls. Springer, Berlin.

Evans S, Roberts N, Ischuk A, Delaney K, Morozova GS and Tutubalina O (2009). Landslides triggered by the 1949 Khait earthquake, Tajikistan, and associated loss of life. Engineering Geology, 108:96-118;

Fanos A and Pradhan B (2017). Rockfall hazard assessment: an overview. Laser Scanning Applications in Landslide Assessment, pp 299-322;

Fannin RJ and Wise MP (2001). An empirical-statistical model for debris flow travel distance. Canadian Geotechnical Journal, 38(5):982–994;

Federal Office for the Environment and Swiss Federal Institute for Snow and Avalanche Research (2007). Defense structures in avalanche starting zones. Bern;

Ferrero AM, Segalini A, Umili G (2015). Experimental tests for the application of an analytical model for flexible debris flow barrier design. Engineering Geology, 185:33-42;

Frattini P, Crosta GB and Imposimato S (2012). Rockfall characterization and modeling. Clauge S (ed), Landslides Types, mechanism and modeling, Cambridge University Press, 267-281;

Geertsema M, Clague JJ, Schwab JW and Evans SG (2006). An overview of recent large catastrophic landslides in northern British Columbia, Canada. Engineering Geology. 83:120-143;

Geertsema M and Cruden D (2009). Rock movements in northeastern British Columbia. Landslide Processes: From Geomorphologic Mapping to Landslide Modelling. Strasbourg, France, pp 31-36;

Geertsema M and Cruden D (2008). Travels in the Canadian Cordillera. Fourth Canadian Conference on Geohazards, Quebec, Canada, pp 383-390;

Gerber W (1998): Waldwirkung und Steinschlag. Schwitter R (ed), Dokumentation der 14. Arbeitstagung der Schweizerischen Gebirgswaldpflegegruppe mit der FAN, Grafenort/Engelberg;

Gerber W: Beurteilung des Prozesses Steinschlag, Forstliche Arbeitsgruppe Naturgefahren (FAN), Herbstkurs Poschiavo, Kursunterlagen, WSL, Birmensdorf, 20 pp., 1994 (in German);

Goodman R and Shi G (1985). Block theory and its application of rock engineering. New Jersey, Prentice-Hall Englewood Cliffs;

Guthrie R.H, Friele P, Allstadt K, Roberts N, Evans S, Delaney K, Roche D, lague J, Jakob M (2012). The 6 August 2010 Mount Meager rock slide-debris flow, Coast Mountains, British Columbia: characteristics, dynamics, and implications for hazard and risk assessment. Natural Hazards Earth System Science, 12:1-18;

Hancox T and Perrin N (2009). Green Lake Landslide and other giant and very large postglacial landslides in Fiordland, New Zealand. Quaternary Science Reviews, 28:11-12;

Hantz D, Vengeon JM and Dussage-Peisser C (2003). An historical, geomechanical and probabilistic approach to rockfall hazard assessment. Natural Hazard and Earth System Science, 3:693-701;

Heidenreich B (2004). Small-and half-scale experimental studies of rockfall impacts on sandy slopes. PhD Thesis, Ecole Polytechnique Fédérale de Lausanne, Swiss;

Hodge R and Freeze A (1977). Groundwater flow systems and slope stability. Canadian Geotechnical Journal, 14(4):466–476;

Hoek E and Bray JW (1981). Rock Slope Engineering. Revised 3rd Edition, The Institution of Mining and Metallurgy, London, 341-351;

Hoffmann K (1989). An introduction to measurements using Strain Gages. Publisher: Hottinger Baldwin Messtechnik GmbH, Darmstadt;

Hübl J, Strauss A, Holub M and Suda J (2005). Structural mitigation measures. 3rd Probabilistic Workshop: Technical Systems + Natural Hazards, pp 24-25;

Hsü KJ (1975). Catastrophic debris streams (Sturzstroms) generated by rockfalls. Geological Society of America Bulletin, 86:129–40;

Hutchinson J (1988). General report: morphological and geotechnical parameters of landslides in relation to geology and hydrogeology. In Proceedings of the 5th International Symposium on Landslides, pp 3–35, Lausanne;

Hungr O, Corominas J and Eberhardt E (2005). Estimating landslide motion mechanism, travel distance and velocity. In International Conference on Landslide Risk Management, pp 99–128;

Hungr O and Evans SG (1988). Engineering evaluation of fragmental rockfall hazards. Proceedings 5th International Symposium on Landslides, Lausanne, Switzerland, 1:685–690.

Hungr O, Evans S, Bovis M and Hutchinson J (2001). Review of the classification of landslides of the flow type. Environmental and Engineering Geosciences, VII:221–238;

Hungr O, Leroueil S and Picarelli L (2014). The Varnes classification of landslide types, an update. Landslides, 11(2):167–194;

Iverson R (1997). The physics of debris flows. Reviews of Geophysics, 35(3):245–296;

Iverson R (2014). Debris flows: behaviour and hazard assessment. Geology Today, 30(1):15–20;

Jaboyedoff M, Dudt JP and Labiouse V (2005). An attempt to refine rockfall hazard zoning based on the kinetic energy, frequency and fragmentation degree, Natural Hazards Earth System Science, 5:621–632;

Jahn J., 1988. Entwaldung und Steinschlag, International Congress Interpraevent. Graz Conference Proceedings, vol. 1:185–198;

Jakob M (2005). A size classification for debris flows. Engineering Geology, 79: 151-161;

Johannesson T, Gauer P, Issler P and Leid K (2009). The design of avalanche protection dams. Technical report, European Commission, Climate Change and Natural Hazard Research - Series 2 Project report, 2009;

Keller EA (2011). Environmental Geology, Upper Saddle River, NJ, Pearson Education;

Kinakin D and Stead D (2005). Analysis of the distribution of stress in natural ridge forms: implications for the deformation mechanism of rock slopes and the formation of Sakung. Geomorphology, 65:85-100;

Kramer SL (2013). Lateral spreading. Bobrowsky PT (ed.), Encyclopedia of Natural Hazards, p 623;

Krautblatter M and Dikau R (2007). Towards a uniform concept for the comparison and extrapolation of rockwall retreat and rockfall supply. Geografiska Annaler 89:21-40;

Krummenacher B (1995). Modellierung der Wirkungsraume von Erd-und Felsbewegungen mit Hilfe Geographischer Informationssysteme (GIS). Schweizerischen Zeitschrift fur Forstwesen, 146:741–761;

Legros F (2002). The mobility of long-runout landslides. Engineering Geology, 63(3-4):301-331;

Lo D (1997). Review of natural terrain landslide debris-resisting barrier design. Geotechnical Engineering Office Report N. 104.

Loew S and Strauhal T (2013). Pore pressure distributions in brittle translational rockslides. Italian Journal of Engineering Geology and Environment, pp 181-191;

Luckman BH (2013). Processes, Transport, Deposition, and Landforms: Rockfall. Treatise On Geomorphology, 7:174-182;

Marchelli M (2018). Debris flow interaction with open rigid barriers - a DEM-LBM approach for trapping efficiency and impact force analysis. Polytechnic University of Turin, doctoral dissertation;

Mazzoccola D and Hudson J (1996). A comprehensive method of rock mass characterization for indicating natural slope instability. Quarterly Journal of Engineering Geology and Hydrogeology 29(1):37-56;

McCalpin JP and Irvine JR (1995). Sackungen at the Aspen Highlands Ski area, Pitkin County, Colorado. Environmental and Engineering Geoscience, 1:277-290;

McColl S (2012). Paraglacial rock-slope stability. Geomorphology, 153-154:1-16;

McDougall S and Hungr O (2005). Dynamic modelling of entrainment in rapid landslides. Can. Geotech. J, 42: 1437-1448. DOI: 10.1139/T05-064;

Mentani A (2015). Modelling the dynamic response of rockfall protection barriers. University of Bologna, doctoral dissertation;

Meissl G (1998). Modellierung der Reichweite von Felsstürzen. Fallbeispeile zur GISgestützten Gefahrenbeurteilung aus dem Beierischen und Tiroler Alpenraum. Innsbrucker Geografischen Studien 28. PhD Thesis, Universität Innsbruck, Innsbruck, 249;

Moro M, Chini, M, Saroli M, Atzori S, Stramondo S and Salvi S (2011). Analysis of large, seismically induced, gravitational deformations imaged by high-resolution COSMO-SkyMed synthetic aperture radar. Geology 39:527-530;

Pedrazzini E, Komarova N, Rentsch D and Vitale A (2013). Traffic routes and signals for the tonoplast. Traffic, 14:622–628;

Philip H and Ritz JF (1999). Gigantic paleolandslide associated with active faulting along the Bogd fault (GobiAltay, Mongolia). Geology, 27(3):211–14;

Pierson T (1986). Flow behavior of channelized debris flows Mount St. Helens Washington. In Hillslope Processes, pp 269–296. Boston, Allen & Unwin;

Pierson TC and Costa JE (1987). A rheological classification of subaerial sediment-water flows. Geological Society of America: Reviews in Engineering Geology, VII:1–14;

Pierson L, Davis S, and Van Vickle R (1990). Rockfall Hazard Rating System – Implementation Manual. Federal Highway Administration (FHWA), Report FHWA-OR-EG-90–01, FHWA, U.S. Department of Transportation;

Piton G and Recking A (2016). Closure to Design of Sediment Traps with Open Check Dams. I: Hydraulic and Deposition Processes. Journal of Hydraulic Engineering 142(10);

Popescu ME (2002). Landslide causal factors and landslide remediatial options. Proceedings of 3rd international conference on landslides, slope stability and safety of infrastructures, Singapore, pp 61-81;

Procter J, Cronin S and Zernack A (2009). Landscape and sedimentary response to catastrophic debris avalanches, western Taranaki, New Zealand. Sedimentary Geology, 220:271-287;

Ritchie A (1963). Evaluation of rockfall and its control. Highway Research Record Washington DC, Highway Research Board, National Research Council, 17, 13–28;

Rickenmann D (1999). Empirical Relationships for Debris Flows. Natural Hazard, 19: 47-77;

Rickenmann D and Zimmermann M (1993). The 1987 debris flows in Switzerland: documentation and analysis. Geomorphology, 8(2-3): 175-189;

Romana M (1988). Practice of SMR classification for slope appraisal, Proceeding in 5th International Symposium on Landslides, Balkema, Rotterdam, 1227–1229;

Roberts NJ, Evans SG (2013). The gigantic Seymareh (Saidmarreh) rock avalanche, Zagros Fold-Thrust Belt, Iran. Journal of the Geological Society, 170(4):685;

Rouiller JD, Jaboyedoff M, Marro C, Philippossian F and Mamin M (1998). Pentes instables dans le Pennique valaisan, Mat-terock: une methodologie d'auscultation des falaises et de detection des éboulements majeurs potentiels. Rapport final ´ PNR31, VDF, Zurich, 239;

Savage W and Varnes D (1987). Mechanics of gravitational spreading of steep-sided ridges. Bulletin of the International Association of Engineering Geology, 35:31-36;

Seed HB and Wilson SD (1967). The Turngaian Heights landslides, Anchorage Alaska. American Society of Civil Engineers Proceedings, Soil Mechanics and Foundations Division Journal, pp 325-353;

Sharpe CF (1938). Landslides and related phenomena. Columbia University Press, New York;

Scheidegger AE (1973). On the prediction of the reach and velocity of catastrophic landslides. Rock Mechanics, 5:231–236;

Schweigl J, Ferretti C, Nossing L (2003). Geotechnical characterization and rockfall simulation of a slope: a practical case study from south Tyrol (Italy). Engineering Geology, 67:281–296;

Schwitter R (1998). Zusammenfassung und Schlussfolgerungen. R Schwitter (ed), Dokumentation der 14. Arbeitstagung der Schweizerischen Gebirgswaldpflegegruppe mit der FAN 1998, Grafenort / Engelberg, 1–5;

Soldati M (2013). Deep-seated gravitation slope deformation. Bobrowsky PT (ed.), Encyclopedia of Natural Hazards, pp 151-155;

Stini J (1910). Die Muren. Verlag der Wagner'shen Universitätsbuchhandlung, Innsbruck, 1910 edition;

Takahashi T (1978). Mechanical characteristics of debris flow. Journal of Hydraulic Engineering, 104:1153–1169;

Takahashi T (2007). Debris flow. Mechanics, Prediction and Countermeasures. Taylor & Francis/Balkema, London, 2007 edition;

Twiss R and More E (1992). Structural Geology 1st edition. WH Freeman & Co., San Francisco;

Updike RG, Olsen HW, Schmoll HR, Kharaka YK and Stoke KH (1988). Geologic and geotechnical conditions adjacent to the Turnagain Heights Landslide, Anchorage, Alaska. Bulletin of the United States Geological and Geographical Survey of the Territories, p 40;

Urciuoli G and Pirone M (2013). Subsurface drainage for slope stabilization. Landslide Science and Practice, 6:577-586;

Van Dine DF (1996). Debris Flow Control Structures for Forest Engineering. British Columbia, Ministry of Forest Research Program;

Varnes D (1954). Landslide types and processes. In E.B. Eckel (eds), Landslides and Engineering Practise (special report 28). Highway Research Board, National Academy of Sciences, Washington, 20-47;

Varnes D (1978). Slope movement types and processes. Schuster RL, Krizek RJ (eds) Landslides, analysis and control, special report 176. Technical report, Transportation research board, National Academy of Sciences, Washington DC;

Vagnon F (2016). Theoretical and experimental study on the barrier optimization against debris flows risk. University of Turin, doctoral dissertation;

Varnes D, Radbruch-Hall D and Savage W (1989). Topographic and structural conditions in areas of gravitational spreading of ridges in the western United States. US Geological Survey Professional Paper, 1496, 28;

Woltjer M, Rammer W, Braune M, Seidl R, Mohren G and Lexer M (2008). Coupling a 3D patch model and a rockfall module to assess rockfall protection in mountain forests, Journal of Environmental Management, 87, 373–388;

Wyllie D and Mah C (2004). Rock Slope Engineering. Revised 4rd Edition;

Yamada M, Kumagai H, Matsushi Y and Matsuzawa T (2013). Dynamic landslide processes revealed by broadband seismic records. Geophysical Research Letters, 40(12):2998–3002;

Zollinger F (1985). Debris detention basins in the European Alps. International Symposium on Erosion, Debris Flow and Disaster Prevention, Tsukuba, Japan, pp 433-438.